MKID Microscopes

BENJAMIN SHAW

SHAW, BENJAMIN (2023) MKID Microscopes. Doctoral thesis, Durham University.

MKID Microscopes

PhD Thesis

Benjamin Shaw

Supervisors: John Girkin, Kieran O'Brien
A thesis presented for the degree of
Doctor of Philosophy

Centre for Advanced Instrumentation
The University of Durham
United Kingdom
December 2023

Abstract

This thesis describes an investigation of the potential of **M**icrowave **K**inetic **I**nductance **D**etectors (MKIDs) to be employed as the photon detector in a confocal, fluorescence microscope. As far as can be ascertained, the results presented here are the first *ex-vivo* observations by such an instrument, an application which has not yet been described in the published literature.

MKID arrays are capable of measuring both the energy and the arrival time of individual photons without false counts, across a wide wavelength range. Consequently they have the potential to become an important technology for the next generation of biomedical photonics. These detectors will enable highly-optically efficient, photon-limited, hyperspectral microscopy. This application will be an advantage in a field which benefits considerably from ultra-high sensitivity of photon-limited imaging for very low power illumination. Broad wavelength detectors with energy resolution in the near-infrared (NIR) range are of value to the field of bioimaging as more and more instruments are designed to observe longer wavelengths because they allow deeper tissue imaging, with reduced phototoxicity. A significant finding central to this work is the confirmation that MKIDs with a spectral resolution (R) $\approx$ 10 are able to resolve and separate the spectra of two fluorescent dyes that have been excited by the same illumination source, while also quantifying the number of photons required to attain the required confidence level. Several analytical tools were created and compared using the mean squared error (MSE) method as the comparison metric to determine which was most appropriate to leverage in a given situation based on their simulated performance. These analysis techniques were then applied to three scenarios.

Binomial tests such as the KS test, were found to be of limited use, but did succeed in correctly identifying 95.85% of 1000 fluorophores when only given 4 photons each time (assuming all photons were from Nile Red fluorophore or Yellow-Green fluorophore). The number of photons required for a given certainty is highly dependent on, and will increase dramatically if, the spectra observed are closer in wavelength, have a broader spectrum, or if there is a noise source such as autofluorescence.

This relationship, while promising is likely to be far higher for fluorophores which are not as widely spectrally separated as the fluorophores chosen, and requires further scrutiny if this is found to be a desirable use case by scientists in the field.

If there is prior knowledge of the fluorescent spectra expected (the *reference spectra*), then it is possible to employ a mathematical model of the fluorophores, and a least mean squares fitting technique, such as χ^2 analysis or *scipy.curve_fit*. It appeared to be the case that *scipy.curve_fit* provided a better fit in low photon counts, whereas χ^2 was superior in high photon counts but this was not thoroughly tested. The absence of readout noise meant subjects could be positively identified to a confidence of 5σ using as few as between 43 and 84 photons.

In the absence of fluorophores (*reference spectra*), two blind spectral un-mixing methods were attempted. Non-negative matrix factorisation (NMF) was found in analysis to have a similar effectiveness to non-blind techniques (with known fluorophores *reference spectra*). This blind technique was applied to the *ex vivo* sample of a nematode worm (see Chapter 8.3) to successfully obtain an image which resembled a reference image taken from a commercial microscope, confirming the MKID microscope was indeed capable of discerning between fluorescent markers based on spectral information.

This research found that MKIDs are a powerful and effective tool, one that promises to be particularly advantageous in the field of biomedical photonics. These developments provide a sound foundation for further work in this domain and related fields.

Acknowledgements

I would like to thank my supervisors John Girkin and Kieran O'Brien, as well as the CfAI team. To my parents, sister and incredible friends and the family added along the way, thank you for your support. Andy, Haz and Chris, who were always there for the difficult questions.

I would like to acknowledge the support of the EPSRC.

Contents

Declaration

The work in this thesis is based on research carried out at the Centre for Advanced Instrumentation, Department of Physics, University of Durham, England. No part of this thesis has been submitted elsewhere for any other degree or qualification, and it is the sole work of the author unless referenced to the contrary in the text.

List of Figures

List of Tables

Nomenclature

ADC analogue-to-digital converter

ADU analogue-digital units

ARCONS **Ar**ray **C**amera for **O**ptical to **N**ear-IR **S**pectrophotometry

au arbitrary unit

BCS Bardeen–Cooper–Schrieffer

CAD computer aided design

CCD charge-coupled device

CDF cumulative distribution function

CMOS complementary metal-oxide semiconductor

DAC digital-to-analogue converter

DARKNESS DARK-speckle Near-infrared Energy-resolving Superconducting Spectrophotometer

DDC digital down conversion

DIC differential interference contrast

E photon energy

EMCCD electron-multiplying CCD

F Fano factor

f_0 resonant frequency

FLIM fluorescence lifetime imaging microscopy

FOV field of view

FPGA field programmable gate array

FWHM full width at half maximum

h the Plank constant

η efficiency factor

HEMT high-electron-mobility transistor

I' in-phase

IDC **i**nter**d**igitated **c**apacitor

IQ in-phase and quadrature

IR infrared

JPL Jet Propulsion Laboratory

JSON **J**ava**S**cript **O**bject **N**otation

k_B Boltzmann constant

KS test Kolmogorov–Smirnov test

LC inductance-capacitance

LED light-emitting diode

LMS least-mean square

LO local oscillator

LSM light-sheet microscopy

MEC MKID Exoplanet Camera

MKID **M**icrowave **K**inetic **I**nductance **D**etector

MSE mean squared error

ν photon frequency

NA numerical aperture

ND neutral-density

NIR near-infrared

NMF non-negative matrix factorisation

$n_{photonsMAX}$ maximum number of photons per fluorophore, per pixel

N_{qp} number of quasiparticles

OIR optical and infrared

PCA principle component analysis

PLIM phosphorescence lifetime imaging microscopy

PMT photomultiplier tube

PDF probability density function

Q' quadrature

QE quantum efficiency

Q_r quality factor

QY quantum yield

R spectral resolution

RGB red, green and blue

S_{21} ratio of the power leaving port 2 and the power entering port 1

SMA SubMiniature version A

SNR signal-to-noise ratio

SNSPD superconducting nanowire single-photon detector

SPAD single-photon avalanche diode

SPIM selective/single plane illumination microscopy

SRON Netherlands Institute for Space Research

STJ Superconducting Tunnelling Junction

T_C critical temperature

T_{OP} operating temperature

τ decay constant

T_C critical temperature

TES transition edge sensor

UCSB University of California, Santa Barbara

VNA vector network analyser

Chapter 1

Introduction

Optical microscopy has been an indispensable tool in our endeavour to understand the natural world, giving us deep insights into the world. Since the first recorded use in 23–79 AD by ’Pliny the Elder’, we have seen great leaps in its utility and possibilities resulting from the invention of film in 1839, and again even more so following in the advent of the MOSFET in 1959, leading to CCDs and CMOS imagers (invented in the late 1960s and 1970s).

Advances in computers have also further accelerated the development and expanded the range and scope of potential applications by permitting gathered information to be rapidly analysed. With each subsequent technological advancement, new possibilities arise.

From a more technical point of view, the ideal optical microscopes would detect photons with a high efficiency and high signal-to-noise ratio (SNR), while utilising wavelength information to distinguish between different features of interest. There are also some advantages to using light which is longer wavelength like NIR and infrared (IR) to allow image deeper into living tissue, at a wavelength which causes less perturbations and damage to cells.

MKIDs are a type of superconducting detector, capable of extracting wavelength information and arrival time from a single photon without inefficient dispersion optics. They do this without read-noise or dark current (Mazin et al., 2019a), so are usually thought of as ’noise free’ in the optical and infrared (OIR) wavelength range. They lend themselves well to being made into an array and to readout via room temperature electronics. For these reasons, they are currently revolutionising many areas of Astronomy, in particular as Integral Field Spectrographs (which provides spectral information over a FOV) because they require fewer optical components, and can extract more information from a given number of photons, than other systems.

By this logic, microscopes would benefit greatly from MKIDs, because these quantum detectors would be ultra-sensitive, spectroscopic, broadband, wide field microscope detectors with a high effective frame-rate.

The aim of the thesis is to perform a proof of concept experiment which demonstrates that MKIDs are capable of gathering spectral information from across a sample and differentiating features, to provide an MKID microscope prototype.

1.1 Background

This section explains how MKIDs can improve the current field of microscopy, and outlines the first steps taken towards the concept being verified and demonstrated. It starts with giving an overview of optical microscopy (which is expanded in Chapter 3) and justifies why confocal microscopes are a good imaging modality to start with.

Since their invention in 2003 (Peter K. Day, Henry G. LeDuc, Benjamin A. Mazin, 2003), MKIDs have had their utility proven in Astronomy, but they have not yet been applied to image biological samples. As stated in the Introduction (Chapter 1), one aim of the present work is to assess and demonstrate the advantages that they could bring to the field. To facilitate this, it is necessary to assess the state of the art at present regarding optical microscopy detection and also MKID applications.

Some current state of the art microscopes use detectors such as semiconductor-based charge-coupled device (CCD) and complementary metal-oxide semiconductor (CMOS) arrays, but microscopes exist with other detector types (Lau et al., 2023) such as photomultiplier tubes (PMTs), single-photon avalanche diodes (SPADs) (Slenders et al., 2021; Bruschini et al., 2019), and increasingly frequently, superconducting detectors such as transition edge sensor (TES) (Konno et al., 2020; Niwa et al., 2017), Superconducting Tunnelling Junctions (STJs) (Jorel et al., 2005) and superconducting nanowire single-photon detector (SNSPD) Buschmann et al. (2023). Detectors used in the field of astronomy also greatly benefit from energy sensitive detectors so have been thoroughly investigated O'Connor et al. (2019).

Astronomical instruments have already been made with MKID devices, and include **Ar**ray **C**amera for **O**ptical to **N**ear-IR **S**pectrophotometry (ARCONS) (O'Brien et al., 2011), DARK-speckle Near-infrared Energy-resolving Superconducting Spectrophotometer (DARKNESS) (Meeker, 2017), MEC (Walter et al., 2018) and others. One of the advantages of MKIDs is their intrinsic ability to provide information on the energy (wavelength) of a photon without the need for spectrally dispersive optics or dichroic filters. Although in the early stages of development, current MKID already have sufficient R to resolve the spectra of some fluorophores and can therefore perform spectral unmixing. As the technology matures and Rs improve, more will become possible in these regards.

In application, optical imaging systems such as microscopes are used to observe living cells amongst other things. In order to perform observations, they rely on light interacting with the sample in some way, and subsequently distinguishing the photons of interest (the signal) from noise in the system (in the form of un-useful photons from the system, or signal introduced by the electronics equipment with which they are read out). A central technique by which this is facilitated is performed by staining features of interest with different species of fluorophore (see Chapter 3.1.6), each functionalised to produce distinct fluorescence spectra. Taking separate images of the resulting sample under illumination with a monochrome detector such as an electron-multiplying CCD (EMCCD), in conjunction with dichroic elements to isolate each stain to produce images shown in 1.1(b), gives the required information to distinguish the fluorescent labels. Spectrally resolving detectors have the potential do this in a single exposure, which is highly desirable in many contexts.

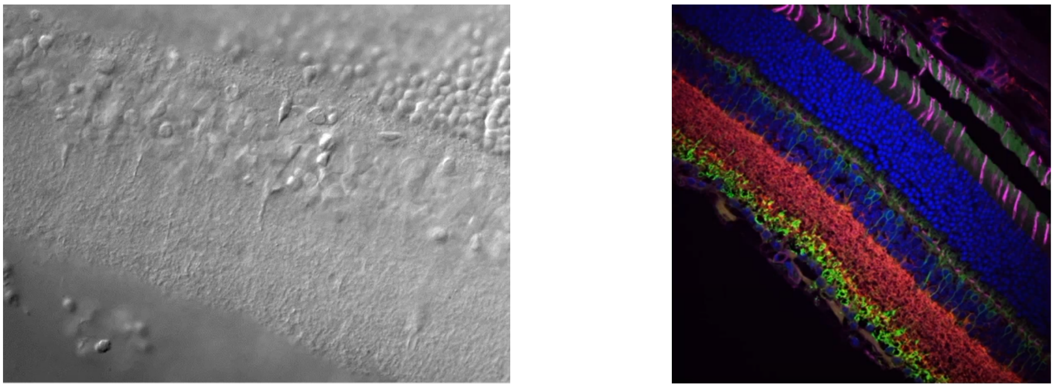

((a)) differential interference contrast (DIC). Credit Dr. Josh Singer, U Maryland

((b)) Fluorescence. Credit Dr Robert Fariss, National Institutes of Health

Figure 1.1: Image of mouse retina, illustrating the amount of information provided by fluorescence microscopy.

Biology is the study of living organisms, so is fundamentally the study of ever changing, dynamic systems. These changes occur on timescales of centuries to effectively instantaneous, and one limitation to our understanding is constituted by our (in-)ability to resolve these features and dynamics with sufficient temporal resolution. Many future discoveries will come about from observing samples in the time domain. MKIDs have a particular advantage here, as they have microsecond time-of-arrival resolution for each photon detected, whilst not sacrificing spectral and spatial resolution relative to alternative detector technologies.

1.2 Motivation

In the quest to obtain deeper understanding of biological samples through imaging, the ideal tool would extract as much information from each photon as possible, while having no noise (false counts), and be sensitive across a wide spectral bandwidth.

MKID arrays are noiseless, photon counting, wavelength-resolving, broadband detectors, and could revolutionise the field of bio-imaging. The advantages offered by a successful MKID array detector based optical microscopy paradigm would permit bio-scientists to perform measurements and studies that go beyond the realms of possibility using the presently employed detector technologies.

Using MKIDs as the detectors in a bio-imaging system would have the following advantages:

- High light sensitivity - this allows either:
  - biological samples to be subjected to less excitation or illumination light which causes damage (light toxicity and photo-bleaching, denaturing of the fixed sample, or damage to the *in vivo* cells).
  - Very faint light sources to be imaged
- Large spectral bandwidth - a spectral sensitivity broader than any one detector currently in use, resulting in a highly versatile sensor. Longer wavelength light has better tissue penetration, so a detector capable of imaging in the NIR, can image far deeper into the body and potentially intracranial imaging through the skull.
- Spectroscopic - Wavelength information is extracted from each photon, so dispersive elements, multiple exposures or duplication of cameras is not necessary. Discussed in Section 2.3.2.
- More optically efficient - Dispenses with gratings, filters, and other lossy components, potentially resulting in a more photon-efficient system.
- Multiplexable - Many individual detectors within the array, can be read off with a single feed-line, reducing the cost, complexity, and wiring needed compared to other superconducting photon counting systems that require readout circuitry for each individual detector. The ability to read out multiple detectors over a single feed-line is important at cryogenic temperatures because each wire is a thermal path. Also, a single HEMT amplifier, and a single set of room-temperature readout electronics can be used to read multiple detectors. This is in contrast to each individual detector requiring its own electronics, which is the case for TES, SNSPDs, amongst others.

MKIDs have been identified as detectors of interest in other fields too, including being on the research road map of CERN: The 2021 ECFA detector research and development Roadmap published by Group.

1.3 Objectives

The objectives of this thesis can be summarised as: to demonstrate that MKIDs can be used to perform optical microscopy; to show that MKID optical microscopy has the potential to obtain images comparable to those produced by standard detectors; and to show that MKID optical microscopy indeed provides advantages above any single available detector type. This will be achieved through qualitative and quantitative characterisation of a prototype MKID microscope via experimental results, to be compared and contrasted against both alternative commercially available optical microscopy systems and against known results from the literature. This thesis also aims to identify some of the areas of bio-imaging which MKIDs has the potential to impact transformatively by surpassing the limitations of the approaches presently used.

- Provide the first experimental proof of concept of MKIDs being used to perform fluorescence confocal microscopy
    - Design and implement a point-scanning microscope system which implements an MKID as the photon detector
    - Obtain the intensity, and spectral data of points across a sample
    - Demonstrate how the spectral information obtained can be used to discern between objects of interest
    - Validate the result against a commercial system
- Identify and justify which microscopy methods would benefit from the advantages offered by MKIDs. For each:
    - Discuss microscopy methods, with an emphasis on the requirements of the detector
    - Identify the limitations imposed by the detectors in each method
    - Discuss which limitations could be overcome by MKIDs for each method
    - Discuss whether the limitations of MKIDs, make it less suitable for each method

1.3.1 Research Questions

In this thesis, a central question is to assess how the field of bio-imaging applications could benefit from adopting MKIDs as the detectors in bio-imaging applications, namely microscopes. This thesis reports on the design, development and operation of a proof of concept MKID microscope system employing a single MKID detector, and it is shown that it can be used to perform observations in ways that would not be possible by existing equipment and methods. Its performance is characterised and validated against existing equipment, and its suitability for bio-imaging is shown by demonstrating that the system offers a significant improvement to the state of the art of biomedical imaging systems for one or more specific applications. These developments will require the application of statistical hypothesis testing in order to provide a more rigorous answer to these questions at the particular level of confidence demanded by the scientific community.

In the simplest case, the research conducted aims to demonstrate that the photon detection capabilities of the MKID microscope can be used to detect the presence of fluorescent sources within a sample using simple photon counting, to create a grey scale image. Further to this, it demonstrates that the available spectral information can be used to distinguish between multiple fluorophores. This will be achieved by analysing the distribution of photon energies from features stained with fluorescent dyes, first in simulation, then using artificial features containing fluorophores and ultimately in a stained *ex vivo* sample. The artificial features used will be in the form of latex spheres loaded with fluorescent dyes. This will be performed on the more common, visible wavelength fluorophores.

When determining whether a finding such as identifying a fluorophore is statistically significant, there are different conventions that are commonly used in different fields, summarised in Table 1.1. For example, it was common to use a p-value=0.05 (Fisher, 1992) which suggests of 21 samples, one would be incorrect. Cases have been made to increase this to $p\text{-}value$ = 0.01 (pIoannidis 2005, Nuzzo 2014) or 0.005 (Aguinis et al., 2021). The discipline of Physics tends to demand a more stringent criterion before it firmly accepts a conclusion, with 3σ being a common requirement, but 5σ being regarded as the gold standard for ensuring a high degree of certainty over a finding, as described in Lyons (2013). This thesis assumes a confidence of 5σ is required to convince the scientific community, but recognises that other fields may tolerate a lower certainty of p<0.005.

σ	**p-value**	**Likelihood**	**Likelihood false**	**False Discovery Rate**	**Usage**
5	3e-07	99.999943%	0.000057%	1744278	Physics
3	0.0027	99.730020%	0.269980%	370	Physics
2.807	**0.005**	99.50%	0.50%	200	Biology (proposed)
2.576	**0.01**	99.00%	1.00%	100	Biology (common)
1.96	**0.05**	95.00%	5.00%	20	Biology (outdated)
1	0.31731	68.27%	31.73%	3	Reference

Table 1.1: List of confidence levels required by different scientific fields, and their conversion between other useful terms.

This thesis undertakes qualitative and quantitative analysis to answer these questions:

1. Is it possible to use MKIDs as a light detector in a confocal microscope, to **detect the presence** of fluorescent sources in a bio-imaging application?
2. Is it possible to **use the energy resolving capabilities of the MKIDs to separate the fluorophores** within bio-imaging applications when used as the detector in a confocal microscope?"
3. Determine how few photons are required to in order to identify the fluorophore to a confidence level of of 5σ, corresponding to a very high degree of certainty of 99.9999427%.

Chapter 2

MKIDs

2.1 Theory

This section explains the theory behind how MKIDs measure photon energy by detecting changes in kinetic inductance. Firstly, the concepts of photons and quasiparticles are explored, and the phenomenon of kinetic inductance is introduced. This theory gives context for how this effect can be exploited to detect incoming photons. Finally, the attributes of the detectors are discussed.

2.1.1 Photon energy

A photon is the smallest possible increment or quanta into which electromagnetic energy can be divided, giving rise to the term 'quantum detector' for detectors able to detect each photon as an individual entity. Many other detectors such as CCDs, instead measure the combined energy of multiple photons.

Photons have a given energy often measured in electron volts (eV). The photon energy, E, is related to wavelength, λ, by the following equation:

$$E = hc/\lambda \tag{2.1}$$

Where h is the the Plank constant ($4.135\,667\,696 \times 10^{-15}$ eVHz^{-1}), c is the speed of light ($299792458 m/s$), and λ is the wavelength of the photon.

2.1.2 Superconductivity, Cooper pairs and Quasiparticles

When a superconductor is below its critical temperature (T_C) (or superconducting transition temperature) which in typical superconductors is of the order of 5 K, the conditions are such that the electrons within the superconducting material are held together in pairs, known as Cooper pairs, by a phenomenon known as the electron-phonon interaction (Tinkham, 2004).

Crystalline superconductors, such as those used in MKIDs, are made of atoms in a lattice structure. Phonons are quantised vibrations, or distortions on the position of these atoms and can result from a photon depositing its energy into the material.

As a negatively charged electron moves through the lattice, it causes it to distort slightly by attracting the positively charged ions in the superconductor towards it, thereby creating a phonon.A Cooper pair occurs because this deflection of positive ions towards an electron, creates a positively charged area which is attractive to another electron in a similar situation, but only if it has an opposing 'spin'. In other words two electrons in proximity to each other, cause an exchange of phonons leading to an attraction which is stronger than the repulsive force present caused by them both being negatively charged. This bond, however, is still fairly weak and can be easily disrupted by thermal energy in the form of phonons, as experienced when energy is introduced in the form of a photon.

2.1.3 Cooper Pair-breaking

The energy with which Cooper pairs are held together is calculated using the Bardeen–Cooper–Schrieffer (BCS) band gap equation (Bardeen et al., 1957)

$$2\Delta \approx 3.5 k_B T_C \tag{2.2}$$

Where Δ is the gap energy of the superconductor, and Boltzmann constant (k_B) is a universal constant.

Photons impacting the superconductor can interact with it and break Cooper pairs if they have sufficient energy. The number of quasiparticles (N_{qp}) created when Cooper pairs are broken, is proportional to the energy of the photon ($h\nu$) and is given by the equation:

$$N_{qp} = \frac{\eta h \nu}{\Delta} \tag{2.3}$$

Where the Plank constant (h) is a universal constant, photon frequency (ν) is a property of the photon detected, and efficiency factor (η) is the amount of photon energy succeeds in breaking Cooper pairs.

The energy from the photon begins to immediately dissipate into the bulk of the material and the Cooper pairs recombine. The N_{qp} decays exponentially until the material returns to its original state, and the amount of time this takes is called the *recombination time.*

2.1.4 Kinetic Inductance

If a voltage is applied to the material, Cooper pairs flow together within the material (as super-current) and while they do not experience electrical resistance , they do store energy in what is known as the kinetic inductance effect, with the implication that reducing this flow would require a reduction in the amount of kinetic energy.

If the density of these charge carriers (Cooper pairs) is reduced, namely by an incident photon, then the internal inductance of the detector increases, as described in Swimmer et al. (2023). The quasiparticles created when Cooper pairs are broken also increase the surface resistance. In practice, there is always some resistance brought about by quasiparticles which have not combined into Cooper pairs.

2.2 Implementation: Detecting the Kinetic Inductance

This section describes how the above theory can be exploited to detect the energy of individual photons by an array of detectors.

2.2.1 Using Resonant Circuit to Sense Kinetic Inductance

In an MKID, a strip of lithographed superconductor is used as the inductor in a resonant, LC circuit which has a resonant frequency (f_0). If an LC circuit (see Figure 2.1) was capacitively coupled to a wire (feed line), and an oscillating signal (TX) of frequency f_0 is transmitted along the feed line, then the return signal (RX) would have the same frequency signal, and be attenuated (due to losses to the resonant circuit).

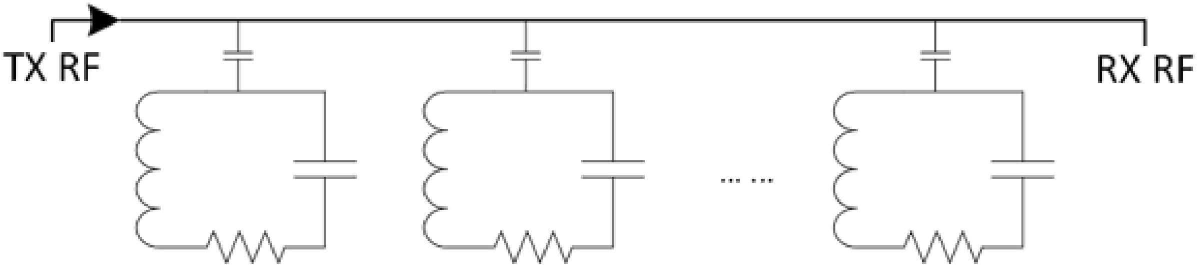

Figure 2.1: Schematic of MKID resonators connected to a feed-line

An increase in the inductance would cause a shift in resonant frequency of the circuit, and the additional quasiparticles would result in a higher surface resistance which would make the dip broader as illustrated in Figure 2.2 .

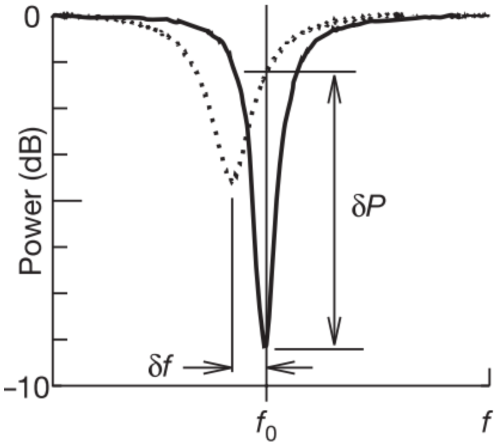

Figure 2.2: All LC circuits by nature have an resonant frequency (at f_0), and attenuate an excitation signal most strongly if it is at this frequency. An increased N_{qp} has the effect of changing the inductance and therefore its resonant frequency to the profile shown by dashed lines. (Credit: Peter K. Day, Henry G. LeDuc, Benjamin A. Mazin (2003))

Figure 2.3 (Bockstiegel, 2019) shows three panes, each showing the resonant frequency dip (i), phase position around the IQ loop with respect to excitation frequency (ii), position around the IQ loop in the complex plane (iii), and absolute phase shift (iv).

The first stage: the MKID resonator in its steady state, excited at its resonant frequency where the attenuation of the signal (S_{21}) is at its greatest, and the IQ position around the IQ loop is $-\pi$.

The second stage: A photon recently struck the inductor, breaking some Cooper pairs into quasiparticles, reducing the kinetic inductance and increasing the resistance. The quasiparticles have already begun to recombine rapidly. The change in circuit properties results in a decreased resonant frequency. The in-phase (I') and quadrature (Q') values measured when exciting with the probe tone frequency, have changed such that they are on a different position on the IQ loop which is 1.5 rad from the original phase angle. The IQ points do not exactly prescribe a circle Gao et al. (2007), but is an adequate approximation for this application.

The third stage: The energy has mostly dissipated from the inductor, allowing the quasiparticles to recombine into Cooper pairs and the I and Q values have almost returned to their steady state position at 0 rad.

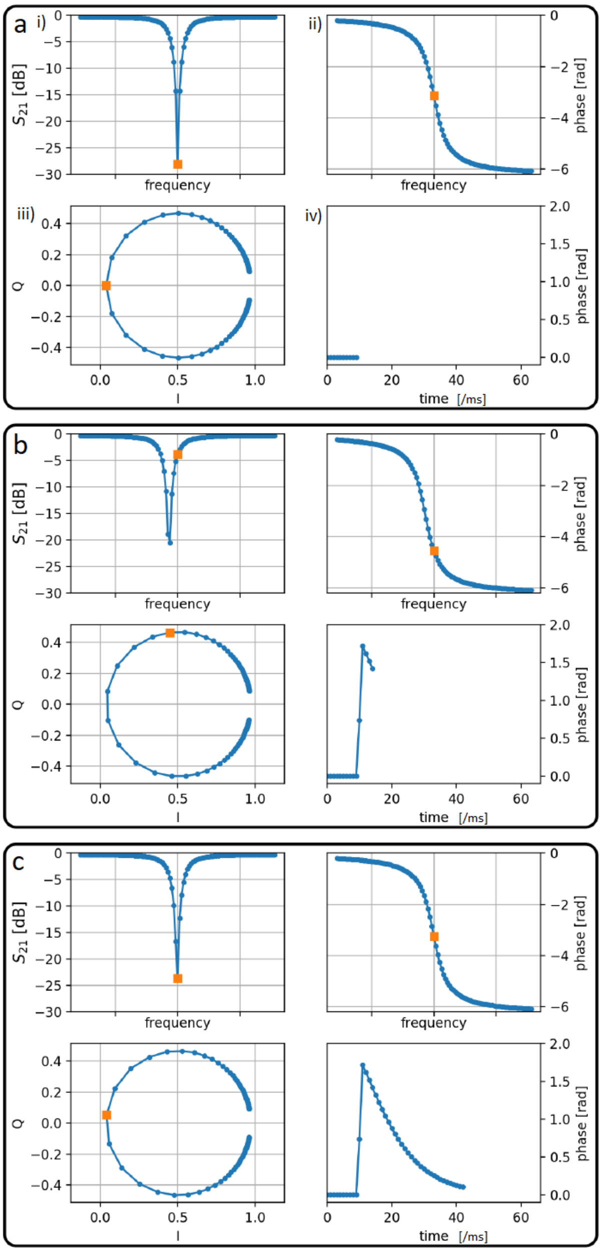

Figure 2.3: Three stages of MKID response after a photon lands on a detector. a) Steady state, with resonator at its stable resonant frequency, b) An incident photon resulting in a change in inductance, and shift in resonant frequency of the inductor and resulting phase shift. c) The phase shift returning to 0 as the Cooper pairs recombine. Credit: Bockstiegel (2019)

The phase time stream (how the phase-offset changes with time) photon profile has a *fast rise, exponential decay* profile which has a peak height which is approximately proportional to the photon energy.

Phase noise limits the ability to resolve the energy of the photon (see Section 2.3.2).

2.2.2 Combining Detectors into Arrays

It is possible to multiplex thousands of these lithographed LC circuits, and read them out on a single feed line using *frequency domain multiplexing*. This involves tuning each resonator to slightly different resonant frequency by varying the geometry of the interdigitated capacitors (IDCs). Figure 2.4 shows a small section of a larger array with clearly visible inductor (a), IDCs (b), coupling capacitor (c) and microwave feed line and ground plane (e).

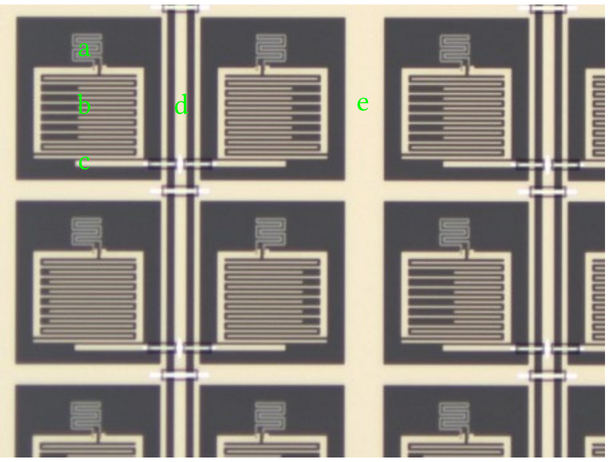

Figure 2.4: Many lithographed MKID detectors, showing inductor (a), MKID capacitors (b), capacitive coupling connection to the microwave feed line (d). The pitch of the circuits is of the order 150 µm (Courtesy UCSB)

Figure 2.5 shows the imperfections in the as-manufactured IDCs, which can result in the f_0 of each resonator being different than designed, resulting in two or more resonators colliding in the frequency space rendering both unusable (discussed further in Section 5.4). Methods have been explored which finely adjust the capacitance in the manner discussed in Szypryt (2017), using a process called focused ion beam milling, however identifying the capacitors needing modification and successfully ablating the material has many challenges and is seldom used.

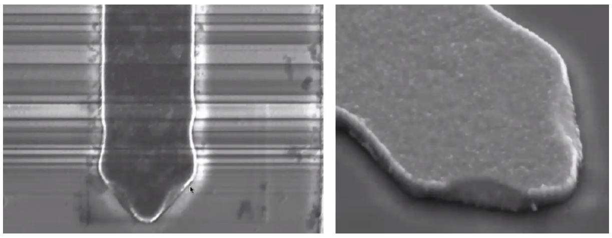

Figure 2.5: The end of a lithographed feature designed to be rectangular. It shows the imperfections in the manufacture process which lead to capacitance values which are different than designed. The width of the IDC is approximately 2 µm (Courtesy SRON)

2.2.2.1 Optical Coupling to Inductors

The MKIDs are designed to detect photons which are incident on the inductors, and the inductors only account for a small proportion of the wafer. In order to maximise efficiency, a micro-lens array is used to focus the incoming light onto the inductors. It is possible to 3D print these lenses to the back side of a transparent (e.g. sapphire) substrate as done by Kouwenhoven et al. (2023). In the case of the ARCONS detector used (see Section 4.4.6.1), the square micro-lens array had an optical fill factor or 92% (Mazin et al., 2013) .

An alignment jig was developed and used to position the lid containing the lens array, into the correct position over the MKID inductor and is shown in Figure 2.6 . It involved securely clamping the MKID array (body) to a fixed mount, and then articulating the micro-lens sub-assembly to the correct angle (using the rotation alignment adjuster) then X and Y position (using translation stages).

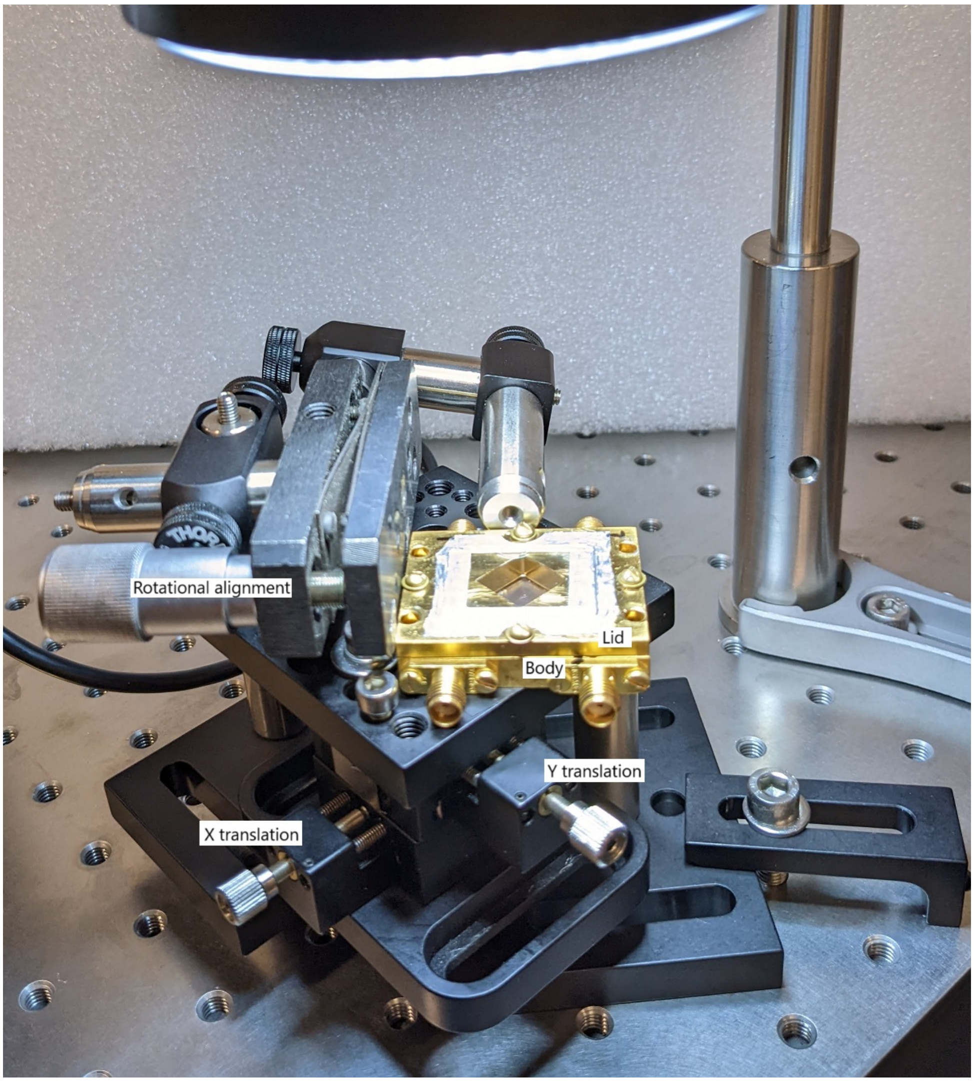

Figure 2.6: Micro-lens array alignment jig. The body was locked to an X,Y,Z-Rotation stage.

Alignment was assisted by taking a reference image of MKID array without the lid to find the positions of the inductors (the centres of which were identified by green circles), then comparing it to the live feed of the micro-lens assembly, so it could be adjusted in real time. The reference image was taken using a microscope with USB camera as the sensor, and a concentric ring light providing illumination (the ring light is just visible in Figure 2.6). The lid was then fitted, and the microscope translated purely in Z to bring the lenses into focus while maintaining the X,Y position. The reflections from the circular ring light in the lenses, indicates the centre of each lens. The live feed was mixed with the reference image, and the green circles were aligned with the circular reflections. 36 of the 2024 LC circuits are shown, showing 4 adjacent detector from each of the corners, 4 from the central edges, and the 4 detectors in the center.

Figure 2.7(a) shows the unaligned assembly, with green circles over the inductors not concentric with the reflections. Figure 2.7(b) shows the system aligned to better than the width of the detector, and clamped.

Feature recognition techniques were explored to find the centre of the lenses, and calculate the average positional error, however in the end the manual method proved more reliable.

While alignment was achieved during assembly at ambient temperatures, it was not possible to verify that it was maintained when clamping into the cryostat or as a result of thermal contraction during the initial or subsequent cool-downs.

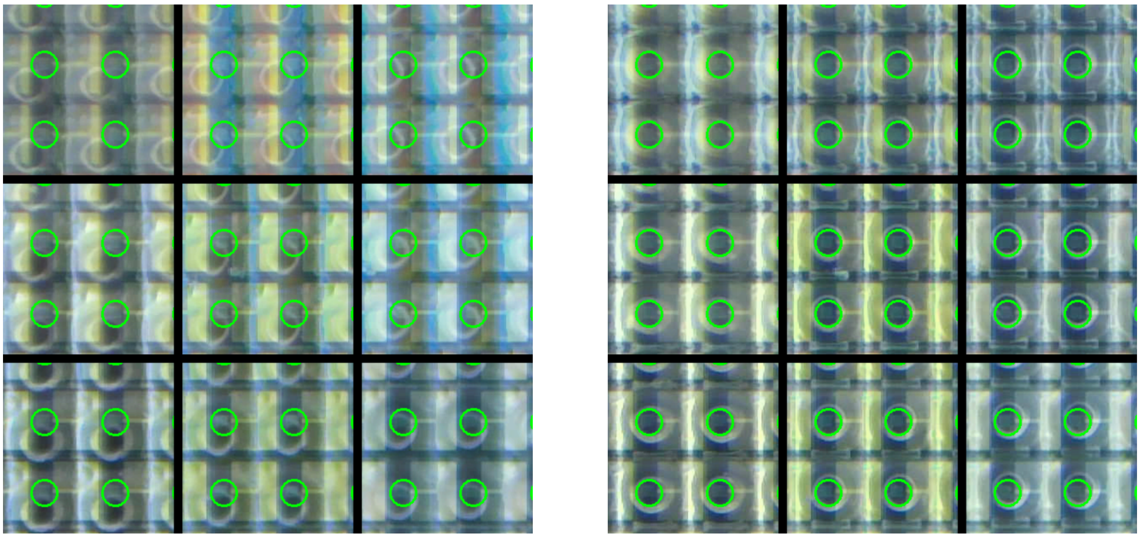

((a)) Lenses are incorrectly aligned to the Green circles (located at the centres of the inductors)

((b)) The lenses are concentric with the green circles, indicating they are aligned with the inductors

Figure 2.7: A composite image used in alignment of the lenses to the inductors on the MKID. The 9 panels show the corners, edge and centre of the imaged area. The green circles were added in software, to be over the inductors and an imaged saved to the PC. Then the micro-lens array was placed on and imaged. The images were added together to create 50% live image, and 50% saved image. The lens array was manipulated to line up the lens array with the inductors.

2.2.3 Interpreting the MKID Response

The electronics which detect changes in the kinetic inductance of each MKID, and interpret the results as individual photon events, are referred to as the readout electronics (Fruitwala et al., 2020). The readout electronics send multiple high frequency signals (5 GHz to 6 GHz) through a feed-line into the cryostat and compare it to the return signal. Ongoing advancements of broadband cellular network technology (4G, 5G, etc) are driving development and reducing costs of key components of these systems. The specific equipment used in this thesis, is described in Section 4.4.2.

The signal processing and computation that is performed to do everything from compare the signals, to produce the data is called the data processing pipeline (Steiger et al., 2022). The processing performed in this thesis is described in Section 5.

2.3 Attributes of MKIDs

2.3.1 Arrival time

MKID resonators respond quickly to changes in inductance cause by photons, so the *arrival time* can be determined by when the detector begins to respond. Because the phase angle is read out at 1 MHz, the arrival time can only be known to ± 1 µs.

Further to this, there is an inherent uncertainty in the arrival time resulting from the detector physics which is called the *timing jitter*.

When the resonant frequency (f_0) is changed by a photon event, it takes a small, often negligible amount of time to stabilise on the new frequency and amplitude. This is called the ring-down time (see Pan et al. (2023)).

2.3.2 Energy Resolution

The 'spectral resolution' (R), also referred to as 'energy resolution', or 'resolving power', is an indication of how close two photons can be in energy, and still be distinguishable as having different energies.

The uncertainty in determining the precise height of the photon pulse is due largely to phase noise, and to a very small degree the precision on the arrival time measurement. The sources of phase noise are primarily from the HEMT amplifier (Szypryt, 2017) (Section 4.4.5), readout electronics, and *two level systems* (TLS) noise Gao et al. (2008, 2007).

R is calculated by:

$$R = \frac{\lambda}{\Delta\lambda} \tag{2.4}$$

Where λ is the wavelength, and $\Delta\lambda$ is the full width at half maximum (FWHM) of the normal distribution.

Typical R values for MKIDs have until recently remained around $R \approx 10$ (Zobrist et al., 2022). Much work is being done by device researchers to improve this such as the non-membrane bi-layers which improve phonon retention in the detector (Zobrist et al., 2022) which improved R from 11 to 20 at 1 µm. Manufacturing MKID on membranes (de Visser et al., 2021) has demonstrated R values of 19 to 52 at wavelengths of 1545 nm to 402 nm respectively, albeit without the phase noise incurred by a multiplexed readout system.

2.3.2.1 Fano Limit

The limit ultimately dictating the energy resolution, is the Fano limit (Fano, 1947). It is caused by the statistical variation on the number of quasiparticles (N_{qp}) and exists because not all phonon energy is efficiently converted into quasiparticles; some photon energy is down converted into phonons with insufficient energy to break Cooper pairs. The theoretical limit is:

$$R_{\text{phonon}} = \frac{1}{2\sqrt{2\ln(2)}}\sqrt{\frac{N_{qp}E}{\Delta(F+J)}} \tag{2.5}$$

Where photon energy (E) is the energy contained in a photon, Fano factor (F) can assumed to be 0.2 (Kozorezov et al., 2000) , N_{qp} takes the value 0.59 (Kurakado, 1982; Rando et al., 1992), and J is the extra phonon loss factor included to account for losses to the substrate as proposed by Zobrist et al. (2022).

Figure 2.8 shows the Fano limit as a function of photon wavelength, and operating temperature. It illustrates the wavelength dependence of R, and suggests that superconductors with a lower T_C have the potential to have higher R.

In the case of the equipment used, the Fano noise was a very small fraction of the total noise in the system. Dominant noise sources were ambient thermal conditions, and impurities in the superconductors introduced by the manufacture process resulting in material defects, operating temperature.

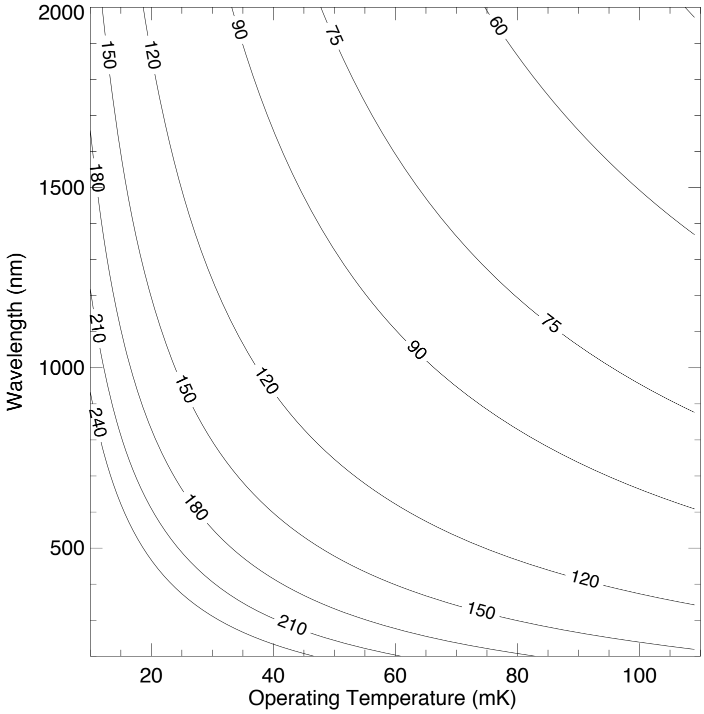

Figure 2.8: Fano limit as a function of T_{OP} and photon wavelength. (Assumes $T_C = 8\ T_{OP}$) Credit Mazin et al. (2019b)

2.3.2.2 Photon Flux

The time taken for the phase angle return to its steady state after a photon event, is called the *recombination time*, and is between 10×10^{-3} s to 10×10^{-6} s (Peter K. Day, Henry G. LeDuc, Benjamin A. Mazin, 2003) depending on the MKID material and geometry, operating temperature, and of course the photon energy. The decay rate can be described to a large extent by decay constant (τ). There are actually two overlapping exponential decays (Colas et al., 2023) but the smaller one was negligible in our case.

Photon events occurring a short amount ($\approx\ 4\tau$) after the previous event, overlap and obscure the photon pulse, making the uncertainty on the height greater, and the process of disentangling the events, far more complex and computationally expensive. Figure 2.9 is an illustration of overlapping photon events, with each photon having an energy of one arbitrary unit (au).

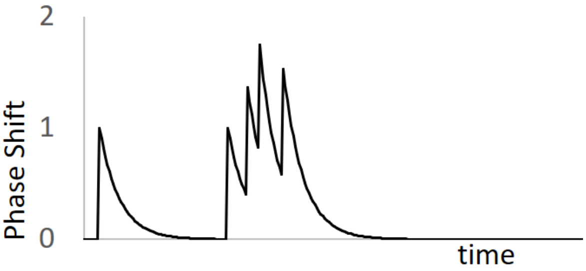

Figure 2.9: Schematic of one photon of energy 1au with sufficient recovery time, followed by several 1au photons in quick succession. Note: the third and subsequent peaks are not at 1au (arbitrary unit).

When using the available equipment (which had τ=3×10^{-5} s), photon stacking caused significant issues with photon fluxes above ($\approx 1000\ photons/s$). Photon fluxes of ($\approx 500\ photons/s$) proved to have very few overlapping photon events.

The recombination time can be tuned to some extent by MKID material selection, detector design, and operating temperature. There is a trade-off between photon flux and energy resolution. Therefore increasing the image acquisition speed comes at the cost of spectral resolution.

2.3.3 Quantum Efficiency

Quantum efficiency (QE) is the ratio of photons incident on the detector, to photons detected. MKIDs are highly efficient at converting an absorbed photon, into a detectable photon event. However, superconducting materials are inherently reflective resulting in QE of $\approx\ 17\%$ for wavelength range 380 nm to 1150 nm (O'Connor et al., 2019). Anti-reflection surface coatings have since improved this to 75% over 400 nm to 1400 nm by using SiO2 / Ta2O5 AR coating on a PtSi superconductors. Alternatively, the detectors can be back-illuminated involving the detected light travelling through the (transparent) substrate and impacting the lithographed detector on the surface bonded to the substrate, resulting in reduced reflections.

Transmissivity is used to describe the (wavelength dependent) thoughput of the overall optical system, taking into account losses from the mirrors, windows and other optical components not including the detector.

Options have also been explored to fabricate a Au/Nb mirror, behind each inductor to reflect photons which have missed the inductor, back towards it Nicaise et al. (2022).

2.3.4 Large Bandwidth

MKIDs respond to any electromagnetic energy above 2Δ (the energy taken to break a Cooper pair), so are sensitive to a large wavelength range. In practice, MKIDs cannot resolve the energy of a photon which has more energy than is taken to break all of the Cooper pairs in the inductor. In such a case, inductor geometry can be increased and material can be changed, so more Cooper pairs are present. On the other end of the spectrum, photons can be so low energy that photon events are indistinguishable from phase noise and that tends to be the limit. In the extreme, large number of low energy photons such as from thermal radiation, result in a high static N_{qp} which cause a lower resonator quality and shifted f_0.

2.3.5 Additional Advantages

MKID are also particularly attractive as a spectroscopic detector, because alternative methods of achieving energy sensitivity have the following drawbacks:

- Less optically efficient detectors
- Non-zero detector noise or readout current
- Higher losses in the optical system, owing to requiring more optical components to achieve the same result
- Reliance upon optical diffraction gratings which are not efficient over the whole wavelength range. For example, Casini and Nelson (2014) describes peak optical grating efficiencies of up to 90% at a single wavelength, but FWHM of 250 nm about 550 nm, or 900 nm about 1100 nm. Further optical losses, aberrations and noise sources are incurred by the additional optics required.
- May require dichroics and multiple cameras, which have losses and inaccuracies associated with alignment, calibration and post processing
- Many detectors require readout electronics for each pixel of the array which increases complexity and cost

CHAPTER 3

Optical Microscopy

In this chapter we introduce the concepts and theory relevant when using MKIDs as a novel photon spectrometer detector, in the field of optical, fluorescence, confocal microscopy. Much of the content of this chapter was informed by Girkin (2019).

3.1 Theory of Confocal Microscopy

3.1.1 Aims of Confocal Microscopy

In the simplest sense, the purpose of confocal optical microscopy in the case considered here, is to create a digital representation of the sample in the form of a numerical array, in which the data in each location corresponds to properties within the sample. A simple example is an array containing a value relating to the total intensity of light reflected from a given point, for several X and Y points over a flat subject. This could be represented as a two-dimensional intensity map.

In a more complicated example, there could be a four dimensional array containing a linear spectrum, for every X, Y and Z point around a 3D volume within a sample. Still more information can be gathered about each point such as the fluorescence lifetime of a dye.

There are several imaging modalities by which the light can be captured using a microscope, the main categories being point-scanned, or wide field.

3.1.2 Contrast and How it is Achieved

Features within a sample are identified by discerning between regions with contrasting properties, such as:

- Intensity - absolute light level (number of photons, or total energy from the received photons)
- Spectral information - the spectrum (a measure of light intensity at many wavelength ranges) received from a source, is often dissimilar to that of other materials in a way that allows them to be differentiated from each other. The human eye does this to a limited extent as it contains three wavelength dependent photo receptors sensitive to red, green or blue light, and can draw out very coarse spectral trends which we describe as 'colours'
- Polarity - if a medium (for example a cell) is optically active, then it rotates the angle of polarisation of light travelling through it. By viewing through a second polarising filter, the 'cell' can be identified by areas which appear darker or brighter than the unaffected background
- A time dependent response, as is the principle behind fluorescence lifetime imaging microscopy (FLIM)

3.1.3 Light, in the Context of Microscopy

Light is electromagnetic radiation of any wavelength, and can interact with the sample in one of four ways: absorption, emission, transmission, and reflection. Many microscopy methods exist to exploit one or all of these interactions, to render information about the sample.

For example, a wide field microscope may illuminate an area of the sample with white light, and observe the light returning from it. Differences in the reflectivity and absorption of the geometry, or features within the sample cause differing returned light levels over the sample. This variation in intensity of the reflected light, gives the necessary information about the sample.

Alternatively, fluorescence microscopes exploit the properties of specific molecules called fluorophores which can absorb a photon in a given wavelength range, and emit another at a lower energy level. This is discussed in more detail in Section 3.1.6.

3.1.3.1 Wavelengths of Light

Light is commonly classified into wavelength ranges, although the boundaries of these ranges are rarely agreed upon. Different wavelengths interact with the sample in various ways, such as having different transmissivities through various materials. While the wavelength ranges used in this study are in the visible range, the concept can be applied to any wavelength range within the very broad operating range of the MKID so a background is given here.

The ranges relevant to this technology are:

- UV range (10 nm to 400 nm) - highest spatial resolution is achievable, but damaging to biological samples and can only image a short distance into a sample
- Optical wavelength range (400 nm to 780 nm) - wavelength of interest for common fluorescent dyes. Auto-fluorescence of biological tissue is strongest in this wavelength range (peaking at $\approx$ 490 nm with FWHM$\approx$90 nm (Stelzle et al., 2017)
- NIR (780 nm to 1400 nm) - Deeper imaging and less damaging to cells
  - NIR-I (0.7 µm to 0.9 µm)
  - NIR-IIa (1.0 µm to 1.4 µm)
  - NIR-IIb (1.5 µm to 1.7 µm)
- Shortwave infrared (SWIR) (1.4 µm to 3.0 µm)

It is possible to achieve better spatial resolution with shorter wavelength light, however, there are valid reasons to perform microscopy at longer wavelengths. Lower energy photons cause less photo toxicity to biological samples because higher energy UV is damaging to cells (Hong et al., 2014). Additionally, longer wavelengths allow imaging deeper into the subject because the light experiences less scattering and absorption by the tissues of the body.

Figure 3.1 shows that there is 15 times less absorption of NIR-I light by blood, than of visible light, meaning that illumination light can reach deeper through skin, fat and blood if it is NIR-I. Additionally, more light of this wavelength range manages to leave the sample to reach the detector.

Figure 3.1 shows that scattering is higher in biological tissue at shorter wavelengths, meaning that imaging in NIR-II will allow higher resolution imaging at greater depths into the sample, than with visible light. This is because the light is able to reach the desired point, and also because it does not return as stray light

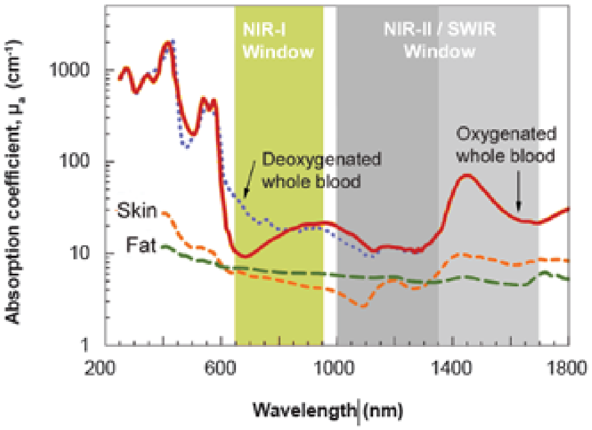

Figure 3.1: "Imaging window" describing the wavelengths of light that can penetrate the sample. Credit: Princeton instruments

The advantages of imaging in the longer wavelengths has driven some researchers to explore further towards the NIR-IIb wavelength ranges (Liu et al., 2020), as it provides better tissue penetration for measuring deeper in the sample (Hong et al., 2014) (Figure 3.2).

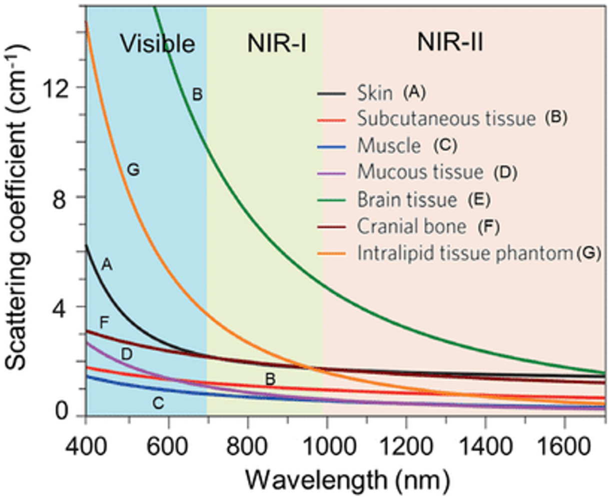

Figure 3.2: Wavelength dependent scattering, indicating longer wavelengths are better for deep tissue imaging (credit: Photoacoustic imaging in the second near-infrared window: a review - Paul Kumar Upputuri, Harvard University)

MKIDs are an attractive option for this wavelength range, with the added benefit of allowing noise free, energy sensitive photon counting.

3.1.4 Confocal Microscope Design

Laser illuminated confocal microscopes such as depicted in Figure 3.3 (Pawley, 2006), focus a collimated laser beam of excitation wavelength using a microscope objective (2) to a point on the focal plane (4) within the sample. Fluorophores present at that point fluoresce and the light originating from that point is collimated by the objective (2), reflects off the dichroic (5), and is focused onto a pinhole (7) which restricts light to the detector (6). Out of plane light from below of above the focal plane (3) is diverging as it leave the objective (2) and so is not focused to a point on the pinhole (7) so only a small amount of light reaches the detector (6).

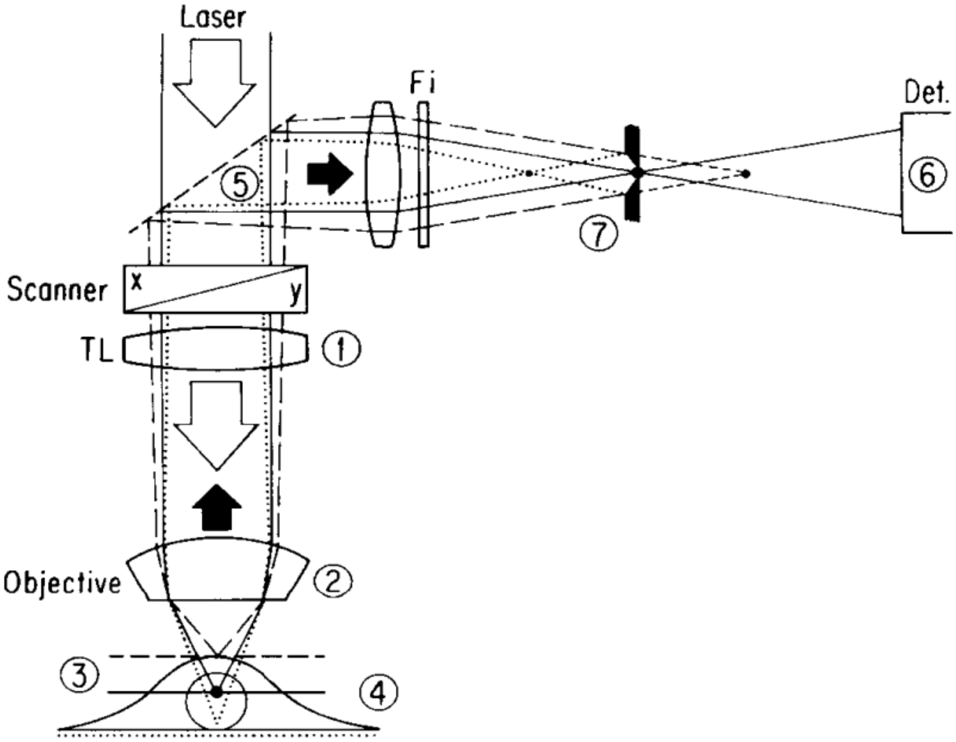

Figure 3.3: Cross section schematic of confocal microscope showing the laser light converging at a point on the focal plane (4) and returning light reaching the detector (6) only if it originates from the same point (Credit Dr. H. Kapitza, Carl Zeiss, Oberkochen)

Filters can be fitted between the dichroic (5) and the pinhole (7) to further attenuate light from the excitation wavelength, while still allowing through light of interest.

X/Y scanners can be added in the beam path if it is necessary for the microscope and sample to remain static while the image is taken. However maintaining an axial beam and traversing the sample has the same effect albeit with limitations to throughput, or the speed of image capture, and movement of the sample if accelerations are too high.

A ’pinhole’ is simply a circular aperture in a plane normal to the beam, such that light will be detected if it travels through. Therefore it can be a small hole in a thin metal foil behind which is a photo-detector, or the circular tip of a fibre which is connected to an MKID.

3.1.5 Optics Theory of Confocal Microscopes

Light cannot be focused to an infinitely small point in space, so it is impossible to distinguish two points as being separate points, if they are too close together.

When a collimated beam is focused to a point on the sample plane by a microscope objective (or similarly when a point source is re-imaged onto a focal plane) it appears as an 'Airy pattern' consisting of bright disc over the source, banded by dark and bright rings, with each bright ring getting progressively less bright. This is because the light waves from a given aperture, converging at a given angle, constructively interfere at the centre of the airy disc, but destructively interfere at a distance away from the centre of the disc as illustrated by Figure 3.4.

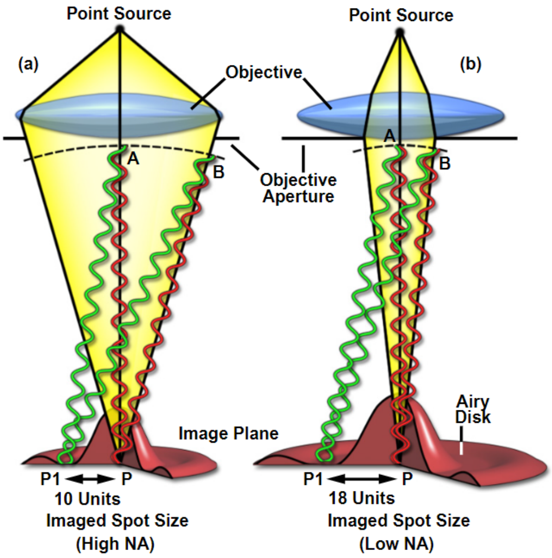

Figure 3.4: Illustration of why a smaller point is resolvable with a larger diameter optic. Credit Nikon MicroscopyU Website (2023)

This relationship describing the size of the airy disc (r_{Airy}) with respect to numerical aperture (NA) of the lens (in this case a microscope objective) is given by the following equation (Pawley, 2006):

$$r_{Airy} = 0.61\frac{\lambda_o}{\mathrm{NA}_{obj}} \tag{3.1}$$

The NA is a dimensionless number defining the acceptance angle of light into the lens (Girkin, 2019).

This also indicates the smallest possible feature resolvable with a particular wavelength of light; the Rayleigh criterion, which states that if two point sources are separated by r_{Airy} then they are resolvable (see Figure 3.5).

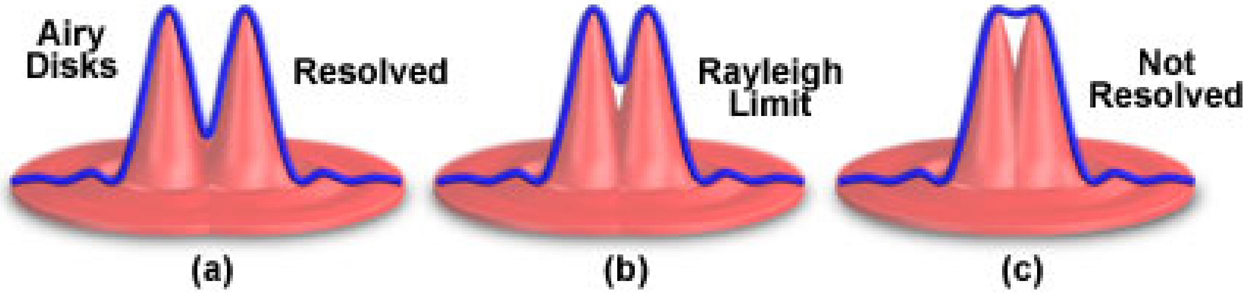

Figure 3.5: Rayleigh criterion restricting the minimum resolvable feature size. Credit MolecularExpressions.com

It is described by the equation:

$$d_{min} = \frac{1.22\lambda}{2\mathrm{NA}_{obj}} \tag{3.2}$$

Where d_{min} is the minimum spacing in a periodic grating that can be resolved. λ_o is the wavelength of light in a vacuum. Any features (such as individual microspheres) which must be identified, must be larger than this dimension if they are to be resolved as being separate.

Resolution in the axial direction determines the distance two point sources can be in the Z direction (normal to the sample plane) while still being resolvable. This relationship is given by:

$$z_{min} = \frac{2\lambda_o \eta}{(\mathrm{NA}_{obj})^2} \tag{3.3}$$

Where η is the refractive index of the object medium.

For the case of the instrument designed, the features of interest within the sample were constrained to a single plane, however the Z resolution advises to what precision the focus must be adjusted. It also implies that a lower magnification microscope objective will have more tolerance in Z alignment relative to the sample.

3.1.5.1 Lens aberration

To achieve diffraction limited imaging, the aberrations introduced from the lenses and optical components, must be less than the diffraction limit. Aberrations arise from manufacturing imperfections (which in this application is negligible), misalignment (which is overcome with careful calibration), using spheric optics (used because they are easier to manufacture and therefore cheaper, but introduce spherical aberrations) and contamination (such as grease or dust on the optics which is controlled by careful assembly and enclosing the system where possible).

3.1.6 Fluorescence

Fluorophores have an electron that can absorb the energy of a photon, resulting in the molecule becoming ’excited’, before emitting (releasing) the energy in the form of a new photon of slightly lower energy (Albrecht, 2008), illustrated by the Jablonski diagram (Figure 3.6). In the case of fluorescence, the emitted photon is released almost immediately (≈1 µs to 1 ms) after the absorption.

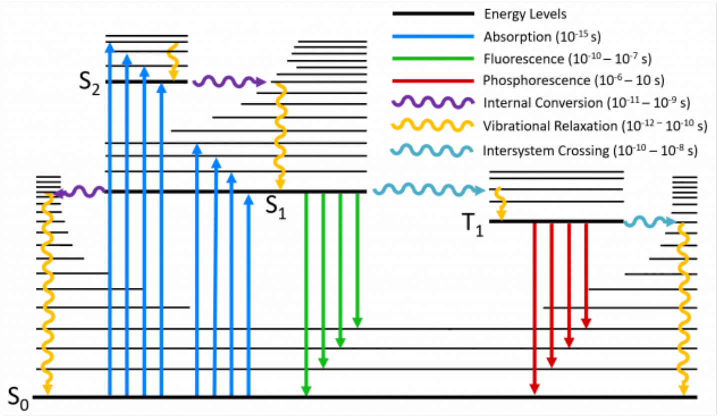

Figure 3.6: Jablonski diagram showing the absorption of an excitation photon, and release of an emission photon for fluorescence and phosphorescence

Flurorophores do not absorb all wavelengths of light, indeed there is a particular wavelength of photon which is most likely to excite the electron, known as the peak absorption wavelength. There is a decreasing likelihood of absorption as the excitation wavelength gets further from the peak. This is illustrated in Figure 3.7. The emission curve is the spectrum of light expected to be emitted from that fluorophore, irrespective of the excitation wavelength.

The excitation curves describe the sensitivity of a fluorophore to excitation by a given wavelength and vary for each fluorophore.

If the fluorophore is illuminated (excited) with a number of photons, not all photons will be absorbed. The metric given to the ratio of photons absorbed, is the quantum efficiency (QE). Of the number of photons absorbed by the fluorophore, the ratio of photons emitted is indicated by the quantum yield (QY) of given fluorophore.

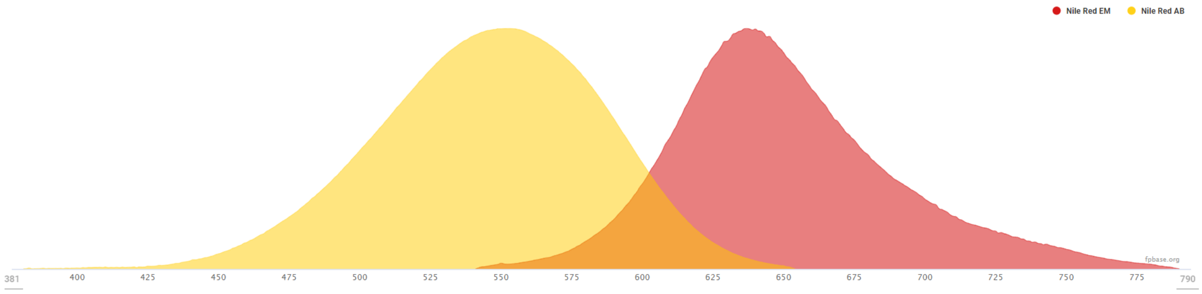

Figure 3.7: Excitation and emission curves for Nile Red, a popular fluorophore and one used in these experiments

Photobleaching is a permanent reduction in fluorescence intensity of a fluorophore, caused by photon-induced chemical damage resulting from prolonged and/or intense exposure to light.

3.1.7 Fluorescence imaging

Fluorescence imaging is a very powerful method of increasing contrast, and involves illuminating with shorter wavelength light than the spectrum of visible light being emitted by the excited fluorophores with which the sample is stained.

By covalently attaching a fluorophore (fluorescent labelling) to a molecule of interest within an otherwise clear and homogeneous sample, they can be used as a contrast agent to identify regions of similar molecules within a biological sample.

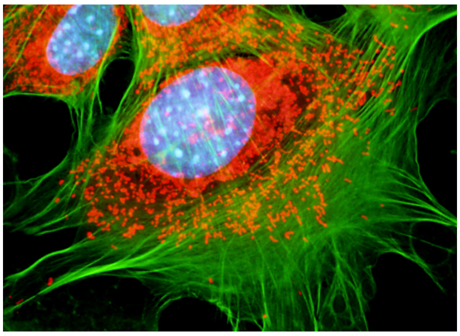

Figure 3.8: Albino Swiss Mouse Embryo Cell Nuclei, Mitochondria, and Actin DAPI-FITC-Texas Red Bandpass Emission (Triple Band Excitation) Set. Credit: MicroscopyU

When determining the illumination level to use, there is a trade-off between SNR and damage to the cells, and photo-bleaching. So lower illumination levels cause less damage and less photo-bleaching, but result in worse signal to noise in the detectors commonly used.

3.1.8 FLIM and Phosphorescence

Fluorescence lifetime imaging microscopy (FLIM) is an imaging technique which infers information about a sample based on how long a fluorophore remains in its excited state before releasing its emission photon (Albrecht, 2008). It is achieved by detecting the time of arrival of a photon, after a very brief pulse of excitation light.

Some molecules experience phosphorescence, a phenomenon with a similar outcome to fluorescence, except the emitted photon occurs after a far longer time, 10×10^{-6} s to 10 s after excitation. The mechanism is sightly different, in that the excited electron undergoes inter-system crossing before decay (involving the electron changing its spin). This longer timescale allows detection of the phenomenon with detectors of lower temporal resolution, which may be more suitable for MKIDs, however this is not examined in this work.

Chapter 4

MKID Microscope

4.1 Introduction

In order to determine the suitability of MKIDs as detectors for use in bio-imaging confocal microscopy applications, it is necessary to devise an instrument that is capable of both exciting fluorescence in a region within the sample, and relaying the photons emitted by the fluorophore to an MKID which detects them. By gathering photons from many points around the sample, it is possible to create an image. The spatial and spectral information is combined, to produce an array of spectra, equivalent to an RGB image but with more colour bins. This image can then be analysed to identify fluorophore spectra within them.

Designing an experiment to demonstrate this concept, and subsequently building an instrument to achieve it, relies firstly on selecting a suitable subject (in this case fluorescent microspheres) which emits light of the desired wavelength and is in a usable form factor for the instrument, from which to create the samples. The experimental equipment was designed to extract the required information from these samples. This necessitated selecting appropriate optics (lenses, dichroics and filters), detectors (CCD based detectors for troubleshooting, reference and alignment) translation stages to position the sample, software, and the integral MKIDhardware.

4.2 The Experiment

The purpose of this expiriment was to demonstrate that a microscope employing an MKID as its optical sensor can form an image that could be used to **detect** a fluorescent subject by simple photon counting, and could also use the inherent energy resolution of the detector to **identify** the specific fluorophore present.

In this experiment, features were identified based on *a priori* knowledge (**reference spectra**) about the two fluorophores making up the sample: Nile Red fluorophore and Yellow-Green fluorophore. Sample spectra were taken at many points within the sample, and each position (pixel, or in some cases region) was categorised into one or other of the two distinct reference spectrum collected from each fluorophore spectrum. Due to practical limitations of the equipment used, it was not possible to use an MKID detector array to provide simultaneous imaging of many points within a sample. Instead, a rastered point scan using a single MKID detector was employed to obtain each spectrum at a time. To achieve this goal, it was necessary to construct an instrument which would obtain the required light spectrum from each point sequentially, with sufficient optical and positional resolution to order to resolve the target microspheres.

This objective was achieved by assembling a confocal imaging system capable of interrogating a ‘point’ (effectively a very small volume due to diffraction limits) and relaying the emitted light, by fibre, to a single MKID. By physically moving the sample using X,Y translation stages, the raster scan image data could be obtained.

The ultimate goal is that MKID microscopes will use spectral information to distinguish between spatio-spectral features within bio-imaging subjects using fewer photons than are currently required by existing instruments. Thus, one objective was to demonstrate this on a simple biological sample. Nematode worms were selected as suitable samples, both because they were readily available, and the research group (CfAI, Physics, Durham University) had experience injecting Nile Red fluorescent microspheres into worms endogenously labelled with a green fluorophore. However, a first step towards this end was to identify more stable fluorescent targets that could be spectrally resolved, and were similar in size to the ultimate subject. This was realised using two species of fluorescent microspheres on a glass substrate.

4.2.1 Design Considerations

The process of deciding which optical elements to choose, which microscope objective to use, and particularly the size and fluorophore in the features of the sample, was guided by several constraints. Some of these are listed below:

Wavelength dependent properties of MKIDs MKIDs have better spectral resolution at shorter wavelengths so the first proof of concept trials to utilise fluorophores in the shorter wavelength end of their operating range where the MKID is better able to resolve spectra. Because they are broadband detectors demonstrated to work in the visible wavelength range, wavelength sensitivity did not factor into the decision. The detector material has wavelength dependent absorbance that will affect the sensitivity across the spectrum. For example, the absorbance of untreated aluminium from which the detectors are made is around 12%, but varies by 8% across the designed wavelength range.

Availability of appropriate fluorophores A key requirement of the experiment is that there are two or more fluorophores that are spectrally resolvable by the MKID. Therefore, a wavelength range must be chosen that contains a suitable combination of fluorophores.

The ideal characteristics of suitable fluorophore combinations are that both could be excited by the same wavelength of light, each would have a narrow emission wavelength range, and there would be as large a separation as possible between their emission peaks.

The excitation curves (see section 3.1.6) and quantum efficiency (QE) vary for each fluorophore, such that a fluorophore tends to emit less light if it is excited further from the emission peak. Because Nile-Red has a very high QE it is an excellent candidate for the Fluorophore that is excited at a wavelength far from its peak excitation wavelength. Pairing Nile-Red with a fluorophore exhibiting lower emissivity at its emission peak, but which is excited close to the peak wavelength, would allow both to be visible simultaneously with comparable photon counts.

The selected fluorophores would benefit from being resilient to photo bleaching (see Section 3.1.6).

All of these constraints narrowed the decision down to three fluorophores. Figure 4.1 shows the emission peaks of each of the 3 fluorophores as well as the likely emission peak as measured after the spectral blurring from an MKID of R=10 at 400 nm:

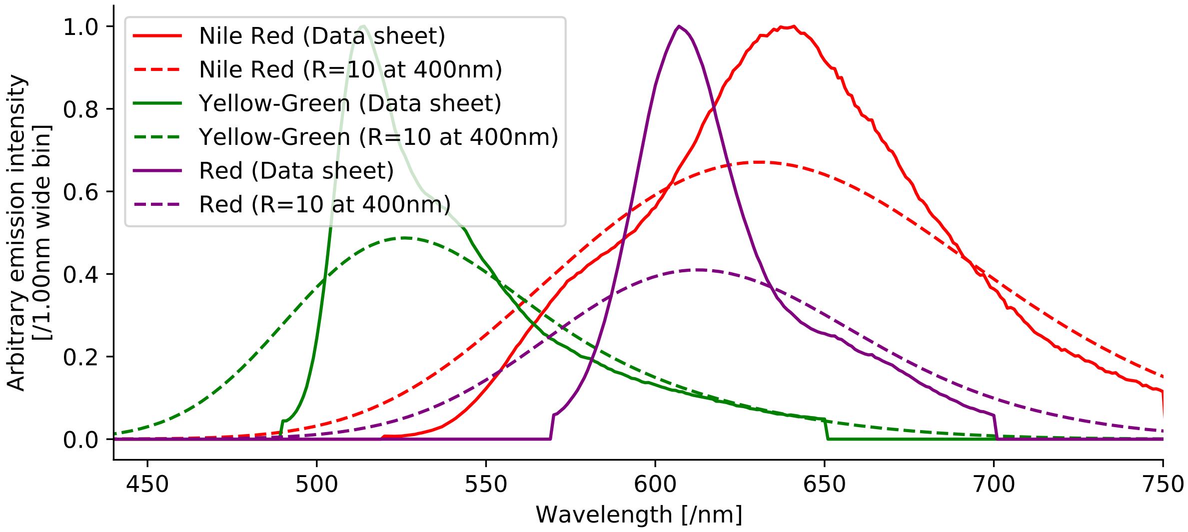

Figure 4.1: Fluorescent curves from three fluorophores, shown with the their claimed spectra, and the spectra that would be seen by the MKID detector with an R=10 at 400 nm

Fluorophore form-factor : Fluorescent microspheres were chosen as the subject because they provide a stable sample that does not degrade in laboratory conditions, can be fixed in place for successive measurements, have a stable, repeatable and known form-factor, and also do not require special conditions or approval (whereas biological cells can degrade and commonly require correct pH, stable temperatures, and a process of ethical approval). FluoSpheres™ supplied by Thermo Fisher Scientific offered consistently sized 2 µm microspheres stained with one of a variety of fluorophores, including the three identified, were selected as potential samples, although only the Nile Red fluorophore and Yellow-Green fluorophore were used.

Working wavelength range of commonly available optics : A common wavelength range for anti-reflective optical coatings is 350 nm-700 nm , such as the 'A' coating from Thorlabs. These optics are more common, and more cost effective than the alternatives, so were selected for the initial equipment. This choice imposed the additional constraint that the laser and fluorophores would need to be within the range 450 nm to 700 nm.

Available excitation lasers, dichroics and filters : A significant constraint placed on the design was the finite number of available laser wavelengths and dichoic/filter combinations. Lasers were selected based upon the criteria described in Section 4.3.4. Filters and dichroic mirrors (described in Section 4.3.3) required throughput of the excitation light wavelengths *to* the sample, for emission light to pass through to the detector while rejecting the unwanted excitation light to prevent it from saturating the detector. This requirement is described further in Section 4.3.3.

4.2.2 Test Sample Construction

Test samples were constructed by depositing a suspension of microspheres onto a flat cover slip and allowing the liquid to evaporate, resulting in a tight collection of microspheres being left behind. This method produced clusters of homogenous microspheres useful for obtaining a reference spectrum. Alternatively, ethanol can be dissolved into the suspension liquid and, when it evaporates, the microspheres that are left behind are distributed more uniformly as shown in Figure 4.2. This method produced instances where small numbers of microspheres of two types were adjacent.

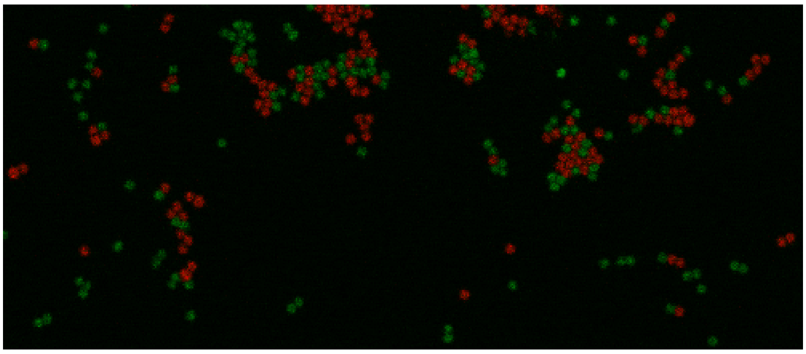

Figure 4.2: Image showing two colours of micro microspheres dispersed over an area

In order to produce a sample in which many fluorescent microspheres were present on the same flat plane under the objective, they were first deposited onto cover slip that was then inverted and suspended over a microscope slide using thin plastic shims as a spacer. The result is shown schematically in Figure 4.3.

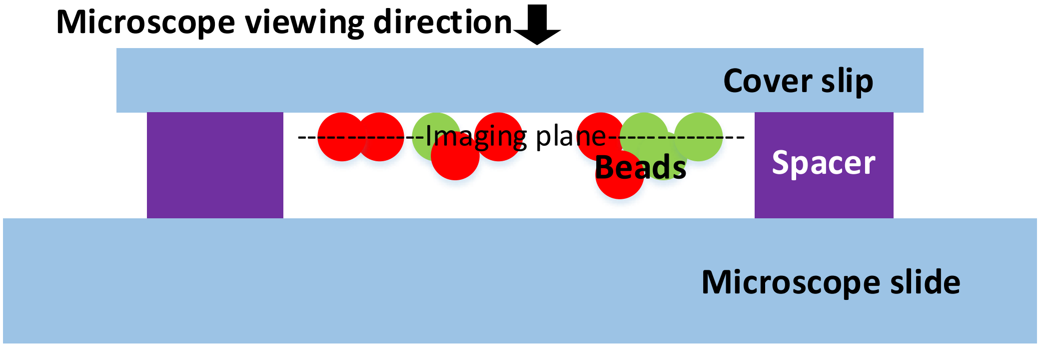

Figure 4.3: Schematic diagram of microspheres deposited on a cover slip. The microspheres nearest to the microscope are all on the same plane, thus can be imaged together, while not being obscured by out-of-plane microspheres.

4.2.3 Required Optical Resolution

The size of features that can be resolved by a confocal microscope is determined by the size of the confocal spot (the volume intersecting the illuminated and observed volumes), and also the accuracy with which this confocal spot can be positioned on the sample. Because this principle can be employed on almost any scale, the initial design could afford to have a relatively low resolution of 0.732 µm. This choice was driven by the following considerations/constraints:

- The largest FluoSpheres (Thermo Fisher) being Ø2.0 µm. (Available as small as 0.02 µm).
- The 40X Nikon microscope objective, which was the highest magnification available that did not require an immersion fluid. It had an NA=0.75 and therefore was capable of producing an illumination spot of 0.732 µm, given by equation 4.1:

$$\text{Diameter}_{\text{LASER SPOT}} = \frac{1.22\ \lambda}{NA} = \frac{1.22 * 450e-9}{0.75} = 7.32\times10^{-7}\ \text{m} \tag{4.1}$$

- Translation stages used could be driven in 29 nm steps, with a reported error of 1 step.
- Larger spot size systems are considerably easier to align, are more resistant to becoming misaligned, and are more resilient to drift of the equipment resulting from temperature changes that cause the system to deform slightly.

4.3 The Microscope

The microscope consisted of two main systems, each with components for illumination and detection:

1. Confocal system - Designed to capture fluorescent light from a single point within the sample. It focuses excitation light from a laser (Section 4.3.4) onto a very small volume within the fluorescent subject, and focuses the returning emission light to a fibre for detection by a spectrometer.
2. Wide field Imaging System - Designed to facilitate alignment of the confocal system to the feature of interest within the sample. An epi-illumination system illuminates an extended area, and reflected visible light is re-imaged onto the CCD of a USB camera allowing real time viewing of the sample.

Figure 4.4 shows a schematic diagram of the final design for the microscope. There are two light sources, six powered optical elements, six reflective elements (two partial mirrors and one dichroic mirror) and several other components. The parallel lines between the optical elements depict the ray paths of the various subsystems. The fibre output can be attached to the MKID, or to the USB spectrometer.

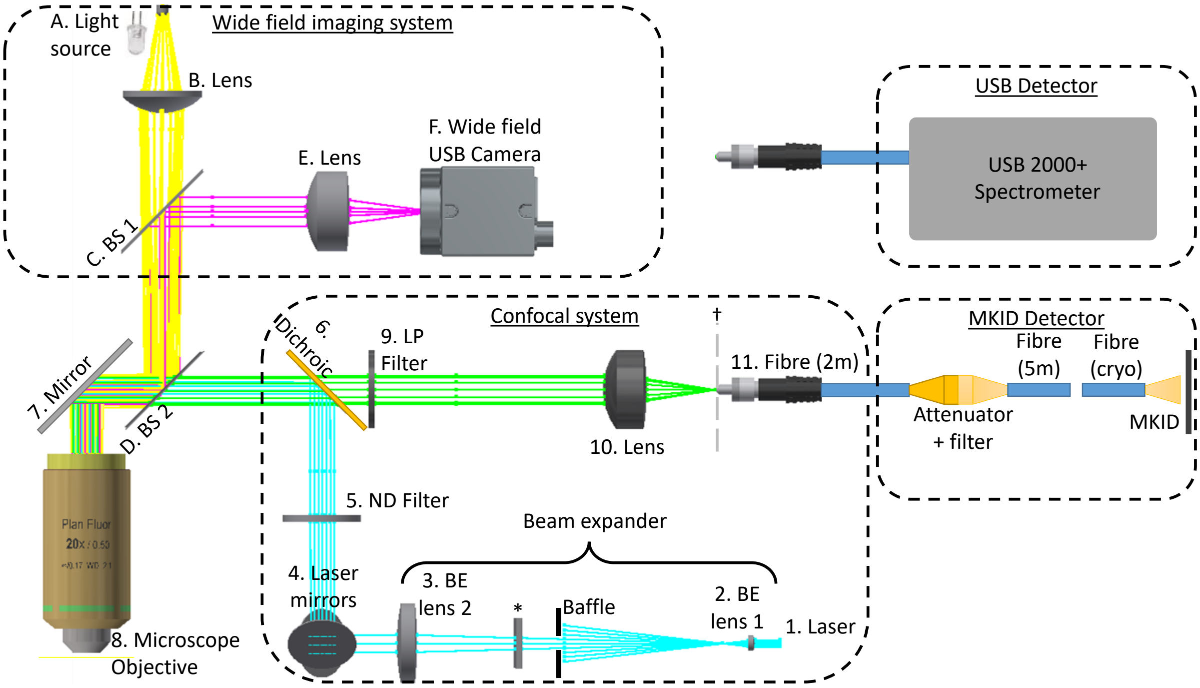

Figure 4.4: Schematic representation of the complete optical train

4.3.1 Subsystems

The subsystems within the assembly are:

Confocal excitation illumination (blue) — The collimated, coherent light from a diode laser (1) is passed through a Keplarian beam expander (2,3) (with a stray-light baffle). Initially, an attenuation filter (*), which allows the laser to be reduced to eye-safe levels, was fitted. However, this was later removed because the laser was completely enclosed and additional power was required for alignment. Two mirrors (each with two degrees of freedom; pitch and yaw) were arranged in a configuration that gives four degrees of freedom of adjustment on the beam entering the microscope objective to achieve the required axial alignment. A neutral-density (ND) filter attenuates the laser light to an intensity that does not photo-bleach the subject. A dichroic (described in Section 4.3.3), reflects the laser light, while allowing the emission light to pass through to the detector. The microscope objective (8) focuses the collimated excitation light to a diffraction-limited spot (of diameter 0.732 μm) at the focal plane of the microscope objective (a point within the sample, that is a given distance from the end of the objective, defined by the working distance of the objective).

Confocal emission collection (green) — Fluorescent light is emitted by the sample from regions of fluorophore that are illuminated by the excitation illumination system. Any emitted light that originates at the focal plane of the objective leaves the sample radially and, therefore, is collimated as it leaves the microscope objective. Light originating along the central axis of the microscope objective travels back through the system. Because the emission light is a longer wavelength than the excitation light, the dichroic (6) allows it to pass through to the detector. There is a long-pass optical filter (9) after the dichroic that further attenuates any stray laser light from reaching the detector. A lens (10, with F=30) focuses the collimated light to the tip of the fibre (11, with diameter 200 μm) such that off axis light (not from the illumination point) is rejected (as per the description of confocal microscopy in Section 3.1.4). It should be noted that in this instrument, the region of the sample that is illuminated (having a diameter of 0.732 μm) is smaller than the region of the sample from which the light is collected (diameter 33.3 μm) so it is not a *true* confocal system. This pseudo-confocal setup accepts out of focus light, resulting in decreased axial resolution and poor optical sectioning but at a level that is acceptable for the purposes of this study.

Wide field illumination (yellow) — An LED (A) produces white light that is directed towards the sample by a spherical singlet optic serving as the 'collector lens' (B). The collector lens is positioned so that it focuses light onto the rear focal plane of the microscope objective to achieve Kohler illumination of the sample, thus creating even illumination of the sample. The white light passes through a beam splitter (C), is reflected off another beam splitter (D) and a mirror before entering the microscope objective where it evenly illuminates the sample.

Wide field imaging (red) — Emission light is emitted from fluorophores within the sample and is collected by the microscope objective where it is collimated and leaves through the back aperture. The collimated light reflects off a mirror (7) and two beam splitters (D then C) is focused by an achromatic doublet lens (E) onto the detector of the USB camera (F).

MKID and USB Spectrometer Detectors — The emission light in the optical fibre was transmitted to an attenuator, where it could be attenuated to a level that would not saturate the detector, before a separate fibre took it to either the USB detector (see Section 4.3.5) or an MKID detector (described in Sections 4.4.6.1 or 4.4.6.2) where it was finally interpreted as a spectrum.

Provisions were made to allow a wide field system to be added to the equipment by creating a 4F optical system and re-imaging the focal plane at the fibre tip (†) to the MKID array.

4.3.2 Opto-Mechanical Design

The optical system depicted in Figure 4.4 was constructed using off-the-shelf optical cage system (as shown in Figure 4.6). This cage rigidly held the kinematic mounts for the optics, as well as providing the required degrees of adjustment necessary to align the optical system.

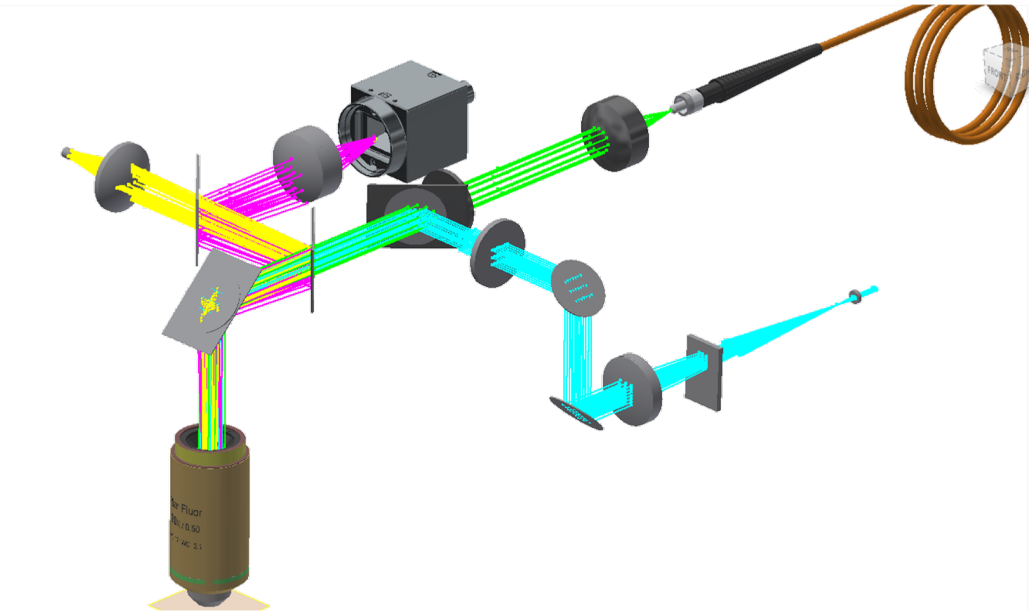

Figure 4.5: CAD model of optical elements and ray paths.

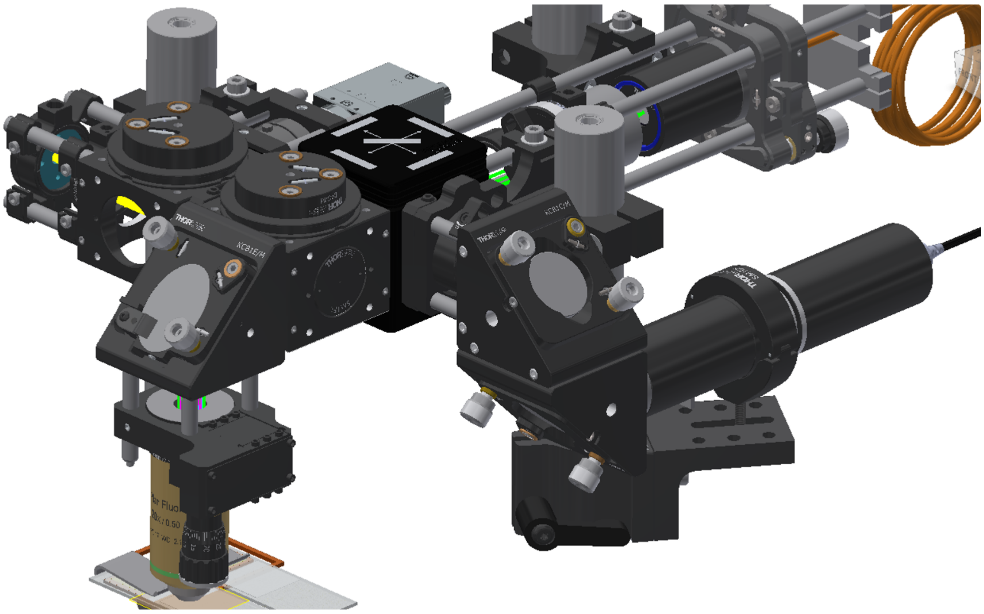

Figure 4.6: CAD model of an off-the-shelf cage system that supports the optical elements and provides the required degrees of adjustment

The assembly ultimately included X,Y translation stages to precisely control the position of a 3D-printed microscope mount (shown in blue in Figure 4.7). Repeatable alignment was achieved by ensuring that the glass microscope slide was in kinematic contact with stainless steel dowels embedded in the mount.

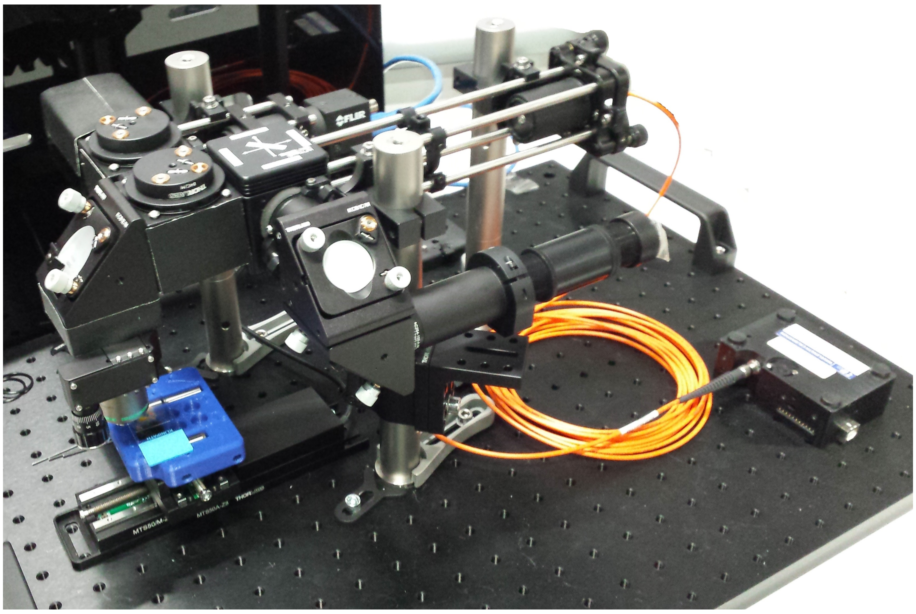

Figure 4.7: Photograph of assembled microscope

4.3.2.1 Alignment and Calibration

In order to achieve a small illumination spot and to collect the emission light using the fibre, as well as to view the sample with the wide field imaging system, it was necessary to ensure that the optics within the assembly were aligned and calibrated. After first adjusting all optics to be centred and nominally correct, an alignment procedure was used:

1. Collimate the laser light from the beam expander using a Shearing Interferometer (Thorlabs SI100). To maximise brightness, the angle of polarisation of the laser light should be perpendicular to the plane of incidence of the shear plate.
2. Adjust the laser mirrors (4) to direct the illumination beam along the central axis of the microscope objective
3. Focus the USB camera (F) at infinity by adjusting the distance to lens (E).
4. Position USB camera (F+E) and adjust beam splitters (C+D) such that the spot is centred in the camera FOV
5. Place a flat object in front of the microscope objective and minimise the spot size by iteratively adjusting:
    a) The microscope Z-height
    b) The spacing between the USB Camera sensor and the doublet lens (E+F)

6. Introduce the wide-field light source and adjust the spacing to the focusing optics until it provides even illumination over the FOV of the microscope
7. Back-illuminate the fibre and adjust the position of the fibre tip (11) until the projected light on the flat surface appears in focus and concentric to the illumination point

4.3.2.2 Measuring Spot Size

When initially aligned with a 40X microscope objective, the theoretical spot size at a wavelength of 450 nm was 0.28 µm. The features observed were microspheres of diameter 2 µm. Consequently, the spot size achieved would need to be smaller than 2 µm in order to resolve the target feature. The spot size of the instrument was tested by traversing the illumination spot over the sharp right angle edge of a fluorescent, translucent target. The intensity was seen to increase as the illuminated spot traversed from free space to within the fluorescent medium as shown in Figure 4.8(a). The rate of change of this curve is plotted in Figure 4.8(b). Performing the same measurement out of focus exposes the fluorescent slide to a larger, more extended section of the beam and, therefore, leads to a more gradual transition with respect to translation distance. Because the optimal Z height is not known, the measurements must be performed at a range of Z heights to interpolate the minimum spot size. The resulting plot is shown in Figure 4.8(c), which also shows the expected theoretical FWHM .

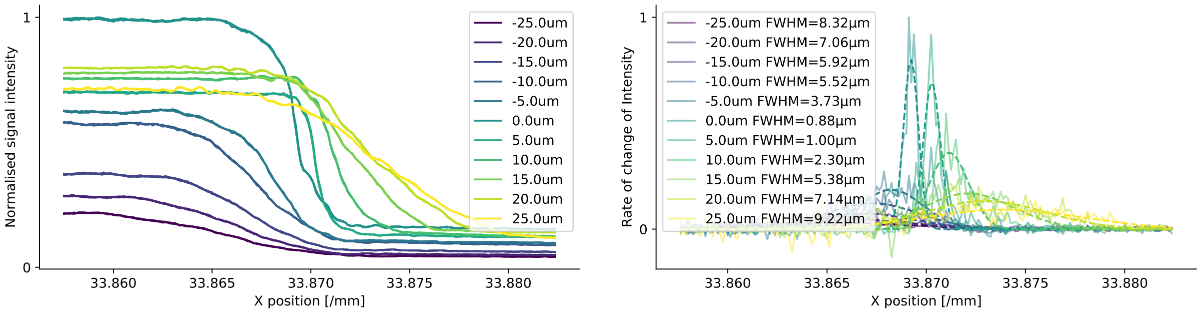

((a)) Spot calibration: Fluorescence intensity with respect to X position

((b)) Spot calibration: The rate of change of fluorescence intensity with respect to X position

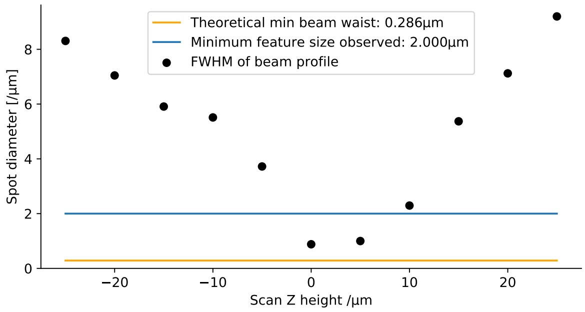

((c)) Spot calibration: FWHM of the spot, with respect to Z height

Figure 4.8: Plots showing verification of the confocal microscope spot size, by scanning the edge of a fluorescent target. The rate of change of signal provides information about the diameter of the confocal microscope's illumination spot

4.3.3 Transmissivity of the System

In the confocal system, the optics relaying the illumination source (excitation) must allow the 450 nm laser light to reach the sample where it can excite any fluorophores present. Conversely, the optics that relay light from the sample to the detector must block the excitation light from reaching, and potentially saturating, the detector, while allowing the emission light from the fluorophores, to reach the detector. For the reasons described in Section 4.2.1, the decision was made to construct a system that operates in the wavelength range of 450 nm- 700 nm, which is within the visible range. The required characteristics were achieved by using a 455 nm dichroic splitter and two identical reflective filters with a low pass cutoff at 465 nm (Chroma AT455DC and AT465lp respectively).

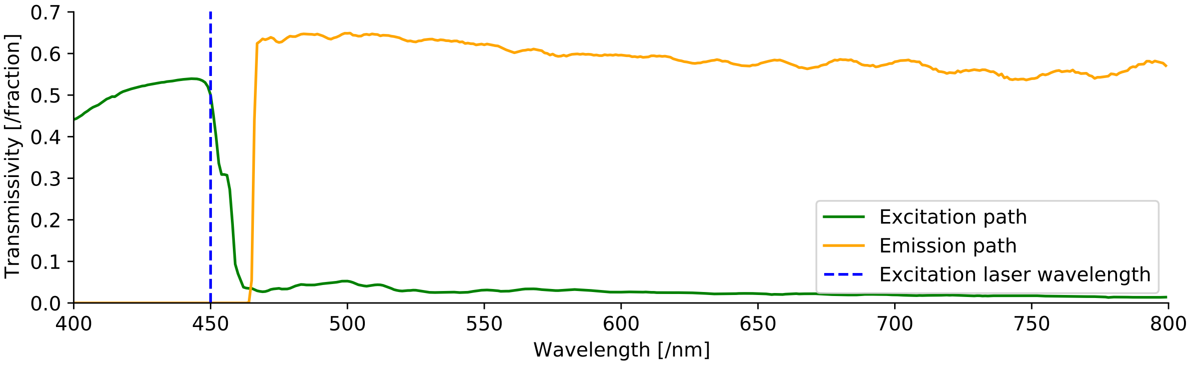

Figure 4.9: Spectral transmissivity of the optical train

In order to facilitate viewing of the system by the wide field system, a beam splitter (partially reflective mirror) was introduced in the path to divert white light from a light-emitting diode (LED) onto the sample, and to relay light from the sample back to the USB camera. To minimise the loss of emission light (produced by fluorescence) to the detector, while still having sufficient illumination light to, and wide field image light from, the sample, a 10% reflective rectangular beam splitter (Thorlabs BSN10R) was selected.

4.3.4 Light Sources

A laser was selected as the light source, because they provide near-monochromatic illumination at a high intensity, are available in a variety of wavelengths, and provide a coherent and easily collimated light source that can be focused to a point by the microscope objective.

Excitation wavelength selection was dependent on the fluorophores used, and the dichroic mirrors and low pass optical filters available. In this case, the laser selected was the 450 nm laser (Thorlabs CPS450) that complimented the specified dichroics (Section 4.3.3).

The beam emitted from the laser diode was a collimated, elliptical beam of 3.2 mm × 1.0 mm having the profile shown in Figure 4.10. In order to fill the back aperture of the microscope objective with an even, circular, collimated illumination (to achieve point illumination at the focal plane of the microscope objective) a 10× beam expander was used.

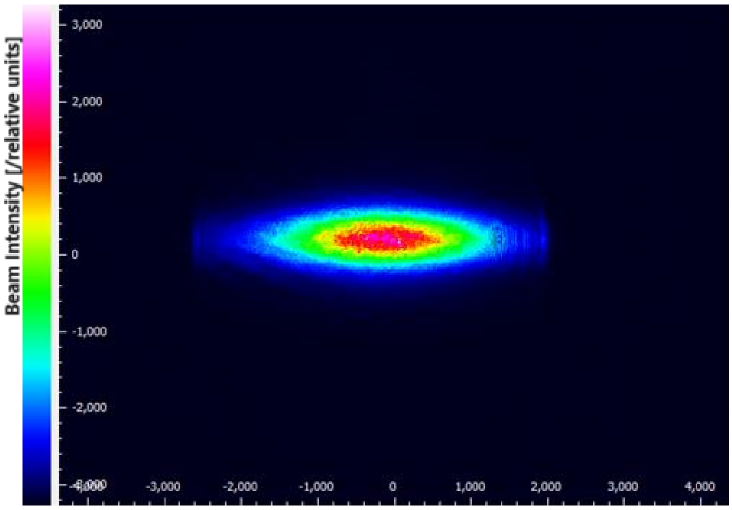

Figure 4.10: Beam profile of the CPS450 laser diode, a 3.2 mm × 1.0 mm ellipse

The inverted Keplerian beam expander, shown in Figure 4.11 incorporates two convex lenses (LA1116-A of FL=10mm, and AC254-100-A-ML of FL=100mm , Thorlabs).

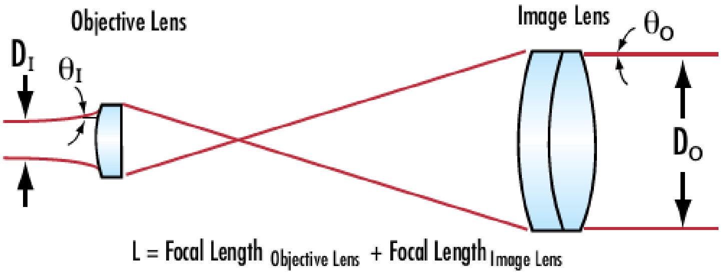

Figure 4.11: A Keplerian beam expander with an internal focus where an aperture can be placed to attenuate the laser light (Credit: Edmund Optics)

In order to reduce the laser illumination to a level where it would provide a sufficiently high fluorescence signal, while not photo-bleaching the fluorophores, the light from the laser diode was attenuated by one of the methods outlined below.

4.3.4.1 Attenuation Using a Pinhole

By placing a pinhole at the focal point of the Keplerian beam expander, it is possible to restrict the light going through the system, and improve the spatial resolution of the laser. However, this system is very difficult to align and to maintain the alignment, and thus would require a more complicated alignment procedure and some additional equipment. Also, each time the illumination level was to be altered by changing the size of the pinhole, the whole system would need to be reassembled and realigned. Therefore this method was not used.

4.3.4.2 Attenuation Using Neutral Density Filters

Neutral-density (ND) filters are used to reduce the amount of light passing through the system by either reflecting or absorbing it. This allowed the illumination level to be readily changed simply by placing a filter of different opacity in the beam path at position of element **5** in Figure 4.4.

4.3.5 USB Spectrometer Detector

Fluorescent light emitted from each point of interest was focused into an optical fibre and then to spectrally sensitive detectors.

For development, calibration, and reference, a USB spectrometer was used to capture a high spectral resolution data cube. The device available in the laboratory was the Ocean Optics' USB2000+ Fiber Optic Spectrometer, which used a Sony ILX511 2048-element linear silicon CCD array detector. The spectral sensitivity of the detector is shown in Figure 4.12. The wavelength dependent sensitivity of this detector (and indeed of the overall system), means that the spectrum detected from a given fluorophore will not exactly match the spectrum from the data sheet.

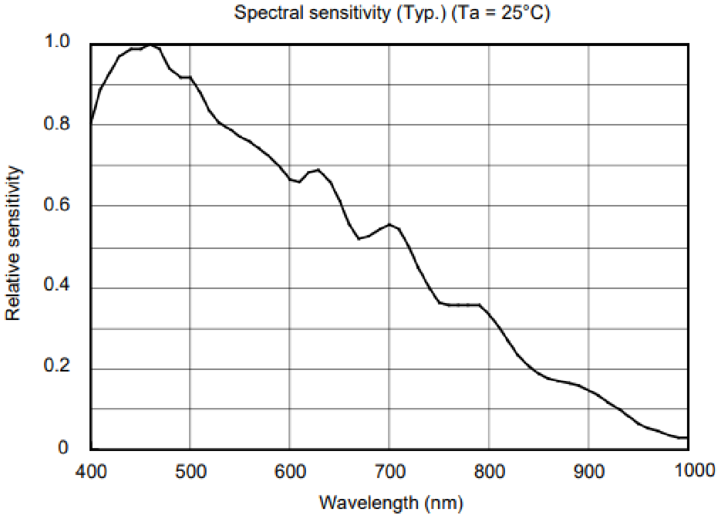

Figure 4.12: Wavelength sensitivity of USB Spectrometer

4.4 Overview of the MKID Hardware Used

The MKID devices require several systems to maintain the very low temperatures required to maintain superconductivity within the inductor of each detector, vital for sensing the small changes in kinetic inductance (indicated by changes in the detectors' resonant frequencies). These conditions and measurements were achieved using the components described below.

4.4.1 Dilution Refrigerator

A dilution refrigerator system (cryostat) was employed to achieve the stable milli-Kelvin temperatures (below 400 mK) required for superconductivity.

Different refrigeration methods exist which are capable of achieving the mK temperatures, one being the Adiabatic Demagnetisation Refrigerator (ADR). ADRs work by magnetising a material, and then allowing it to demagnetise. As it demagnitises, it loses entropy resulting in a decrease of temperature. This means that a single ADR cannot run continuously, and also that there is a fluctuating high magnetic field, which the MKIDs are sensitive to, and so must be shielded, from. There are, in development, continuous mK coolers that weigh under 5kg (Bartlett et al., 2022) which have two ADRs which take turns cooling/ charging.

The model selected was the off-the-shelf SD Dilution Refrigerator System manufactured by Bluefors, a cryogen-free dilution refrigerator with a cooling power of over 250 µW.

The cryostat is a large cylindrical steel barrel with two 40mm diameter ports that allow 40 mm clear aperture windows. One port is located on the underside, in the centre, and the second is located at ≈1.13 m above floor level on the side facing the optical table. Inside the cryostat there are five circular "flanges", each colder than the one above, with a corresponding shroud to minimise radiative heating (Figure 4.13). The lowest "mK flange" is temperature controlled to values as low as ≈25 mK under no load. The temperature can be precisely regulated to the optimal operating temperature of the MKID.

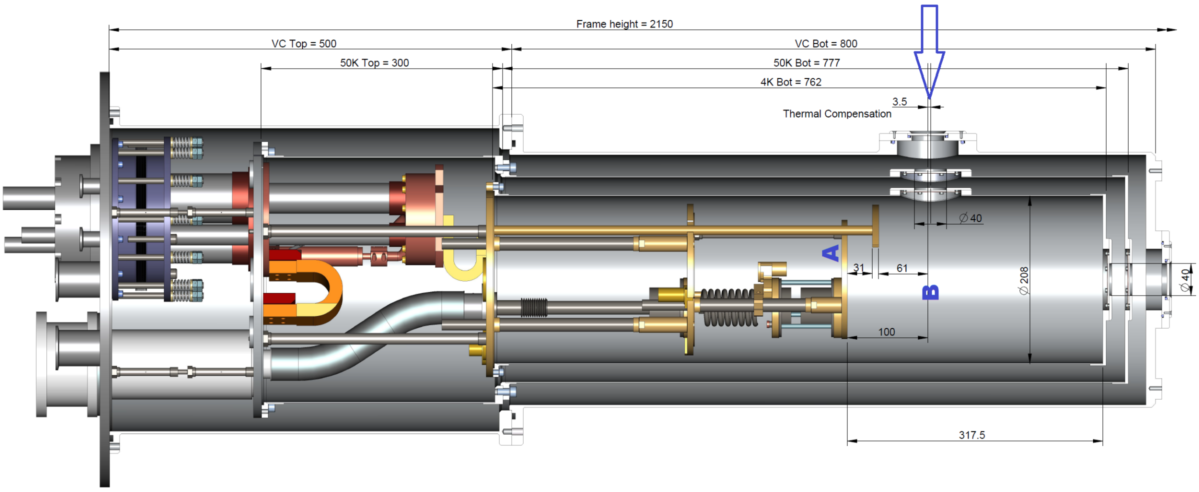

Figure 4.13: CAD drawing of the Cryostat (image is rotated; top to the left). Each successive flange (horizontal plate) and shroud is colder than the preceding one, with the final flange maintained at an operating temperature of 120 mK. A platform at 4 K has been added, and is shown. MKID fibre detectors can be located at "A", and the wide field imaging assembly can be located at "B". (Image credit Bluefors)

MKID Instrumentation can be mounted to the underside of the mK flange, extending down into the available envelope that is 310 mm deep and 180 mm in diameter. There is a custom 4 K platform to support optics, magnetic shields, high-electron-mobility transistor (HEMT) amplifiers, *etc.*. The MKID instrument used in the experiments was mounted to the top of the mK flange, placing it closer to the fibre inlet, given that it did not require access to the windows. An optical fibre entered the cryostat through a port in the top, and was optically coupled to the MKID (see Section 4.4.6.3)

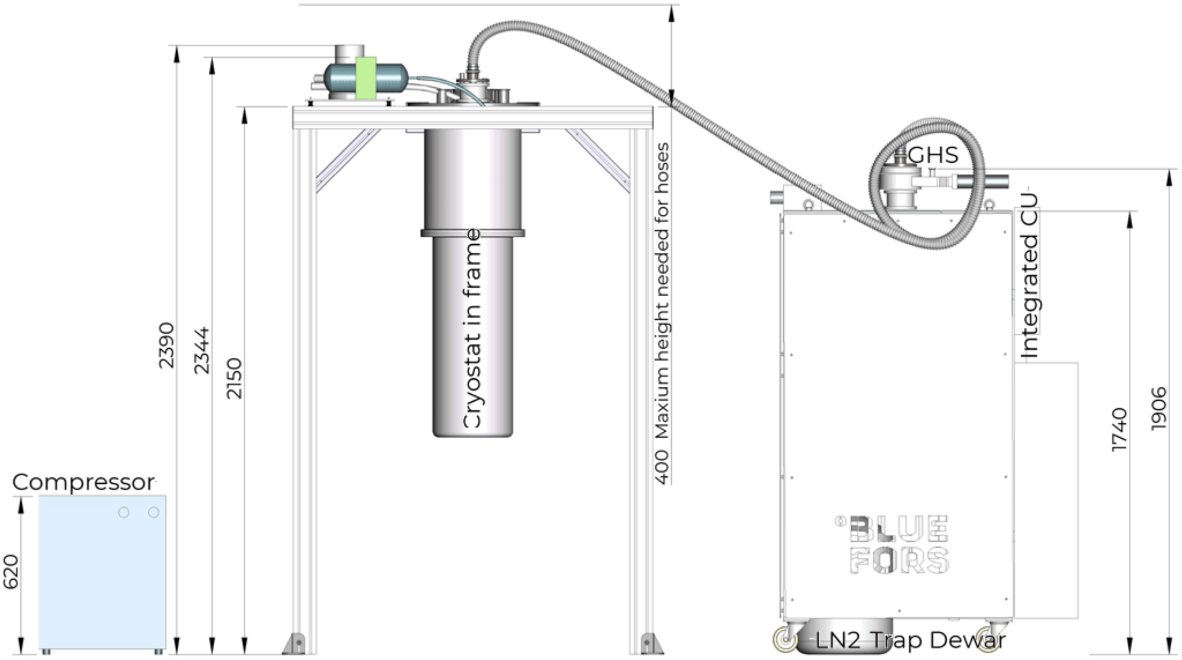

Figure 4.14: Cryostat in frame with ancillary equipment. The cryostat is suspended in its frame, with a transparent window (behind the chamber, not shown)

4.4.2 Readout Electronics

The equipment was required to detect changes in the resonant frequency of the MKID as explained in Section 2.2.3. The readout electronics selected contained a microwave signal generator that produced a low-phase-noise, microwave frequency, probe tone that was chosen specifically for one device, which it then compared to the returning signal. The probe tone is generated and interpreted by an off-the-shelf board (Zynq® UltraScale+™ RFSoC ZCU111). One of the eight DACs (14-bit 6.554GSPS) produces a probe tone that can be heterodyned with a local oscillator (6kHz) to create an excitation frequency of 4GHz or above. The returning signal can similarly have the local oscillator (LO) frequency removed by downconversion, and the result read by one of eight ADCs (12-bit 4.096GSPS). Processing is performed by onboard field programmable gate arrays (FPGAs). A similar system is described by Baldwin et al. (2022).

For the first experiments, the readout board was connected to a Windows PC using PYNQ. It was operated using Jupyter Notebook, running a script that interfaced with the XILINX board over Ethernet. The output of this was a 4Gb '`.bin`' file that was processed by a digital down conversion (DDC) program written in C+. Subsequent updates have allowed the readout electronics board to be Python-controlled, thus enabling more time efficient data capture at a range of inputs and facilitating the determination of optimal settings.

The firmware that controls the ZCU111 was laid-out as shown in Figure 4.15. The control PC instructs an ARM processor to gather data. The complex signal produced by the Waveform Generator is sent to the MKIDs (via the IF111 amplification board, to be attenuated if required) through the **TX** cable. The returning signal passes through a pre-amplifier in the IF111 board and then undergoes digital down conversion (DDC) to produce the raw IQ values. These IQ values are channelised to isolate the signal from each resonator. Each isolated IQ-time-stream undergoes analysis to be converted to phase angle and stored to disk. Post-processing of the stored data enables photon events to be identified by one of several methods.

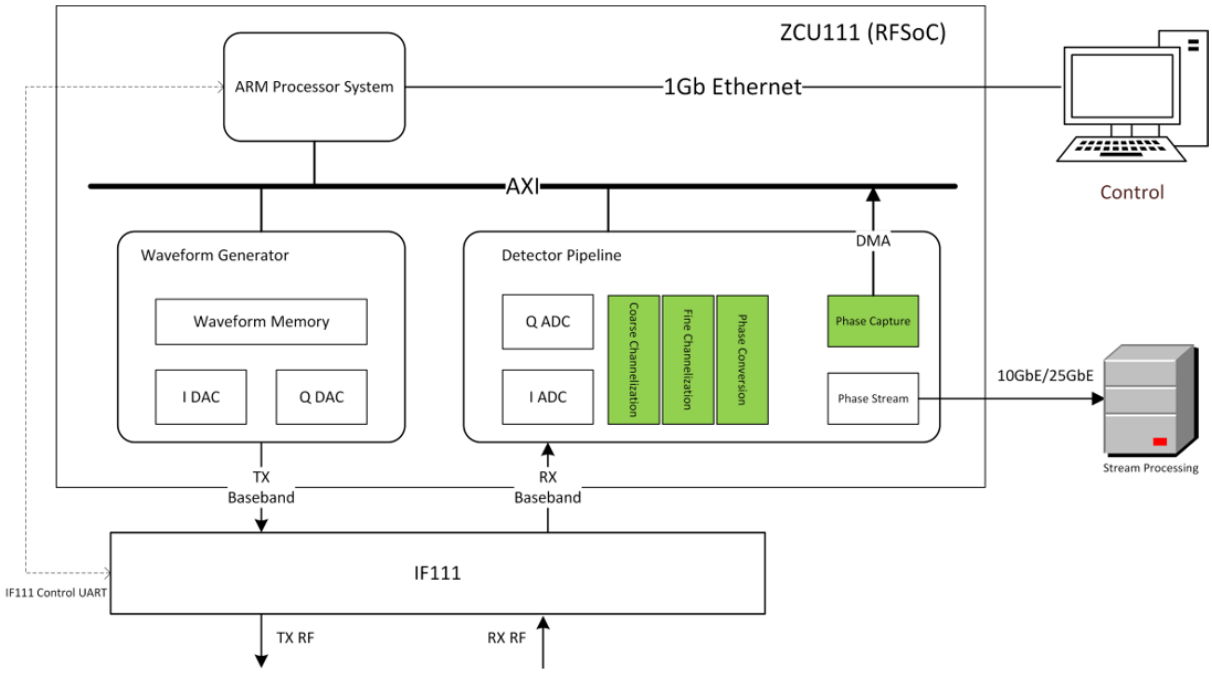

Figure 4.15: Schematic of the readout firmware. a Control PC controls the processor on board the ZCU111, which controls the waveform generated (TX) and the processing of the received signal (RX) before sending the phase stream to a server for processing

4.4.3 Coaxial cables

Coax (coaxial) cables are shielded electrical cables used to transmit the high frequency (5 GHz to 8 GHz) radio-frequency (RF) signals between the RF shielding enclosure that contains the MKID device and the readout electronics.

Because both the core and cladding of each feed-line acts as a thermal path between the device enclosure at milli-Kelvin temperatures and the 293 ° K ambient, thermal sinking is necessary along the cables. This procedure, which reduces the heat load through the cable, takes the form of thermal clamps, and attenuators. At the time of writing, only a single device was used. This offered negligible thermal load compared to the cooling power available from the cryostat used.

Semirigid coax cables for applications below 4K are made from NbTi, whereas those for use above 4 K are of Stainless Steel. The cables were supplied by Coax Co., Ltd..

Other coax products exist, such as the **FL**exible co**AX**ial ribbon cables (FLAX) concept by Smith et al. (2021), and the Cri/oFlex®3 by Delft Circuits (Figure 4.16), which offer lower thermal load and lower profile cable routing. However, these were not chosen because only a single feedline was required.

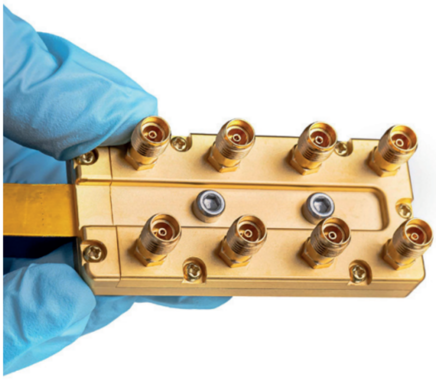

Figure 4.16: Image of a Cri/oFlex®3 ribbon cable, with a rectangular connector and eight threaded SMA terminals

4.4.4 Attenuators

To maximise the SNR of the signal from the tone generator relative to the thermal noise introduced along the cables, it is advantageous to transmit a large amplitude signal through the coax cables and attenuate the signal at each stage of cooling. The attenuators were selected such that the signal reaching the device had the correct power. The value of the attenuators at the 50 K and 4 K flanges was 20 dB. Attenuators have the added benefit of ensuring that the central core of the coax cable has a good thermal conduction path to a flange, which would have otherwise not been thermally connected.

4.4.5 High Electron Mobility Transistor Amplifier

Each channel from the MKID device has its output signal amplified by a HEMT amplifier. The Indium Phosphide (InP) HEMTs used are field-effect transistors that offer good signal amplification at high frequencies, operate at cryogenic temperatures, have low noise. The HEMT for each feed-line (although only one feed-line was used) is attached to the >4 K flange cryo-cooler. Thus, the signal is amplified before thermal noise is introduced by warmer cables. The low temperature coax cable that connects it to the MKID in the device box is maintained at 80 mK to 120 mK. The HEMT model used was the LNF-LNC4-8C supplied by Low Noise Factory. These models have a noise temperature of 1.5 K. Power is supplied by a special low noise amplifier circuit that operates at ambient temperature.

4.4.6 The MKID Detectors

4.4.6.1 MKID Detector from UCSB

The MKID array that was available for the initial setup and development of the equipment was an early version of the TiN 2024 pixel MKID array used in ARCONS Mazin et al. (2013). This model was developed by University of California, Santa Barbara (UCSB) and manufactured by the Jet Propulsion Laboratory (JPL). The array shown in Figure 4.17(a), provided courtesy of UCSB, was the starting point. The intention was to use one or more of the detectors to develop and prove the readout electronics prior to acquiring the latest generation detector. Figure 4.17(b) illustrates that the wafer hosts many devices, but only a single detector from this board was used. The documented QE for this detector is around 17% at longer wavelength ranges (Szypryt, 2017), but may vary between devices, and was not verified for this device. The reported maximum rate at which photons could be read before it became difficult to separate individual pulses, was 2500 counts/pixel/second (Mazin et al., 2013).

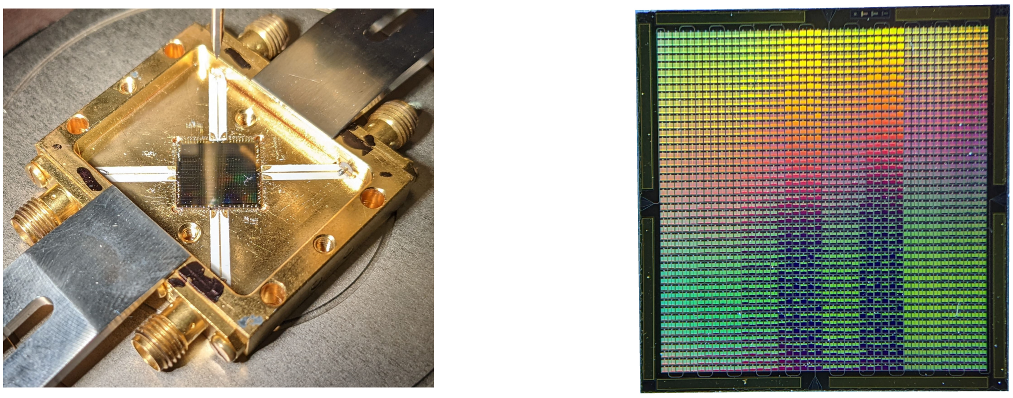

((a)) Image of mounted wafer from UCSB containing MKIDs, with feed-lines attached with wire bonding

((b)) Close-up image of MKID features (device from UCSB)

Figure 4.17: MKID device from UCSB

4.4.6.2 MKID detector from SRON

The Aluminium on Silicon nitride (Al on SiN) MKID device described by de Visser et al. (2021) was made available to Durham University, by SRON. The device featured four dissimilar, experimental detectors, two of which are manufactured with a thin substrate, that has been proven to increase R through improved phonon trapping (more efficient use of photon energy, into breaking Cooper pairs). The selected resonator, which had a resonant frequency of 4.0 GHz, was the preferred choice for recording the experimental results for reasons described in Section 5.2. Using the equipment at SRON, this resonator had a demonstrated R of 19 to 52 at wavelengths between 1545 nm to 402 nm respectively. The wafer was mounted in a copper box (Figure 4.18(a)) and two SubMiniature version A (SMA) connectors were attached to either end of the feed line that is shown passing near the four detectors in Figure 4.18(b).

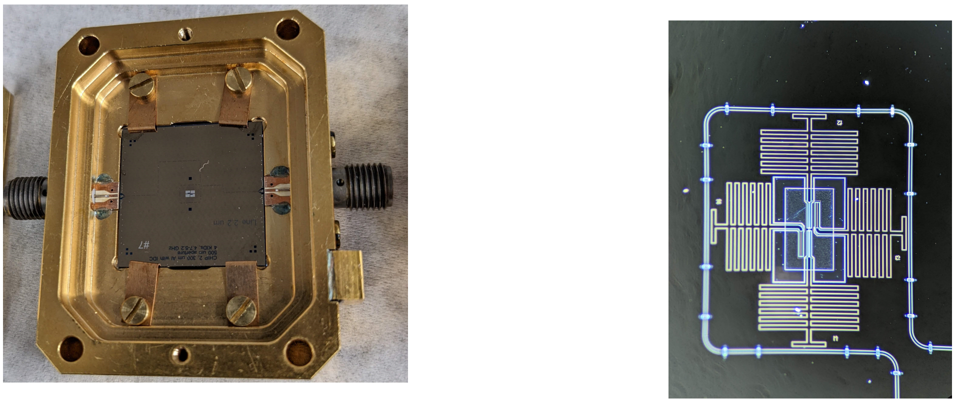

((a)) Image of mounted wafer containing MKIDs, with feed-lines attached with wire bonding (device from SRON)

((b)) Close up image of MKIDfeatures (device from SRON)

Figure 4.18: MKID device from SRON

4.4.6.3 Optical Couplings

Light leaving the fibre was coupled to the MKIDs by supporting the fibre ferrule a fixed distance from the array and allowing the cone of light from the fibre to flood illuminate the detectors. Figures 4.19(a) and 4.19(b) show the CAD models and finished items that coupled light to the SRON device. Given the large area illuminated by the fibre and the small photosensitive area, optical efficiencies were consequently low.

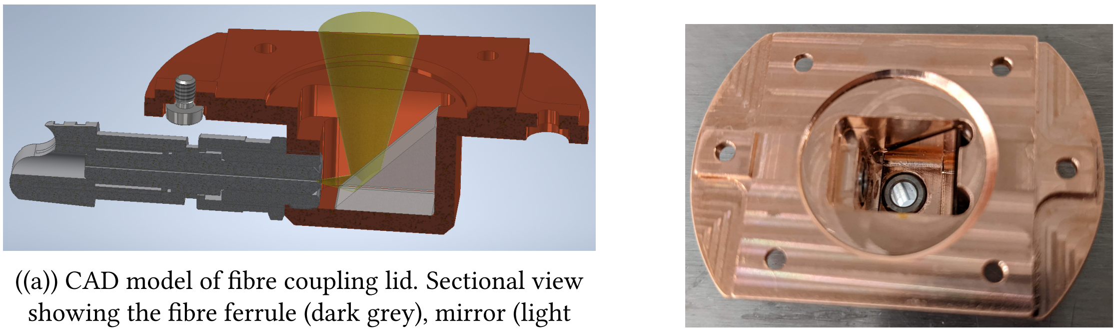

((a)) CAD model of fibre coupling lid. Sectional view showing the fibre ferrule (dark grey), mirror (light grey), light path reflected in mirror (yellow) and copper fibre coupler (copper). The MKIDis located at the end of the light path

((b)) Fibre coupling lid fitted over the MKIDdevices to divert light from the optical fibre to the MKIDs

Figure 4.19: Components to optically couple the vertical fibre inside the cryostat, and to divert the collected light horizontally onto the detector

4.5 Microscope Control Hardware

MKID images were obtained using two synchronised PCs. One PC captured MKIDdata, and the other PC controlled the microscope. The layout is shown in Figure 4.20.

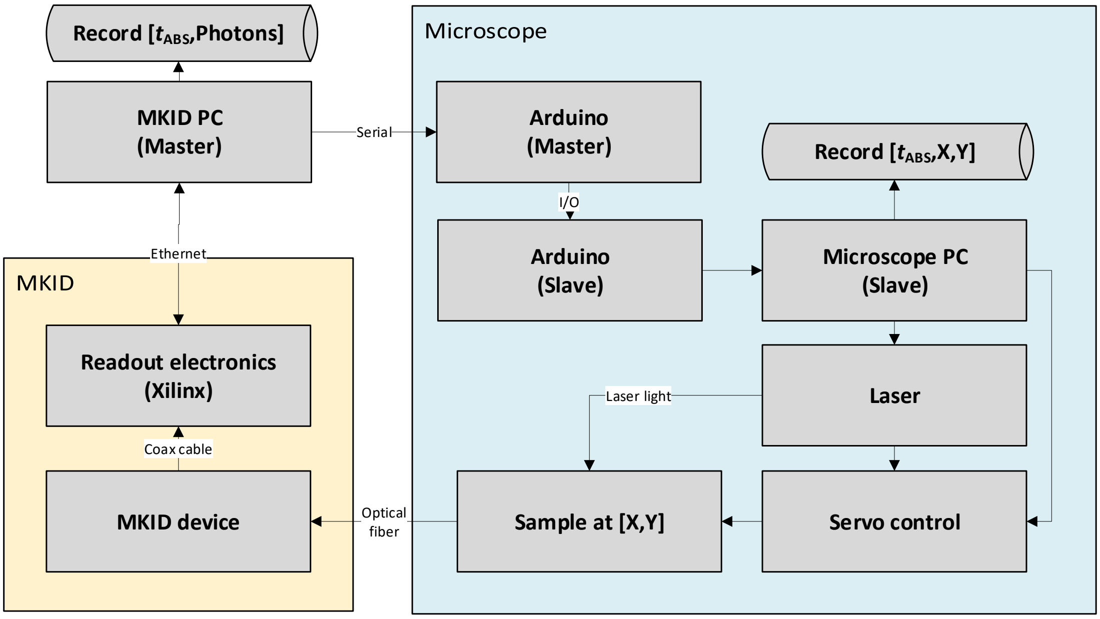

Figure 4.20: Network of PCs used to acquire MKIDMicroscope images

The first of the PCs was an MKID data acquisition computer (MKID PC) that sent instructions and recieved data, from the readout electronics over Ethernet. A script running on the MKID PC instructed the microscope computer (acting as a slave) to illuminate the sample for 8.2 seconds, and then immediately instructed the readout electronics to take an 8s photon capture. The MKIDPC would then download the photon capture data over Ethernet (taking between 8 minutes, and 50s depending on the version of the readout electronics used), while in parallel the microscope PC positioned the stage at the next location ready for image capture (typically taking 0.2s). At the end of the scan, the records of each position (timestamped by the microscope PC) and the photon lists generated by the MKID PC (with a timestamp) were compiled in the method described in Section 5.

4.6 MKID Microscope Control Software

Control software, written in Python, managed each component within the microscope system. It directed the various functions required to reach the point of acquiring sequential spectral scans at a grid of points within the sample. These functions included:

- Generating the spectral scan location points over the region of interest

- Controlling the two linear translation stages that positioned the spot in the correct location to:
    - Initially locate the region of interest in the sample
    - Sequentially move between the scan points
- Servo-control the Z-axis adjustment to obtain focus and to iterate through scan layers to obtain a 3D scan
- Interface with the USB spectrometer to capture the spectrum and put into wavelength bins, for generating data-cubes comparable to those produced by the MKID
- Turn the excitation laser on and off at the appropriate times
- Control the wide-field imaging USB camera and associated LED illumination
- Interpret the images from the USB camera so that it could be used:
    - As a real-time display for coarse manual location of the sample
    - To bring the target into focus prior to scanning
    - For aligning the microscope optics
- Spectral deconvolution of the data cube to extract the fluorophores
- Display the outputs during scanning for troubleshooting
- Record all relevant data and meta-data required for interpreting the results

4.7 Summary

The MKID microscope was capable of locating the feature of interest (with a wide-field system) and gathering fluorescence light from a sample with an MKID detector (or reference spectrometer). Fluorescent microspheres, containing one of two different fluorophores, were selected as the test samples. Numerous test runs and frequent fine-tuning demonstrated that the performance of the microscope was sufficiently refined to observe these microspheres. Collection of spectral data was achieved by the use of appropriate control hardware to manipulate both the sample illumination and data collection. Control software was employed to direct and monitor the location of data sampling points.

Chapter 5

Data Acquisition and Processing

The sequence of operations that process the information generated by the raw input of detected photons, via output by from the readout system and encompassing subsequent post- processing, into a data product (*e.g.* image or numerical array, etc.) is here described as the data acquisition system. This sequence involves laboratory equipment, computer hardware, computer software, and processing algorithms.

This chapter presents an overview of the steps in the data acquisition system, with an explanation of how each step is achieved. Also described are the equipment involved, the limitations imposed by the equipment, and how the performance is expected to improve as the equipment is developed. Beginning with data processing of the MKID output to create photon lists, the chapter continues by describing how these are saved in an output format that facilitates the creation of data products, namely images. The creation of data products, including the identification and isolation of fluorophores based on spectra found by analysing the photon lists, is addressed in Chapter 6.

Much of the equipment was still in the developmental stage, and thus required continual refinement in order to progress to a point where it could generate photon lists. Some of this development is detailed below, although the presentation is streamlined for clarity.

The main stages and topology of the data acquisition system for the MKID are illustrated diagrammatically in figure 5.1, and explained in the following sections.

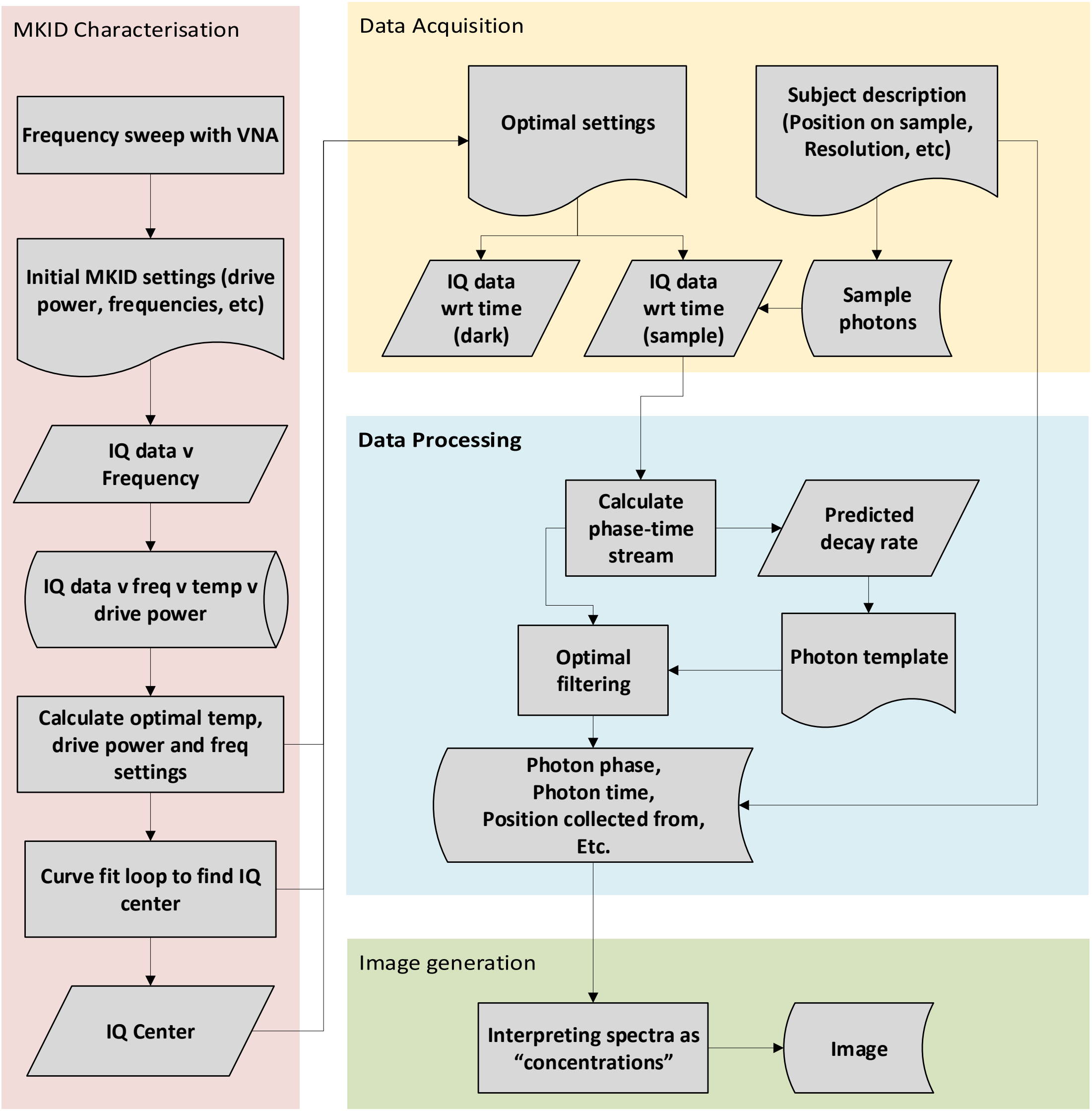

Figure 5.1: MKID Microscope data acquisition system

5.1 Identification of Resonators

MKID operation is made possible by a harmonic oscillator in the form of a linear LC resonant circuit, as described in 2.2.3. In practice, several MKID devices, comprising several distinct LC circuits with various resonant frequencies, are read out by a single feed-line that is created on the chip at die level. These are designed to be well-separated in the frequency domain, permitting specific MKID resonator devices to be addressed using frequency domain multiplexing. The resonators of interest are initially identified by conducting a **frequency sweep with the VNA**, which is an item of test equipment described in Section 5.1.1. From the VNA output, the approximate resonant frequency of each resonator and an approximate drive power can be measured. The resulting resonant frequency and drive power are used as the **initial MKID settings**, and serve as a starting point for conducting a grid search with the custom readout electronics (see Section 4.4.2).

Resonant frequencies are decided at the design stage and tend to be in the 4 GHz to 8 GHz range, as described in Section 2. Once manufactured, the actual resonant frequency of each MKID often differs from its designed value due to variations in deposition thickness, mask tolerance, material purity, *etc.*, as well as their dependence upon drive power and temperature. For these reasons, its optimal drive parameters must always be determined empirically.

The output from the scan measures the reverse reflection, as well as the transmission, magnitude and phase change of the signal transmitted through the system, is referred to as the S-parameter (which in this case is theS_{21}). This is done at many frequencies. The result will look similar to Figure 5.2, where narrow troughs indicate each of the high quality factor (Q_r) resonators.

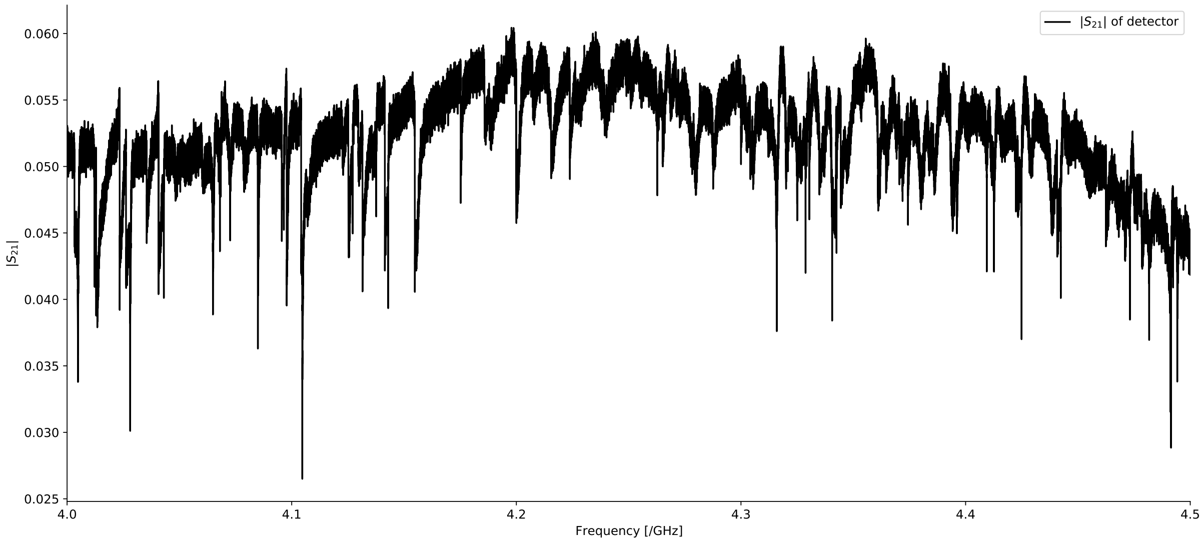

Figure 5.2: Frequency sweep showing several sharp troughs, corresponding to resonant frequencies from many MKIDs on a single feed-line. This isS_{21} with respect to frequency, between 4 GHz to 4.5 GHz taken with a VNA, from the MKID array manufactured by UCSB.

Figure 5.3 shows a resonator from the MKID array manufactured by UCSB when driven at various VNA drive powers, and the asymmetry that develops in the S_{21} profile when the drive power exceeds a certain level. This phenomenon is called bifurcation.

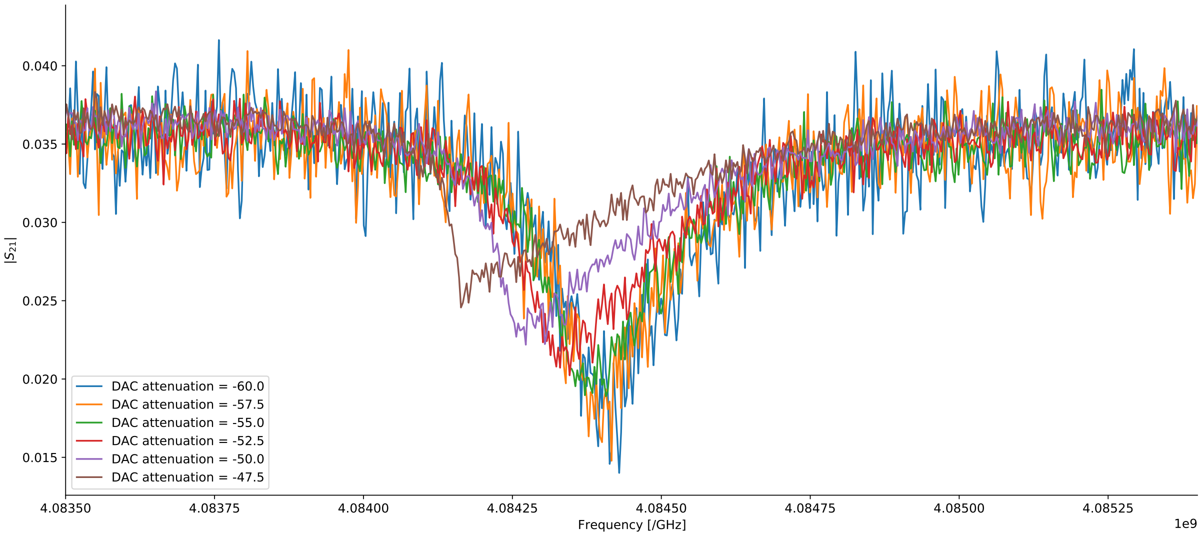

Figure 5.3: The effect of resonator drive power on resonator asymmetry, showing higher drive powers (lower DAC attenuation) results in bifurcation. This data was taken at various input power settings on the readout electronics.

Bifurcation, described by Zmuidzinas (2012), occurs when the resonator drive power is significantly higher than the optimal value and the response becomes bi-stable. Figure 5.4 shows a simulation of a resonator driven at various non linearity parameters (a), resulting in certain frequencies having more than one possible S_{21} value for range of probe tone frequencies below f_0. For example, in the case of $a = 5$, at $y_g = -2.5$ the S_{21} could be 0 or -2.5dB (but not -1.4dB), and the value taken depends on whether the frequency was achieved by ascending or descending frequency sweep. Bifurcation was always avoided.

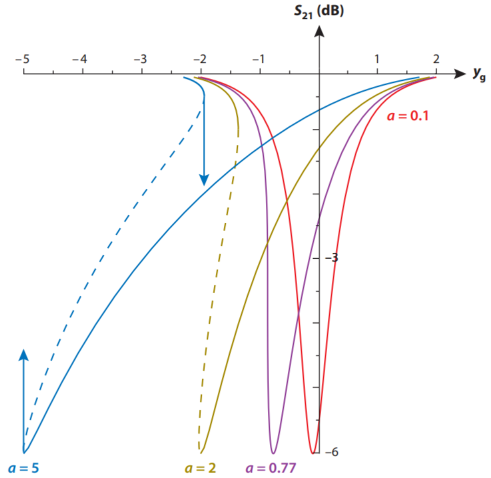

Figure 5.4: S_{21} with respect to normalised generator detuning factor (y_g) for different non-linearity parameters (a). The bifurcation regime happens beyond $a \gtrapprox .77$ Values along the solid lines can be found experimentally, but the dashed region is never achieved. (Credit: Zmuidzinas (2012))

5.1.1 VNA Equipment

A VNA (Keysight, PNA-L) was used to perform a wide-sweep of the frequency-space, and identify the approximate frequency of detectors. The output is given as either ratio of the power leaving port 2 and the power entering port 1 (S_{21}), or in-phase and quadrature (IQ) points. The local minima of the S_{21} curve was sufficient to determine a particular detector's resonant frequency, and IQ data could be used to characterise large numbers of detectors with respect to drive power, etc.

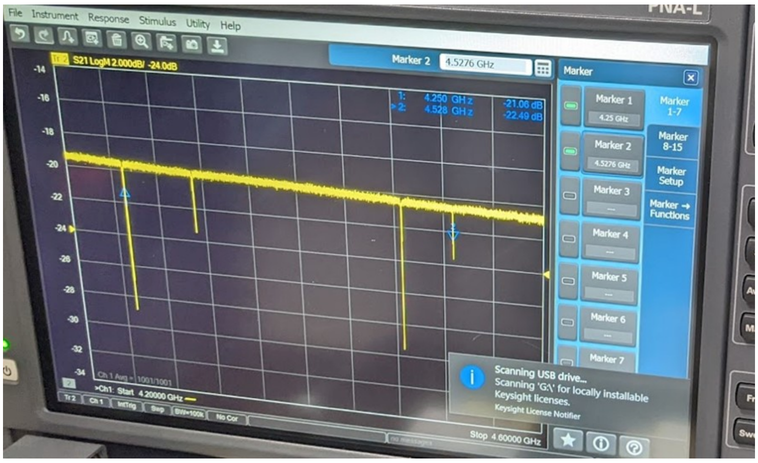

Scanning USB drive...
Scanning 'G:\' for locally installable Keysight licenses.
Keysight License Notifier

Figure 5.5: Image of VNA used, showing the four resonator peaks from the SRON device

.

5.2 Characterise Resonators

Optimal settings for drive power and probe tone (frequency at which a resonator is excited during operation), are found by testing the MKID at various settings and then mathematically characterising the resonators.

Each resonator is profiled using the readout electronics (described in Section 4.4.2), by **obtaining the IQ signal with respect to Frequency**. This profiling is performed at different drive powers (voltages of input probe tone), device temperatures, and frequency settings and analysed using code written by the author for this purpose. By analysing the resultant outputs, it was possible to determine which settings give optimal operating MKID R, as well as other characteristics mentioned below. This procedure is best performed through experimentation using the exact equipment that will be used.

5.2.1 Temperature Set-point

The operating temperature of the device primarily affects the quasiparticle recombination time, which in turn governs the decay rate and device noise, which both dictate R. The control electronics for the Bluefors cryogenic refrigerator allow the operator to temperature-regulate the condenser flange to which the device is thermally coupled (see 4.4.1), to select a temperature that is optimal for operation of the MKID device. The optimal operating temperature for the device is below the T_C of the material, and is determined experimentally, from the literature, or by the general rule:

$$T_{op} \leq T_C/8 \tag{5.1}$$

where T_{op} is the optimal operating temperature for the kinetic inductance effect (cite: Mazin (2022)).

In the case of the UCSB device, the temperature was set at $\approx$ 80 mK, and the SRON device was set at $\approx$ 120 mK.

As the temperature increases, the recombination time of the quasiparticles decreases, (τ), and the half life of the exponential decay of the peak decreases. These factors result in fewer data points on the decay curve (for a fixed sample rate) on which to perform statistical fitting. Consequently, the uncertainty in the photon energy reading is greater (*i.e.* a lower *energy resolution*, R).

5.2.2 Drive Power

Each resonator is driven with a sinusoidal wave at a user-defined frequency, as described in Section 4.4.4. To achieve optimal energy resolution, each resonator should be driven at its optimal probe tone frequency and amplitude. If the amplitude of the signal reaching the resonator is too high, it will cause over-driving and bifurcation and potential instability. Conversely, a signal that is low leads to a poor SNR. Because both extremes would ultimately result in poor R, the parameter space must be explored to find the optimal values.

In practice, the probe tone amplitude experienced by the MKIDs is dictated by the individual waveform setting (a number up to 1) describing what portion of the output signal is used by that signal frequency, and the attenuators on the feed-line.

5.2.2.1 Signal Amplitude

The DAC outputs the sum of potentially thousands of sinusoidal signals of different amplitudes that must, when combined, not have peak amplitude exceeding the output voltage of the DAC. Therefore in the case of a single resonator it is advantageous to set it to one. Because the voltages within the signal are discretised into a finite number of voltage levels (depending on the bit resolution of the DAC), it is advantageous to use the full range of the analogue-to-digital converter (ADC) (assuming no non-linearity at the extremes, which was the case with our equipment) for several reasons:

- The sinusoidal waves will have less signal-to-quantisation-noise ratio s they because they use more of the bit range
- The signal is higher relative to the noise floor of the DAC, so the SNR is better
- The signal is higher relative to the noise introduced along the path to the DAC attenuator, so the SNR is better

It should be noted that this is the stage at which the relative drive powers are set.

5.2.2.2 DAC Attenuation

The resonator(s) receive a probe tone signal with an amplitude that is dependent on the DAC signal amplitude, the cold-stage attenuators, and the DAC attenuation levels. Optimisation of drive power is achieved by assessing each of the resonators' performances at a range of DAC attenuation values, and finding the value that produces optimal results.

5.2.2.3 ADC Attenuation

The ADC converts an incoming voltage to one of 2^{14} values (14bit, see 4.4.2) and the ADC attenuator serves the purpose of attenuating the signal to be within this range. The voltage read by the ADC should be as large as possible in order to improve the SNR, while remaining within the linear range of the operating envelope of the ADC, otherwise there is distortion and clipping that results in a loss of information.

5.2.3 Characterising Large Numbers of Resonators

This method of manually finding each resonator and exploring the drive power and operating parameter spaces was suitable for this experiment because only a few resonators required identification. However, as array sizes increase, the time required increases, with a 2000 pixel feed-line reported to take as many as 4 to 6 hours. In such cases, it becomes prudent to apply automation such as the deep learning methods that have been developed to accelerate this process, as described by Fruitwala (2021) and Dodkins (2018).

5.3 Fit to Resonator Loop

Readings for IQ are taken at various DAC settings and frequencies. A mathematical model is fitted to the results to determine the optimal fitting parameters, and to **find the centre of the IQ loop**. These parameters include the resonant frequency (related to the optimal probe tone frequency at which to drive the resonator), and the centre of the loop (about which the photon-event-induced phase shift can be calculated), as well as the quality factor of each resonator that is valuable for deciding which settings should be adopted to drive the resonator.

5.3.1 Circle Fit and S21 Fit

This approach is explained in Gao (2008), and is a two-part approach: firstly, to fit a circle to the points in the IQ plane to obtain the loop centre and, secondly, to fit a curve to the S_{21} values using the following equation:

$$t_{21}(f) = ae^{-2\pi j f\tau}\left[1 - \frac{Q_r/Q_c e^{j\phi_0}}{1 + 2jQ(\frac{f-f_r}{f_r})}\right] \tag{5.2}$$

Figure 5.6 shows the least-mean square (LMS) fit of the above equations to a frequency sweep obtained from a SRON detector, and the best fit for a circle to the data in the complex plane. Both fits show good

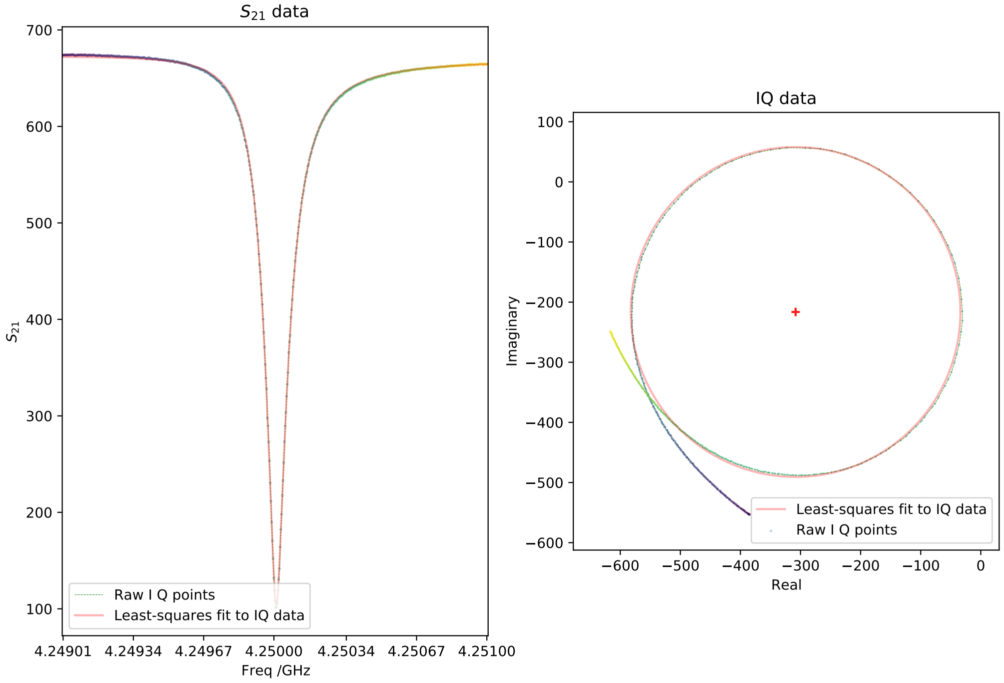

Figure 5.6: Fit to the S_{21} profile and circle fit to the IQ points

5.3.2 Loop Fit

A mathematical model for the ’resonance transmission curve in the complex plane’ of microwave resonant circuits is described by Mazin (2005) (Section 6.1) who explains the origins of the python code, below (courtesy of by K. O’Brien), and the nine parameters received by the function (see table 5.1).

Parameter	Symbol	Python symbol	Description
Q	Q	`Q_val`	Resonator quality factor
f_0	f_r	`f_0`	Resonant frequency
Amplitude	a	`a`	Off resonance amplitude
IQ velocity	v	`v`	Off resonance IQ velocity
Carrier offset	c	`c`	Linear offset of the beginning and end of the resonance curve
Rotation angle	θ	`rot`	Rotation angle about the origin
I gain	g_I	`I_gain`	Gain of I
Q gain	g_Q	`Q_gain`	Gain of Q
I centre	I_c	`I_cen`	Loop centre in I
Q centre	Q_c	`Q_cen`	Loop centre in Q

Table 5.1: Table of variables in ’res model’

The equation can be written as a function in Python to output a 1D array of floats that can be used in Python’s `scypy.curve_fit`, a program that performs LMS fitting to determine optimal parameters.

```
def res_model(freq2, Q_val, f_0, a, v, c, rot, I_gain, Q_gain, I_cen, Q_cen):
    freq=freq2[:len(freq2)//2]
    dx= (freq-f_0)/f_0
    f_val= np.zeros(len(freq),dtype=complex)
    f_val= 0 + (2*Q_val*dx)*1j/(1+2*Q_val*dx*1j)
    f_val=f_val-0.5+c*dx + a*(1-np.exp(1j*v*dx))
    IQ=I_gain*np.real(f_val) + 1j*Q_gain*np.imag(f_val)
    IQ=IQ*np.exp(1j*rot*np.pi/180.0)
    IQ=IQ + (I_cen + 1j*Q_cen)
    return np.concatenate((np.real(IQ), np.imag(IQ)))
```

These variables are then used to define the fitted loop, seen overlaid on the IQ points (see Figure 5.7):

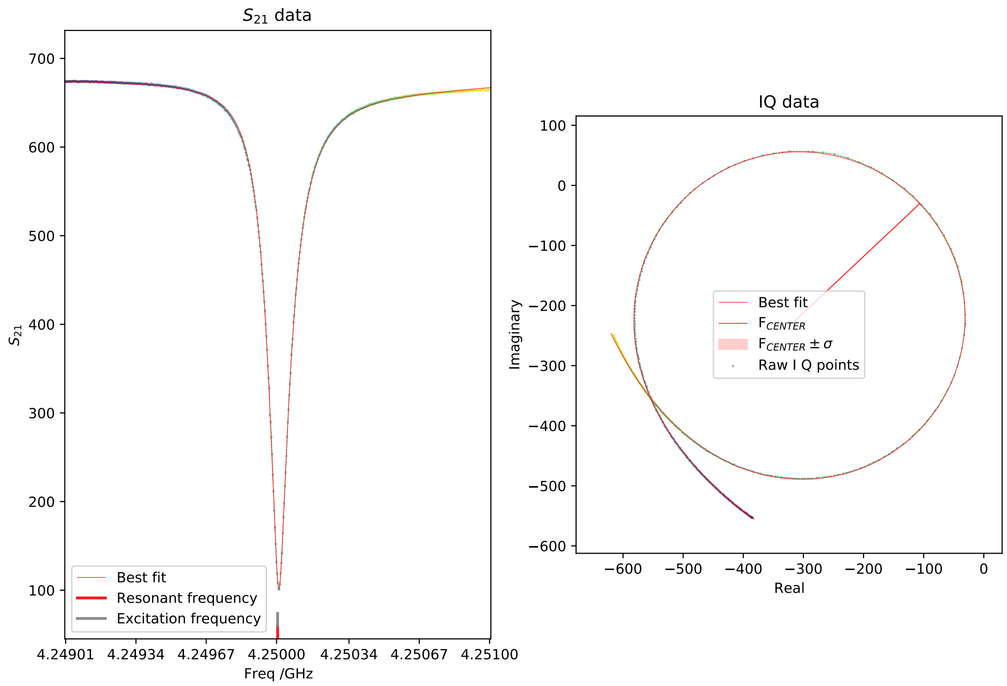

Figure 5.7: Fit to the 'res model' profile in both S_{21} dimension and IQ plane

The quality of the fit is highly sensitive to the initial estimates for the parameters. Consequently, they are first approximated using a combination of calculated values based on the features of the loop (such as the loop's centre position and diameter and position relative to the origin) and other values that are found by a grid search based on known, sound values, or by the far more time-consuming Monte Carlo method. When repeatedly fitting to the same resonator, good results can be obtained by using previously determined optimal parameters, a procedure that is considerably faster.

5.4 Select Resonators

When operating the microscope in confocal scanning mode, the MKIDs act as a fibre spectrometer. Therefore, it is possible to use only one MKID. The decision of which resonator to select is influenced by:

- Defective feed-lines: Imperfections in the deposition, contamination during lithography, damage in handling or assembly, or failed wire bonding, could all result in there being a break in the feed-line, such that a signal is not transmitted through that section of the device.
- The quality factor: Higher quality factor resonators give a larger response to a photon, whereas low quality factor detectors have poor R, or even imperceptible photon responses.

- The proximity to other detectors in the frequency space: While resonators are designed to be well separated in the frequency space, 'frequency scatter' during manufacture can cause resonators 'collide' in frequency space (see Figure 5.8). Two or more resonators that have similar excitation frequencies may be excited by each other's probe tone, or cross-talk (Nagai et al., 2020).

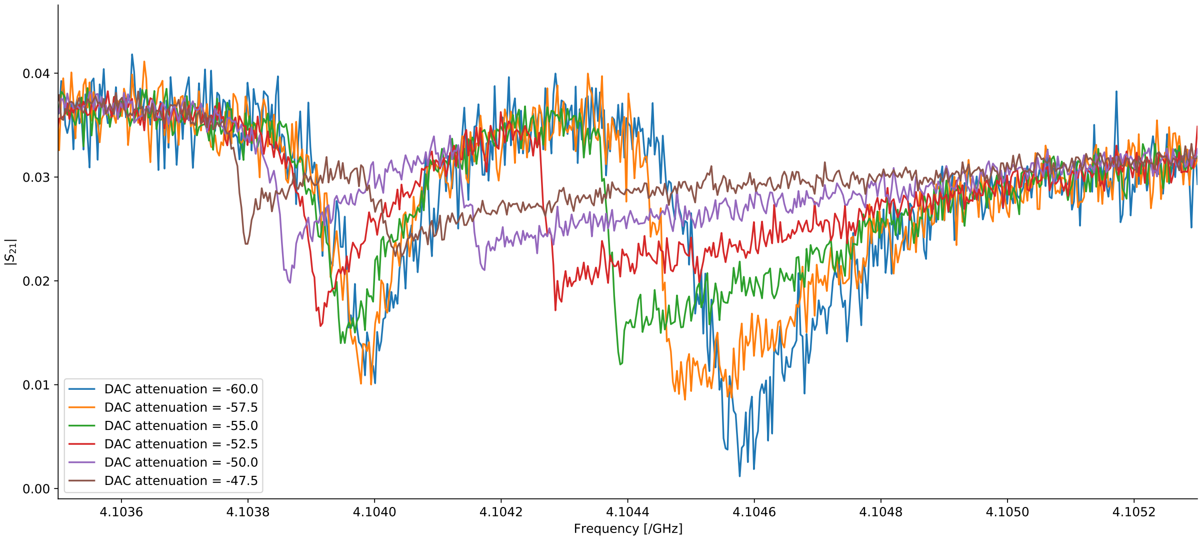

Figure 5.8: S_{21} amplitude w.r.t. frequency at a range of drive powers, showing two resonators that have collided frequency space

- Quantum efficiency of the system: Specifically, the quality of the optical coupling to the MKID, which is dependent on the alignment of the lens array shown in section 2.2.2.1.
- Whether the resonant frequency of the detector was within the operating range of the readout electronics: Because the readout electronics were capable of 4 GHz to 8 GHz, any detectors falling below this value were not readable by the system.

Figure 5.9 , shows the spectral resolution R of each detector in the MKID Exoplanet Camera (MEC) instrument (ref: Steiger et al. (2022)), illustrating the challenges with detector yield. Pixels with a value of $R = 0$ are unusable. They are a result of frequency collisions, poor f_0, hot/cold pixels, or defective feed-lines (of which there are three, shown by the large strip of dead pixels).

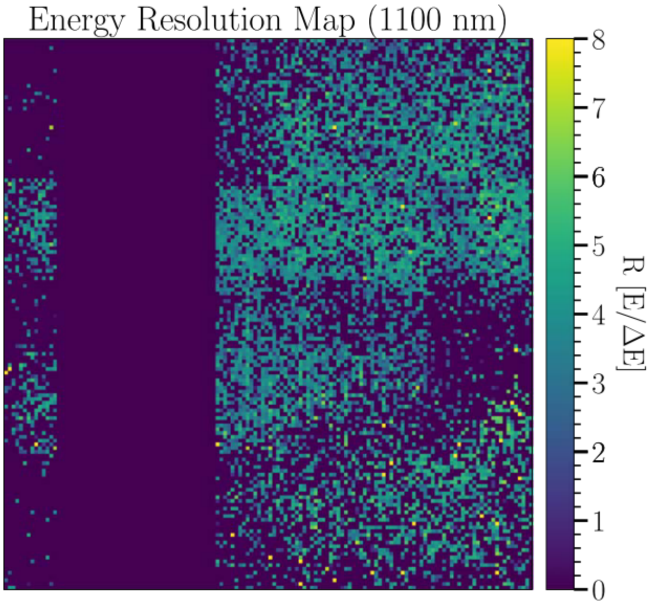

Figure 5.9: Image showing the energy resolution of the MEC instrument described in Steiger et al. (2022) . There are several pixels that are dead, due to defective feed-lines (dead strip on the left), frequency collision, or any of the reasons described above.

5.5 Select Optimal Settings

Once the resonators have been chosen, the **optimal settings** must be determined. Temperature and ADC settings affect all resonators, but the probe tone and drive power can be tailored to each individual resonator. These factors would be taken into consideration when deciding the settings for a complete array. However, for the initial test, only a single detector was used. Consequently, the fitting was more straightforward.

Several tools were available to perform this optimisation, and are discussed below.

5.5.1 SuperConducting Resonator Analysis and Plotting Software

A powerful tool in characterising and optimising settings for resonators was SCRAPS (SuperConducting Resonator Analysis and Plotting Software) devised by Carter et al. (2017). The program allows Monte Carlo fitting to each S_{21} curve, to find the best fit (with errors), or least mean squares fitting. This results in a transparent comparison based on parameters such as drive power and temperature (see Figure 5.10(b)). Because only one detector was used in these tests, it was possible to perform analysis in a less automated way.

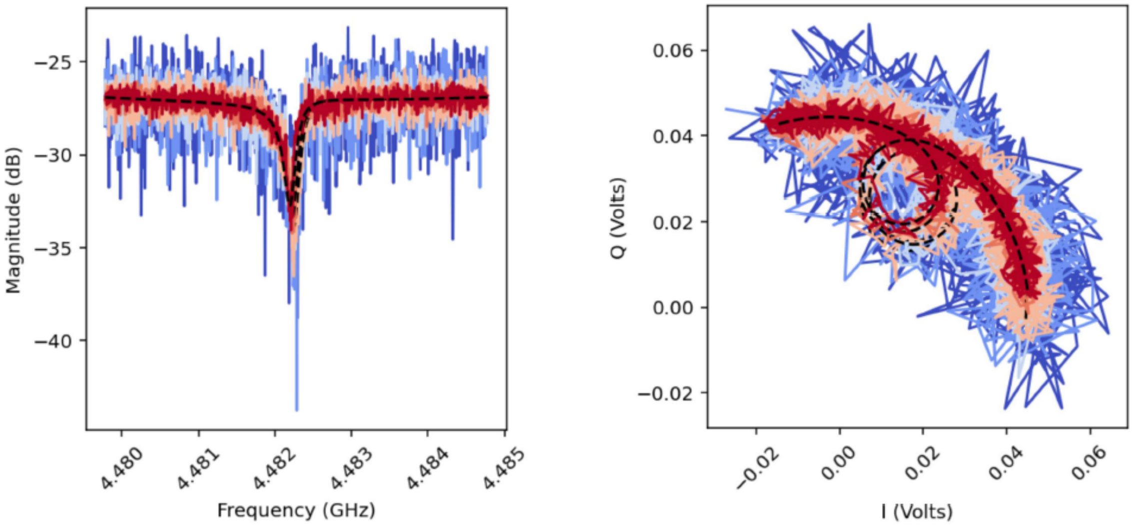

((a)) Plot of S_{21} w.r.t. frequency, at various drive powers ((b)) Plot of IQ at various drive powers

Figure 5.10: The output from the analysis package SCRAPS

5.6 Calculating Phase Time Stream Data

In order to detect individual photons, each selected MKID is excited with a fixed frequency and the IQ values are read out at close to 1 GHz sampling frequency (see 4.4.2).

The phase, or "phase angle", of a given sample is the relative angle from the centre of the calculated IQ loop, given in degrees (or radians). Figure 5.11 shows the IQ points plotted over the best-fit loop found by the method outlined in Section 5.3.2. From the image, it is possible to see a collection of points about the excitation wavelength, and also a tail from some points extending anticlockwise around the IQ loop (red). The latter result from photon events.

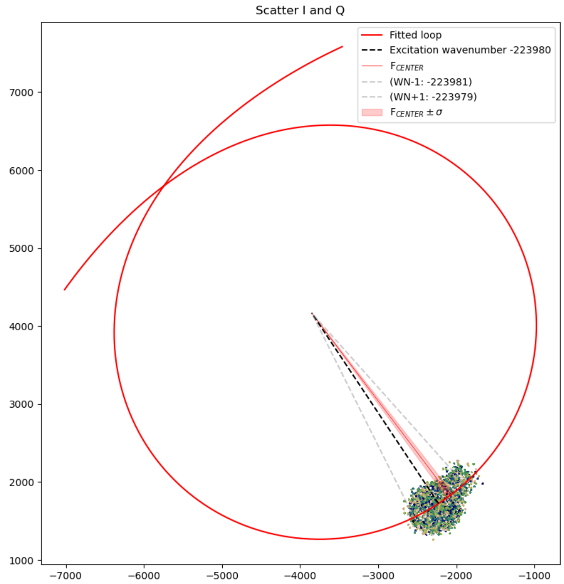

Figure 5.11: IQ points (yellow to green dots) at a chosen excitation frequency, overlaid onto IQ loop. Some photon events are present, causing the cloud to be extended slightly in a tail extending anti-clockwise.

Figure 5.12 shows the angular position of these points about the loop centre, with respect to time. Clearly visible are four distinct photon events characterised by a rapid increase in phase angle, followed by a gradual relaxation back to the stable point (or **fast-rise, exponential decay** profile), from which 'photon arrival time' and 'photon energy' information can be extracted.

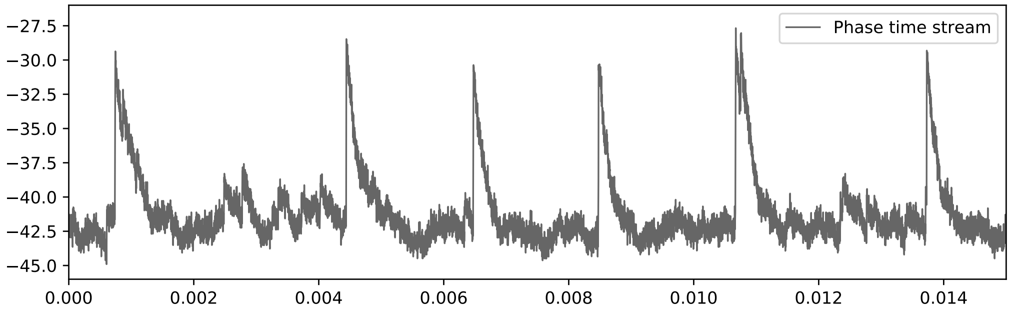

Figure 5.12: Phase angle with respect to time, showing a fast-rising signal when a photon arrives, and an exponential decay back to baseline

A 'dark reference' is taken each time, to establish the unperturbed phase angle distribution to better understand the noise spectrum (not analysed here).

5.7 Characterise Decay Constant

Assuming that an initial estimate for τ is not available, it is possible to arrive at an approximation by averaging all peaks (making the coarse assumption that all peaks above 4σ of the background noise are photons) and fitting the resulting averaged profile (shown in red in image 5.13) to the equation for the fast-rise, exponential decay curve (shown in orange). This can then be adopted as an initial profile to be used in a convolution function to identify real photon events.

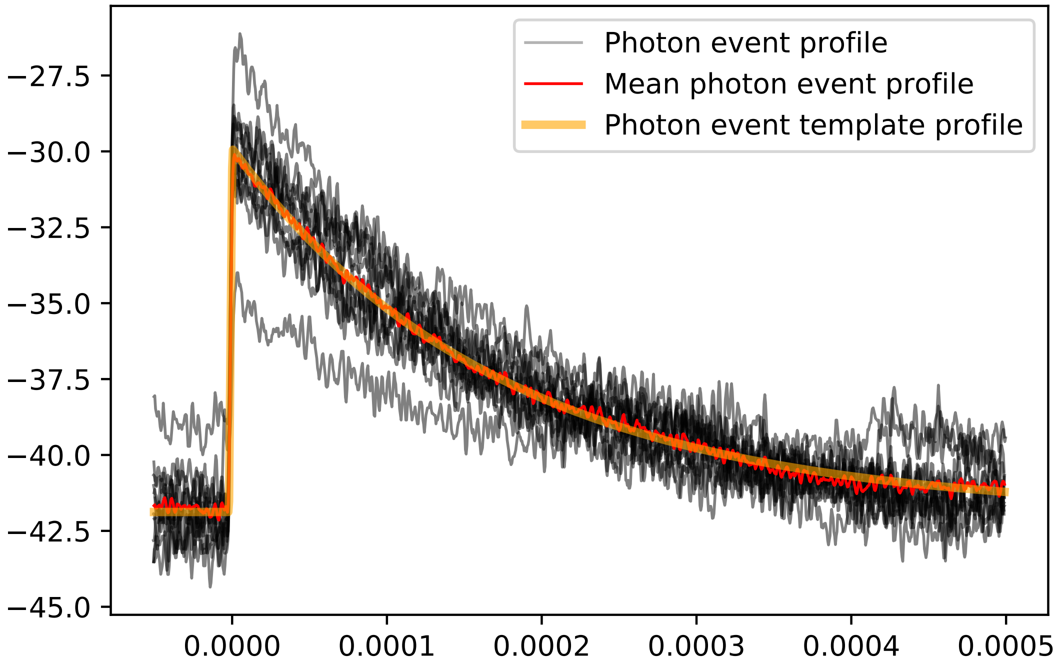

Figure 5.13: Multiple photon decay curves (black), averaged (red) to allow fitting of the model of a photon profile (orange). Curve fitting found decay rate, $\tau = 6.67{\times}10^{-4}s$

This coarse profile can be convolved onto the phase time stream, to identify all photon events within the sample(s) analysed. This collection of photon events can then be screened to exclude profiles that include multiple photon events, or events with a phase shift under a certain cut-off. The resulting list can then be averaged and fitted to in a similar manner to that described above to produce a *photon event template profile* that is used to identify photon events as described below.

5.8 Identifying Photon Events

Once the *photon event template profile* has been found (see Section 5.7), it is possible to use it to find similar features in the phase time stream in the manner described below. There are events resembling very high energy photons, which must also be identified.

5.8.1 Cross-Correlation and Curve Fit

The profile for a photon event and phase time stream can be compared to identify instances in which they are similar, indicating a photon event using cross-correlation. A known photon profile can then be fit to each 'photon event' identified in this way, to determine the 'phase change angle'.

To perform the cross-correlation, a *kernel* is first created by reflecting and normalising the *photon event template profile* (such that it becomes an exponential rise, fast decay pulse, with an area under the curve of 1). This kernel is then convolved with the *phase time stream* using the python `scipy.signal.convolve` function to create a third signal.

Figure 5.14 shows the peak occurring in the resultant cross-correlation signal (orange) corresponds with a fast-rise in the phase time stream (grey) which would be expected at the time that a photon event occurred.

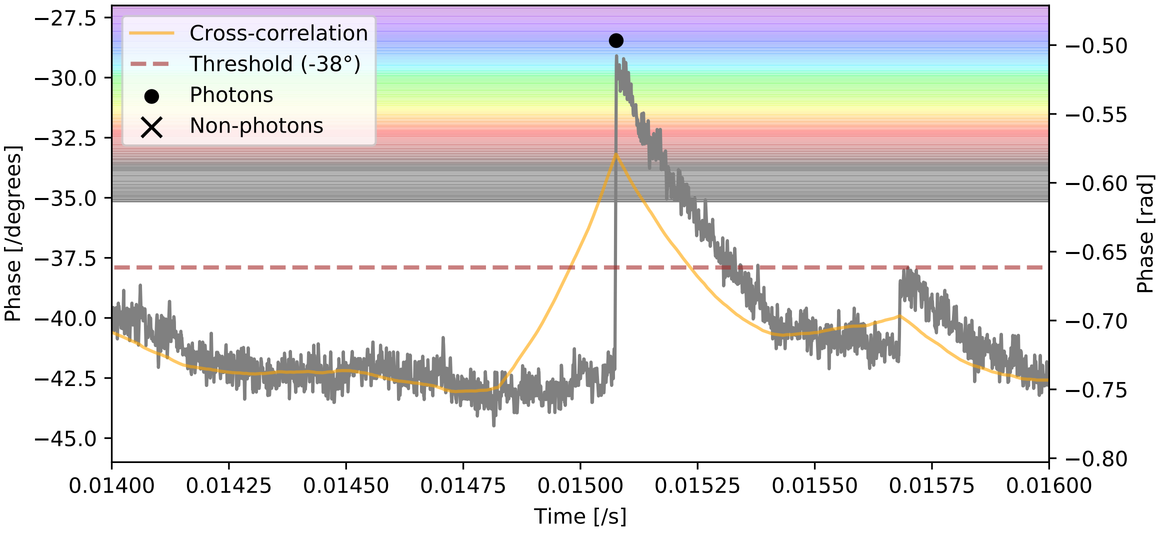

Figure 5.14: The output (orange) from the 'photon template' cross-correlated with the phase time stream (grey). The peaks occur at photon events, and their height indicates photon energy.

The time and height of the cross-correlated signal can be used as initial parameters for a further LMS fit of the *photon event template profile* to each event, as shown in Figure 5.15. A chi-squared test is performed on the fit to determine whether there is good agreement between the model and the data. Points with poor agreement are discarded (indicated by the ×).

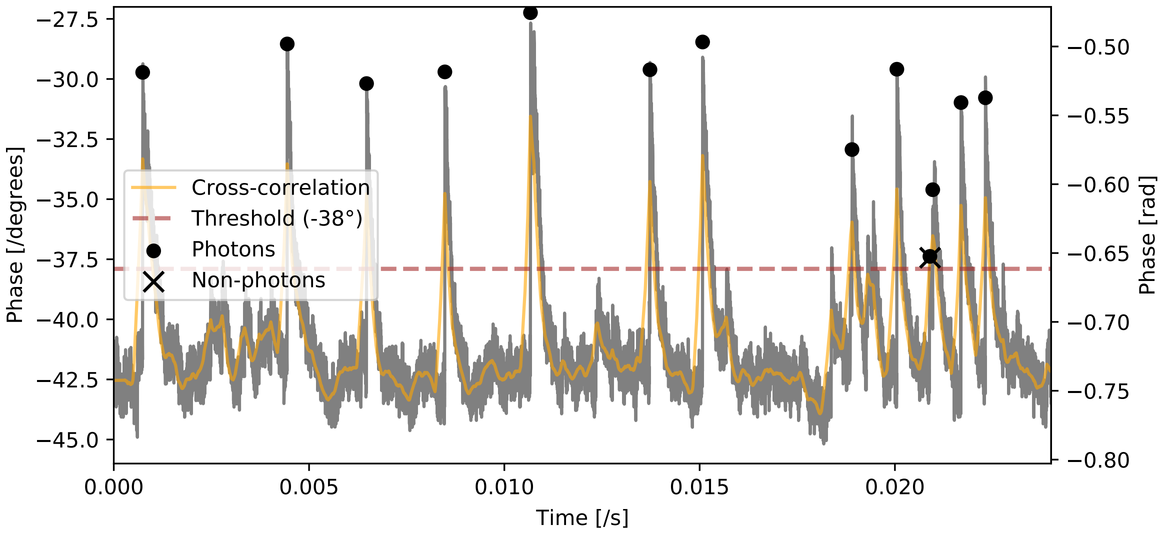

Figure 5.15: Phase time stream from an MKID experiencing photon events caused by a 635 nm red laser. The photons are identified using a convolve function, then fitting is used to more accurately determine the photon phase change (correlating to energy) and arrival time. Multiple peaks indicate the arrival of multiple photons.

5.8.2 Cosmic Ray Rejection

Cosmic rays are high energy particles that travel through the equipment. If they pass through an MKID detector they will appear as a very high energy photon event in the phase-time stream. They are sufficiently infrequent to not cause issues with the readings. Because they have phase shifts several standard deviations away from optical photons they can be identified and removed as anomalies.

5.9 Wavelength Calibration

The phase shift caused by a photon, is (to a good approximation) proportional to the energy of the photon and the calibration step ascertains this relationship. This is done by measuring a large number of photon phase shifts caused by known wavelengths, and is most reliably done with multiple lasers of known and stable wavelength, or other monochromatic light source. Because of noise and uncertainties on the height of the phase change event, many photons are required to build up a distribution. Figure 5.16 shows eight distributions of phase shifts, each created by photons of different energies provided by a monochromator isolating a narrow wavelength range from a white light source. This data was collected using the MKID array manufactured by SRON using an early version of the readout system so the R found is lower than it was for the final experiments.

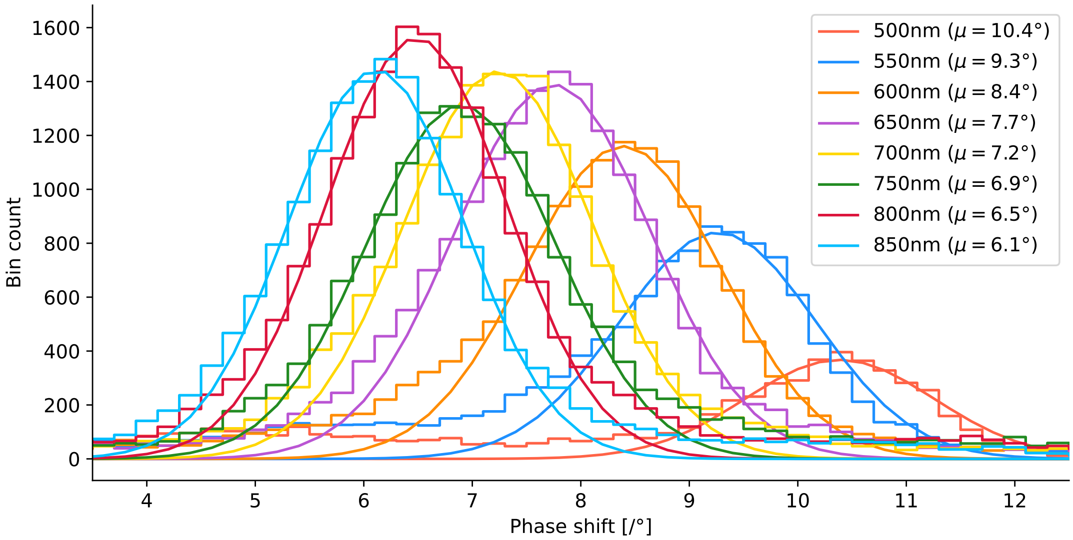

Figure 5.16: Calibration phase shift vs wavelength. A histogram of all photons gathered from a particular monochromatic light source of the wavelength stated in the key, and a mean phase shift of μ

Figure 5.17 plots the known photon energy against the mean phase shift, with a line of best fit assuming a proportional relationship (Equation 5.3).

$$E_{PHOTON} \propto \Delta\theta_{PHOTON} \tag{5.3}$$

where E_{PHOTON} is photon energy and $\Delta\theta_{PHOTON}$ is phase shift caused by the photon.

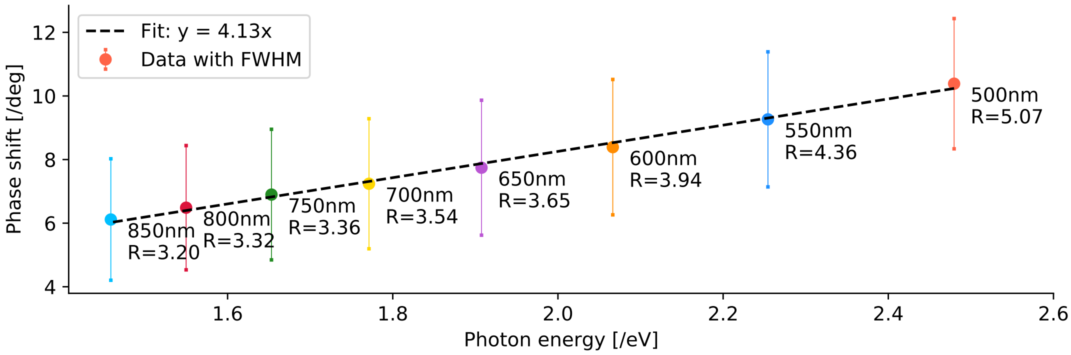

Figure 5.17: Graph plotting phase shift w.r.t. photon energy, and a line of best fit assuming the phase shift is directly proportional to phase shift.

5.9.1 Energy Resolution

The FWHM of each distribution is used to calculate R which in the case of this resonator (the MKID array manufactured by SRON, Resonator at 4.000 GHz, at a bath temperature of 120.0 mK) and using the readout equipment, was found to be 5.07 at 500 nm, and 3.36 at 700 nm, given by equation 2.4

5.10 Create Image or Data Product

Once a phase-time stream has been acquired for a particular location on the sample and the list of photons determined, the process can be repeated for each spatial position in the sample. Section 4.6, describes how the custom control software, written to control the microscope, enables identification of the region of interest, and how data acquisition at each point is based on settings for **position and resolution**. The data was written to a python dictionary **J**ava**S**cript **O**bject **N**otation (JSON) file with 3 items:

- **MKID Scan** data: a list of entries each containing [x position, y position, [$\delta\theta_{PHOTON1}$,$\delta\theta_{PHOTON2}$, ...]]
- **Spectra** of known fluorophores
- Scans taken with the **USB spectrometer**, and x,y,lambda values

The JSON is in the following format:

```
{
  "mkid_scan": [[0,0,[7.84002, 2.80077, ...]],
                 [0,1,[4.28417, 1.41869, ...]],
                 ...],
  "spectra": {"fp1": [5.71553, 5.71553, ...],
              "fp2": [11.7558, 8.29731, ...]},
  "usb_scan": {"array":usb_data,
               "xvals":x_positions_mm,
               "yvals":y_positions_mm,
               "wavevals":wavelengths}
}
```

At this stage, the **location within the sample and photon information are known**. It is therefore possible to create a spectra at each location in x and y, that would produce a datacube of X,Y,λ. This is demonstrated in Chapter 8 and taken a step further by analysing the distributions of these photons and extracting more information from them. In this instance, each point is captured sequentially, but with an array of detectors, all points would be captured in parallel.

In the case of fluorescence spectroscopy, the arrival time-information on each photon is not required so can be discarded. In the case of FLIM and phosphorescence lifetime imaging microscopy (PLIM) images, this information would be relevant so could be stored by adding another dimension to the array.

Chapter 6

Simulating Fluorophore Spectra

In this chapter, a simulation is created that can assess the several analysis tools proposed. This is achieved by generating *sample spectra* (simulating the spectra detected by the MKID) and applying some preliminary analysis tools to find the *output values* (the fluorophore intensities that will be found by the analysis), and then comparing the *input values* used to create the spectrum. Figure 6.1 describes the steps of the simulation.

The models adopted are based on the known characteristics of the fluorophores selected in Section 3.1.6. The aim is to produce a list of photon energies (*sample photons)* which are in a similar distribution to what would be detected by the MKID according to the properties of the detector of a given spectral resolution (R). These simulated photons can be binned to create one *sample spectrum* for each x,y location that is then passed through several analytical tools specifically created to identify the presence and/or respective concentrations of each component. The results can then be compared to the input data to confirm the viability of the analysis tools. The analytical tools described in this chapter involve methods that are informed by known *reference spectra*, as opposed to blind methods that require many *sample spectra* in order to infer what components best describe the samples (such as PCA/NMF. which are addressed in Section 7.3 and 7.4). This analysis is repeated with real experimental data as described in Section 8. This analysis of 1D spectra lays the groundwork to analyse both simulated and real images.

The purpose of the analysis is to determine the abundance of each fluorophore in terms of photons per unit time. Because applications of microscopy benefit considerably from rapid analysis of samples, emphasis is placed on determining the minimum number of photons that are required to obtain the required degree of certainty to positively identify a feature (indicated by a fluorophore).

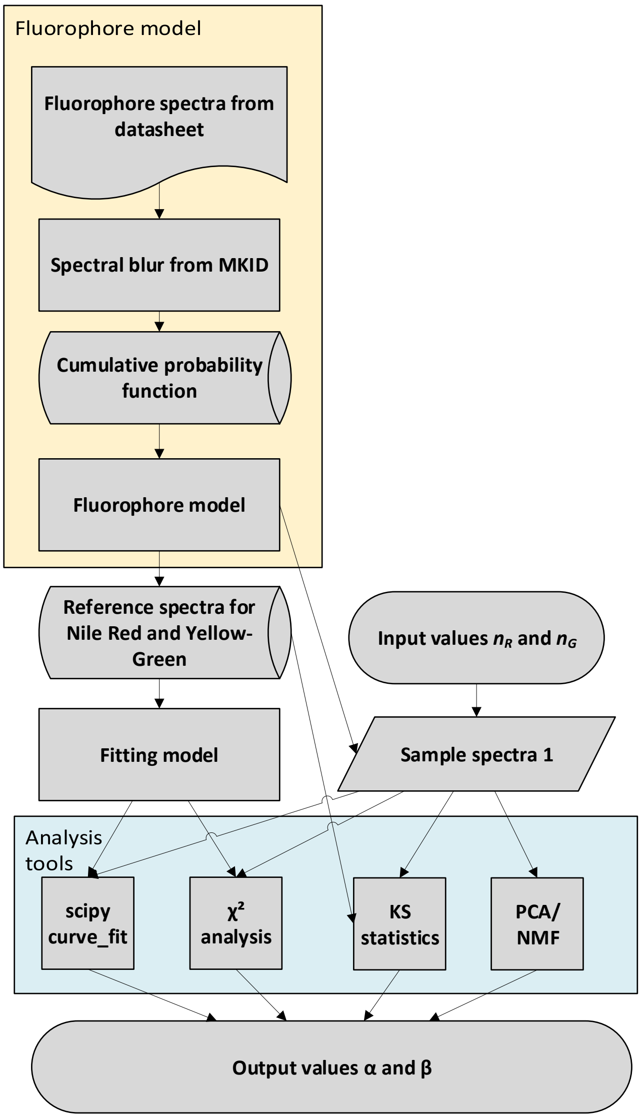

Figure 6.1: Flow diagram showing the processes described in this chapter. A *fluorophore model* is created to generate simulated data, which is one of several analytical tools.

6.1 Mathematical Models

6.1.1 Fluorophore Model

This section describes how photons detected by a single MKID detector are simulated based on a known fluorophore spectrum, at a given R (initially assumed to be R=10). This mathematical model is referred to as the *fluorophore model*. When two fluorophores are excited and detected simultaneously, the MKID receives a combined spectrum that can be simulated as the sum of each of the scaled spectra. This model produces an exact number of photons. However, in practice, there are several factors that affect the relative number of photons (N_{EM}) received by the detector from each fluorophore for every excitation photon. These include, but are not limited to:

- The excitation wavelength, and the excitation efficiency that it achieves on that particular fluorophore
- The quantum yield (QY) of each fluorophore
- The collection efficiency of the microscope system
- The relative abundance of fluorophores in the excited volume
- The optical efficiency of the equipment, which is often wavelength dependent

The two fluorophores selected were Nile Red fluorophore and Yellow-Green fluorophore (their method of selection is described in Section 4.2.1) although the experimental approach is the same with any combination of fluorophores. Excitation and emission spectra data, which is provided by the manufacturers and plotted in Figure 6.2, were used to generate the template spectra. This template is based on the assumption that the spectrum is the same as the data sheet, whereas in practice the spectrum observed through the system is dependent on the components in the optical chain such as lenses, mirrors, dichroic mirrors, filters, fibres, *etc.* To overcome this uncertainty the *reference spectra* for all spectra adopted in the experiments are best obtained empirically.

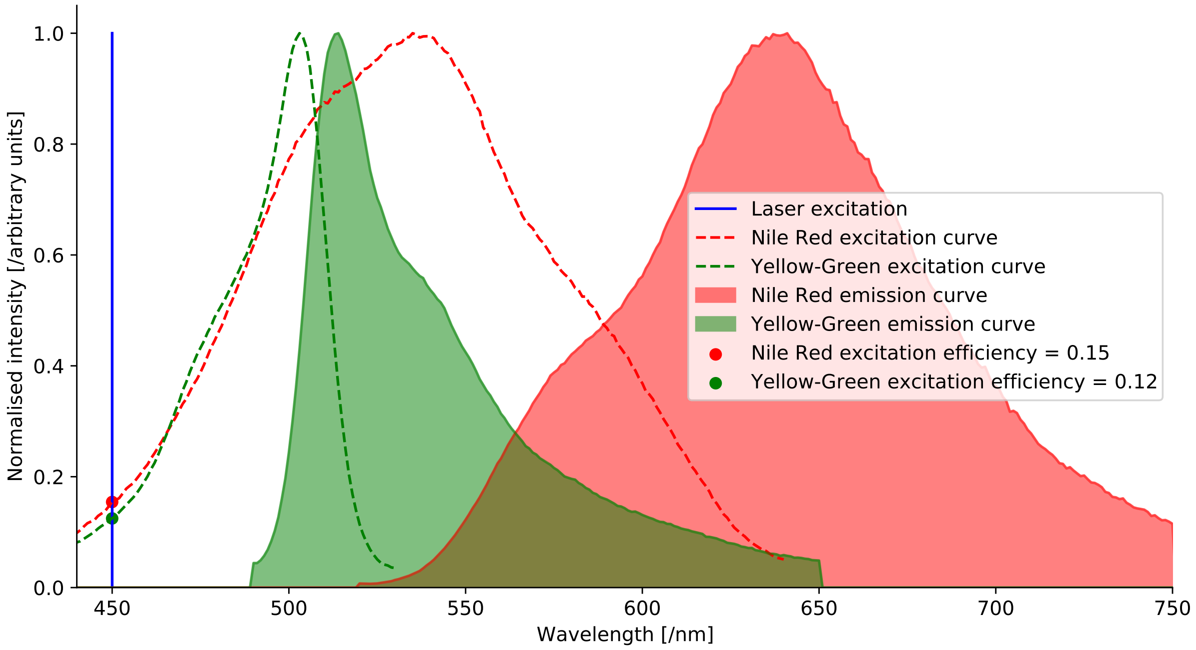

Figure 6.2: Normalised excitation curves and emission curves of two fluorophores used. Also shown is the excitation wavelength from the 450 nm laser, and the efficiency with which each fluorophore is excited.

Although the relative abundance of fluorophores is not known, the input to the simulation is taken to be the absolute number of photons received by each detector on the basis that the illumination and exposure time will be adjusted until that quantity is achieved.

Because of the background noise inherent in the readout system, there is an error contained in the measurement of the photon energy due to this phase-noise. As a consequence, it is not possible to precisely determine the energy of the photon. The phenomenon is equivalent to wavelength-dependent Gaussian blur that produces measured spectra with wider, less pronounced features, with the result that the smaller spectral features are lost. This feature is a function of spectral resolution, R, as shown in Figure 6.3.

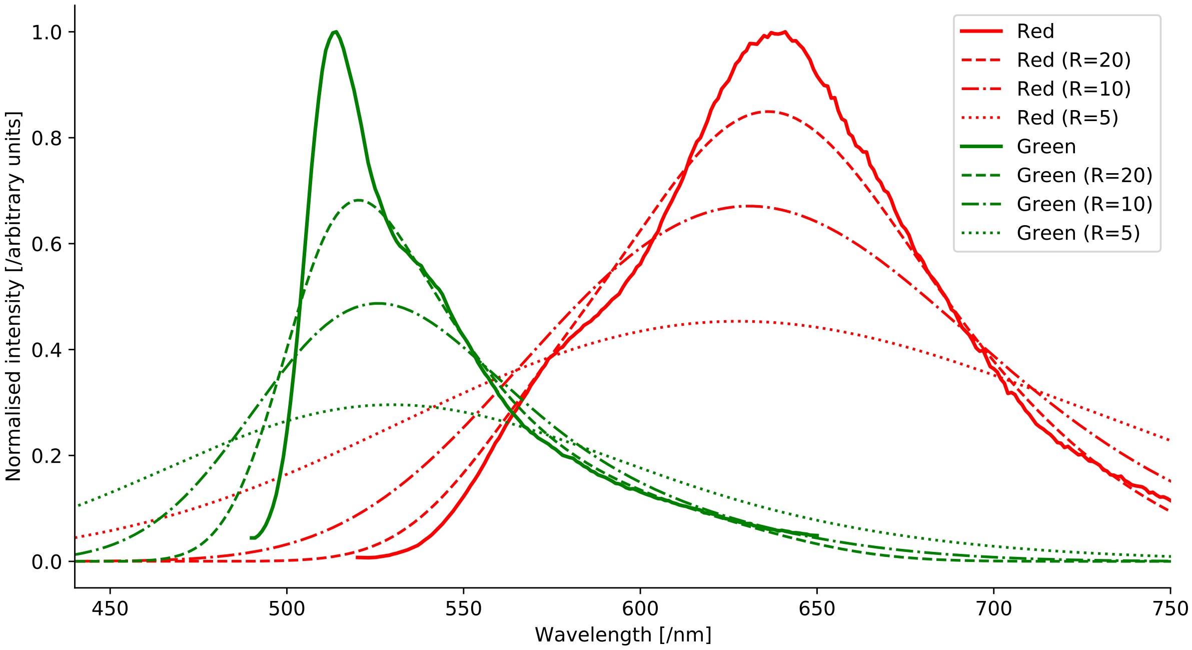

Figure 6.3: Fluorophores chosen, and the effective spectra as measured by the MKID.

The MKID readout electronics measure 'peak phase shift', which can be converted to photon energy using an approximately linear function as described in Section 5.6. It is possible, with appropriate calibration, to convert the units from phase shift to wavelength using a wavelength calibration function. However, this is not a necessary step for the purposes of spectral analysis.

For this reason, the simulation was performed in units of photon energy, avoiding the need to convert into phase shift with an arbitrary conversion factor.

The same fluorophores are plotted in Figure 6.4 after having been converted to photon energy (*i.e.* 635nm is 1.95eV, and 514nm is 2.41eV).

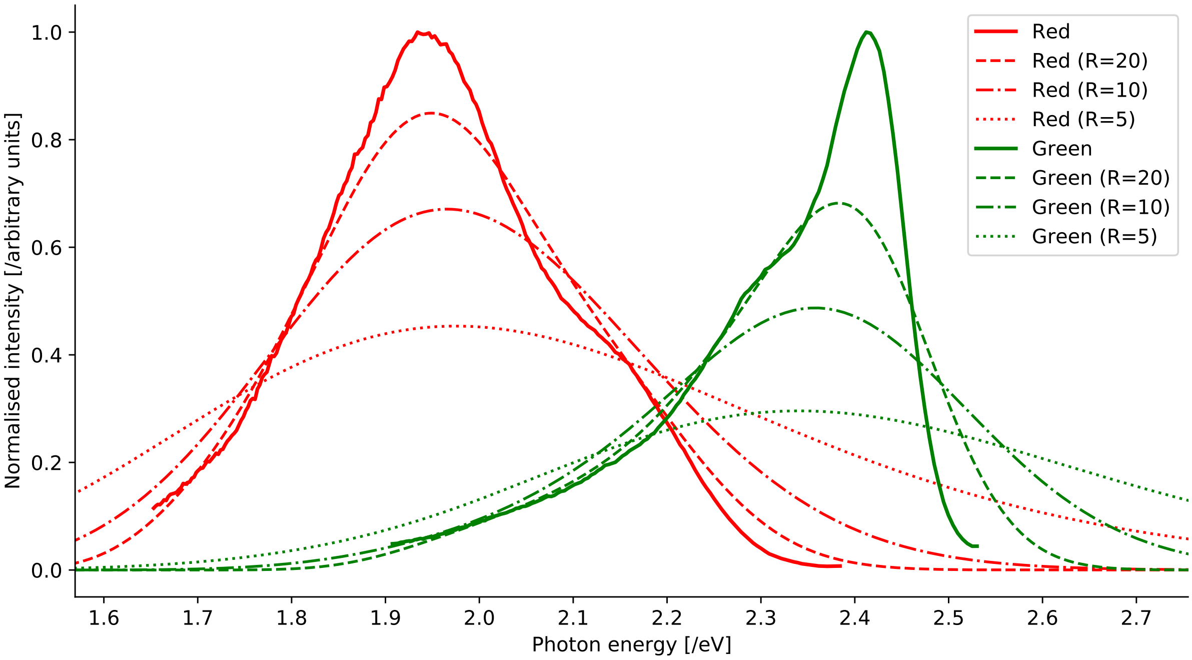

Figure 6.4: Fluorophores chosen, and the effective spectra after being measured by the MKID, in terms of photon energy in electron volts.

The next step is to generate photons that follow the same distribution as these curves. It is possible to achieve this using the rejection sampling method in which two values are randomly generated corresponding to photon energy and intensity. If the resulting point lies below the curve it is accepted, otherwise it is rejected. Because the rejection sampling is computationally inefficient it was abandoned in favour of the inverse transform sampling method, in which the probability density function (PDF) (dotted lines in Figure 6.4) is converted to a cumulative distribution function (CDF) shown in Figure 6.5. Once the CDF has been created, then by generating a random value between 0 and 1 and looking up the corresponding photon energy a simulated energy for a photon is returned.

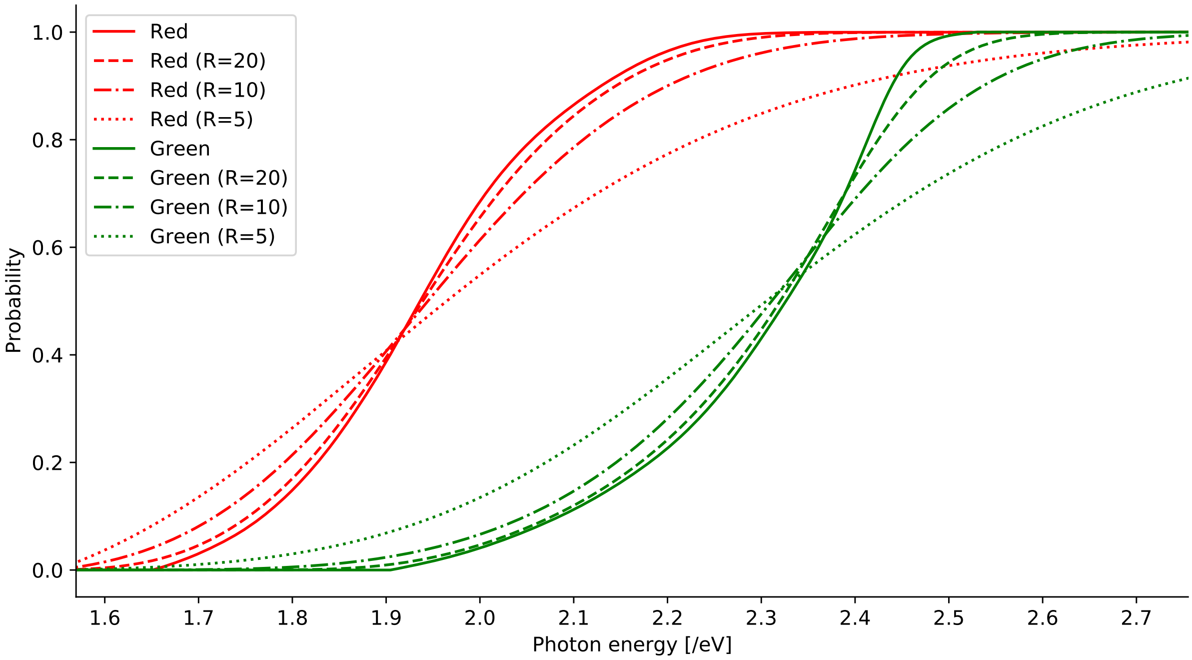

Figure 6.5: Fluorophores chosen, the cumulative distribution function (CDF), in terms of photon energy in electron volts.

A list of n_R photons from the Nile Red source, is appended to a list of n_G photons from the Yellow-Green source, to create a combined spectrum. This model, which yields a combined spectrum from given values of n_R and n_G, is referred to as the *fluorophore model*.

The *fluorophore model* assumes there are only two fluorophores, and that there is no background noise such as auto-fluorescence from either the microscope optics or the support media. Noise characteristic of most detectors (such as dark noise and readout noise) does not need to be added to this spectrum because MKIDs do not produce false photon counts.

6.1.2 The Fitting Model

This section describes how the *spectra fitting model* is created and applied. It is a mathematical model that is fitted to the data to determine the proportion of each fluorophore present.

The *spectra fitting model* was created to combine an amount (α) of the *reference spectra* for Nile Red fluorophore, and β amount of Yellow-Green fluorophore, before binning the photons by their energies. The equation is:

$$M_i = \alpha * \frac{A_i}{\sum_{i=1}^{n} A_i} + \beta * \frac{B_i}{\sum_{i=1}^{n} B_i} \tag{6.1}$$

Where M_i is the bin-value of the model, α and β are the contributions of each fluorophore spectrum, A are all bins in the *reference spectra* for Nile Red fluorophore (and similarly B is for Yellow-Green fluorophore), and n is the number of bins.

Because each spectrum is normalised (*i.e.* divided, in this case, by 10,000 such that the sum of all bin values is 1), then α and β are an estimate of the number of photons from each fluorophore.

The noise is characterised by equation 6.2 below. The model takes into account the noise on the *reference spectra* (which decreases if more photons are gathered to define each spectra), and the Poisson noise expected from the model itself (which decreases as α or β increase). The total noise on the all bins of *reference spectra* A or B (referred to as 'the data'), is given by the square root of the total number of photons ($\sqrt{10000}$). Because the relative noise on each bin is proportional to the square root of the bin value, then a scaling factor is applied to each distribution to account for this. Because the contribution of the model noise is small, the assumption is made that the error from the model can be included in noise on the data. The result is the following:

$$\text{Noise}_i = \sqrt{(\sqrt{M_i})^2 + \left(\alpha \frac{\sqrt{A_i}}{\sum_{i=1}^{n} A_i} \frac{\sqrt{\sum_{i=1}^{n} A_i}}{\sum_{i=1}^{n} \sqrt{A_i}}\right)^2 + \left(\beta \frac{\sqrt{B_i}}{\sum_{i=1}^{n} B_i} \frac{\sqrt{\sum_{i=1}^{n} B_i}}{\sum_{i=1}^{n} \sqrt{B_i}}\right)^2} \tag{6.2}$$

Where $\sqrt{M}$ is the Poisson noise from the model, A_i is a single bin in *reference spectra* α, and $\sqrt{A_i}$ is the Poisson noise on the bins of the *reference spectra.*

Because a large number of photons were collected, the assumption was made that the noise on the *reference spectra* was insignificant compared to the noise from the data. If, however, it becomes necessary to use a smaller quantity of photons for the *reference spectra*, then analytical methods such as *total least squares method* should be used (which takes into account the errors of both the data and the model).

6.2 Creating the simulated data

The *fluorophore model* is used to generate both the *reference spectra* that is used by the *spectra fitting model*, and each of the *sample spectra* that are analysed by the various techniques, as described below.

6.2.1 Reference Spectra

A large number of single-source, simulated photons create an observed spectra for each fluorophore (referred to as the *reference spectra*, A or B), as displayed in Figure 6.6. From this sample, possible values for α and β can be estimated using the fitting model described in Section 6.1.2. A sample of 10,000 photons was chosen for each of the *reference spectra* because that number is significantly larger than the maximum number of photons expected to occur in a single *sample spectra* (up to 1000 photons). As a result, the noise from the *reference spectra* is relatively small, and the capture time is not unreasonable.

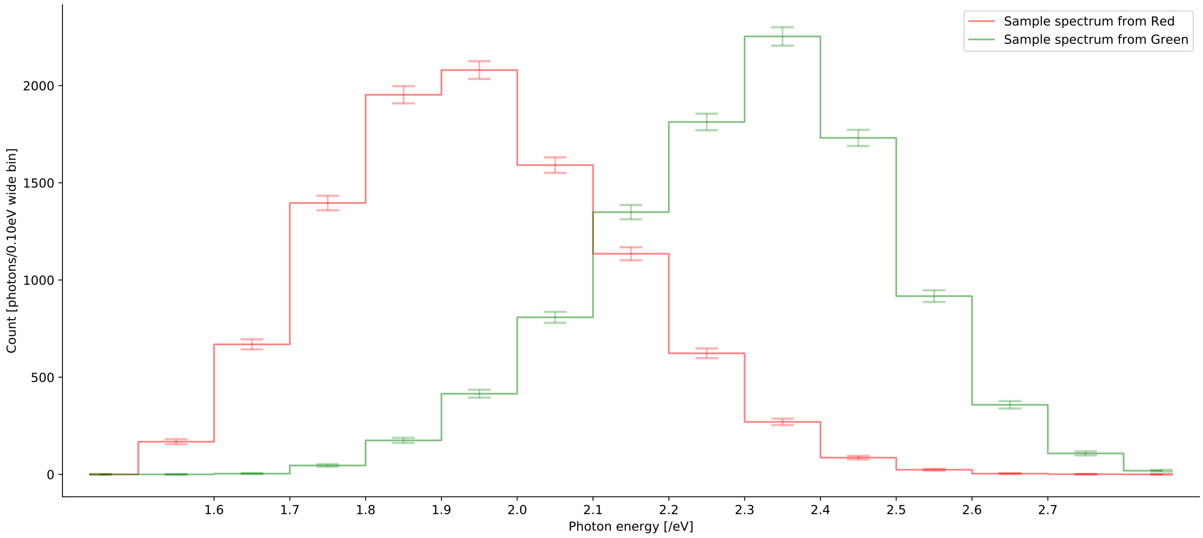

Figure 6.6: Simulated spectra (in electron Volts), consisting of 10,000 photons from Nile Red fluorophore and 10,000 photons from Yellow-Green fluorophore. The simulation assumed R=10.

6.2.2 Sample Spectra

The *fluorophore model* is also used to generate smaller numbers of simulated photons to emulate the light originating from a point in the sample, which could be from a combination of both fluorophores (referred to as the *sample spectra*). The number of photons that make up a *sample spectra* is assumed to be a maximum of 1000 for each spectra. Experimentation showed that this number was slightly more than was necessary to confidently identify the spectrum, and was also a reasonable number to sample given that the equipment took 4 s per reading and was optimal with photon rates of ≈ 500 photons$/s$. Two examples of sample spectra are shown in Figures 6.7 and 6.8.

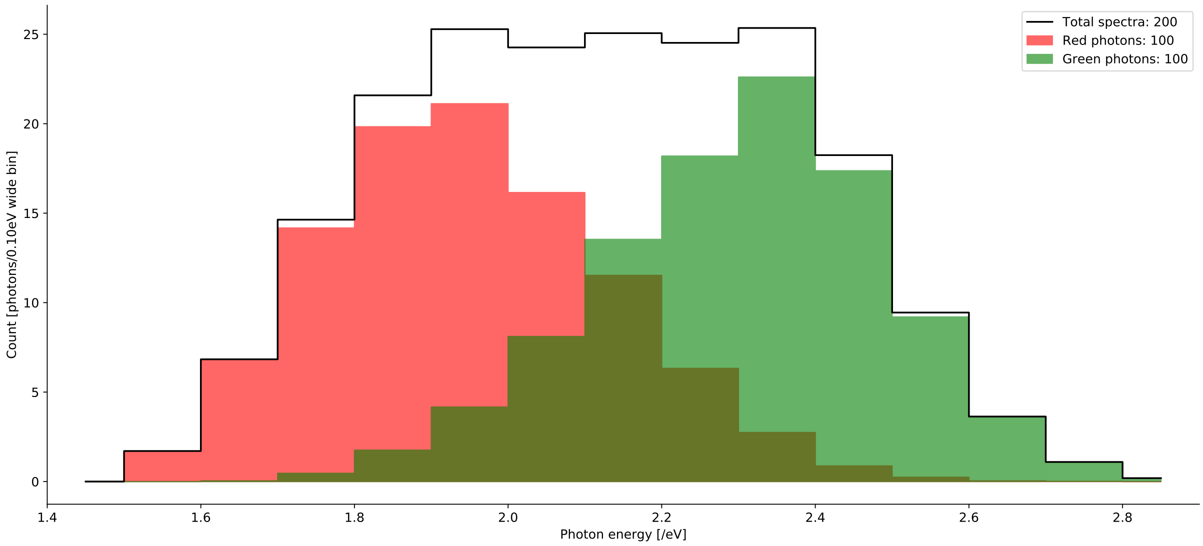

Figure 6.7: A spectra of 200 photons, created from 100 Nile Red fluorophore, and 100 Yellow-Green fluorophore photons.

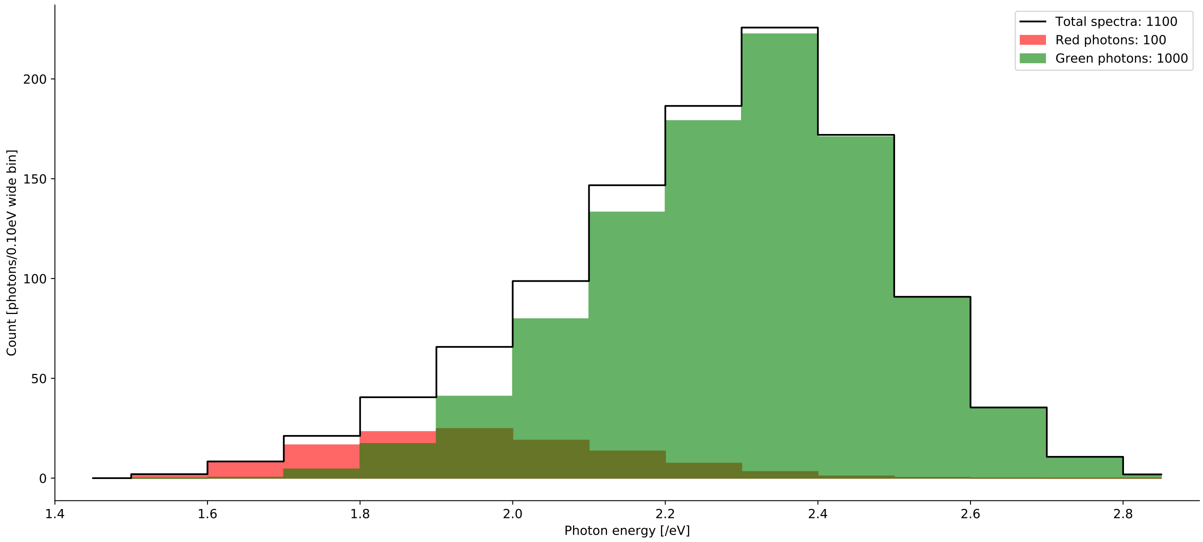

Figure 6.8: A spectra of created from 100 Nile Red fluorophore, and 1000 Yellow-Green fluorophore photons.

The simulation can be run multiple times with different values of n_R and n_G to empirically determine how few photons are required to confidently identify which fluorophores are present (and if possible, to what degree of certainty). The analysis will ultimately enable processing of images in which each pixel in an image can display the level of fluorophore present to a chosen degree of confidence.

6.3 Curve Fitting to Found Spectra

The *spectra fitting model* can be compared to each *sample spectra* using a least-mean squared fitting algorithm (`scipy.curve_fit` Python library).

scipy.curve_fit gives the optimal values of α and β (as `popt`) and the covariance matrix (`pcov`) that can be used to calculate the one standard deviation error by taking the square root of the diagonals. Figures 6.9 and 6.10 show the fits to two generated *sample spectra*, and the *area* of the shaded regions, each of which represent the proportion of fluorophores contributed by each fluorophore. The objective is to recover the input variables n_R and n_G from the *sample spectra* as variables α and β.

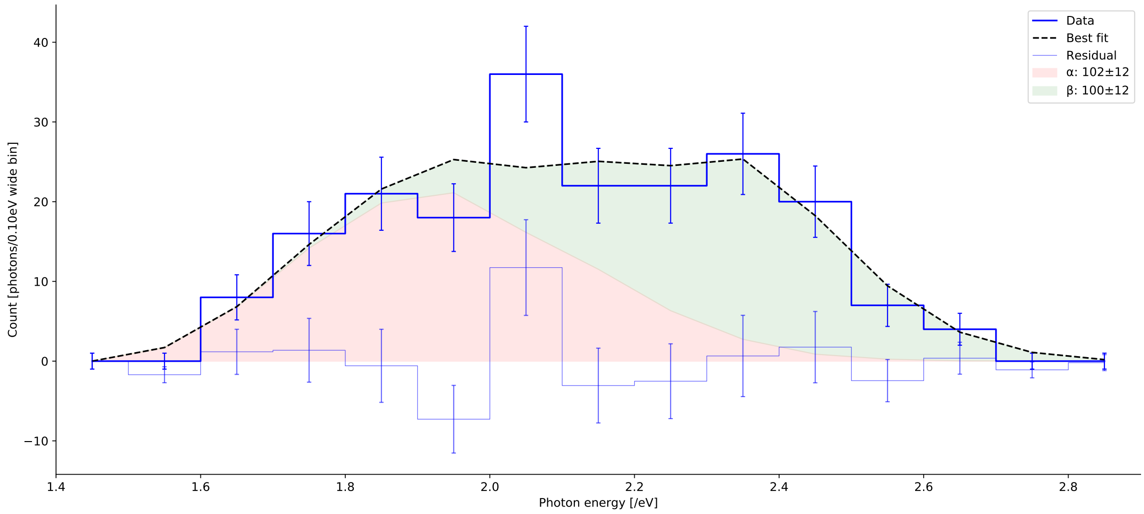

Figure 6.9: A spectra of photons created using the *fluorophore model* with inputs $n_R = 100$ and $n_G = 100$, and curve fit returning the output $\alpha = 102 \pm 12$ and $\beta = 100 \pm 12$.

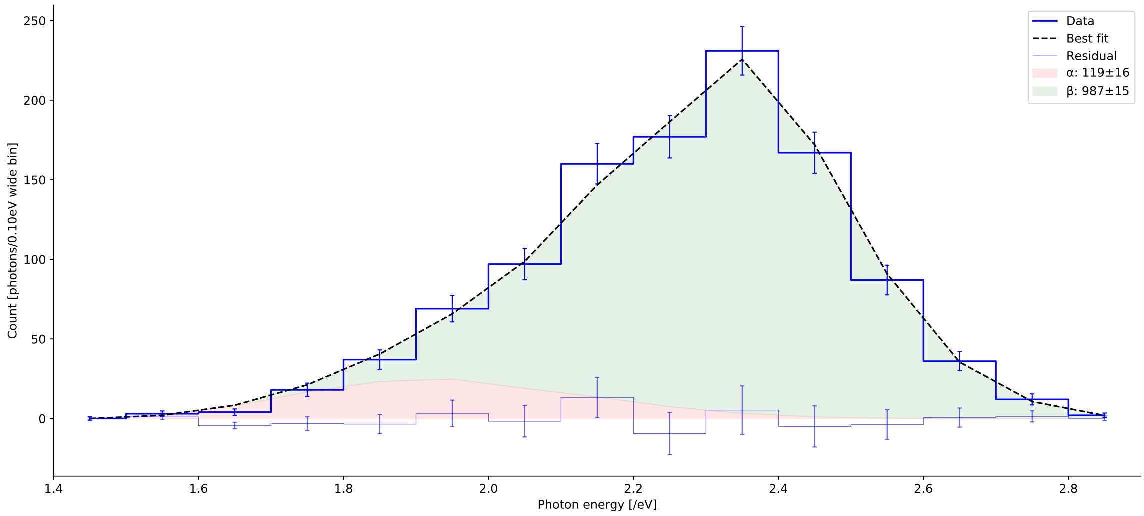

Figure 6.10: A spectra of photons created using the *fluorophore model* with inputs $n_R = 100$ and $n_G = 1000$, and curve fit returning the output $\alpha = 119 \pm 16$ and $\beta = 987 \pm 15$.

Table 6.1 illustrates the α and β determined for various values of n_R and n_G, indicating that the inputs can be recovered from the *sample spectra*. The error, in terms of photons, tends to increase with the total numbers of photons in the *sample spectra*, whereas the relative error (photons error, per total number of photons) decreases.

n_R	n_G	α	σ_α	$\sigma_{\alpha\mathbf{ERR}}$	β	σ_β	$\sigma_{\beta\mathbf{ERR}}$
0	100	3	4	-0.60	95	4	1.15
0	500	10	11	-0.91	497	10	0.30
0	1000	17	30	-0.57	981	29	0.64
100	0	93	8	0.82	7	8	-0.90
100	100	107	10	-0.74	96	9	0.41
100	500	99	14	0.10	504	14	-0.30
100	1000	138	27	-1.39	982	27	0.65
500	0	501	16	-0.05	1	15	-0.05
500	100	496	14	0.29	102	14	-0.16
500	500	512	31	-0.40	477	31	0.75
500	1000	530	24	-1.24	964	24	1.51
1000	0	984	20	0.79	-2	20	0.08
1000	100	1017	23	-0.73	91	23	0.41
1000	500	1024	25	-0.95	491	25	0.35
1000	1000	1009	34	-0.27	997	34	0.08

Table 6.1: Table showing the results from curve_fit analysis, and how accurately the input values were recovered from the data (as a proportion of σ).

6.4 χ^2 Analysis

χ^2 analysis is used to analyse the goodness of fit, as a metric for the suitability of the model to the data. It can also be used to explore the parameter space in α and β, which is known as the error surface, or χ^2 contour surface. The minima on this surface are the α and β values of best fit. The χ^2 contour also reveals the α and β values that correspond to a particular level of uncertainty, which in turn give the confidence intervals (a range of photon counts, between which the actual value is likely to lie).

6.4.1 Confidence Intervals

The best fit occurs at the minimum of the error surface, and the confidence intervals are where the contour is at a given value above this minimum, *i.e.* has a $\Delta\chi^2$ of a given value. The confidence intervals of 68.3% occur where $\Delta\chi^2 = 1.00$ (*i.e.* a value of 1, greater than the minimum). Similarly, 90.0% is found at $\Delta\chi^2 = 2.71$, as discussed by Hughes and Hase (2010).

Figure 6.11 shows the χ^2 contour plot for a single simulated scenario of 100 photons from the Nile Red fluorophore and 100 photons from the Yellow-Green fluorophore. Similarly, Figure 6.12 shows the χ^2 contour plot for 100 and 1000 photons. The top right panel shows the error surface, with $\Delta\chi^2$ contours indicating the values within which the true/actual value is likely to lie within a particular degree of certainty. The top left panel shows the binned photons as 'data', and the results for the curve-fit algorithm, as well as the best fit from the χ^2 analysis. The residuals plot (middle left) shows the difference from the curve fit, and the standard residuals (bottom left) shows the same residuals normalised by the error. The standard residuals are plotted as a histogram with the best fit Gaussian distribution overlaid, and a one sigma distribution for reference, which is what would be expected if the model were perfect.

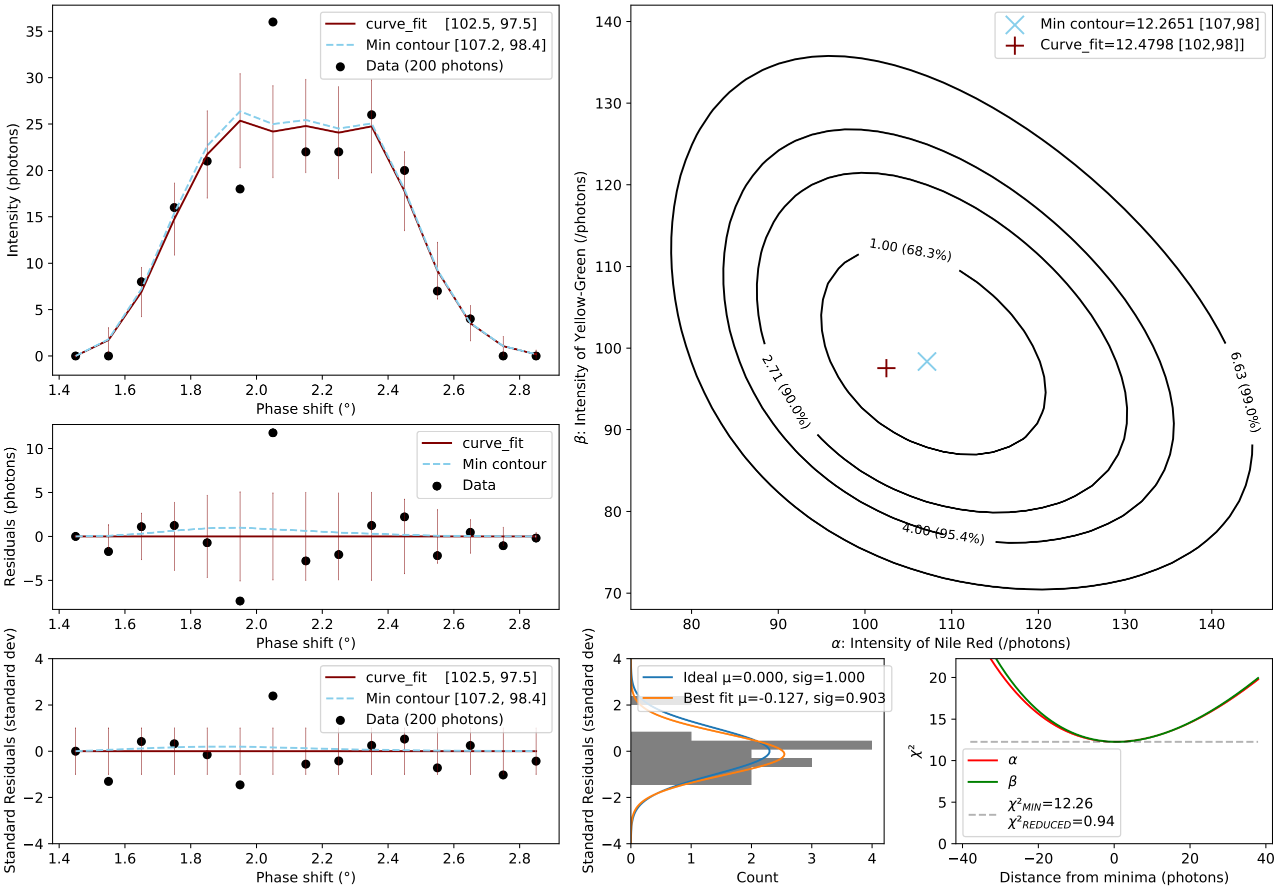

Figure 6.11: χ^2 contour plot of the simulated data containing 100 Nile Red fluorophore and 100 Yellow-Green fluorophore photons.

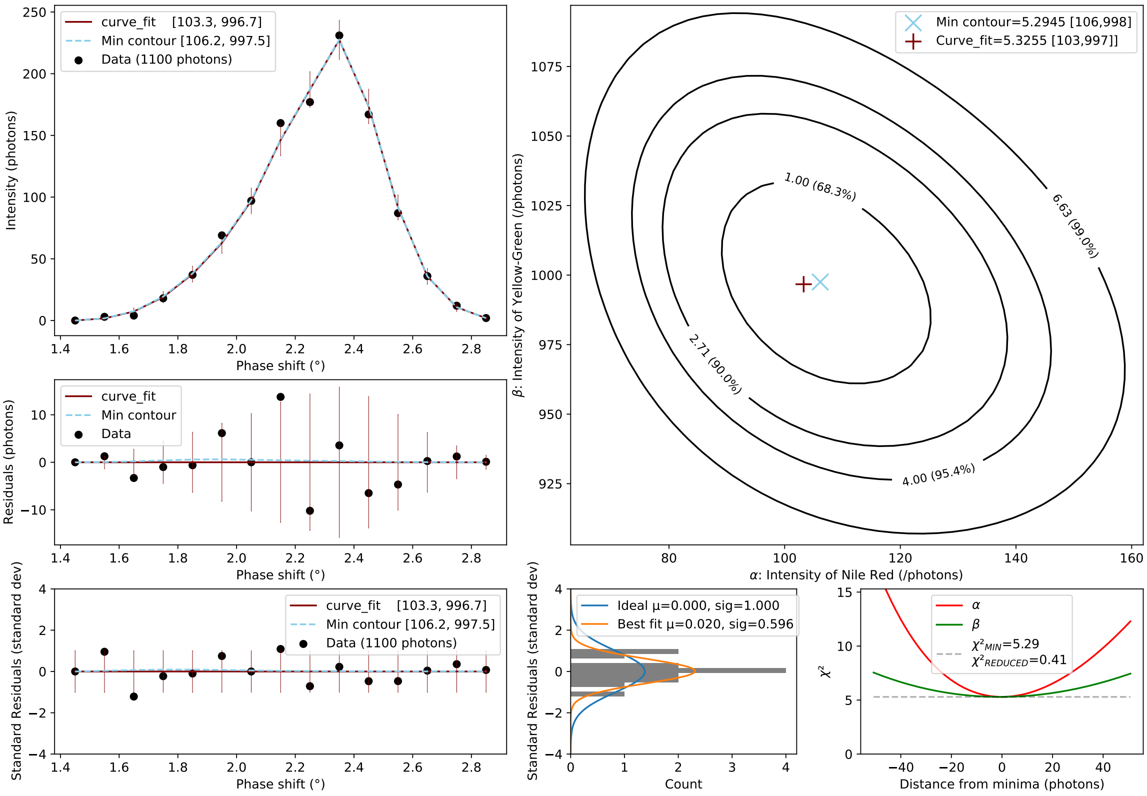

Figure 6.12: χ^2 contour plot of the simulated data containing 100 Nile Red fluorophore and 1000 Yellow-Green fluorophore photons.

Table 6.2 presents the results for a range of values of n_R and n_G. It demonstrates that the χ^2 analysis is able to satisfactorily recover the input information and that the fractional error decreases as the photon count increases.

n_R	n_G	α	$\mathrm{CI}_{\alpha,UP}$	$\mathrm{CI}_{\alpha,LOW}$	$\mathrm{ERR}_\alpha/\mathrm{CI}$	β	$\mathrm{CI}_{\beta,UP}$	$\mathrm{CI}_{\beta,LOW}$	$\mathrm{ERR}_\beta/\mathrm{CI}$
0	100	1	4	-2	-0.40	108	10	-10	-0.77
0	500	8	8	-6	-1.17	498	24	-24	0.07
0	1000	3	10	-4	-0.44	1003	33	-33	-0.08
100	0	109	11	-8	-0.94	10	4	-3	-2.96
100	100	107	13	-11	-0.58	98	13	-11	0.13
100	100	102	12	-12	-0.20	107	11	-13	-0.58
100	500	80	15	-11	1.58	523	26	-22	-0.96
100	1000	106	18	-15	-0.37	998	35	-35	0.07
100	1000	101	17	-14	-0.09	1008	30	-35	-0.23
500	0	511	23	-23	-0.47	-5	8	-2	0.90
500	100	487	25	-21	0.55	121	14	-14	-1.48
500	500	476	29	-24	0.89	529	29	-25	-1.05
500	1000	494	29	-29	0.21	1010	38	-38	-0.26
1000	0	1008	35	-35	-0.22	5	14	-9	-0.39
1000	100	1003	35	-35	-0.07	101	18	-13	-0.08
1000	500	987	42	-31	0.35	518	29	-29	-0.61
1000	1000	1006	40	-34	-0.17	1002	40	-40	-0.05

Table 6.2: Table showing results from χ^2 analysis, and how accurately the inputs were recovered from the data. n_R and n_G are the input values, α and β are the values recovered, CI are the 1σ confidence intervals (higher and lower), and ERR/CI is the error as a fraction of the mean confidence interval.

There are ways to improve this χ^2 fitting model, based on the fact that the total number of photons, is known. For example in Figure 6.11, the MKID records 200 photons, whereas the minimum contour suggests that $\alpha = 107.2$ and $\beta = 98.4$ (giving a total of 205.6, which is obviously incorrect). One approach would be to scale α and β such that their total is 200, but the ratio remains the same.

6.5 Statistical approach 2: Kolmogorov-Smirnov Goodness of Fit Test

This approach assesses whether the *sample spectrum* in question, is likely to have been drawn from the same distribution as a given *reference spectra* by performing a KS test with them. It is particularly useful in a binomial case, when trying to determine which of two known fluorophores the sample is most likely to be from. However, the test can be adapted by comparing against spectra that consist of a given ratio of both fluorophores to find which one it is most similar to.

The tool for this, used *scipy.stats.kstest* Python package to apply a KS test which produced the following outputs:

- *p-value* - a number that describes how likely it is that the sample of photon phase shifts are *not* part of of the reference sample from a known fluorophore (*i.e.* they occurred under the null hypothesis). If this number is above a certain value such as 0.05 (for the case where the certainty is 1.96σ), then the null hypothesis can be rejected, and the conclusion reached that the sample is part of the reference data.
- *KS Statistic* - the probability that the sample is drawn from the same probability distribution as the reference sample.

6.5.1 Binomial Classification

The KS test can be used to classify fluorophores in a binomial case with far fewer photons than are required to determine the ratio. By comparing the $p\text{-}value$ from the KS test between Nile Red fluorophore ($p\text{-}value_{Red}$) and Yellow-Green fluorophore ($p\text{-}value_{Green}$) it is possible to determine which fluorophore the sample distribution is most likely to belong to. Figure 6.13 shows the $p\text{-}value$ results from each test, for a series of red only or green only *sample spectra* (denoted by the red cross, or green circle respectively). It is apparent that the red spectra very often have lower $p\text{-}value_{Red}$ than $p\text{-}value_{Green}$. Consequently, it can be concluded that comparing the relative $p\text{-}value$s is a reliable method of estimating which *reference spectrum*, the *sample spectrum* is from.

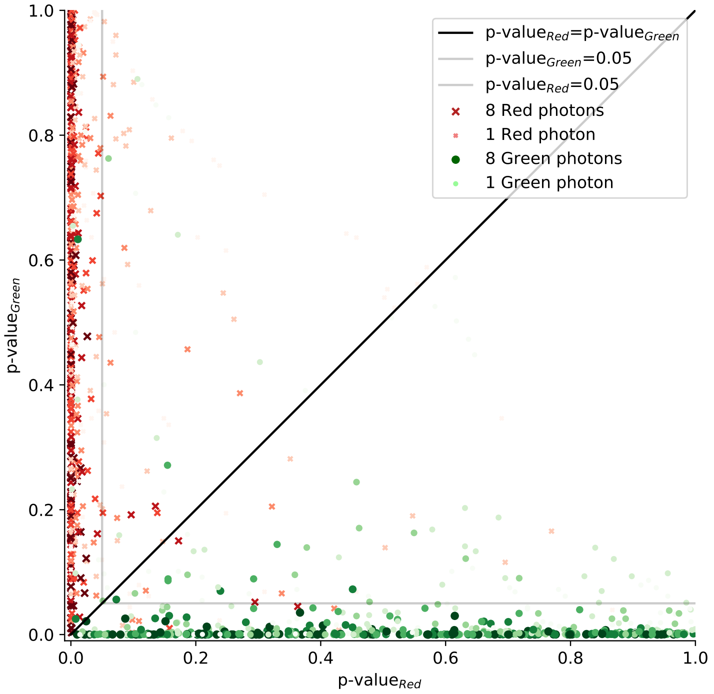

Figure 6.13: Plot of the $p\text{-}value_{Red}$ against $p\text{-}value_{Green}$ for 100 sample distributions, which contain of between 1 and 8 photons (indicated by the marker size). The red photons ('x' marks) are in most cases, separated from the green ('o' marks), indicating that it is possible to determine the origin fluorophore (either Nile Red fluorophore or Yellow-Green fluorophore) from the ratio of the two p-values.

Figure 6.14 shows the success rate of binomial classification in classifying small distributions of photons, with respect to the number of photons in the sample distribution. The method suggests that only four photons are required to confidently discern between a Nile Red fluorophore or Yellow-Green fluorophore using the KS test, with a success rate of over 95% which is sufficient for some fields. The number of photons to achieve a 5σ confidence level is far higher, and explored in Section 7.7.

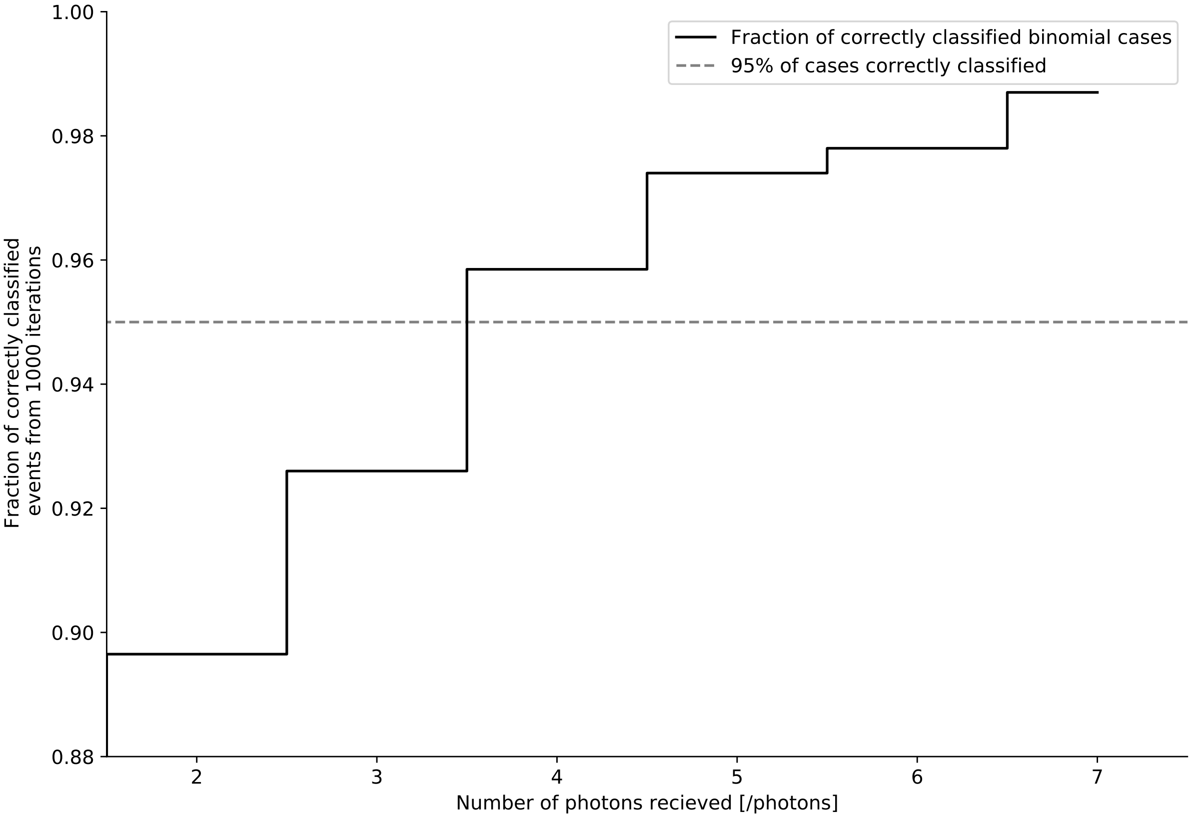

Figure 6.14: The success rate of binomial classification, at different sample sizes, performed 1000 times. This suggests that KS tests performed with just 4 photons, were able to classify between Nile Red fluorophore and Yellow-Green fluorophore 95.85% of the time

The number of photons required to perform binomial classification will increase in cases where the spectra are closer together, when using fluorophores which have more spectral overlap, and where a higher degree of certainty is required. Conversely fewer photons will be required, per location as the MKID system develops and R improves, or as spatio-spectral information is used.

6.5.2 Classifying Ratios

In real world applications it is common for measured spectra to contain more than one source spectra (such as from additional fluorophores or auto-fluorescence). Consequently, a method is proposed here that allows the KS test to be applied to determine mixed fluorophores. The method involves calculating the $p\text{-}value$ between the *sample spectra*, and a new distribution consisting of one-part Nile Red fluorophore photons, and one-part Yellow-Green fluorophore photons (in the case of a 50% ratio) as shown in Figure 6.15. The graph shows that the cumulative distribution function (CDF) of seven *reference spectra* each containing a different ratio of $n_R : n_G$, with the CDF of four *sample spectra* overlaid, each of which has a different ratio. The "$n_R = 200, n_G = 0$" CDF is very close to the CDF calculated from the 100% red *reference spectra* indicating that the $p\text{-}value$ will be lowest when the KS test is performed on those two spectra. The same is true for the other ratios.

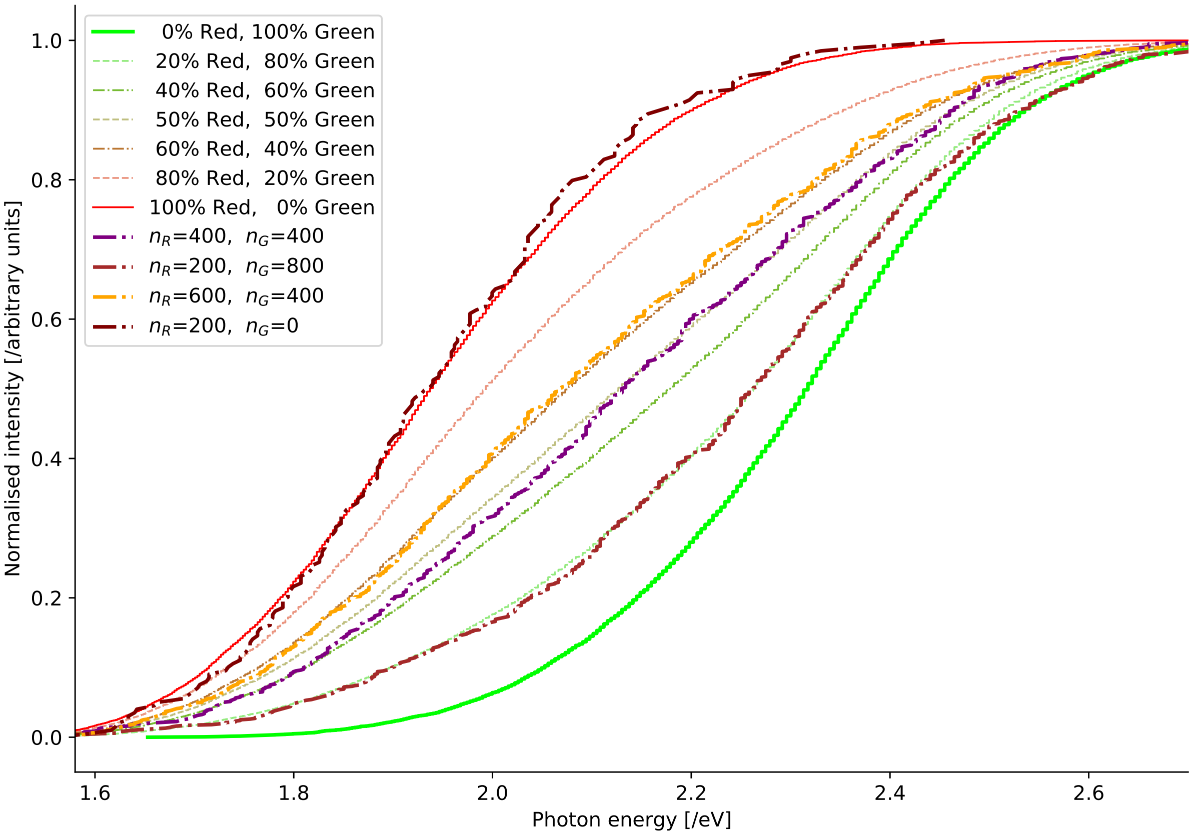

Figure 6.15: Several cumulative distribution functions given by creating a sample comprising of photons from A and B in the appropriate ratio, and three distributions from *sample spectra* of various n_R and n_G values. The distribution represented by the orange line has a ratio of 1000:200 photons, and closely follows the line corresponding with a 1.0:0.2 ratio.

Table 6.3 shows the $p\text{-}values$ derived from comparing a given sample distribution with a reference distribution consisting of multiple Nile Red fluorophore and Yellow-Green fluorophore spectra. The values indicate that the p-value is lowest when comparing the *sample spectra* against the reference distribution of the same ratio. These results suggests it can be used to determine the ratio of fluorophores using only tens of photons.

n_R	n_G	**_% Red**	$p_{0\%Red}$	$p_{20\%Red}$	$p_{40\%Red}$	$p_{50\%Red}$	$p_{60\%Red}$	$p_{80\%Red}$	$p_{100\%Red}$
400	400	50%	0.339	0.211	0.083	**0.021**	0.066	0.184	0.313
200	800	20%	0.154	**0.026**	0.120	0.184	0.248	0.377	0.505
600	400	60%	0.400	0.273	0.147	0.084	**0.020**	0.136	0.265
200	0	100%	0.655	0.527	0.399	0.335	0.271	0.147	**0.036**
40	160	20%	0.115	**0.063**	0.183	0.244	0.307	0.434	0.562
120	80	60%	0.407	0.279	0.152	0.088	**0.041**	0.135	0.265
200	0	100%	0.639	0.512	0.384	0.320	0.256	0.136	**0.044**
36	144	20%	0.159	**0.032**	0.136	0.193	0.254	0.380	0.505
108	72	60%	0.383	0.254	0.129	0.072	**0.044**	0.172	0.300
180	0	100%	0.645	0.518	0.390	0.326	0.263	0.135	**0.092**
32	128	20%	0.112	**0.077**	0.194	0.257	0.320	0.449	0.578
96	64	60%	0.408	0.279	0.152	0.095	**0.054**	0.133	0.256
160	0	100%	0.666	0.540	0.414	0.351	0.289	0.163	**0.060**
28	112	20%	0.193	**0.067**	0.126	0.189	0.252	0.377	0.504
84	56	60%	0.402	0.283	0.164	0.105	**0.048**	0.144	0.272
140	0	100%	0.754	0.626	0.497	0.433	0.369	0.240	**0.111**
24	96	20%	0.126	**0.066**	0.171	0.226	0.289	0.415	0.542
72	48	60%	0.463	0.334	0.205	0.140	**0.084**	0.096	0.222
120	0	100%	0.655	0.525	0.396	0.331	0.266	0.136	**0.054**
20	80	20%	0.173	**0.072**	0.166	0.219	0.281	0.403	0.525
60	40	60%	0.407	0.278	0.158	0.113	**0.068**	0.163	0.285
100	0	100%	0.662	0.532	0.408	0.345	0.283	0.158	**0.072**
16	64	20%	0.167	**0.065**	0.189	0.253	0.317	0.444	0.572
48	32	60%	0.509	0.380	0.251	0.186	**0.121**	0.111	0.218
80	0	100%	0.635	0.512	0.389	0.328	0.266	0.143	**0.094**
12	48	20%	0.179	**0.082**	0.164	0.222	0.283	0.408	0.536
36	24	60%	0.444	0.316	0.187	0.136	**0.123**	0.131	0.260
60	0	100%	0.643	0.524	0.407	0.348	0.290	0.176	**0.064**
8	32	20%	0.124	**0.149**	0.267	0.327	0.386	0.505	0.623
24	16	60%	0.384	0.271	0.161	0.123	**0.150**	0.211	0.333
40	0	100%	0.759	0.632	0.504	0.440	0.376	0.248	**0.159**
4	16	20%	0.234	**0.112**	0.179	0.237	0.297	0.422	0.547
12	8	60%	0.398	0.289	0.180	0.139	**0.199**	0.318	0.438
20	0	100%	0.758	0.629	0.502	0.438	0.375	0.248	**0.133**

Table 6.3: Results of the KS test for a sample (generated from a quantity of red and green photons), against several different reference distributions. For a sample distribution consisting of a number of photons (between 1000 and 20), in a certain ratio of n_R and n_G, the $p\text{-}value$ will be lowest when performing a KS test against the population distribution with the same ratio. Entries in **bold** are the $p\text{-}values$ corresponding to the actual ratio

6.6 Summary

This chapter proposed a model (*fluorophore model*) which is capable of producing a list of photon energy values, with a distribution that is likely to be seen in the actual application. The model was then used to generate a *reference spectra* and a *sample spectra*.

A least mean squares fit, and χ^2 analysis was carried out on the *sample spectra* generated, to compare them against known *reference spectra*, and then successfully recover the input values, within acceptable limits.

A KS test was performed to successfully classify the *reference spectra* as either Nile Red fluorophore or Yellow-Green fluorophore, in a simple binomial case and managed a 95% success rate using as few as 4 photons. It should be noted that this is a best case scenario, and that far more photons would be required if there is significant background noise, there are different fluorophores with less separated spectra, there is lower MKID spectral resolution, or there are uncertainties introduced by the instrumentation.

It is concluded that the KS test can be applied to compare the *sample spectra* with combined spectra (created from the *reference spectra*) to successfully identify the approximate mixture of fluorophores contained within the sample. Experimentation concluded that reliable results could be achieved with only a few tens of photons rather than several hundreds.

Chapter 7

Simulating Images

In this chapter, the analytical tools introduced in Section 6 are expanded upon with the introduction of blind spectral analysis techniques. All methods are applied to a contrived image (or a matrix of α and β values), and assessed using the MSE metric to determine how succesfully the techniques recover the original image from initial inputs. Blind spectral analysis techniques employed are principle component analysis (PCA) and non-negative matrix factorisation (NMF), which finds the main components featuring in all spectra.

7.1 Generating Artificial Data

In order to test the analysis tools, photon data (lists of photon energies from each [X,Y] location within the sample) are generated from n_R and n_G values, corresponding to the input values for Nile Red fluorophore and Yellow-Green fluorophore respectively. The n_R and n_G values at each point on the sample, are input into the *fluorophore model* to create a list of photons of various energies, as described in Section 6.2.2. These photon lists are then binned into spectra, and each is analysed with the tools described, to recover the found values for photons from each fluorophore, referred to as α and β respectively. The values for n_R and n_G are advised by intensity values from contrived images of 'microsphere' features. The contrived images used an optical image of a microsphere to give a realistic intensity profile, and converted to grey-scale and normalised to have a pixel value between 0 and 1. This artificial image was designed such that some of the microsphere features were isolated, and some overlap in different intensities. The number of photons per [X,Y] location (corresponding to a pixel) was based on a value referred to as the maximum number of photons per fluorophore, per pixel ($n_{photonsMAX}$), multiplied by the pixel value at [X,Y] location, and rounded to an integer number. In this way, it is possible to simulate spectra at different photon fluxes.

Both intensity maps for the example case of '$n_{photonsMAX}$ = 50' are shown in Figure 7.1. In this example, there would be up to 50 photons of Nile Red fluorophore and 50 photons of Yellow-Green fluorophore from each location (pixel), such that there are some pixels with up to 100 photons in them, as is the case in Figure 7.2(b).

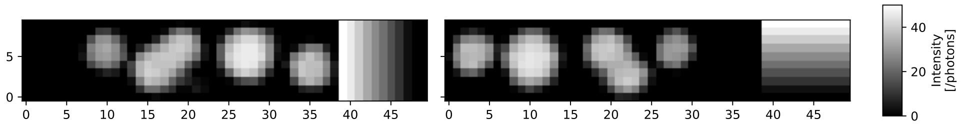

Figure 7.1: Artificial model: an input intensity map for each fluorophore, n_R (left image, corresponding to Nile Red fluorophore), and n_G (right image, corresponding to Yellow-Green fluorophore), with up to 100 photons (50 photons from each fluorophore). Intensity gradients on the right, allows comparison between many ratios, but the spectra from these is not used by PCA or NMF.

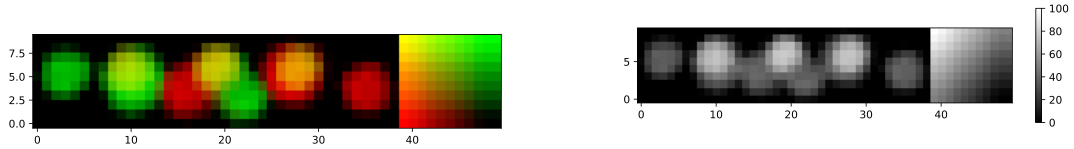

((a)) RGB image of the artificial image. Values are relative to the most intense value.

((b)) An intensity map of the artificial image, consisting of the total number of photons in that pixel. There are as many as 50 photons per fluorophore, per pixel.

Figure 7.2: The artificial image used in the simulations below. There is an isolated 'microsphere' feature of Nile Red fluorophore, towards the right hand side and similarly a Yellow-Green fluorophore microsphere feature on the left-hand side. The microspheres between have overlapping spectra. On the far right of the image there is a series of gradients which allow comparison of many ratios of fluorophore and intensities.

On the right of the image, there was a region with a gradient (*gradient feature*), which allows comparisons of many ratios of the two spectra. It should be noted that this region was not used in the PCA or NMF analysis, so as not to give an unrealistic advantage to the fitting algorithms. In order to simulate different photon fluxes, this intensity map is scaled by the maximum number of photons per fluorophore, per pixel ($n_{photonsMAX}$), so in the case of '50 photons max', there are as many as 50 photons of Nile Red fluorophore and 50 photons of Yellow-Green fluorophore from each location (pixel) as is the case in Figure 7.2(b).

7.2 Image Comparison Metric (MSE)

The artificial images were an intensity map of n_R and n_G values (I), which were fed into a simulation, which returned found values of α and β (K) and had the same size ($M \times N$). This section defines a quantitative test to determine whether the two intensity maps match.

The method selected was MSE because it gave a metric by which the input and output images could be quantitatively compared to determine the perceived image quality by measuring the differences between the absolute values of the pixels. It does this by summing the squared differences between the pixels in each image, using the equation below:

$$\text{MSE} = \frac{1}{MN} \sum_{m=0}^{M-1} \sum_{n=0}^{N-1} [I(m,n) - K(m,n)]^2 \tag{7.1}$$

Where $I(m, n)$ and $K(m, n)$ are the intensities at (m, n) in each image. A low value indicates a good agreement between the images and zero indicates a perfect fit. The MSE values can only offer a relative comparison, so a reference to random noise.

MSE was chosen in favour of other techniques which are designed to compare other characteristics between the images. Structural Similarity Index (SSIM), Normalized Cross-Correlation (NCC) and Cosine Similarity techniques all compare the relative structure of the image (pixel intensities relative to neighbouring pixels), and are magnitude agnostic meaning the absolute value of the pixels was ignored, however the relative magnitude is of significant interest in this application.

Each analysis method is assessed by this metric at various photon counts, and a graph is provided in the conclusions (Figure 7.13). In addition, the MSE metrics are provided for a selection of $n_{photonsMAX}$ values. For context, the MSE metric for an image made from random noise, is approximately 1.7e-1 (or for 12 photons is 1.5e-1, for 50 photons is 1.72e-1, and for 500 photons is 1.75e-1).

7.3 Principal Component Analysis

For blind spectral analysis, where there is no *reference spectra* available, it is possible to run principle component analysis (PCA) to extract principle components from the recorded data which is comprised of many combined spectra. PCA is a dimensionality reduction technique, used to express the many degrees of freedom from the data, as fewer components; in this case two profiles. It becomes particularly useful when accounting for unknown and uncharacterised components which are contributing to the spectra, such as additional fluorophores, or backgrounds such as auto-fluorescence of other materials in the samples.

The *scikitlearn.decomposition.PCA* Python package is used to find the principal components of all of the spectra (except for those in the *gradient feature*). Figure 7.3, show the two components which the PCA algorithm has found best describe all of the spectra for the simulated data.

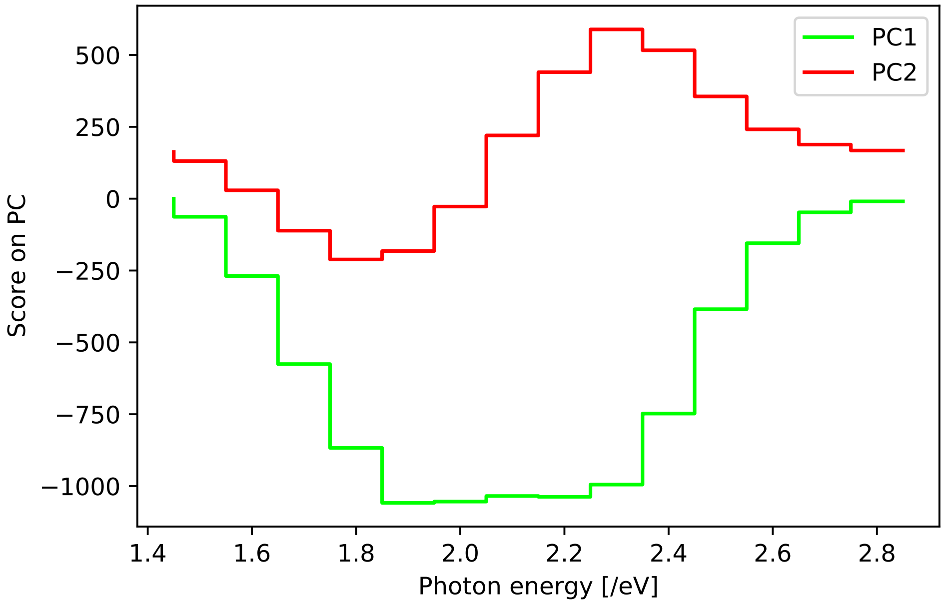

Figure 7.3: Components found in PCA analysis, based on an artificial sample with as many as 1000 photons (500 photons from each).

Since every spectra is comprised of these two components, it is possible to represent each of the spectra in terms of these two components by fitting using *scipy.curve_fit*. Figure 7.4 shows the PCA values which give the optimal fit, for each of the spectra. They are colour-coded based on their known colour which is calculated by the relative ratio of $n_R : n_R$. The graph shows a strong correlation between that ratio, and the location in the 2D parameter space (specifically the angle about the origin). This correlation suggests that PCA analysis can be used to extract the relative number of photons from each source based on a several given sample spectra, **without prior knowledge of the spectra** from which they are comprised.

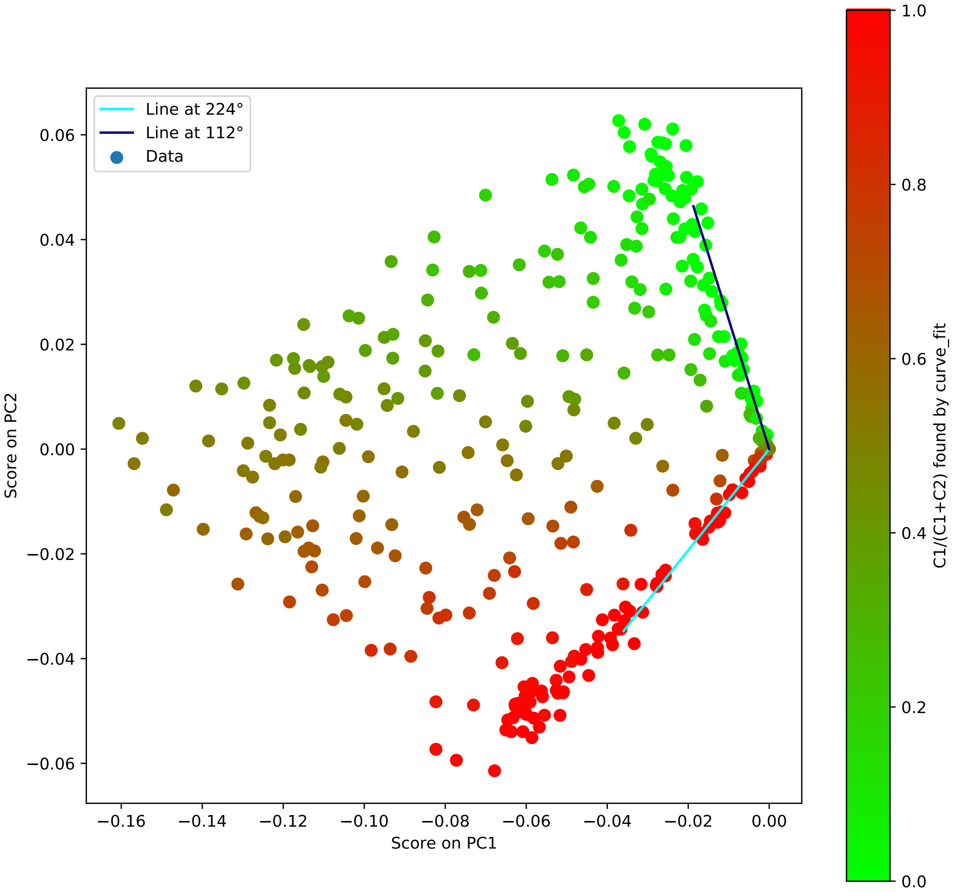

Figure 7.4: The presence of both PCA components, in each spectra. There is good separation between known Red and Green regions in the 2D parameter space (Score on PC1, and score on PC2) suggesting their position can reveal information about the intensity at each point. Points along the 224 degree line contain only fluorophores from the green source, and similarly for the line at 112 degrees being red. A relative ratio can be calculated based on their relative angles, giving the ratio of $n_R : n_G$, and since the photon count is know, n_R and n_G can both be calculated.

In order to interpret the results in terms of numbers of photons per fluorophore, the angle relative to the origin [0,0] was calculated for each pixel, and this angle was converted to a fraction relative to the two angles defined in Figure 7.4 (112° and 224°). Because the number of photons at each pixel is known, they can be distributed between the α and β intensity maps according to that ratio. The result is shown (Figure 7.6 bottom plots) directly compared to the input data plots for n_R and n_G (top plots).

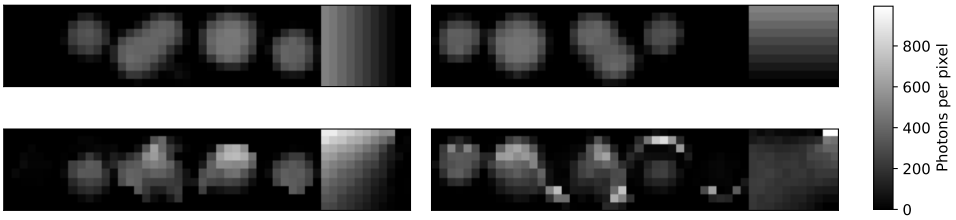

Figure 7.5: The intensity map of α (bottom left), vs β (bottom right) compared to the intensities which were used to create the data set (top plots). There was a maximum of 500 photons, per fluorophore, per pixel.

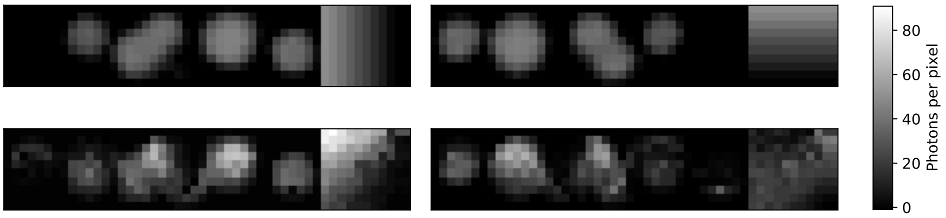

Figure 7.6: The intensity map of α (bottom left), vs β (bottom right) compared to the intensities which were used to create the data set (truths). There was a maximum of 50 photons, per fluorophore, per pixel.

The accuracy achieved is very low, and this method as it is executed, confuses high values of n_R and n_G, for high values of n_R and misrepresents the relative intensities. It identifies single sources, adequately but offers no advantage over the other methods examined.

For the red channel, the MSE metric for 12 photons is 0.104, for 50 photons is 0.117, and for 500 photons is 0.164. For the green channel, the MSE metric for 12 photons is 0.104, for 50 photons is 0.117, and for 500 photons is 0.129. Given that a low MSE implies a good fit.

7.4 Non-Negative Matrix Factorisation Analysis

Non-negative matrix factorisation (NMF) is similar to PCA in that it is a dimensionality reduction technique, however it constrains the components to only contain non-negative values. This is more in line with reality, where the presence of one fluorophore is not likely to result in reduction in another part of the spectrum, or a 'negative number of photons' which is impossible.

The Python package *sklearn.decomposition.NMF* is used to process the spectra for each [X,Y] position described above, and suggests that the components are as shown in 7.7.

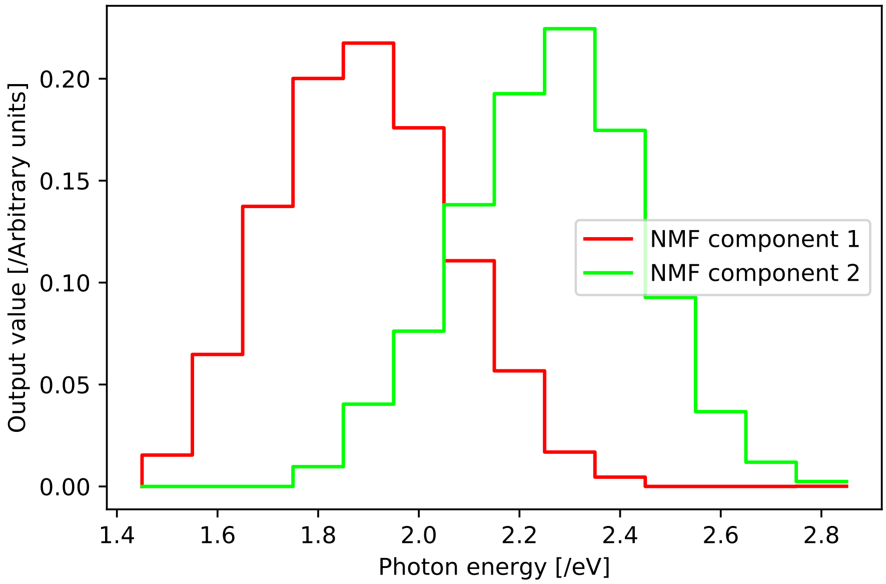

Figure 7.7: Components found in NMF analysis, based on an artificial sample with as many as 1000 photons (500 photons from each).

Figure 7.8 shows the score on both NMF components, and of particular interest is that they follow very closely, the input values of n_R and n_G and mostly return positive values for α and β, because the components suggested are only positive.

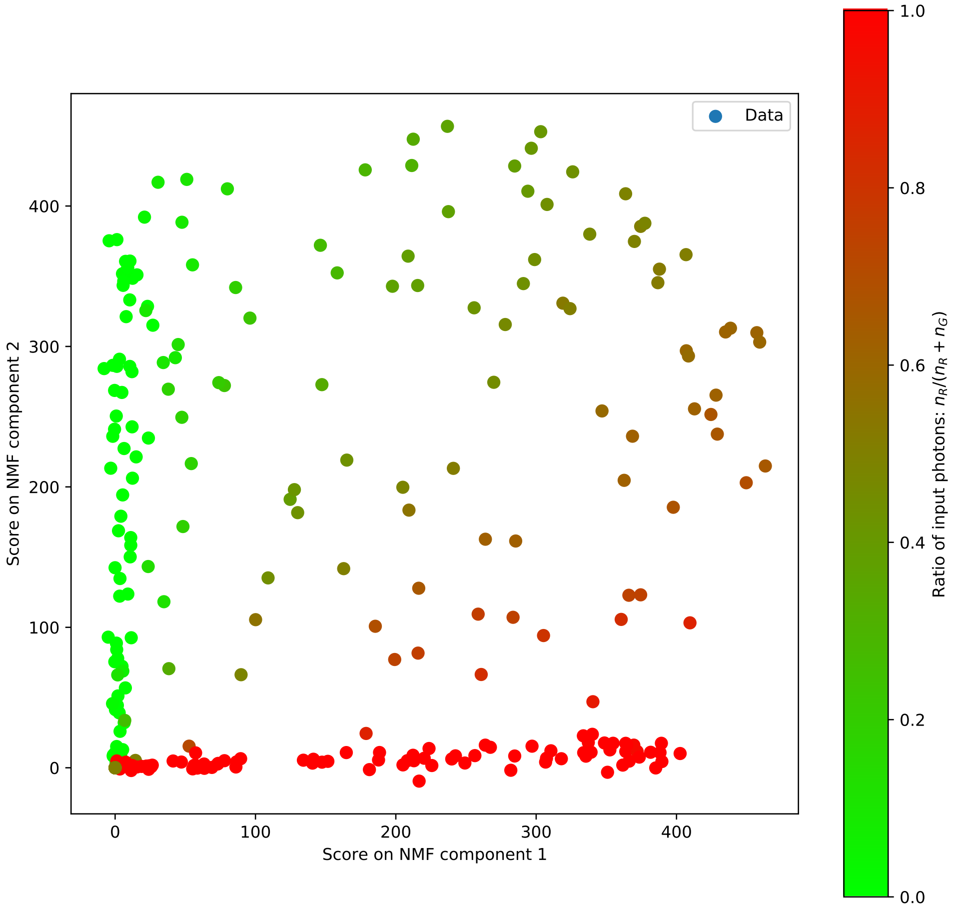

Figure 7.8: The magnitude of both NMF components, in each spectra. There is good separation between known Red and Green regions in the 2D parameter space (Score on PC1, and score on PC2) suggesting their position can reveal information about the intensity at each point.

By using the score on NMF component 1, as α and the score on component 2 as β, the intensity maps for α and β can be calculated. The result is shown in Figure 7.9 (bottom plots) closely resemble the input data plots for n_R and n_G (top plots).

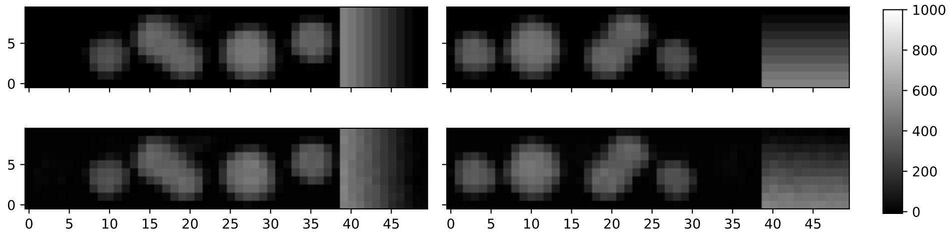

Figure 7.9: The intensity map of α (bottom left), vs β (bottom right) compared to the intensities which were used to create the data set (truths). There was a maximum of 500 photons, per fluorophore, per pixel.

With 500 photons per fluorophore per pixel, there was good agreement between the n_R and n_G and α and β, for example when viewing the α channel, the α-only feature is visible and the β-only feature is not present, and similarly with the overlapping features. Figure 7.10 illustrates that this agreement deteriorates as the number of photons decreases, until there is no resemblance when using 2 photons. Images taken with fewer than 12 photons, begin to misrepresent the initial image. This is quantified in the Figure at the end of the Chapter 7.14.

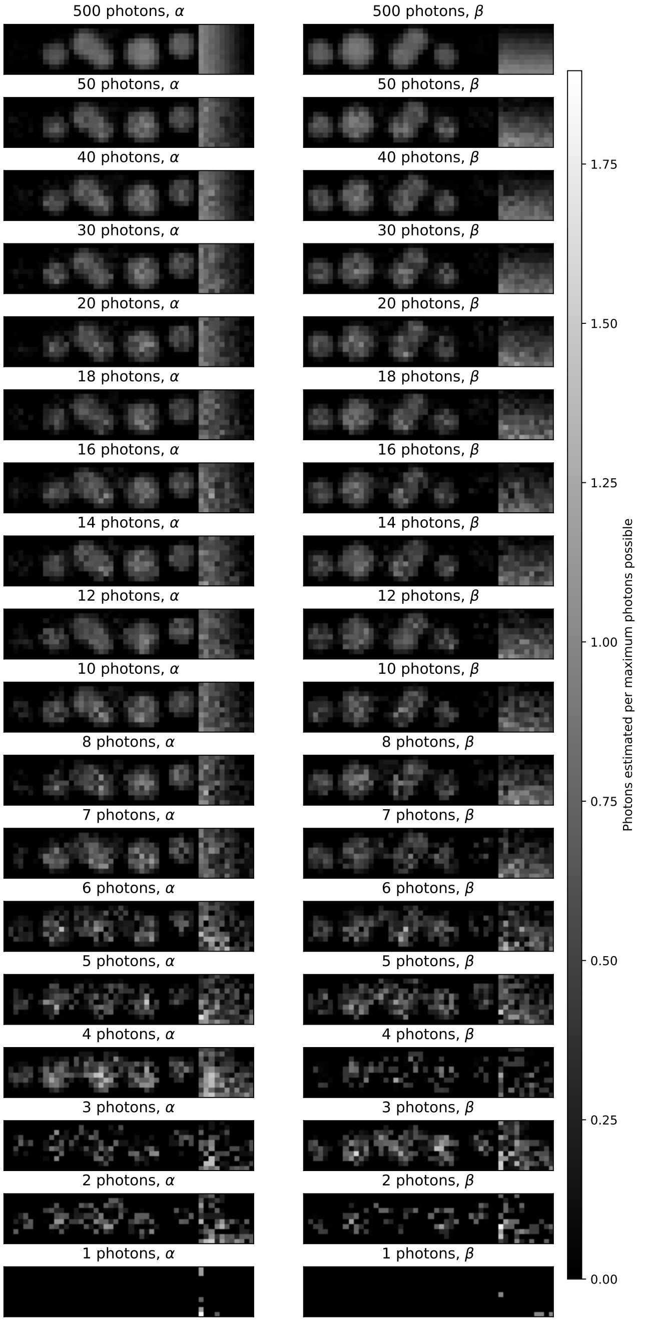

Figure 7.10: The intensity map of α and β found by NMF analysis. Left column is α , right column is β, each row is the result of using a different number of photons to perform the analysis. The value of each pixel is the number of photons found by the analysis, divided by the maximum number per fluorophore (*i.e.* ratio of α or β, to $n_{photonsMAX}$).

7.4.1 Error Analysis

Calculating the confidence intervals using NMF, is less straight forward than when using a reference spectra with predictable errors. This is because the reference spectra are inferred from the measured measurements, so are affected by the uncertainties on each of the measured spectra. Methods exist to quantify these errors using more advanced statistical techniques, however it is beyond the scope of this thesis. The general approaches involve:

- Bootstrapping - By processing the data set many times, each time modifying the data by a known amount, it is possible to obtain a distribution of profiles (in this case, factorisations) and from that infer their likely distribution. This is very computationally expensive.
- Residual analysis - by doing multiple simulations which calculate the difference between the NMF result, and the input values, it is possible to establish a likely uncertainty in instances with similar NMF results. However this is also a computationally expensive route, potentially requiring generating a large number of scenarios to refer to.
- Multiple initial starting points - The reference spectra found by NMF, are sensitive to the initial parameters used by the algorithm. By re-running with many different initial parameters, it is possible to see how much the reference spectra varies. If the variation between the different reference spectra generated in this way, is low, then that indicates a greater confidence level.

For the red channel, the MSE metric for 12 photons is 1.37e-2, for 50 photons is 7.23e-3, and for 500 photons is 5.13e-4. For the green channel, the MSE metric for 12 photons is 1.43e-2, for 50 photons is 5.76e-3, and for 500 photons is 5.08e-4.

7.5 χ^2 Analysis

The χ^2 analysis described in Section 6.4, was performed on each of the spectra produced in the manner described in Section 7.1. The analysis returned α and β, as well as the 1σ confidence intervals which can be used to calculate the likelihood that a given fluorophore is present (by calculating how *likely* it is, that the quantity in the pixel is *not* 0). Figure 7.11 represents this likelihood as a percentage.

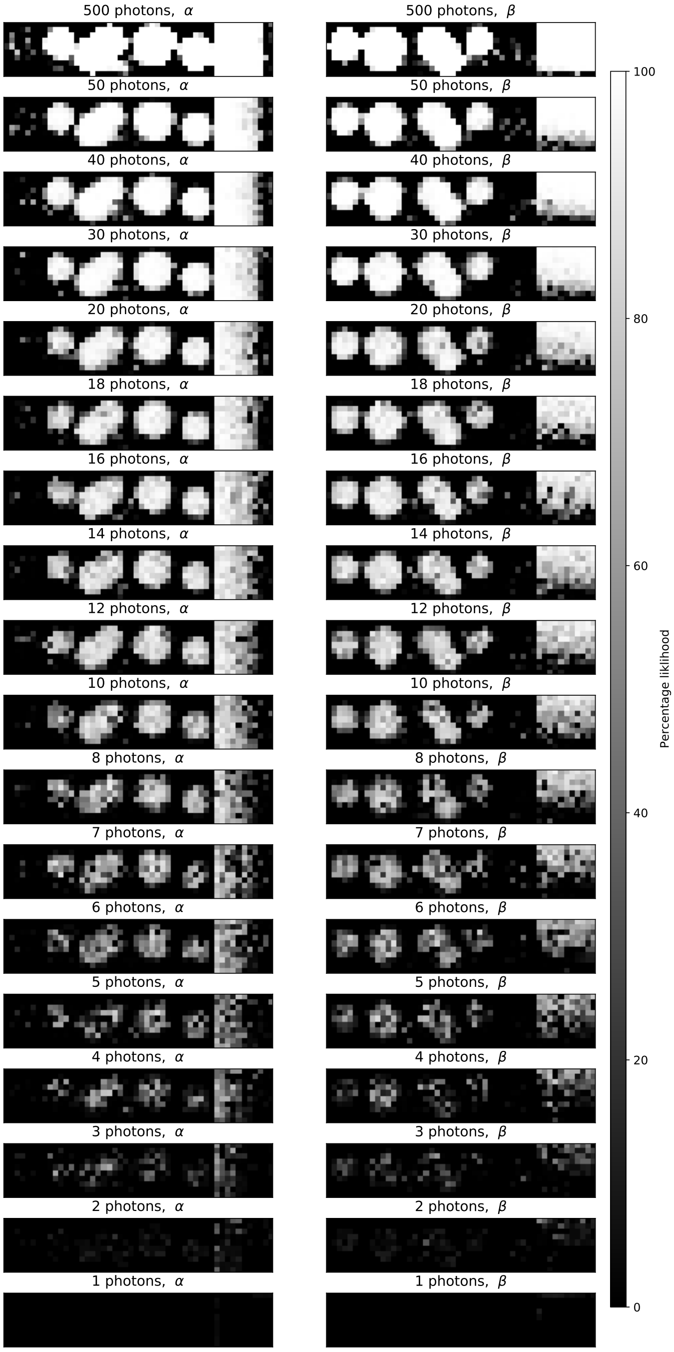

Figure 7.11: χ^2 result: Maps of likelihood that the pixel does not contain none of the respective fluorophore (α representing Nile Red fluorophore, and β representing Yellow-Green fluorophore).

The results indicate that the presence of fluorophores can be identified to high degree of certainty, over 5σ with large photon numbers, and less so with very low photon numbers, however as few as $n_{photonsMAX}$ = 12 photons are required to identify a given fluorophore, even in the presence of other fluorophores.

For the red channel, the MSE metric for 12 photons is 1.04e-2, for 50 photons is 2.48e-3, and for 500 photons is 2.23e-4. For the green channel, the MSE metric for 12 photons is 1.27e-2, for 50 photons is 2.77e-3, and for 500 photons is 2.53e-4

7.6 Image Comparison Using *scipy.curve_fit*

The *scipy.curve_fit* analysis described in Section 6.3, was applied to calculate the likelihood of each fluorophore being present, in the same way as in 7.5, to produce the results shown in Figure 7.12.

The results indicate that the presence of fluorophores can be identified to high degree of certainty with large photon numbers, and less so with very low photon numbers, however as few as $n_{photonsMAX}$ = 12 photons are required to identify a given fluorophore, even in the presence of other fluorophores.

For the red channel, the MSE metric for 12 photons is 1.10e-2, for 50 photons is 3.45e-3, and for 500 photons is 6.14e-4. For the green channel, the MSE metric for 12 photons is 9.13e-3, for 50 photons is 3.43e-3, and for 500 photons is 5.15e-4.

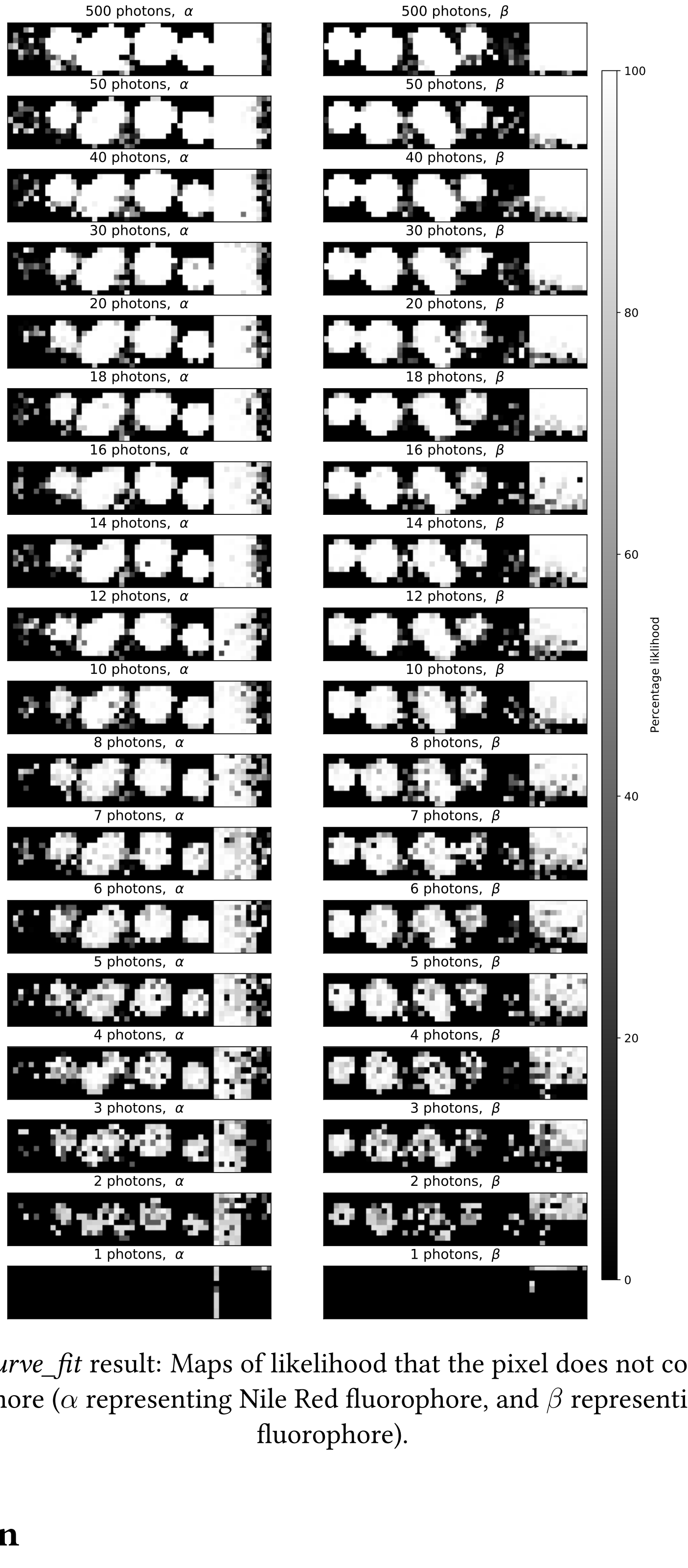

Figure 7.12: *scipy.curve_fit* result: Maps of likelihood that the pixel does not contain none of the respective fluorophore (α representing Nile Red fluorophore, and β representing Yellow-Green fluorophore).

7.7 Conclusion

This chapter presented several analysis techniques, applied to simulated images (which contained a range of fluorophore intensities, and mixtures). Figure 7.13 shows the techniques applied, to a single case in which 40 photons were used in the simulation.

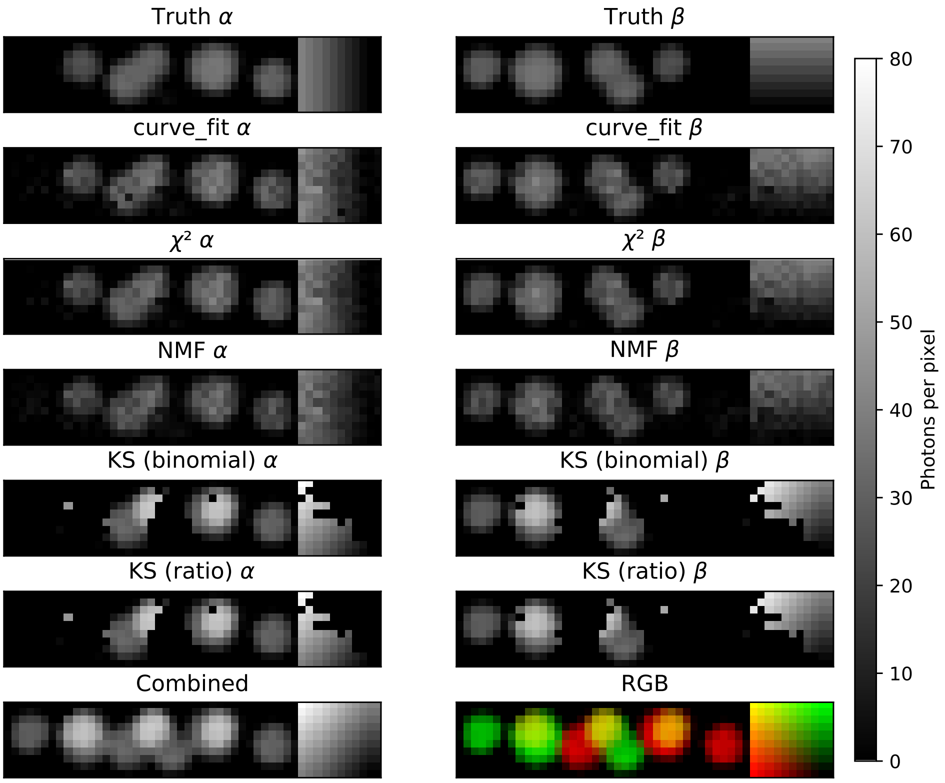

Figure 7.13: Comparison between the various analysis techniques described. The 'truth' plots show the generated values of n_R and n_G, which have a maximum value of 40 photons. Subsequent plots show the result from each method being applied. The 'combined' image shows the intensity map of the total number of photons detected, per pixel.

Figure 7.14 compares the MSE metric for each of the analysis techniques as the number of photons increases. On initial inspection, the trend is not smooth and indeed in some cases appears to get worse with more photons, however this is an artefact of each method only having been simulated once. The graph indicates that the *scipy.curve_fit* method is effective at low photon counts, but is exceeded in performance by the χ^2 analysis method at higher photon counts. The NMF method is relatively poor at very low photon counts (likely because there is very little data on which to base the reference spectra), but quickly becomes one of the best techniques. It should be noted that NMF is a blind technique and does not require prior knowledge of the spectra so can be used in cases where the spectra is not know. Also shown in the graph, is a reference metric when the truth image is compared to random noise.

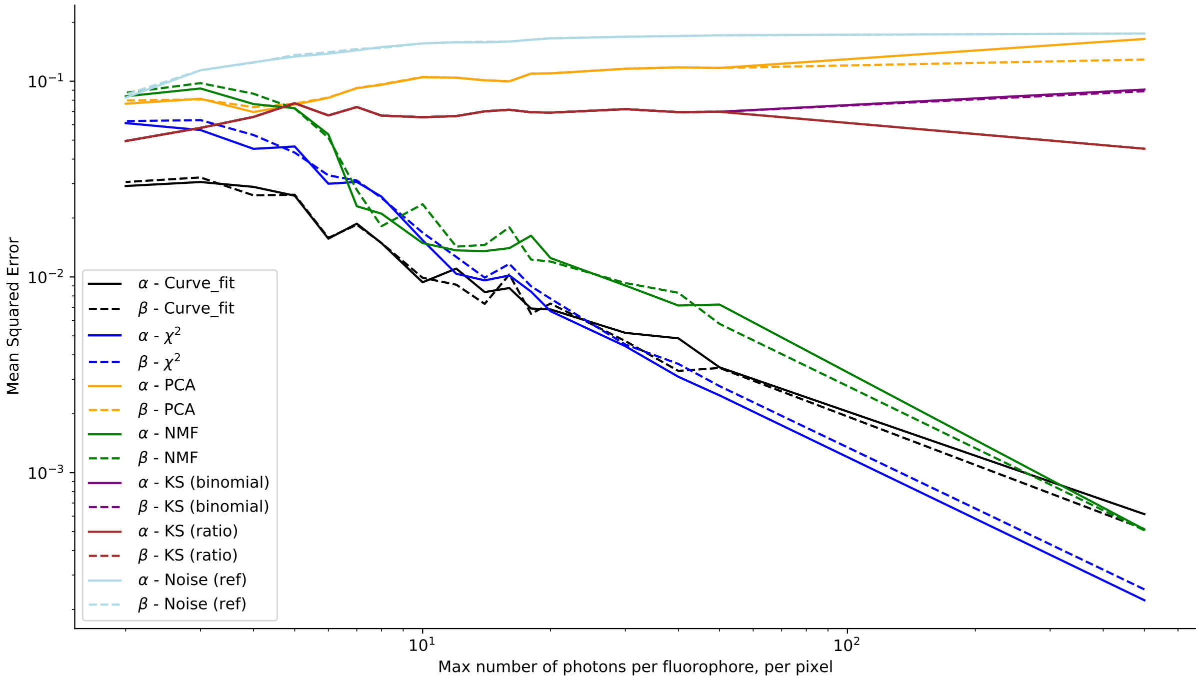

Figure 7.14: MSE results for the various analysis techniques described above. The best performing analysis tool *scipy.curve_fit* at lower photon values, and χ^2 at high photon counts, but the NMF technique was able to recreate the reference image with similar accuracy while having no prior knowledge of the spectra.

In summary, the best option to recover the reference spectra from the artificial data, is by using χ^2 analysis if reference spectra are available, or by using NMF technique in instances where analysis must be performed blind (with no reference spectra).

Given more time it would be useful to run more simulations and build up some statistics on each of the methods to establish a smoother trend and from which to calculate error bars.

Chapter 8

Results

In alignment with the Research Questions (chapter 1.3.1), three experiments were performed to demonstrate that the MKID microscope can be used to **detect** the presence of microspheres (Research Question 1), and then use spectral information to **identify** the type of microsphere based on the fluorophore it contains (Research Question 2).

These initial studies also quantify the number of photons required (related to the integration time, or image capture time) to achieving the required certainty of 5σ as discussed in Research Question 3. Answering these questions is the first step towards identifying fluorophore stains in a biological sample, which will permit discernment between features such as structures within a cell (as described in Section 1.1).

These questions are answered by conducting a series of three experiments corresponding to the columns in Table 8.1, each increasing in complexity and scope from the first to the third. Firstly, two isolated fluorophores are examined and spectral resolution of the fluorophores is demonstrated (verified with a USB spectrometer). Secondly, multiple individual microspheres are resolved with the MKID microscope (again, verified with the USB spectrometer). Lastly, an *ex vivo* sample is examined.

	2 Drops	**3 Beads**	***ex vivo***
Image of sample	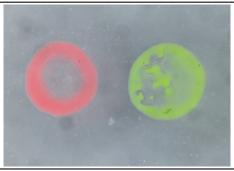	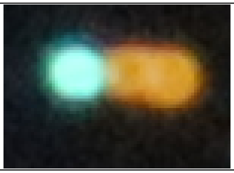	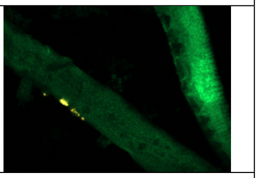
Origin of detector used	UCSB	SRON	SRON
Informed spectral analysis (χ^2)	Section 8.1.5	Section 8.2.9	*(Not performed)*
Blind spectral analysis (NMF)	*(Not performed)*	Section 8.2.10	Section 8.3.5
Contains combined spectra?	Pure	Mixed	Mixed
Verified against microscope type	USB Spectrometer	USB Spectrometer	Commercial
Required photon count calculated	*(Not performed)*	Section 8.2.11	Section 8.3.6

Table 8.1: Table describing the analysis performed on each sample.

8.1 Sample: Two Drops of Fluorophore

8.1.1 Aim

This test demonstrated that the MKIDs device manufactured by JPL/UCSB was capable of **detecting** and then **identifying** fluorophore microspheres. The test consisted of collecting and analysing a series of spectra, calculated from the photons obtained from two pure unmixed spectra collected from the two selected fluorophores using an MKID. χ^2 analysis was then used to recover an intensity map of each fluorophore with confidence intervals. The confidence intervals indicate whether the identification of a given fluorophore is statistically significant or a chance occurrence. This is validated by comparison with a similar analysis performed using the USB spectrometer, and in doing so acts to verify that that the spectral sensitivity of the MKID can be used to identify the fluorophores in this particular high-signal case. These developments provide the first proof-of-concept in the literature, to the best knowledge of the author.

Additionally, the spectra from the USB spectrometer are converted into photon energy data using the same method as in the simulation, and compared to the MKID spectra to provide further validation of the methods of this thesis. In doing so, an estimation of the spectral resolution (R) and phase shift to photon energy conversion factor is given.

8.1.2 Description of the Sample

The first sample was designed to give a high, unambiguous fluorescence spectra for each fluorophore with no mixed spectra, to verify the ability of the MKID to spectrally resolve two fluorophores. Relatively large ($\approx$850 µm), spatially separated collections of fluorescent microspheres were imaged in wide field. The samples were prepared by placing a drop of each fluorescent microsphere solution onto the cover slip, and allowing to dry so the residue was on a single plane, which was then mounted upside down using spacers so that a flat plane was presented to the downward-pointing microscope. A photograph of the sample is shown in Figure 8.1.

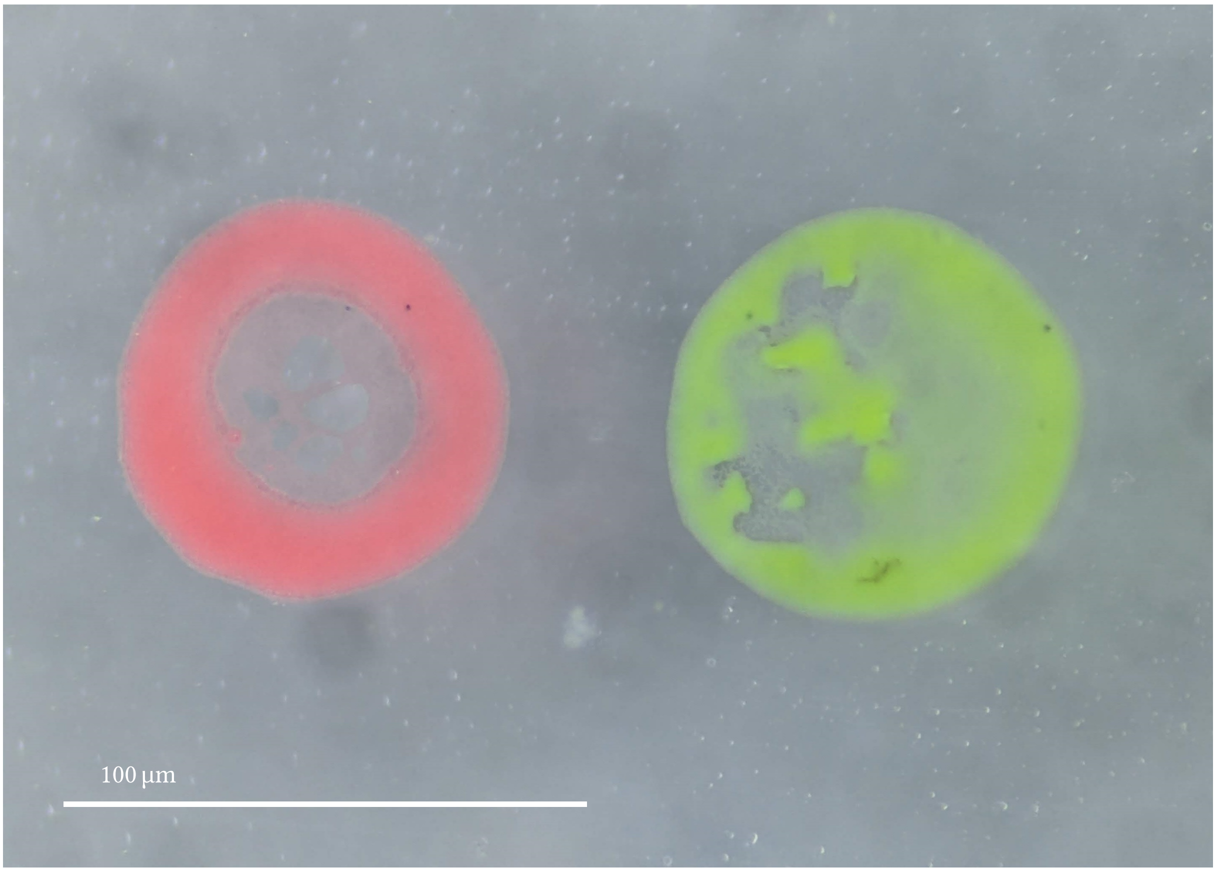

Figure 8.1: Wide-field optical microscope image of the residue from two drops of fluorescent microspheres, deposited on a cover slip and viewing the side in contact with the glass (left is Nile Red fluorophore, and right is Yellow-Green fluorophore). Imaged using an RGB camera.

Figure 8.2 shows a scan taken with the USB spectrometer. There is a grey scale image (top left), and orthographic projections of the X, Y, λ data cube (top right and bottom left), as well as a plot of several of the spectra (bottom right). Every spectrum in the 'plot of spectra', appears to be some amount of one of two spectra, as expected.

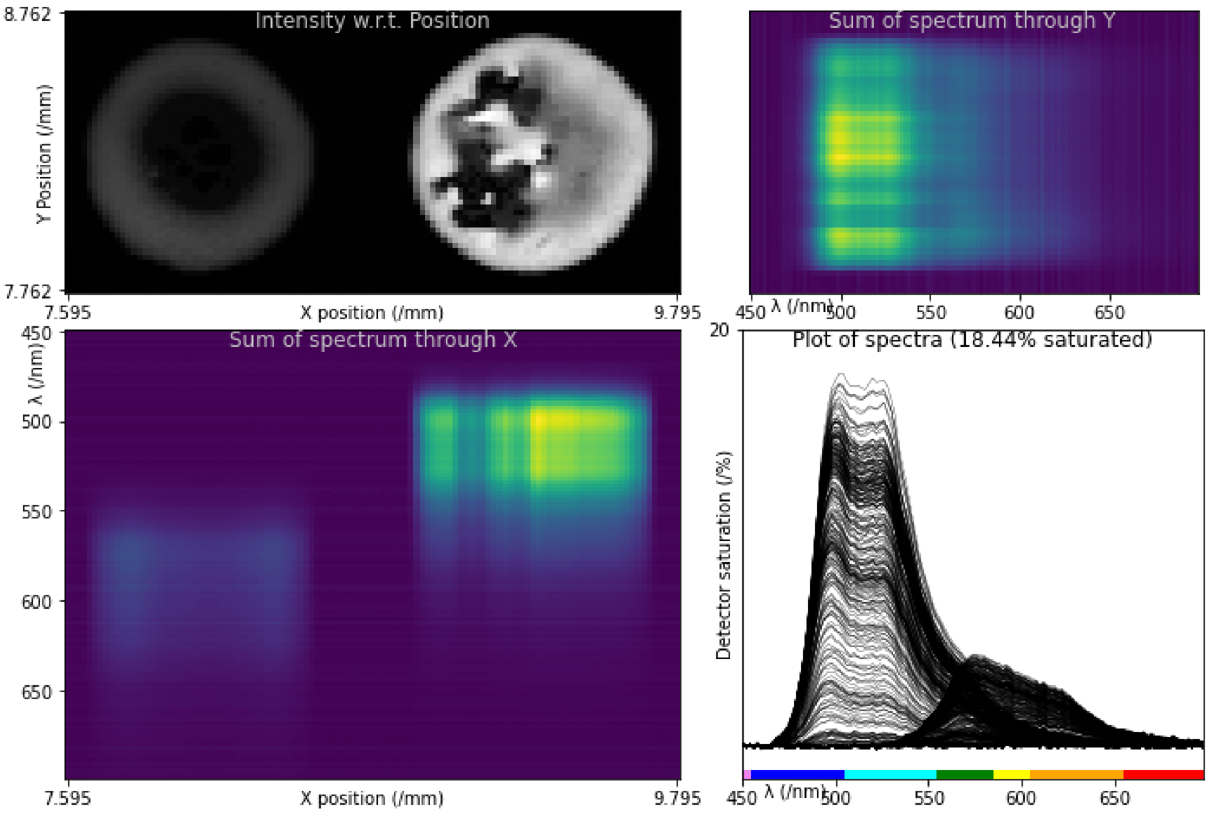

Figure 8.2: Scan of two drops, using USB spectrometer as the detector. Top left: intensity map of spectrometer readings, summed. Shows location of the drops in the FOV Bottom left and top right: intensity map through the Y and X axis respectively, plotting the intensity w.r.t. wavelength. Shows that the two fluorophores have different emission wavelength peaks. Bottom right: Spectra of several points within the sample. It indicates that all samples exhibit one of two spectra, albeit at varying intensities.

A series of points along the centre of the two drops was selected to be measured by the microscope using the MKID as the photon detector. Because the readout time for the MKID was significant for each sample (4.5 minutes per point), only a 51 x 2 section through both drops was observed in this way.

The USB spectrometer records measurements, in wavelength, while the MKID outputs individual photon energies in terms of phase shift (see Section 2.2). Figure 8.3 shows the spectra at points along the centre of the drops (i.e. X axis representing the spatial dimension through the drops, and Y representing the photon energy as wavelength (a) or phase shift (b), and the pixel shade representing photon count at this photon energy). It is apparent from the plots that higher phase shift correlates to a shorter wavelength (lower photon energy) as would be expected.

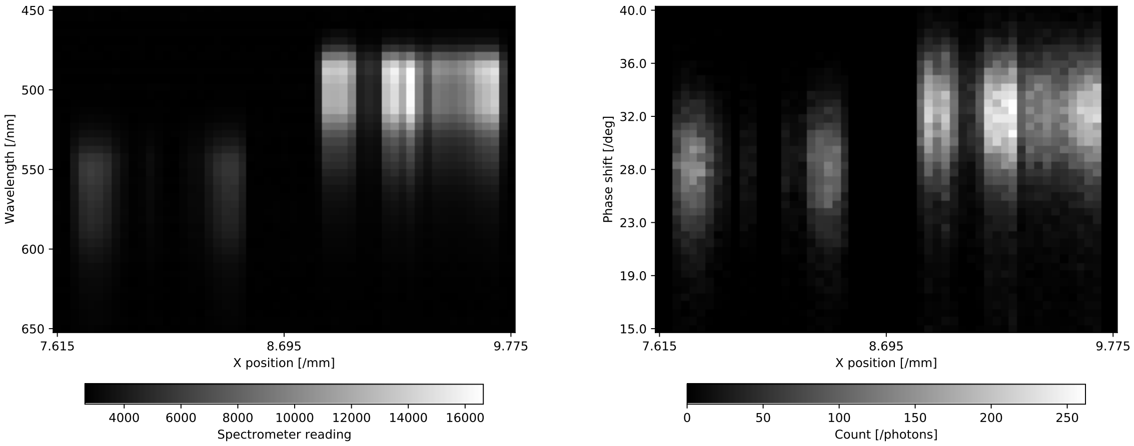

((a)) USB spectrometer as the detector

((b)) MKID as the detector.

Figure 8.3: Spectra of a cross section through the centre of the drops, taken with the USB spectrometer (left) and MKID (right).

8.1.3 Obtaining the Reference Spectra

The Nile Red fluorophore fluorophore spectra was obtained by combining all photons collected from the left half of the scan, which were known to contain the red fluorophore, and the Yellow-Green fluorophore spectra was determined in a similar way. The resultant *reference spectra*, are shown in Figure 8.4.

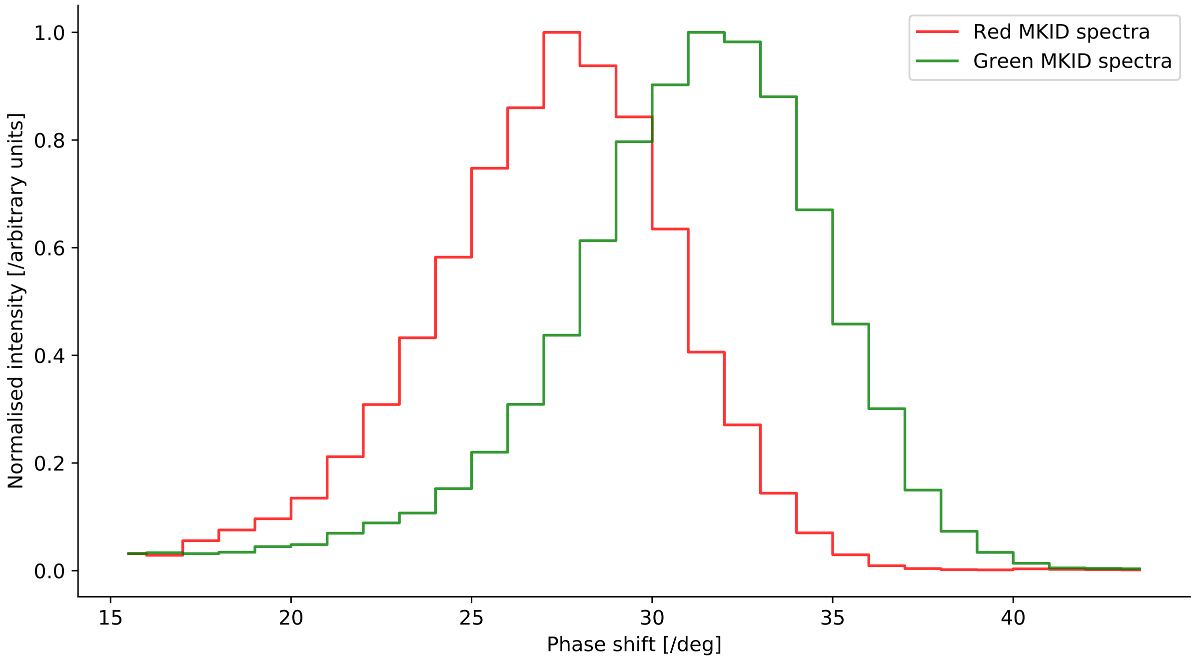

Figure 8.4: MKID spectra of both fluorophores, normalised to the maximum bin value

8.1.4 Verifying the Reference Spectra Model

In order to determine an indicative conversion rate (phase shift to wavelength) and also to test the assumption made in Section 6.1.1 that assumes that the MKID spectra can be calculated from the fluorophore spectra, the following comparison is made. The spectra of each fluorophore as measured by the USB spectrometer and represented in terms of wavelength, undergoes a wavelength dependent Gaussian blur of a given R, then plotted in terms of photon energy (which relates to photon energy by a given scaling factor) resulting in a spectrum in terms of phase shift. These modified spectra are normalised, and compared to the normalised spectra from the MKIDs, then the R and scaling factors are optimised to minimise the MSE, to arrive at the result shown in Figure 8.5. The best fit is obtained when detector has a scaling factor is 12.79 ° eV^{-1} and $R = 10.40$ at 400 nm. The two spectra do not match exactly, and this is likely a result of the MKID and USB spectrometer having a wavelength dependent sensitivity, and the USB spectrometer having readout noise and being unable to detect photons of wavelength longer than 1100 nm owing to the silicon band-gap of silicon.

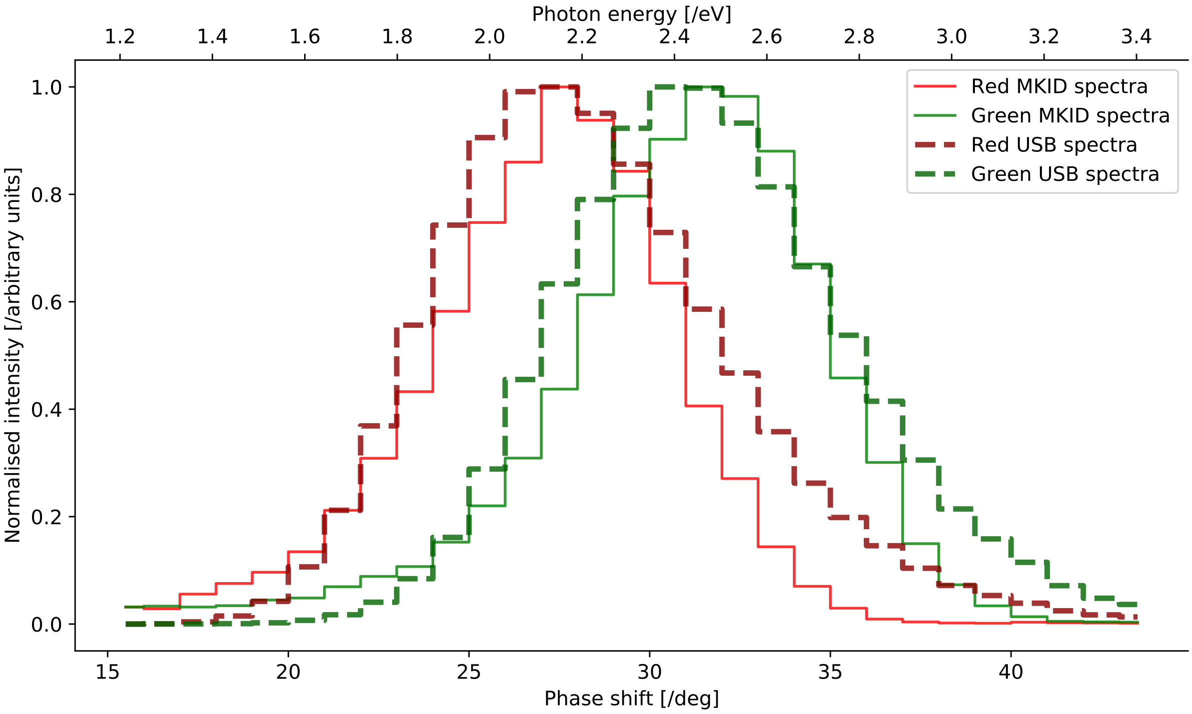

Figure 8.5: Graph of the MKID spectra of both fluorophores, compared to their counterparts from the USB spectrometer which have undergone spectral broadening (assuming $R = 10.40$ at 400 nm), and scaled to convert from phase and photon energy assuming a directly proportional relationship of 12.79 ° eV^{-1}.

8.1.5 χ^2 Analysis

When χ^2 analysis is performed on each MKID scan location, an intensity map can be made for both α and β (representing fluorophores Nile Red fluorophore and Yellow-Green fluorophore), as shown in Figure 8.6. This intensity map has regions and patterns with high α values that line up with features on both the photograph (Figure 8.1) and the comparable intensity map obtained from the USB Spectrometer (Figure 8.7).

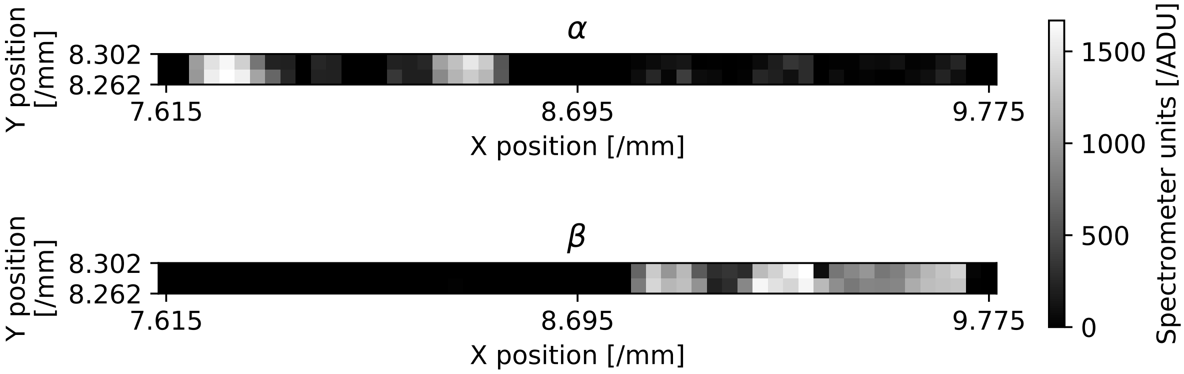

Figure 8.6: χ^2 analysis of MKID microscope plot - Intensity map showing the number of photons of each fluorophore, represented by α and β.

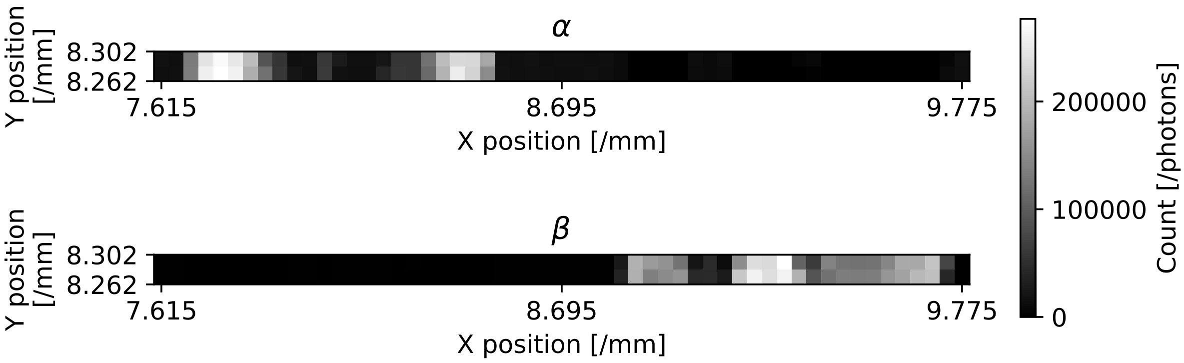

Figure 8.7: χ^2 analysis of USB spectrometer microscope plot - Intensity map showing the number of photons of each fluorophore, represented by α and β.

Because the fluorophores were not mixed, each spectra should have either an α component and no β component, or *vice versa.* Instead, the results indicate that spectra with a large β component, overestimate the α component, but the β value is not overestimated. This is likely an effect caused by the fact that the red spectra overlaps significantly with the green spectra, so it is a possibility that the green spectra is comprised of some amount of red.

In order to discuss the χ^2 fitting, some examples have been selected to investigate in more detail. Table 8.2 lists a few χ^2 results, describing the α and β values found, their associated errors and the X,Y location within the plot.

α	σ_α	α/σ_α	β	σ_β	β/σ_β	$x_{\textbf{INDEX}}$	$y_{\textbf{INDEX}}$
979	48	20	-31	13	-2	4	0
0	1	0	0	1	0	27	0
168	54	3	1639	77	21	39	0
176	53	3	1656	74	22	42	0
432	33	13	-7	12	-1	6	1
127	18	7	5	10	1	11	0
149	20	7	1	10	0	17	1
879	44	20	-22	13	-2	20	1
0	1	0	0	1	0	27	1
36	43	1	1222	65	19	33	0
84	45	2	1255	66	19	34	1
6	21	0	308	32	10	36	1
-17	21	-1	360	34	10	37	1
-13	42	0	1250	64	19	43	0
133	51	3	1392	69	20	40	1
64	47	1	1334	68	20	52	0
-2	3	-1	9	6	2	53	0

Table 8.2: Table showing a subset of the results from the χ^2 analysis performed on spectra from two unmixed fluorophores.

Figure 8.8 is a graphical representation of all results, their 1σ error bars (with the chosen points, highlighted), and regions describing the approximate 5σ confidence level that all photons are from a single fluorophore. The green region, for example, contains points which have a 5σ probability of containing only Yellow-Green fluorophore and is bounded by the line described in equation 8.1, and $\alpha = 0$.

$$\alpha = \beta \times \sum_{i=0}^{n} \frac{5 \times \sigma_{\alpha i}}{\beta_i} \tag{8.1}$$

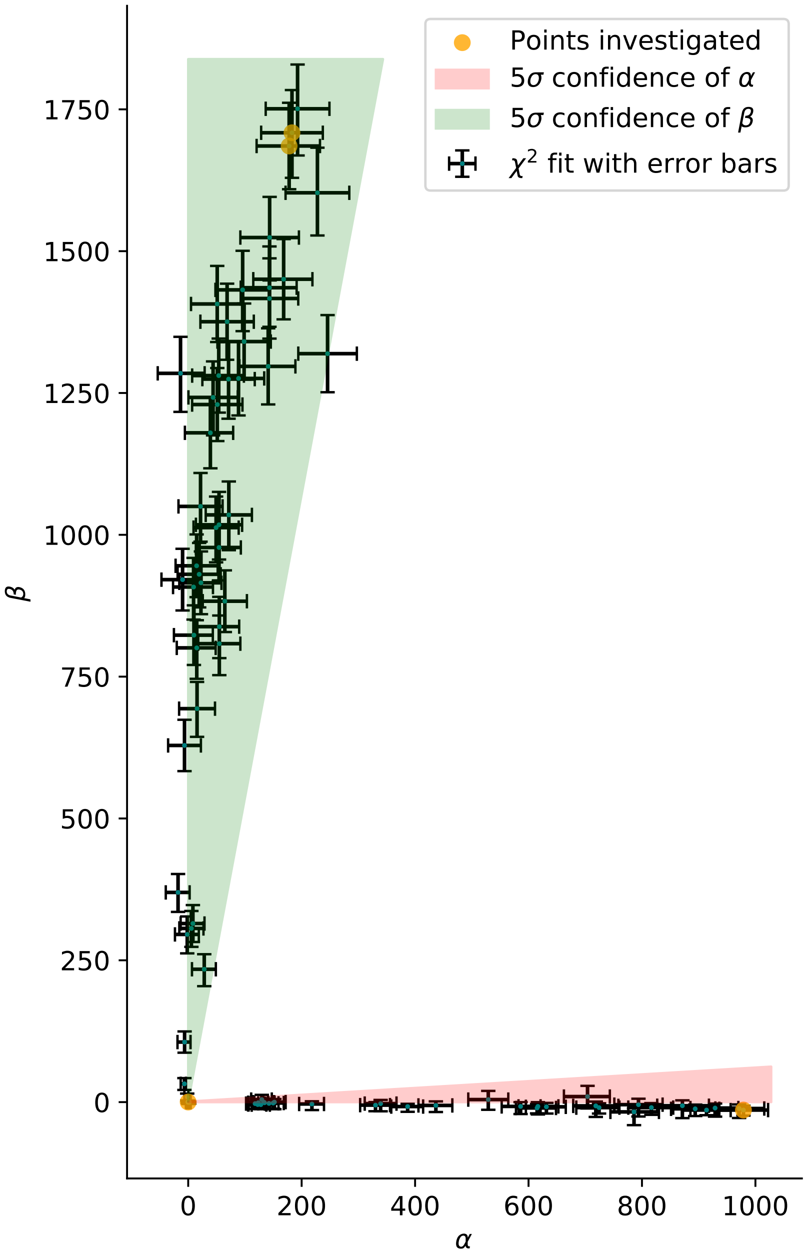

Figure 8.8: The results from performing χ^2 analysis on spectra from each point in the MKID scan of the 2 drop sample

The following examples show the χ^2 results and confidence intervals are given by these results. Four points were selected, in the locations shown in 8.9 and are discussed below. These four points appear in Figure 8.8 in orange. The values for best fit in the table, differ from those on the contour plots because the bin ranges used to analyse each spectra was slightly different, however the method remains the same.

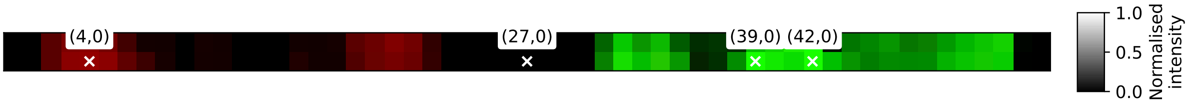

Figure 8.9: Composite RGB image of the MKID scan of the 2 drops sample, overlaid with the locations of the pixels identified for further analysis.

Nile Red fluorophore only : The point occurring at index (4 0) is a spectra of the Nile Red fluorophore only, and the MKID recorded 906 photons. χ^2 analysis of the spectrum from this point, indicates it has 979^{+-31}_{-48} photons from Nile Red fluorophore and -31^{+13}_{-2} photons from Yellow-Green fluorophore. The value for the red fluorophore is in line with expectation, however there cannot be a negative number of green fluorophores so the value of -31 is impossible. In this case we know that there are 0 green photons contributing to the spectrum, and this is 2.4σ from the value found. Figure 8.10 shows the χ^2 best fit (dotted line) to the data (blue step plot), with the filled areas representing the relative contributions of the two fluorophores. Figure 8.11 shows the contour plot of the data.

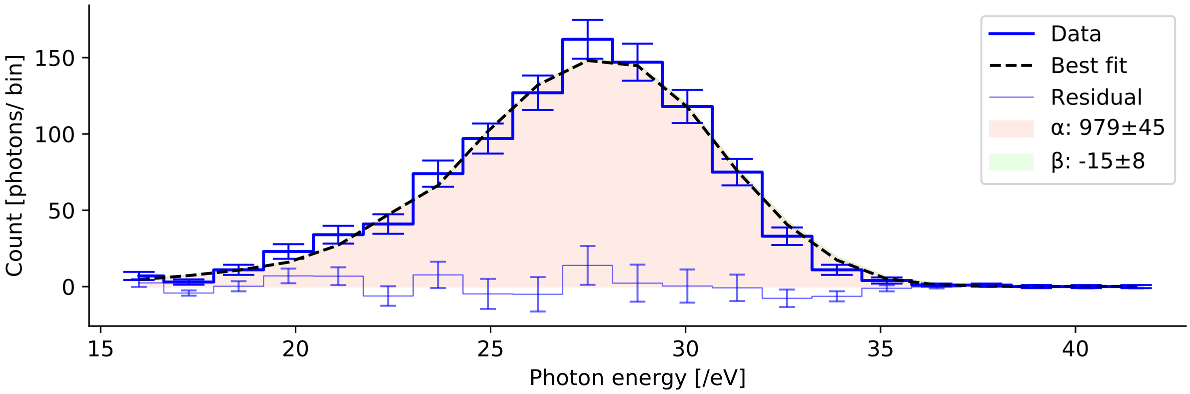

Figure 8.10: The results from χ^2 fitting to point (4,0), indicating that this point is observing the red fluorophore.

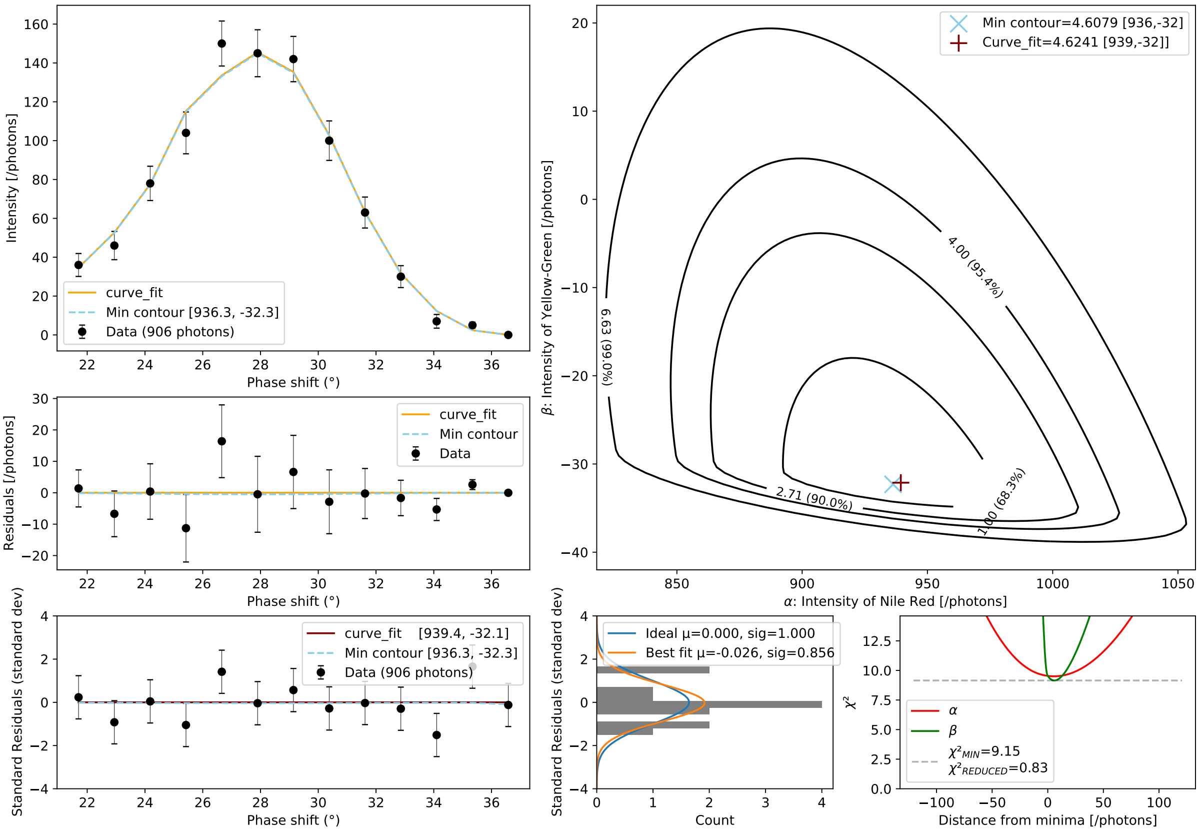

Figure 8.11: χ^2 analysis performed on point (4,0).

Yellow-Green fluorophore only - Point (39 0) is of an area that is only green fluorophore, the analysis indicates that there are 1639^{+79}_{-75} green photons, giving a confidence of 20.4σ, well above the 5σ required to positively identify the fluorophore. The analysis also indicates there are 168^{+54}_{-54} photons from the red fluorophore, or a 3.01σ confidence that the number of red photons, is not 0. It is known from the setup that there are no red photons present. The nature of confidence intervals, suggests that there will be outliers, and this should occur 1 in 385 times.

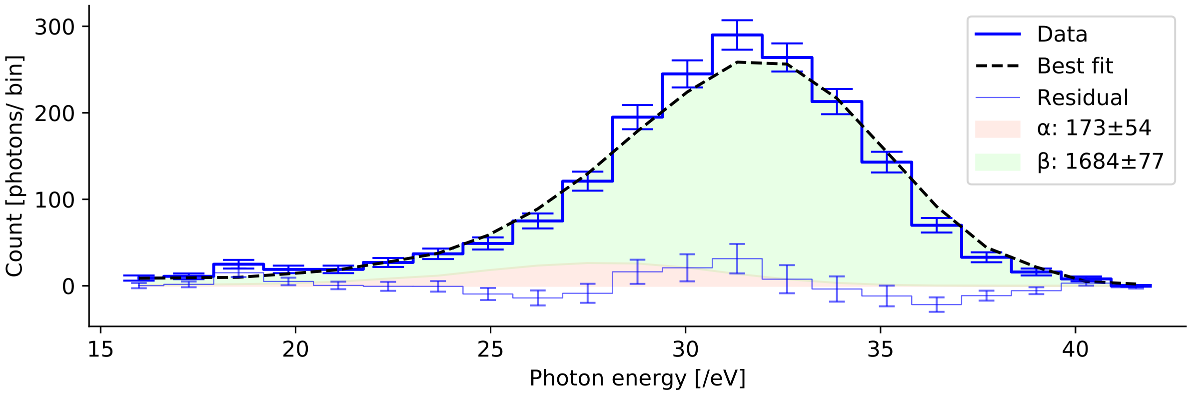

Figure 8.12: The results from χ^2 fitting to point (39 0), indicating that this point is observing the green fluorophore with a small red component (8%). It is known that this spectra does not contain any Nile Red fluorophore.

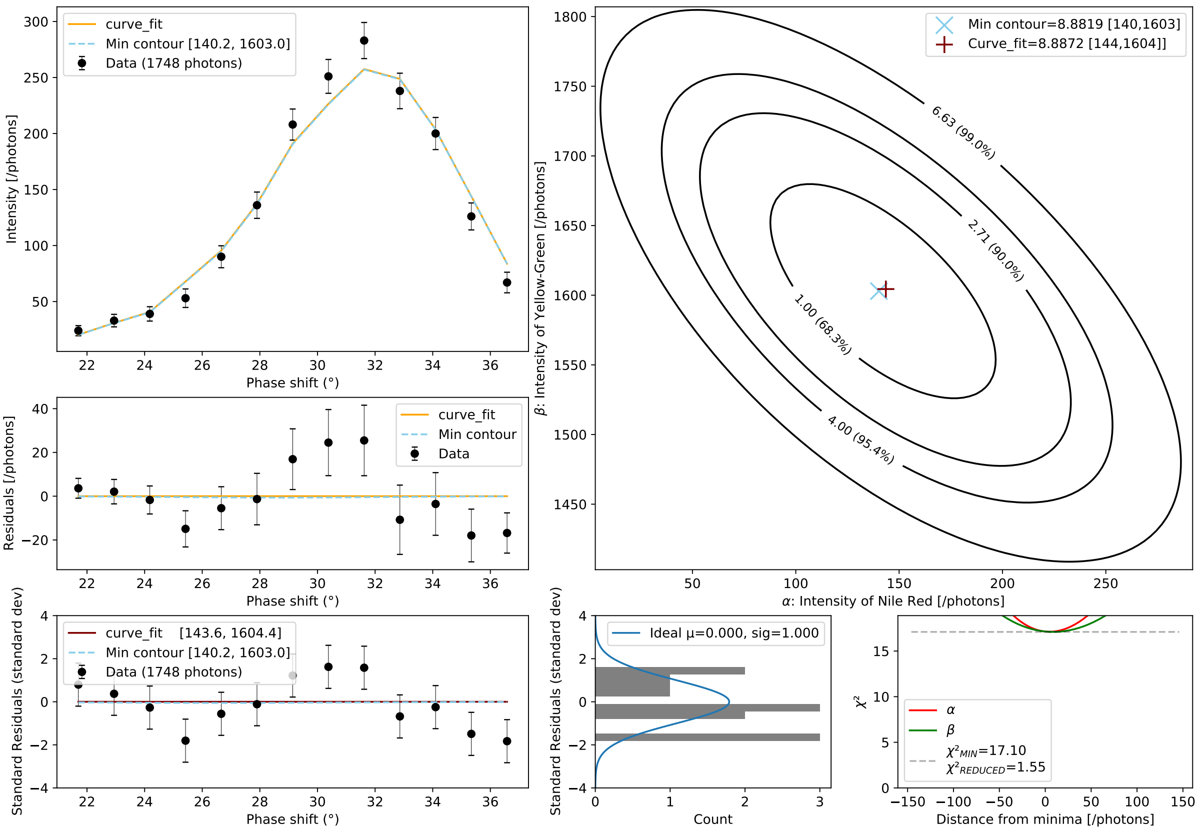

Figure 8.13: χ^2 analysis performed on point (39 0).

Empty spectra - In the case of point (27 0), no photons were detected, and the model handles the zero condition correctly by returning an expected photon count of 0^{+1}_{-0} red and 0^{+1}_{-0} green. The graphs of this result are shown in Figures 8.14 and 8.15.

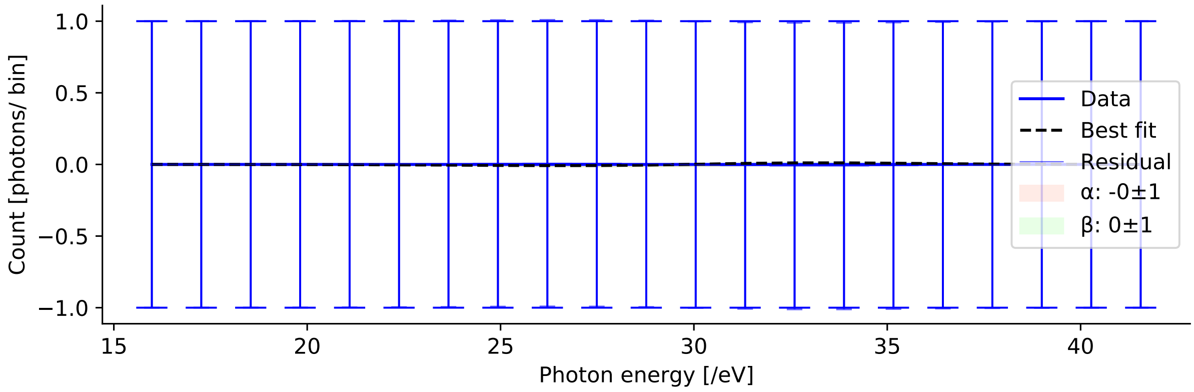

Figure 8.14: The results from χ^2 fitting to point (27 0), indicating that this point contains no photons.

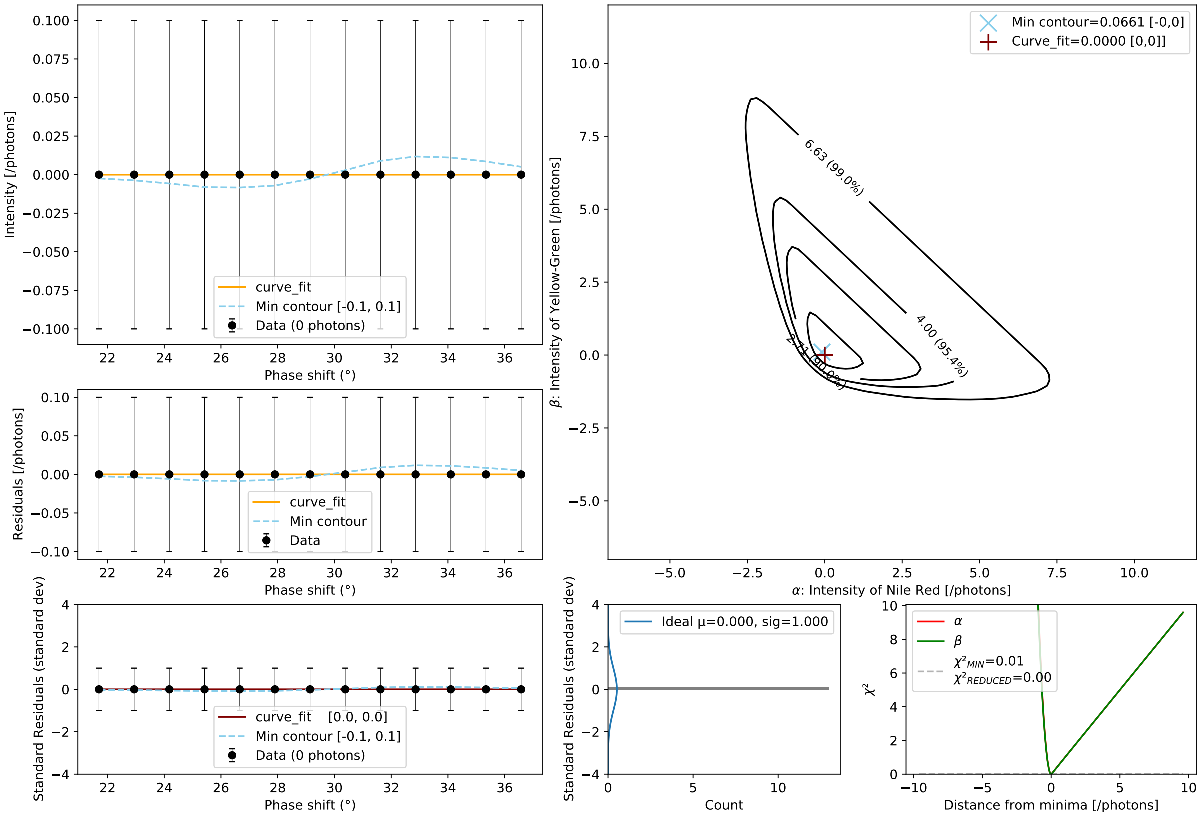

Figure 8.15: χ^2 analysis performed on point (27 0).

8.1.6 Discussion

The scan taken of the two fluorescent drops with the confocal microscope using the MKID as a detector, returned spectra which when analysed, returned high numbers of photons from locations containing fluorophores, indicating they were able to detect fluorophores (answering Research Question 1).

Moreover, performing χ^2 analysis described in Section 6.4, on the spectra, returned larger α values in areas with Nile Red fluorophore present (detected with USB Spectrometer, and based on knowledge of the sample), and similarly had high β values in areas with Yellow-Green fluorophore. In addition, features were visible which were common between all 3 'images', and while not quantified, this visual confirmation satisfied the level of scrutiny required for this initial experiment. This result suggests that the MKID detector can also spectrally separate, and therefore **identify** the fluorophore (answering Research Question 2).

8.2 Sample: Three microspheres

8.2.1 Aim

Individual microspheres containing different fluorophores were imaged to first demonstrate that the microscope was able to spatially resolve discrete microspheres using the photon counting detector. Secondly, the system was able to use the energy resolving capabilities of the MKID, to determine the fluorophore contained in the microsphere, even in circumstances where there was an overlap in spectra.

In order to answer research Research Question 3, the photon fluxes are decreased in post processing, and the corresponding deterioration in the confidence metric is quantified. This gives insight into how few photons are required to identify a fluorophore to the required confidence level, and after how much time, that was achieved.

8.2.2 Description of the Sample

A mixture of green and red microsphere solutions containing microspheres of diameter ≈2 µm, was dispensed on the surface of a cover slip and allowed to dry, causing random arrangements of microspheres to form on the flat surface. Three adjacent microspheres were identified with a Nikon Fluorescence microscope, an image of which is shown in Figure 8.16, and selected because both fluorophores were present, and importantly they were touching so there would be a region of mixed fluorophore. These microspheres were found on the microscope slide, with assistance from the wide field system of the *MKID microscope*.

Once the subject had been located, a relatively quick USB spectrometer scan was conducted to locate these microspheres in terms of X,Y,Z coordinates in the microscope, and obtain a reference image, before the more time consuming scans with the MKID detector. Scanning was performed at a pixel pitch (i.e. translation stage increment) of 0.5 µm. The same area was scanned 11 times, producing 11 lists of photons (and associated arrival times) for each X,Y position which can be concatenated into a single list per X,Y position.

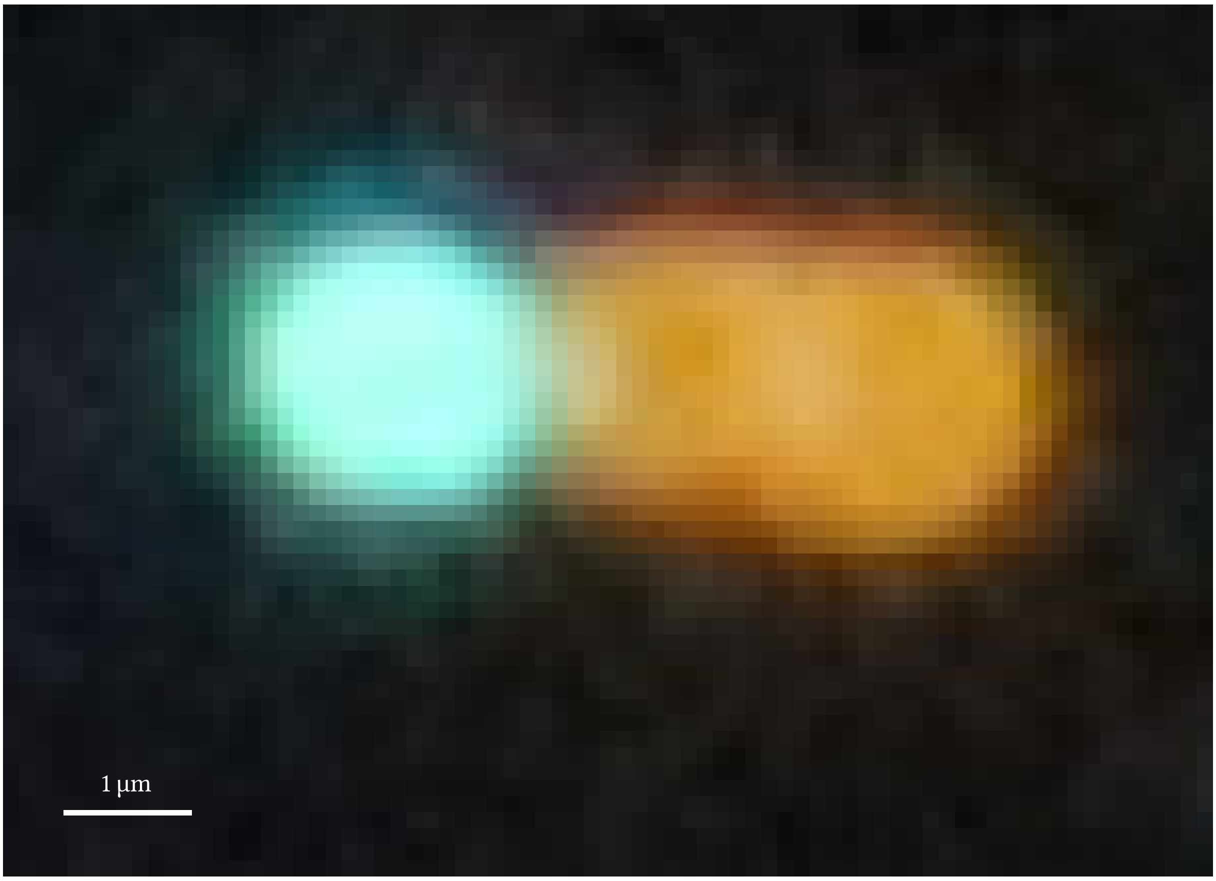

Figure 8.16: Wide-field fluorescent image of 3 microspheres (one Yellow-Green fluorophore, and two Nile Red fluorophore), using an RGB camera attached to a Nikon fluorescence microscope

8.2.3 Raw Scan Results

Figure 8.17(a) shows an intensity map obtained from a scan of the sample using the USB spectrometer to obtain a spectrum, with an intensity correlating to the average USB spectrometer reading in analogue-digital units (ADU). The scan shows the location of one bright microsphere next to two faint microspheres. This is corroborated by the results from the 11 similar scans, using the MKID as the detector shown in Figures 8.17(b) and 8.17(c) which show the same pattern, and how it decreases in photon flux with respect to time.

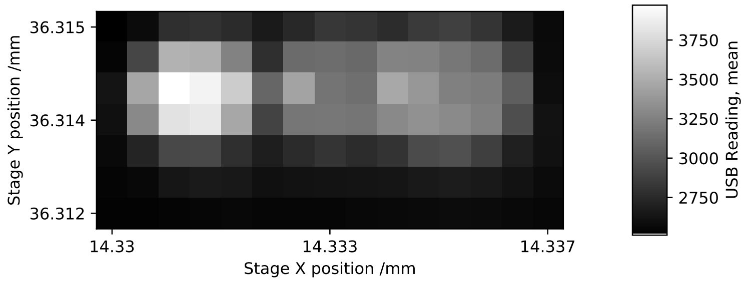

((a)) Scan of 3 microspheres, using USB spectrometer

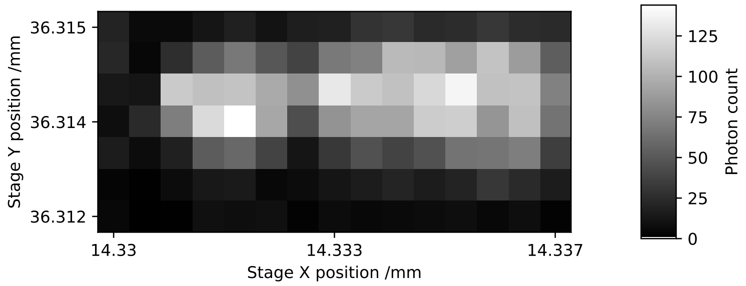

((b)) First of 11 scans of 3 microspheres, using MKID spectrometer

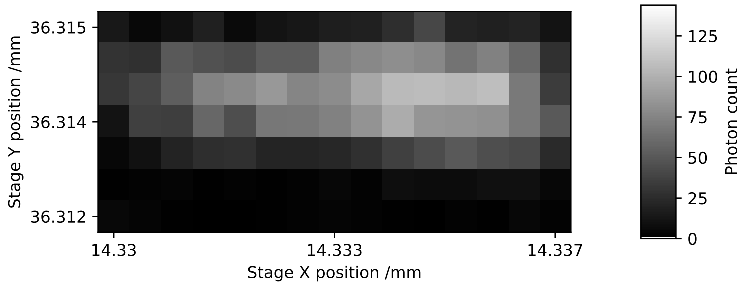

((c)) Final of 11 scans of 3 microspheres, using MKID spectrometer

Figure 8.17: Point-scanned monochrome images of 3 adjacent microspheres

The same scan was taken using the MKID detector to collect the photons, and each scan point yielded fewer than 150 photons over the 8s exposure. Several scans were taken to improve the photon count, and the number of photons decreased with each subsequent scan, due to photo-bleaching.

8.2.4 Spectra Cross Section

The data is processed as a data cube, with dimensions X,Y and Wavelength. Collapsing and viewing this cube orthogonal to the Y dimension (normal to the X, Wavelength plane) for the MKID detector, and USB spectrometer are shown in Figure 8.18 (left and right respectively). It is apparent that there is a feature at X=14.3315mm which emits higher energy photons detected by the MKID, that is also present in the USB scan as light with a mean of around 520 nm. It is also evident that there is a spectrally separate feature on the right hand side, emitting lower energy photons and longer wavelength light.

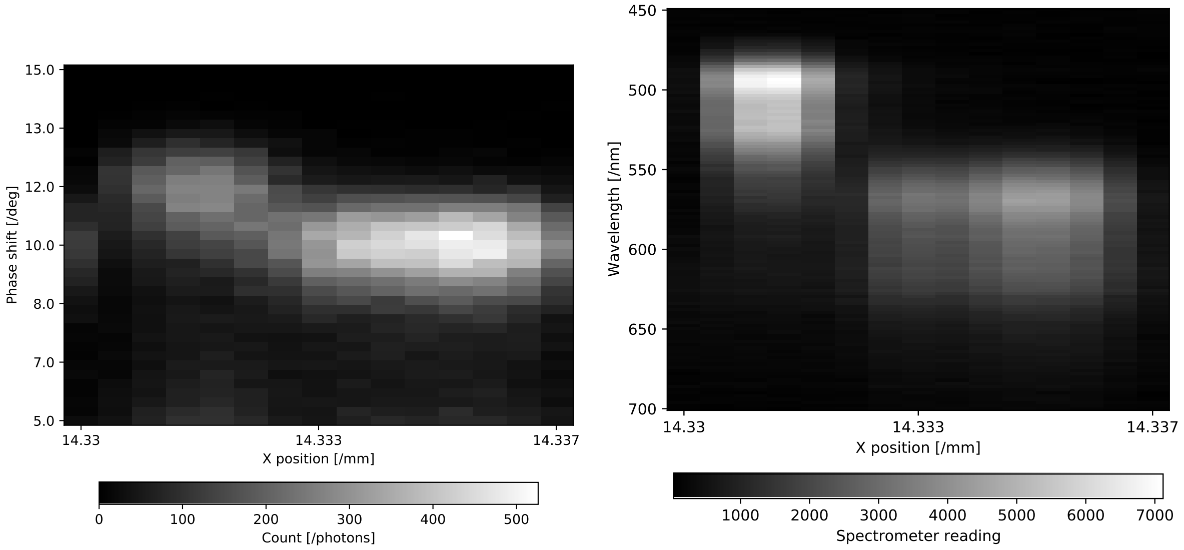

((a)) Phase shift

((b)) Wavelength

Figure 8.18: Cross section of spectral data cube, collapsed in the Y axis to reveal the spectral features (in phase shift from the MKID or wavelength from the USB spectrometer) against the X position

8.2.5 Instrument Dither

Over the duration of the scans, the subject moved in the field of view by a quarter of a pixel, or 0.122 µm. In cases where the subject moves more than 1 pixel pitch, the images can be cross-correlated to find the offset (in integer number of pixels) required to align the images.

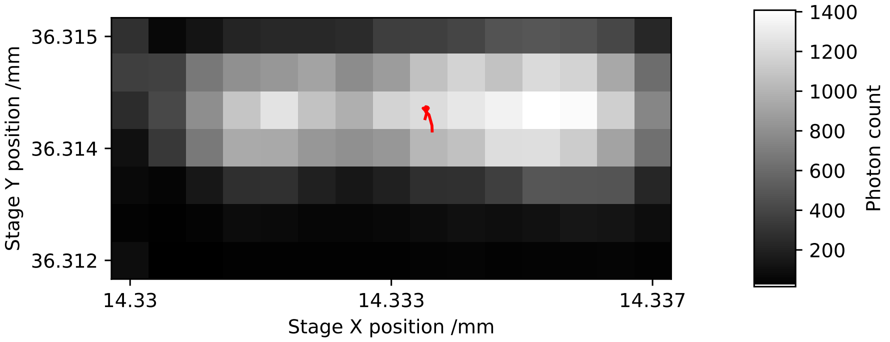

Figure 8.19: The photon count from all 11 scans of the 3 microspheres, with the centroid of the image overlaid in red, showing 0.122 µm of drift between samples.

Because the dither was less than 1 pixel, the images were not adjusted, however it should be noted that this variation will have an effect on the outcome of the stacked images. The dither results from instabilities in the setup, seemingly correlating to temperature fluctuations of the components and surrounding enclosure, settling of the equipment, repeatability of the stages, and other factors which come into play when requiring a repeatability of 10s of nano-meters.

8.2.6 Photo Bleaching

As visible between images 8.17(b) and 8.17(c), the number of photons from each point, decreases. There is an overall decrease of 24% across the 11 exposures (each of 8 seconds), as illustrated in Figure 8.20.

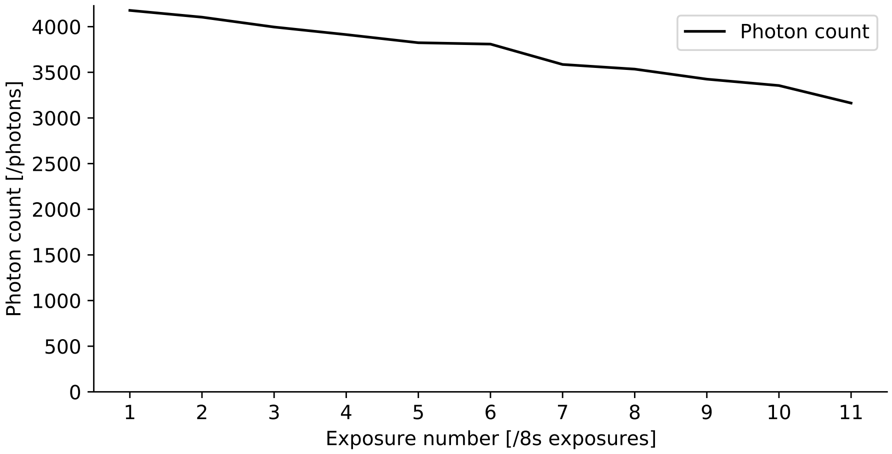

Figure 8.20: The total number of photons gathered per frame, as a function of exposure number, each exposure being 8 s in duration, and showing a 24% decrease over the 104 s.

It is possible to determine this as a function of time and phase shift (correlating to photon energy), as shown by the decreasing pixel intensities with respect to exposure number in Figure 8.21(a) (for the red microspheres, integrating over pixel columns 7 through 14) and Figure 8.21(b) (integrating over the pixels which see only green microspheres, columns 1 through 5). There is also a change in mean phase shift over the course of the experiment, which may be accounted for by changes in the fluorophore, or more likely a drift in the IQ centre of loop the which results in a systematic offset to the observed phase shift.

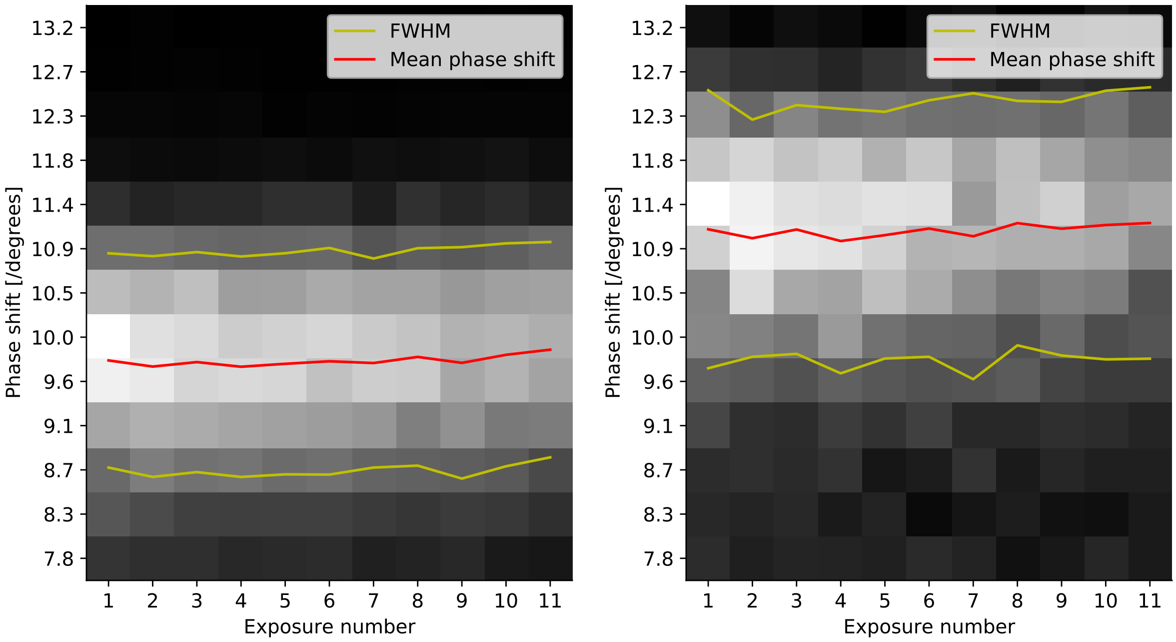

((a)) Red microspheres ((b)) Green microsphere

Figure 8.21: Change in spectrum with respect to exposure time. Each exposure lasts 8 seconds, and sees fewer low energy photons emitted with each subsequent exposure.

8.2.7 Verification Against an Image

In order to validate the MKID image against an independent reference, the intensity contours of the MKID image (of photon count) are overlaid onto the wide field photograph of the same scene, shown in Figure 8.22. The fact that the contours line up with the photograph, suggests the MKID image is an accurate representation of the subject.

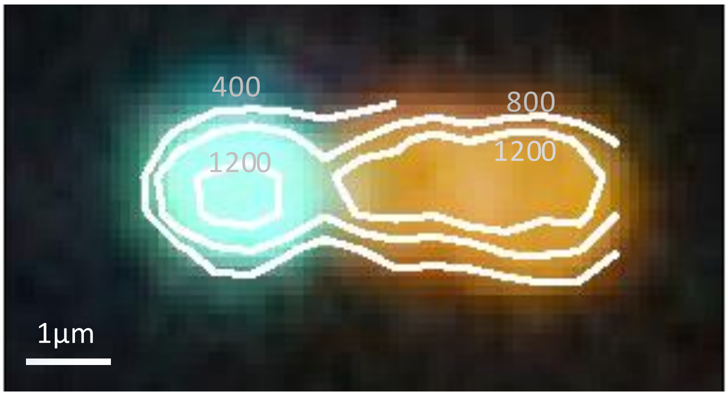

Figure 8.22: Contour lines of different intensity from the MKID scan, overlaid onto a wide field image of the sample.

8.2.8 Reference Spectra

Spectra were obtained from features elsewhere on the slide, which consisted of collections of only red, or only green microspheres. The spectra obtained were normalised (to have an area of 1), and presented in Figure 8.23.

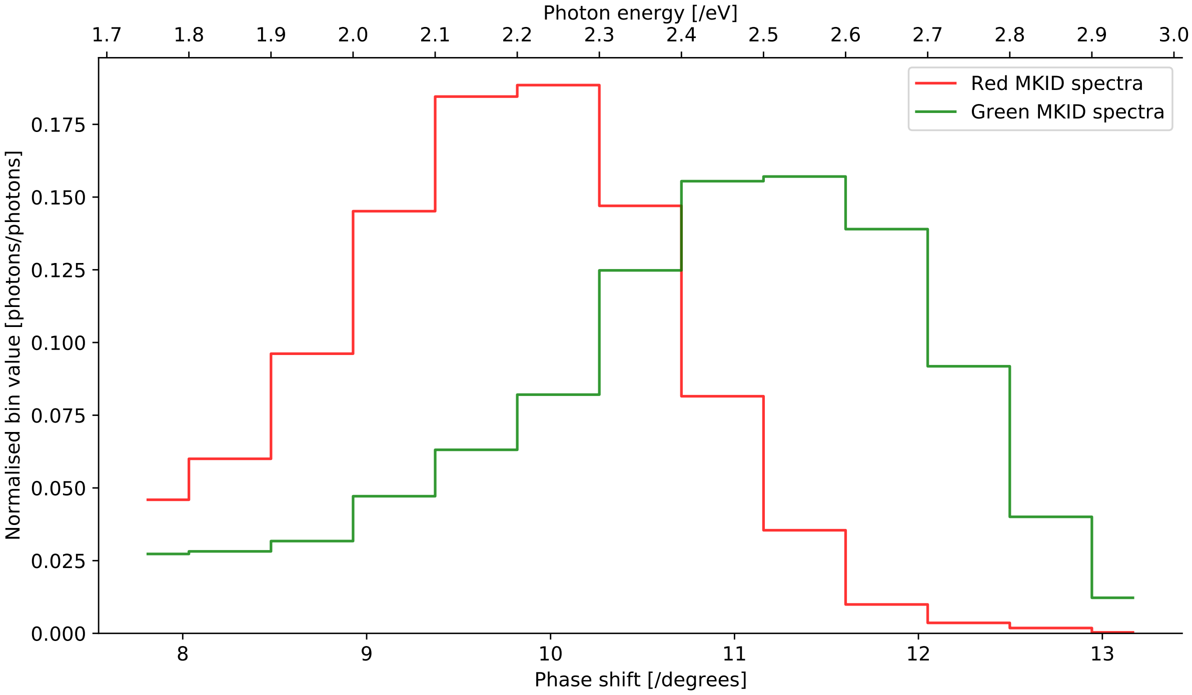

Figure 8.23: MKID spectra of both fluorophores obtained from taking a spectra of a known, pure fluorophore. Curves normalised to have an area of 1.

8.2.9 χ^2 Analysis

χ^2 analysis is performed on each MKID scan location of the 3 microsphere sample, producing the results shown in the intensity map for both α (Figure 8.24) and β (Figure 8.25), corresponding to fluorophores Nile Red fluorophore and Yellow-Green fluorophore respectively.

Figure 8.24: Plot showing the concentration of each fluorophore in the αchannel found using χ^2

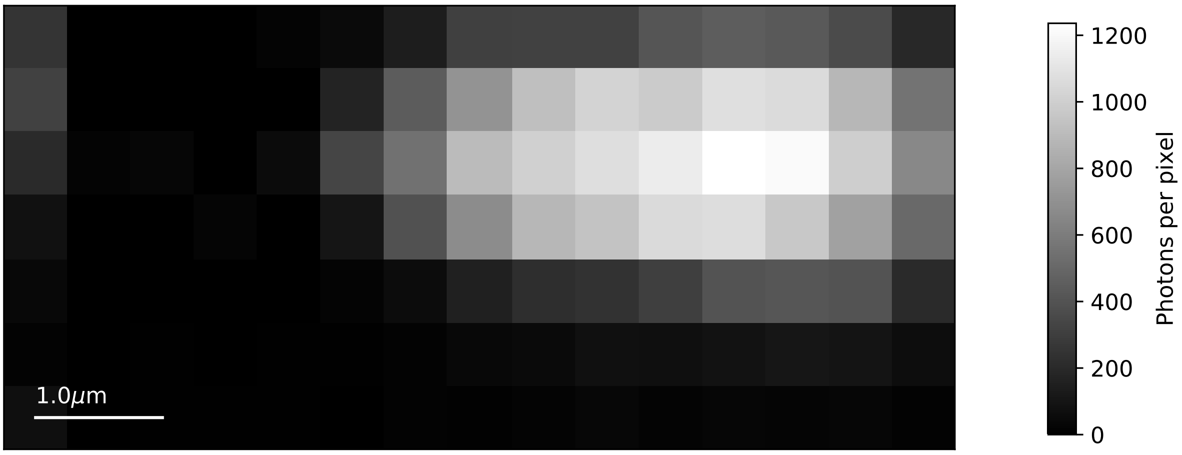

Figure 8.25: Plot showing the concentration of each fluorophore in the β channel found using χ^2

8.2.9.1 Further Explanation of χ^2 Fitting

The following examples show the χ^2 results and confidence intervals given by the analysis. Four points were selected, in the locations shown in 8.26 to be discussed in detail below, and are summarised in Table 8.3 along with other selected points.

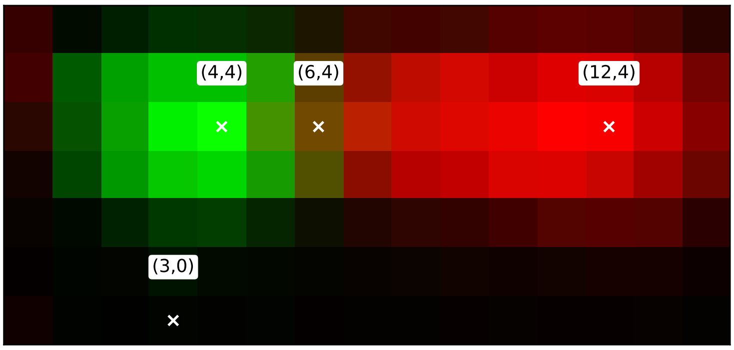

Figure 8.26: Composite RGB image of the MKID scan of the 2 drops sample, overlaid with the locations of the pixels identified for further analysis.

α	σ_α	α/σ_α	β	σ_β	β/σ_β	x_{INDEX}	y_{INDEX}
6	7	1	15	8	2	3	0
54	43	1	962	59	16	4	4
551	45	12	277	39	7	6	4
1209	53	23	-1	21	0	12	4
84	15	6	8	9	1	0	3
321	27	12	3	13	0	0	5
260	25	11	1	11	0	0	6
-39	30	-1	606	46	13	2	5
-9	13	-1	115	20	6	2	6
6	7	1	15	8	2	3	0
60	17	4	60	17	4	6	2
392	41	10	302	38	8	6	3
551	45	12	277	39	7	6	4
13	8	2	9	8	1	7	0
31	10	3	6	7	1	13	0

Table 8.3: Table showing a subset of the results from the χ^2 analysis performed on spectra from 3 beads.

Yellow-Green fluorophore- ($\alpha = 1209^{+52}_{-55} = 23.4\sigma$ and $\beta = -1^{+23}_{-18} = 0.05\sigma$) The point occurring at index (4 4) is over the Nile Red fluorophore microsphere, but may also be detecting some green fluorophore (Figure 8.27). χ^2 analysis of the spectrum from this point (Figure 8.28), indicates it has $\alpha = 54^{+43}_{-43}$ and $\beta = 962^{+62}_{-56}$. The value for the red fluorophore, as well as the 1.3σ likelihood of there being some amount of Yellow-Green fluorophore in the spectra, is in line with expectations.

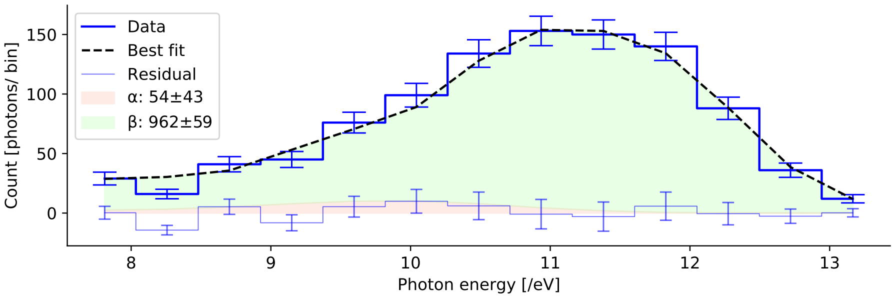

Figure 8.27: The results from χ^2 fitting to point (4 4), indicating that this point is observing the green fluorophore.

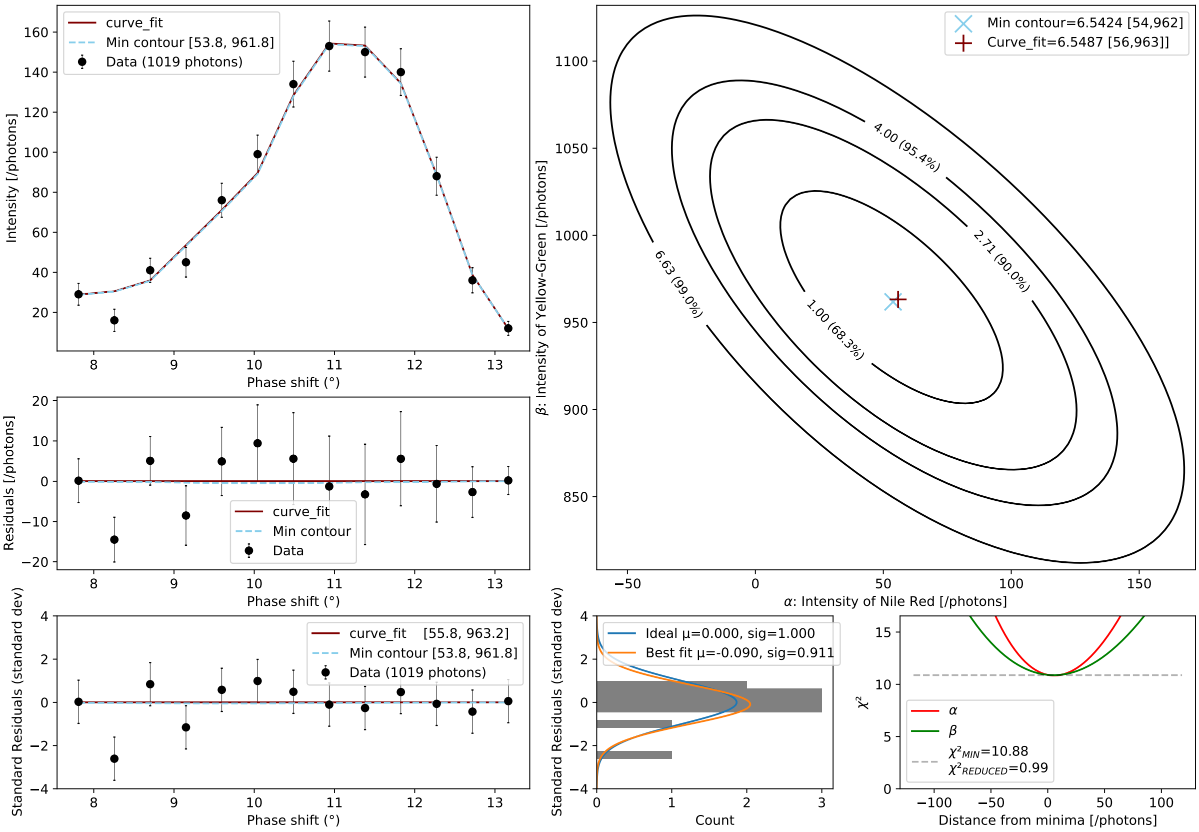

Figure 8.28: χ^2 analysis performed on point (4,4).

Nile Red fluorophore only - Point (12 4) is over a red microsphere and is far from a green microsphere, so the result ($\alpha = 1209^{+52}_{-55} = 23.4\sigma$ and $\beta = -1^{+23}_{-18} = 0.05\sigma$) aligns with expectations. Figure 8.29 shows the large red component of the spectra, with negligible green spectra, and Figure 8.30 show the χ^2 contour plot.

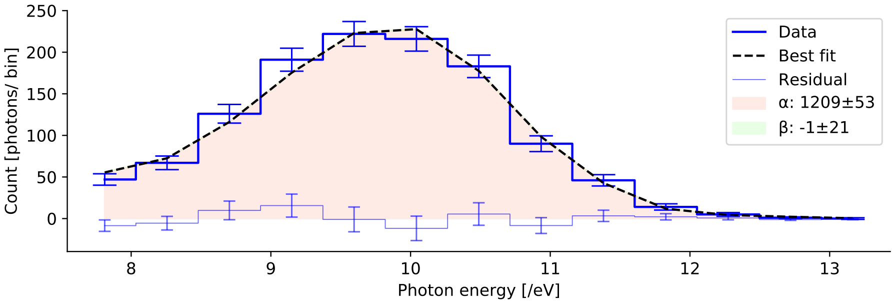

Figure 8.29: The results from χ^2 fitting to point (12 4), indicating that this point is observing the red fluorophore.

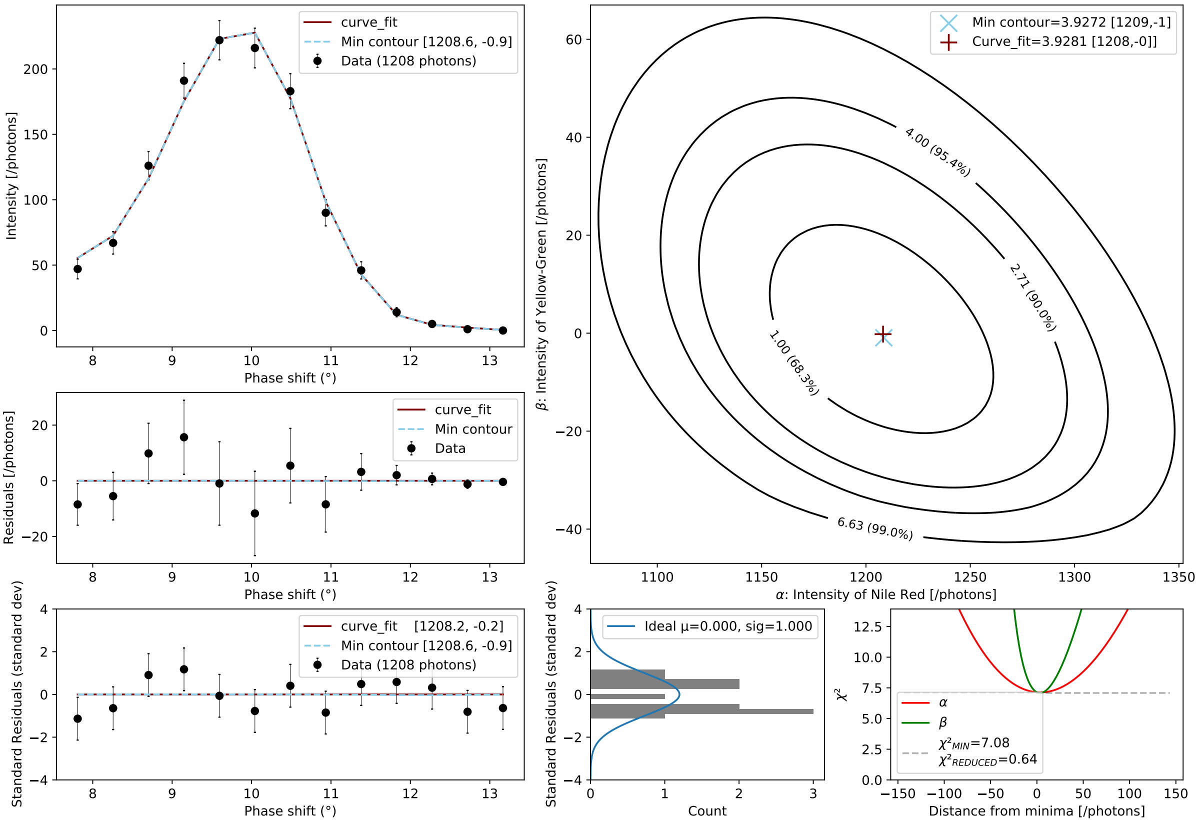

Figure 8.30: χ^2 analysis performed on point (12 4).

Mixed Fluorophore - Point (6 4) contains both red and green fluorophores, the analysis indicates that there are $\alpha = 277^{+41}_{-37}$ and $\beta = 551^{+43}_{-46}$, giving a confidence of 7.5σ that there is some amount of a red microsphere, and 12.7σ that the spectrum contains photons from the Yellow-Green fluorophore source. These are well above the 5σ required to positively identify the fluorophore. Figures 8.31 and 8.32 show the best fit and χ^2 contour plot for this point.

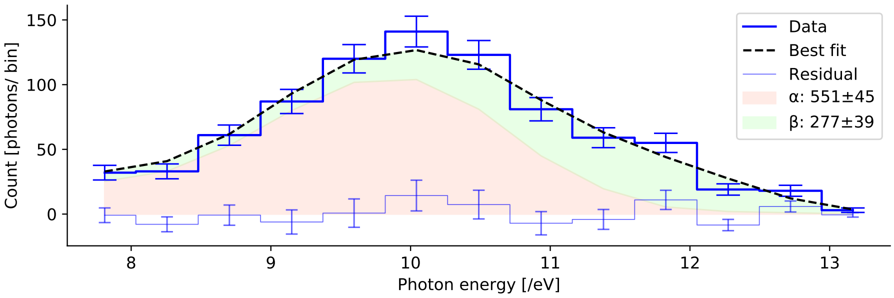

Figure 8.31: The results from χ^2 fitting to point (6 4), indicating that this point is observing the green fluorophore.

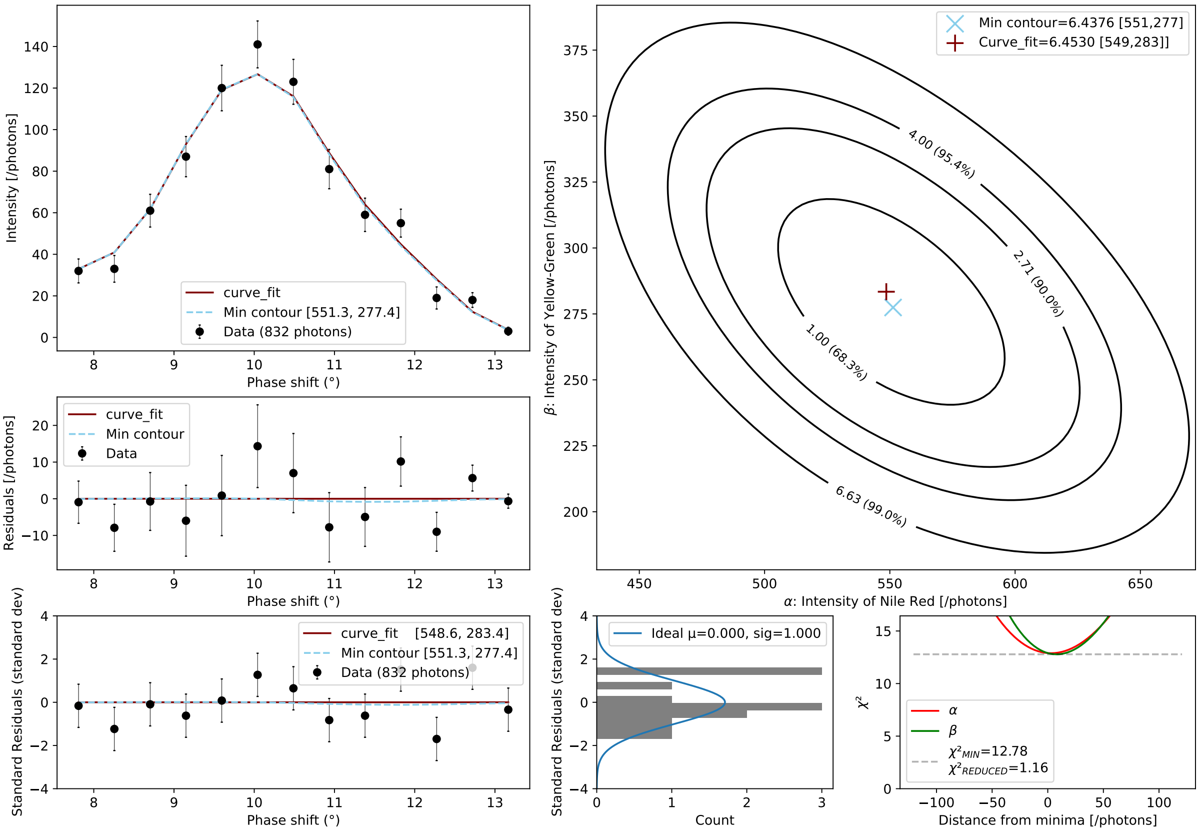

Figure 8.32: χ^2 analysis performed on point (6 4).

Empty area - Figures 8.33 and 8.34 show the best fit and χ^2 contour plot for point (3 0) which is of an area not expected to contain microspheres. There is still a 2σ confidence level that there is some red microsphere (given $\alpha = 15^{+9}_{-8}$), and a 1σ confidence that there is green, given $\beta = 6^{+8}_{-6}$.

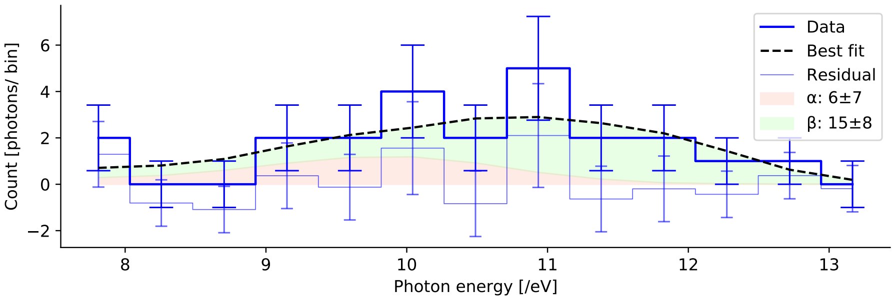

Figure 8.33: The results from χ^2 fitting to point (3 0), indicating that this point is observing the green fluorophore.

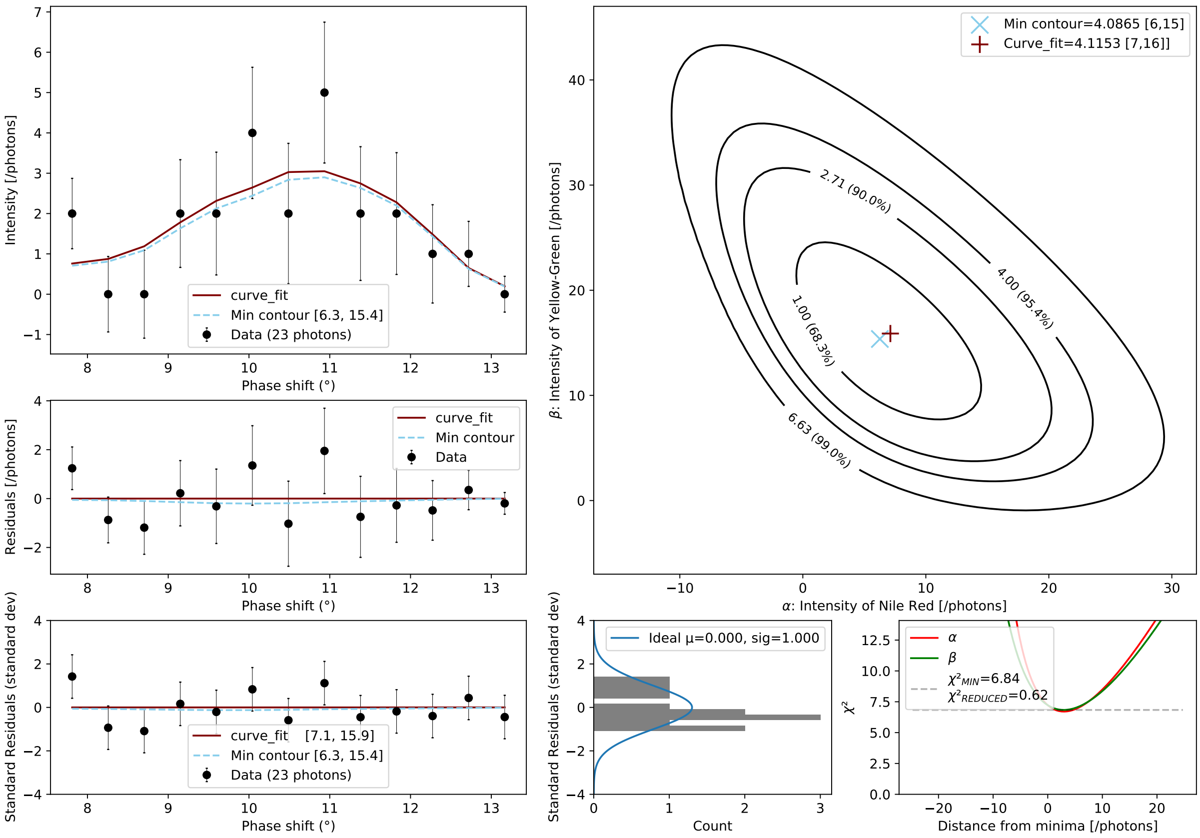

Figure 8.34: χ^2 analysis performed on point (3 0).

8.2.10 Blind Spectral Analysis (NMF)

By using NMF (described in Section 7.4) it is possible to extract the fluorophore spectra (referred to as components), and use the *scipy.curve_fit* algorithm to determine the abundances of both fluorophores. The results are shown in Figure 8.35.

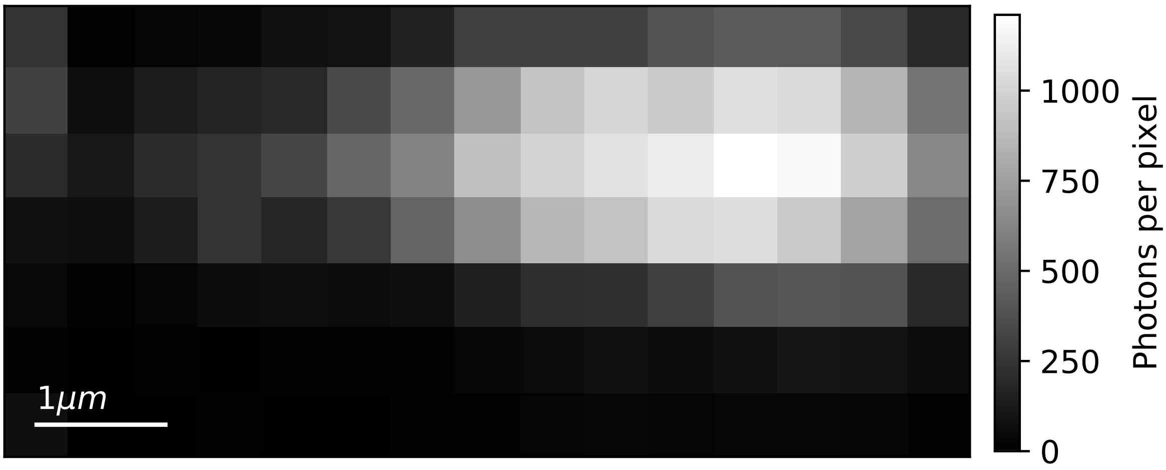

((a)) α channel (MKID)

((b)) β channel (MKID)

Figure 8.35: Intensity maps of photon counts found by NMF analysis performed on spectra created from a scan from the MKID microscope

There are strong similarities between these results from the NMF analysis and the χ^2 results shown in Figures 8.24 and 8.25, although it must be determined from context which fluorophore is which.

Figure 8.36 shows a cross section through Row 4 of both the χ^2 and NMF profiles. Knowledge of the sample suggests there should be green photons coming from the left half of the image (between 0.0 µm to 2.5 µm), and red from the right half (between 3.5 µm to 7.0 µm), with a mixture of the two at around 2.5 µm. The χ^2 analysis succeeds in this, showing very low α and high β values around 1.5 µm, and the opposite at 4 µm and beyond. The NMF analysis, however, mis-attributes 200 of the 900 photons at the 1.5 µm position, to being the Nile Red fluorophore. Indeed it consistently overestimates α. This is likely due to how the fact that the components used to perform the fitting against, are not good representations of the actual *reference spectra*. This would be greatly improved by using a far larger sample of spectra to obtain the components (this is a far smaller sample size than would ever be seen in any real application), using initial starting conditions based on prior knowledge, and generating many componnets (based on different starting coditions) and taking an average as elabourated on in Section 7.4.

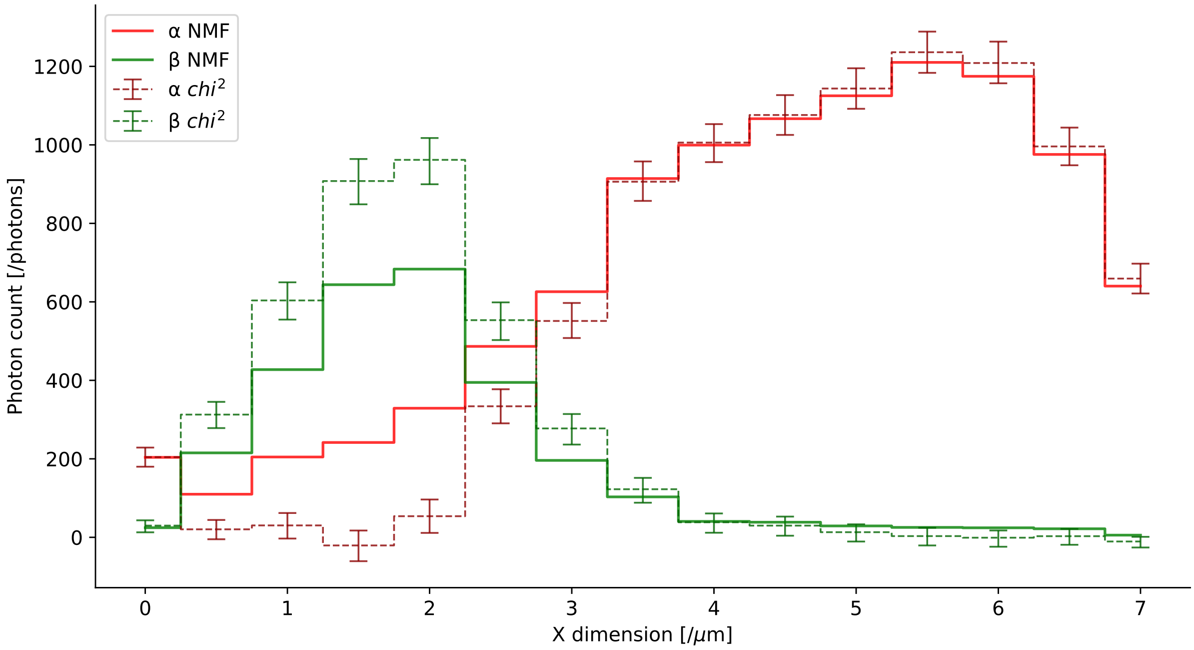

Figure 8.36: Comparison between NMF and χ^2 results, showing a section view of the profiles through the centre of the microspheres (5th row from the bottom). There is agreement between the two methods in identifying the Nile Red fluorophore, but NMF is not able to identify the Yellow-Green fluorophore, due to not identifying the components, an issue which will be improved by taking a larger image or running the NMF with different starting parameters and selecting the best spectra.

8.2.11 Imaging with Fewer Photons

The following test describes a method of determining how short the integration time can be, while still correctly identifying the fluorophore of a microsphere to within 5σ confidence interval.

Photons from known microsphere locations (see Figure 8.37), were combined into a single spectra, on which, χ^2 was performed. From the χ^2 analysis, the confidence can be determined by α/σ_α for the red microspheres, and similarly for the green microsphere.

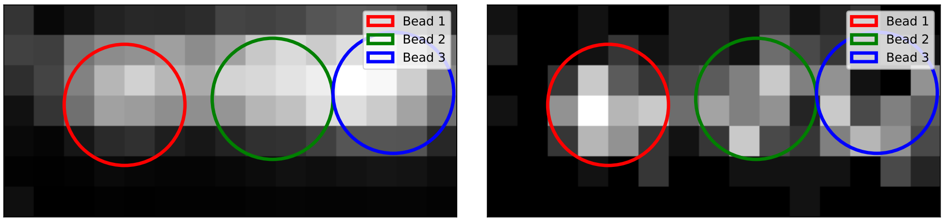

((a)) Full integration time (104s) ((b)) 0.63s integration time

Figure 8.37: Bead locations, overlaid onto an intensity maps showing two different integration times.

The analysis suggests that the microspheres are identified to better than 5σ, after an integration time of 0.63s. An integration time of 0.2s is required for a confidence of 3σ.

σ	**p-value**	**Bead 1**	**Bead 2**	**Bead 3**
5	3e-7	83	45	61
3	0.0027	32	24	24
2.807	**0.005**	27	23	21
2.576	**0.01**	22	22	19
1.96	**0.05**	21	16	18

Table 8.4: Table indicating how many photons are required, in order to identify the fluorophore to a given confidence level.

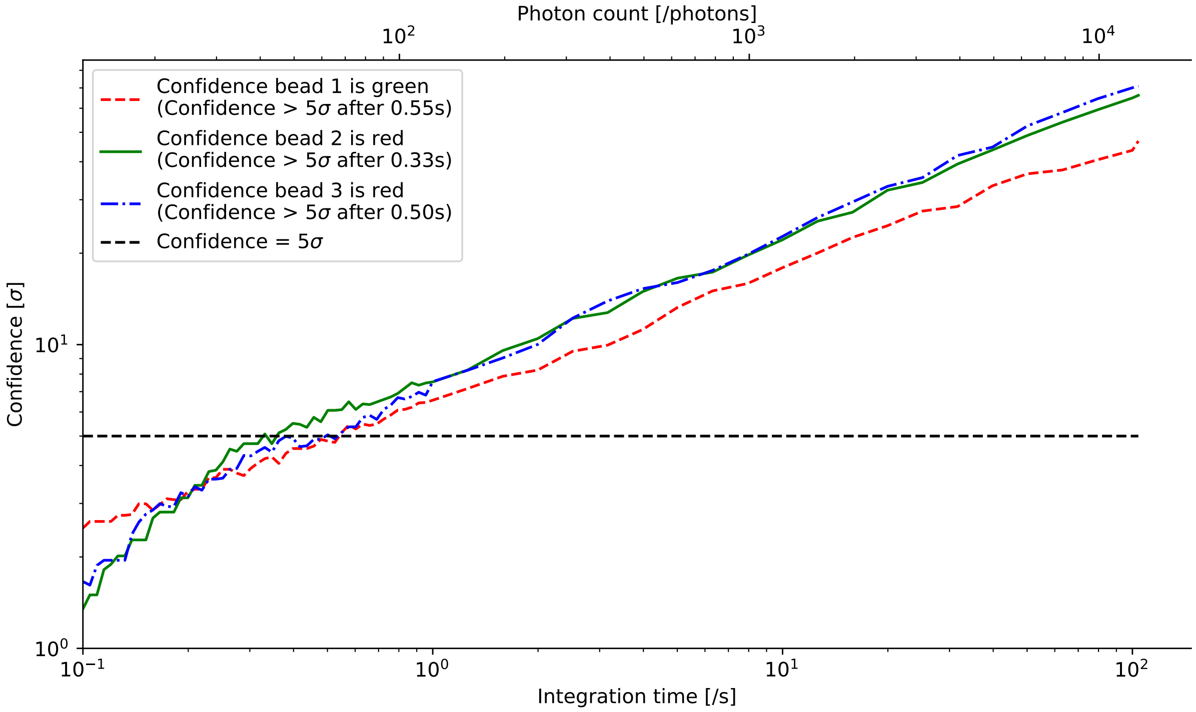

Figure 8.38: Plot of the confidence level that the microsphere has been correctly identified. At the photon fluxes experienced in the experiment, the plot suggests that the microspheres can be correctly identified to a high degree of certainty (5σ) after 0.63s. Similarly, the confidence level of microsphere 1 being red, stays below 0.6σ at all photon counts.

8.2.12 Discussion

Using an MKID as a detector on the confocal microscope, allows the **detection** and **identification** of three separate 2 µm microspheres. A confidence of 5σ, can be achieved in under 0.64 s corresponding to a photon count of between 45 and 83 for each microsphere.

8.3 Sample: *ex vivo* Nematode Worm with Red Microsphere

8.3.1 Aim

The aim of this study was to demonstrate that the MKID can be used as the detector in a confocal microscope system, to detect and identify fluorescent regions in an *ex vivo* application, making it the first bio-imaging application to do so. The result is verified by a commercial microscope system, the AiryScan microscope. The detector used, was manufactured by SRON. The image took 125 minutes for the single capture (not including the time required to collect the reference spectra) owing to the fact that the readout electronics at the time of recording took ≈ 50s per reading. The collection time will decrease drastically as more processes are moved to the onboard electronics and will eventually run in real time.

8.3.2 Description of the Sample

A number of red FluoSpheres™ inside of a worm labeled with GFP using a pulled glass needle, as shown in Figure 8.39. The sample was then viewed on an AiryScan microscope (producing the image shown in Figure 8.40) before a small area of which was scanned with the MKID-based system.

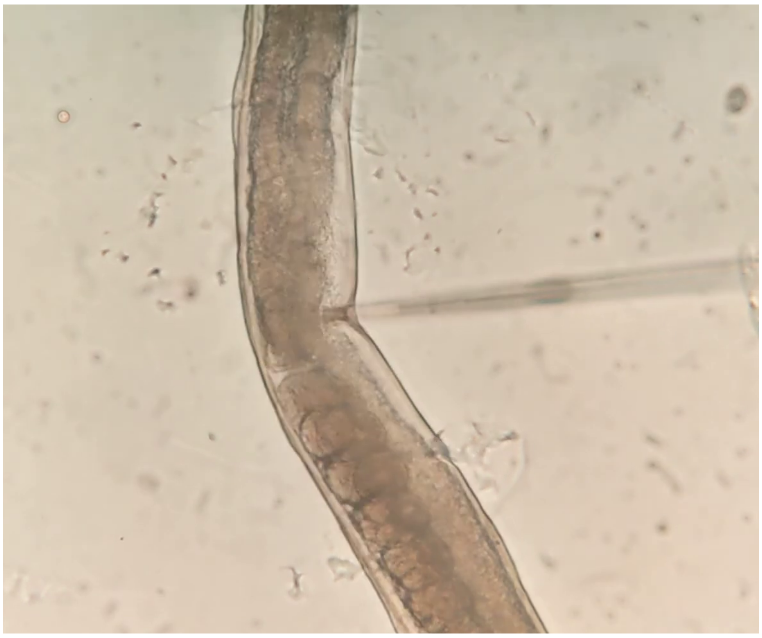

Figure 8.39: Wide field microscope image of red microspheres being injected into a green GFP stained worm using a pulled glass syringe.

The nematode worm used, was modified to have Green Fluorescent Protein (GFP) tags on the "nmy-2" gene (non-muscle myosin gene, see WormBase: Nematode Information Resource) , such that its cell cortex (cytoplasmic proteins on the inner side of the cell membrane) fluoresced green under UV light.

It was endogenously tagged, meaning that its genes are altered, so new cells which are produced by the worm, also fluoresce green.

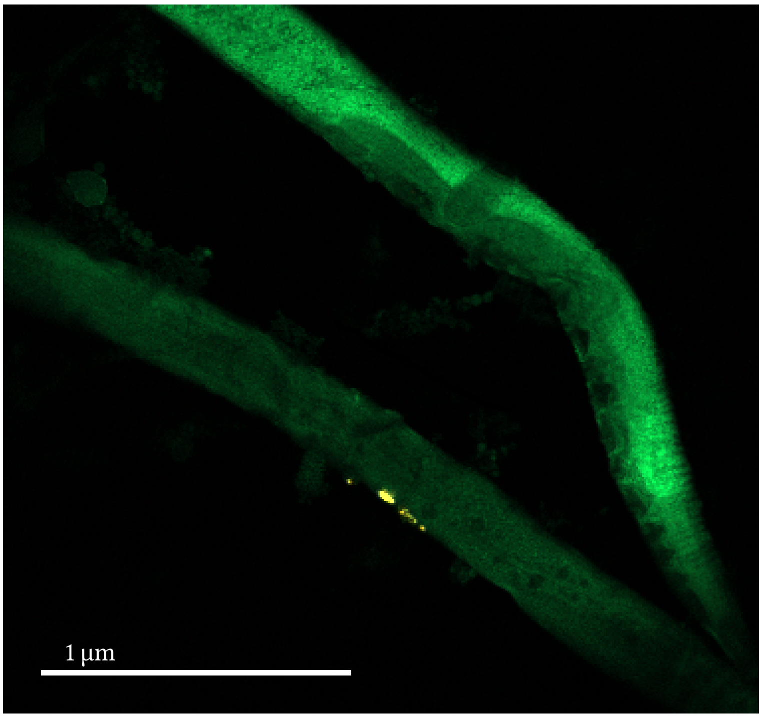

Figure 8.40: AiryScan microscope image of red microspheres (seen as yellow in the image) inside one of two worms labeled with GFP (shown in green)

8.3.3 Reference Image from Commercial Microscope

In order to obtain a reference image, and indeed to find the small microspheres in the relatively large worm, the more optimised and user-friendly, AiryScan microscope system was used to obtain a two channel image of the worm (Figure 8.40), and a region of this was identified for observation by the MKID microscope.

The AiryScan microscope performed two passes, one to obtain an intensity map of the Nile Red fluorophore (referred to herein as the red channel), and the other of the GFP (green channel). The red microspheres had a far greater density of fluorophores, so released orders of magnitude more light than was released by the fluorophores in the worm. This was compensated for by adjusting the excitation level of each channel to bring the different subjects into the desirable range for detection by the detector (laser settings in Table 8.5).

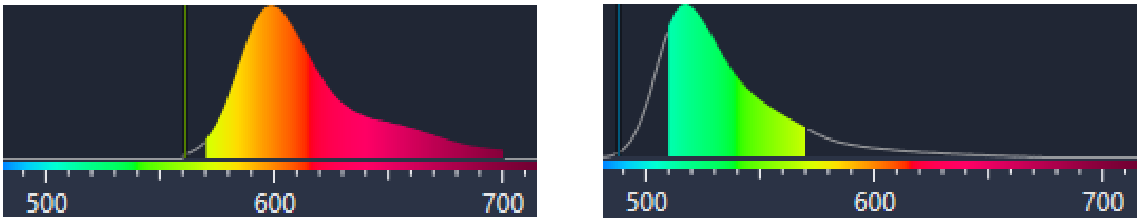

((a)) Red channel ((b)) Green channel

Figure 8.41: AiryScan microscope detection wavelengths (units in nm) for each channel, showing the emission curve from a data sheet, and the wavelengths captured by the detector in the scan. Note that the Nile Red fluorophore spectrum extends into the wavelength range detected by the green channel.

Because the tail of the red fluorophore spectrum extends into the green channel (see Figures 8.41, evidence of the red microsphere appears in the green channel. This is exacerbated by the fact that the red microspheres are many times brighter than the green worm. While post-processing techniques exist to quantify and minimise it, this is one of the limitations of the equipment.

Channel	**Fluorophore**	$\lambda_{\mathbf{EX}}$	**Laser Power**	**Exposure Time**	**Detection Wavelength**
Red	Nile Red	488 nm	0.2%	8.24 µs	575 nm to 700 nm
Green	GFP	488 nm	11.0%	8.24 µs	490 nm to 535 nm

Table 8.5: Table summarising the AiryScan microscope settings used during capture.

Figures 8.42(a) and 8.42(b) show the red and green channels respectively, with a bounding box describing the region scanned by the MKID microscope. The red microspheres is visible in both the red and green channels. Figure 8.42(c) is a schematic of a possible scene imaged by both systems; a collection of red microspheres distributed along the inside edge, of a wide green worm, and a non-fluorescing medium (in this case, a substance to paralyse the worm called Tetramisole) in the lower left corner.

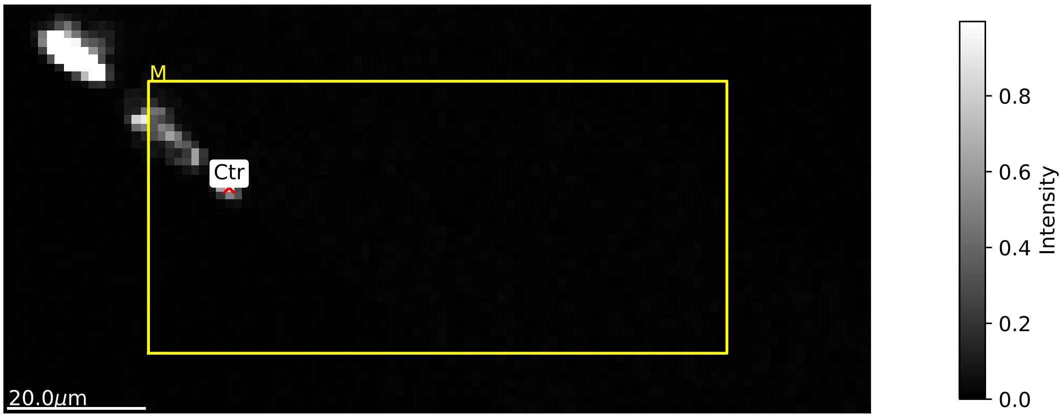

((a)) Red channel

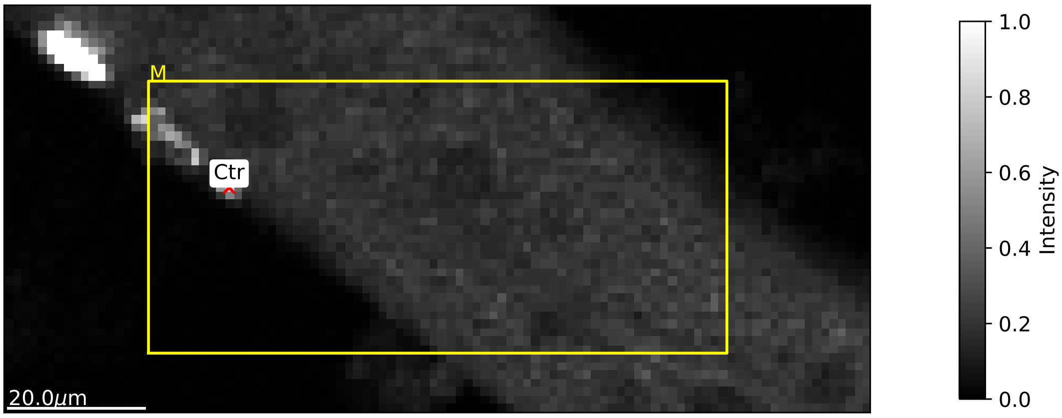

((b)) Green channel

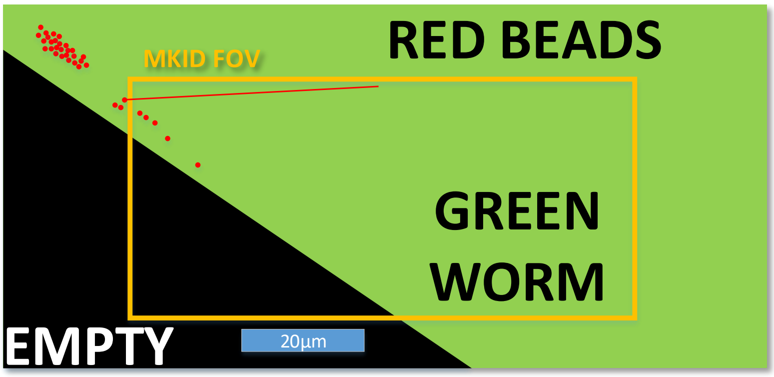

((c)) Schematic of what is likely being viewed by the AiryScan microscope. There is a worm labelled with green fluorophore, with many individual red FluoSpheres™ clumps, and an absence of fluorescent material in the bottom left corner. Many microspheres have clumped together in the top left of the image, with a single microsphere isolated on the bottom right of the collection of microspheres. The spheres are to scale, but microsphere positioning is likely different.

Figure 8.42: AiryScan microscope images and schematic.

8.3.4 χ^2 Analysis

8.3.4.1 Reference spectra

Each *reference spectra* was obtained by scanning an area of the worm, known to contain a high concentration of this fluorophore. Because the reference spectra was measured from a collection of microspheres which were inside the worm, the red spectrum will also include photons from the green fluorophore. In the absence of a better reference spectrum, the effect of this 'spectral contamination' is assumed to be negligible.

In this case, 79642 photons were captured to obtain a spectrum for the red fluorophore and 8762 photons were captured in the case of the green fluorophore. Both spectra are shown in Figure 8.43, normalised to have an under the urve of 1.

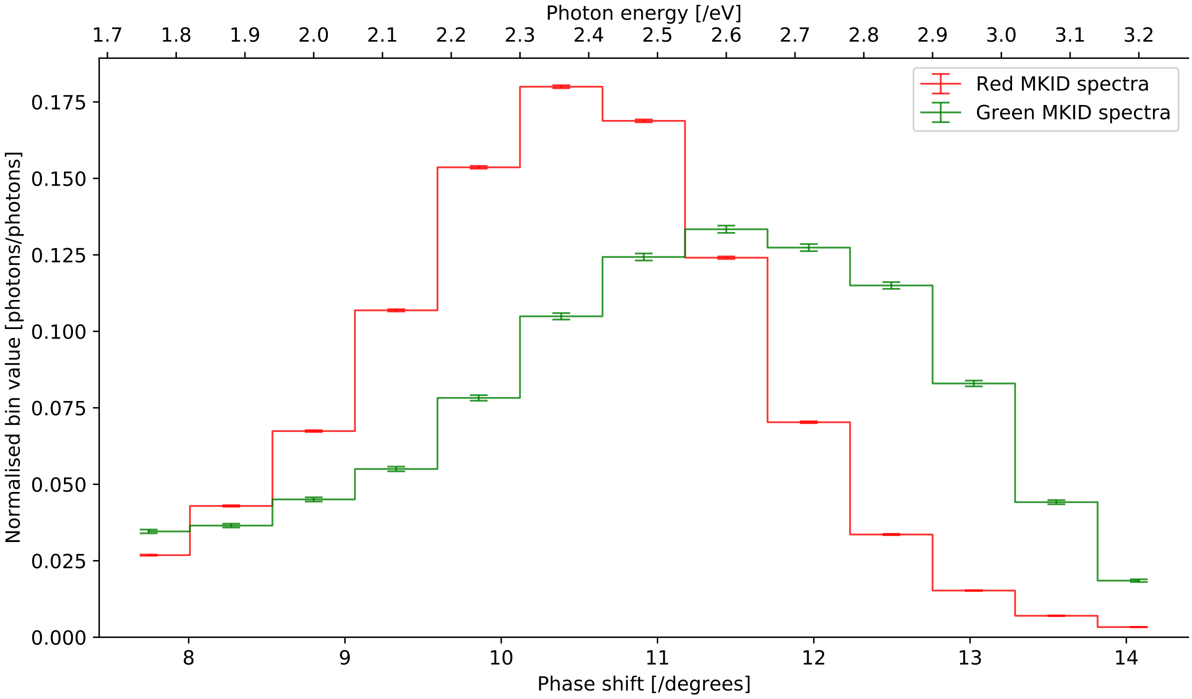

Figure 8.43: Spectra obtained from known fluorophores, in phase shift. Approximate Photon energy is displayed on the top axis.

Table 8.6 lists a few χ^2 results, describing their found α and β values. Figure 8.8 shows the full data set plotted with error bars (with the chosen points, highlighted). Because the fluorophores were not mixed, each spectrum should have either an α component and no β, or *vice versa*. Instead, the results indicate that spectrum with a large β component, overestimate the α component.

α	σ_α	α/σ_α	β	σ_β	β/σ_β	x_{INDEX}	y_{INDEX}
446	39	11	-34	25	-1	1	5
-12	26	0	151	33	5	16	0
29	16	2	24	16	2	4	5
14	6	2	-3	3	-1	4	1
195	28	7	-1	20	0	3	5
318	32	10	-32	18	-2	0	6
257	31	8	-21	21	-1	0	7
97	20	5	0	15	0	2	3
56	20	3	28	19	2	4	4
41	18	2	25	17	1	4	6
6	20	0	80	25	3	7	5
27	26	1	113	30	4	11	3
44	25	2	78	26	3	16	1
0	1	0	0	1	0	9	5
22	20	1	57	23	3	16	4
1	14	0	36	16	2	16	5
-1	12	0	25	14	2	16	6

Table 8.6: Table showing the results from curve_fit analysis, and how accurately the input values were recovered from the data (as a proportion of σ).

8.3.4.2 Analysis of Individual Points

Four examples have been selected for more detailed analysis, selected to have a range of α and β values. Figure 8.44 shows the points selected, and where they occur on the image.

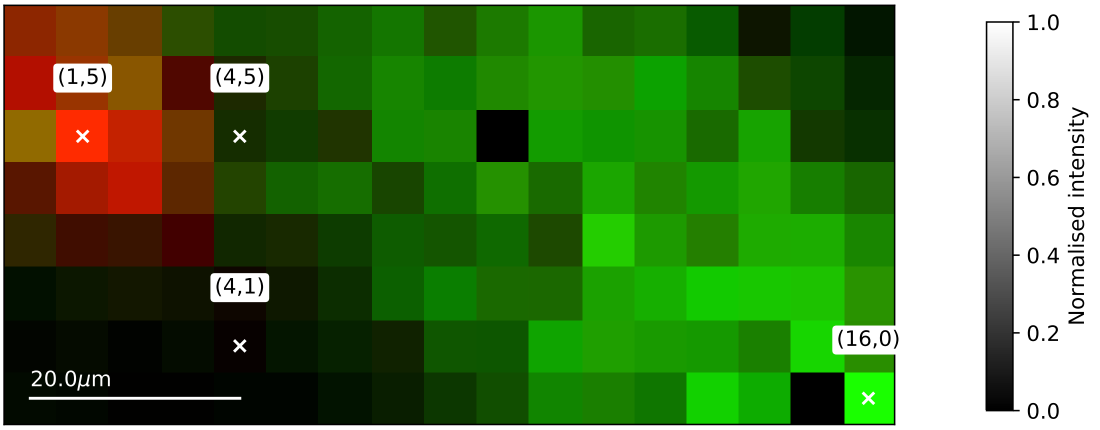

Figure 8.44: Locations of the scan points, described in the χ^2 analysis.

χ^2 Example with high α - The spectrum taken at point (1 5) produced the best fit at $\alpha = 446^{+39}_{-39}$ (11.5σ confidence) which is in line with where the fluorophores were located in the AiryScan microscope image. χ^2 analysis is presented in Figure 8.45 (description of panels, in Section 6.4. The reference image also indicated there would be some level of green fluorophore, but the value returned was very low, at $\beta = -34^{+27}_{-22}$. This is likely due to the fact that the red reference spectrum included photons from both sources.

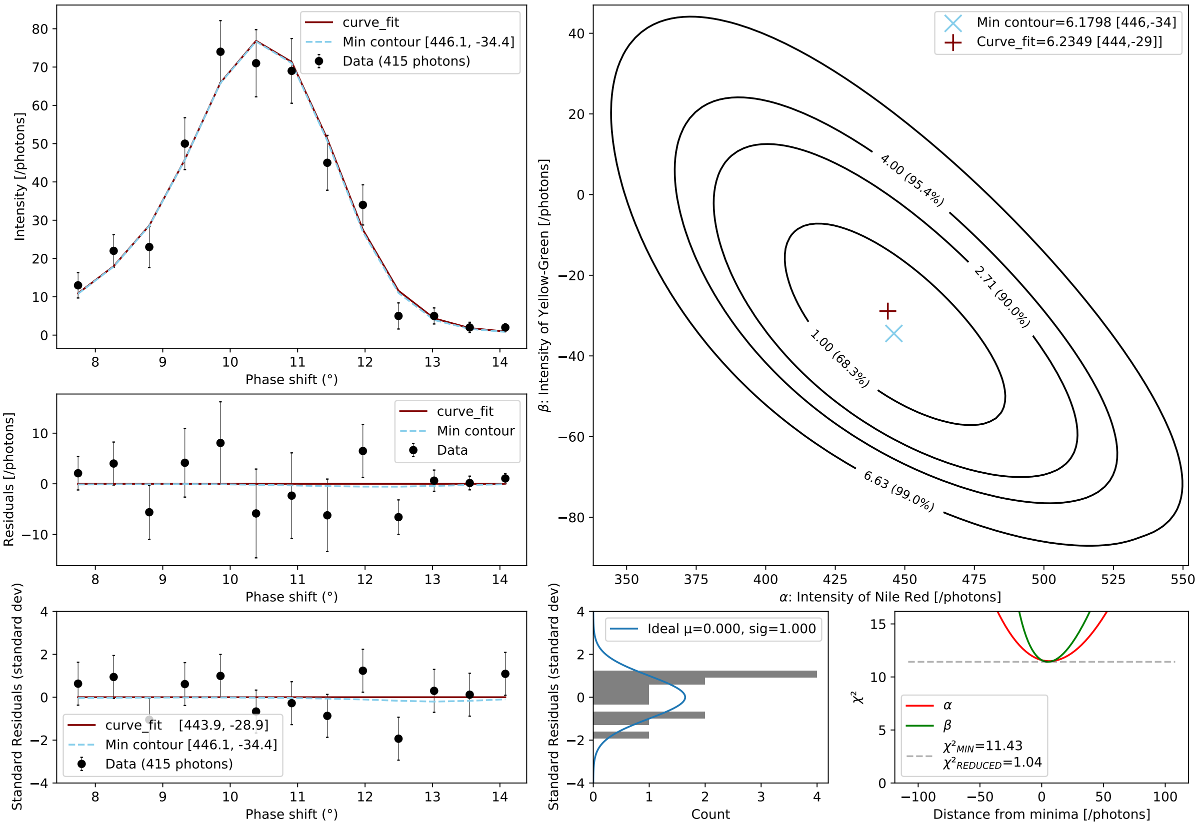

Figure 8.45: χ^2 analysis of the point containing the highest value for α

χ^2 Example with high β - The points acquired at location (16 0) had $\alpha = -12^{+26}_{-27}$, and $\beta = 151^{+34}_{-31}$ or a 4.4σ confidence as described in Figure 8.46. This agrees with what is expected based on the AiryScan microscope image indicating green fluorophore in the area where the sample was taken.

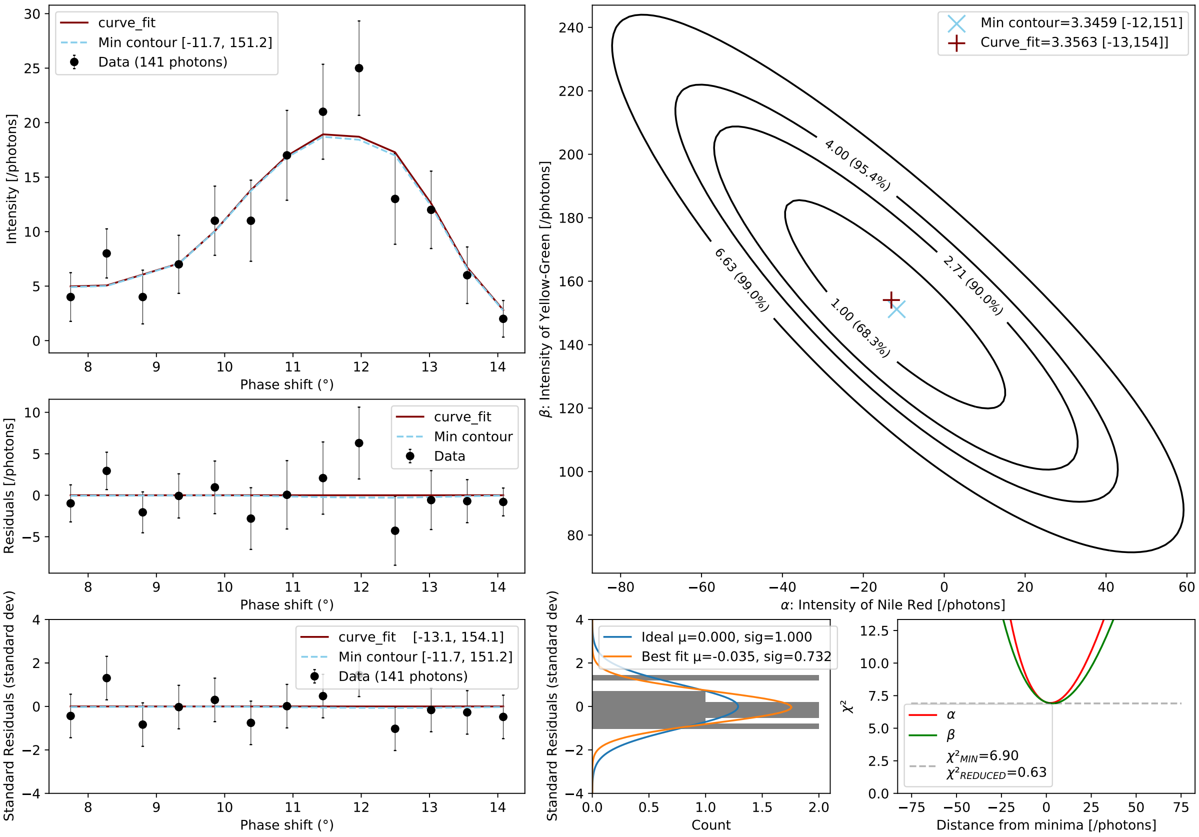

Figure 8.46: χ^2 analysis of the point containing the highest value for β

χ^2 Example with mix of α and β- The points acquired at location (4 5) had $\alpha = 29^{+16}_{-15}$ or a 1.8σ confidence, and $\beta = 24^{+17}_{-14}$ or a 1.5σ confidence as shown in Figure 8.47. This agrees with expectations, and measurements conducted by the AiryScan microscope.

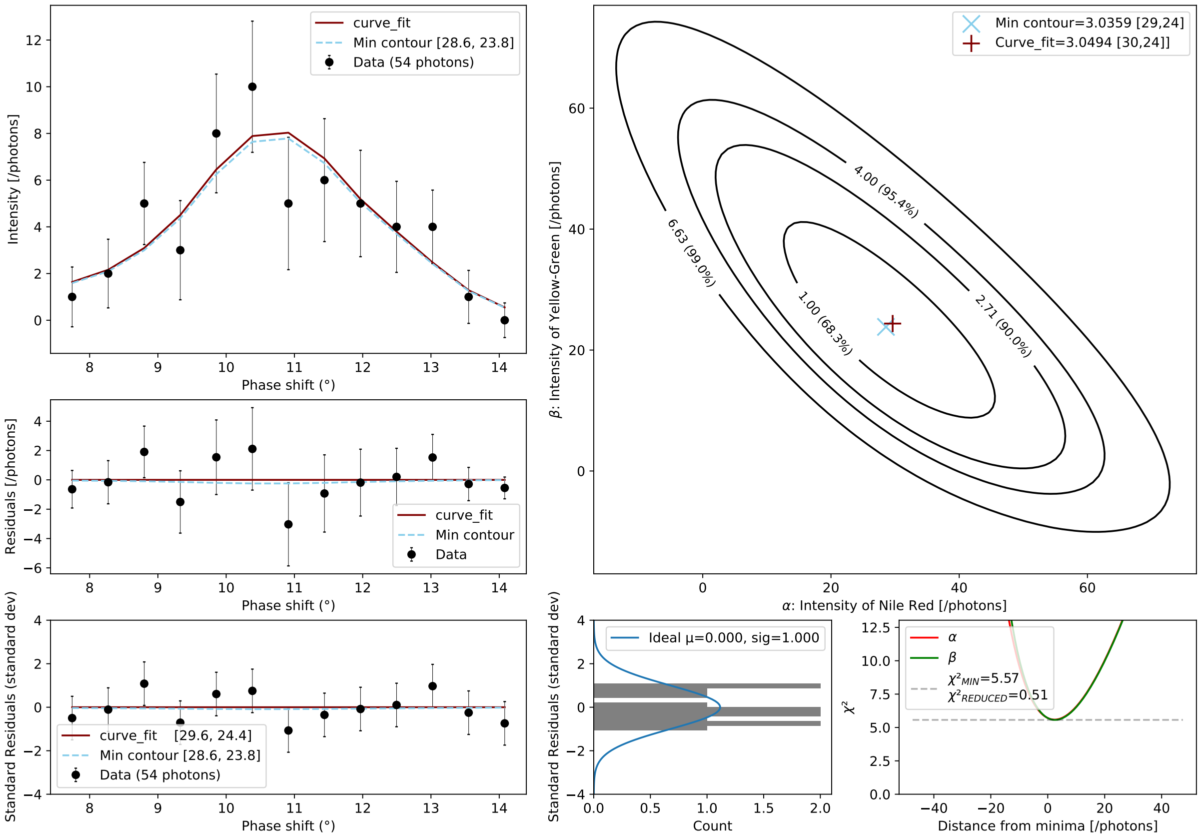

Figure 8.47: χ^2 analysis of the point containing similar values of α and β

χ^2 **Example with low values of α and β-** At location (4 1), the reference image indicated very little of each fluorophore, and this was confirmed by the found values of $\alpha = 14^{+6}_{-5}$ (2.6σ), and $\beta = -3^{+4}_{-2}$, analysis shown in Figure 8.48

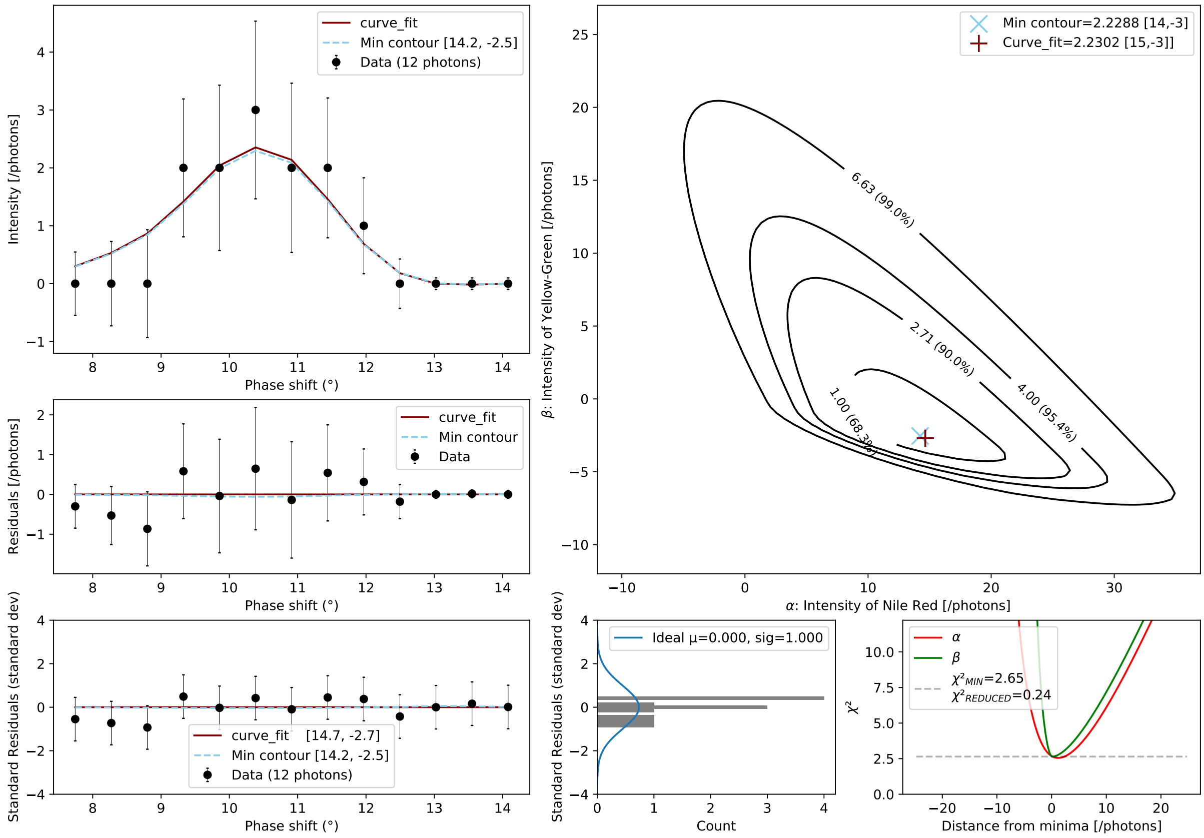

Figure 8.48: χ^2 analysis of the point containing low values of α and β

8.3.5 Blind Spectral Analysis (NMF)

NMF analysis was performed assuming two components, using as inputs, the spectra obtained at each location in the image (see Figure 8.49). The components found (shown in Figure 8.50), serve as the reference spectra against which all spectra analysed to find α and β.

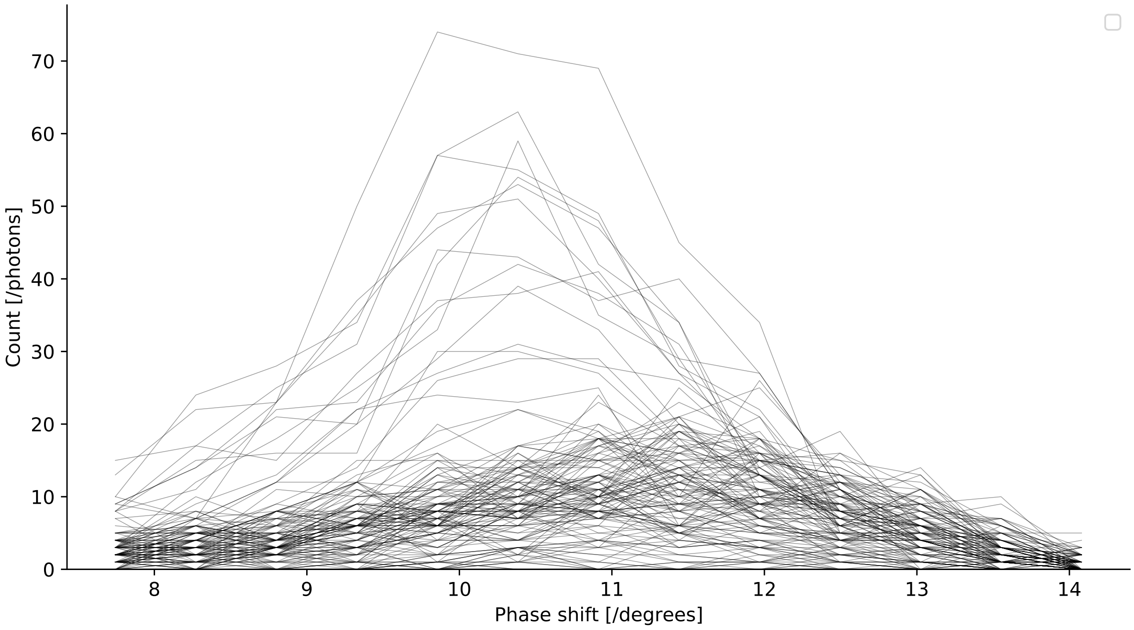

Figure 8.49: Spectra present in actual scan

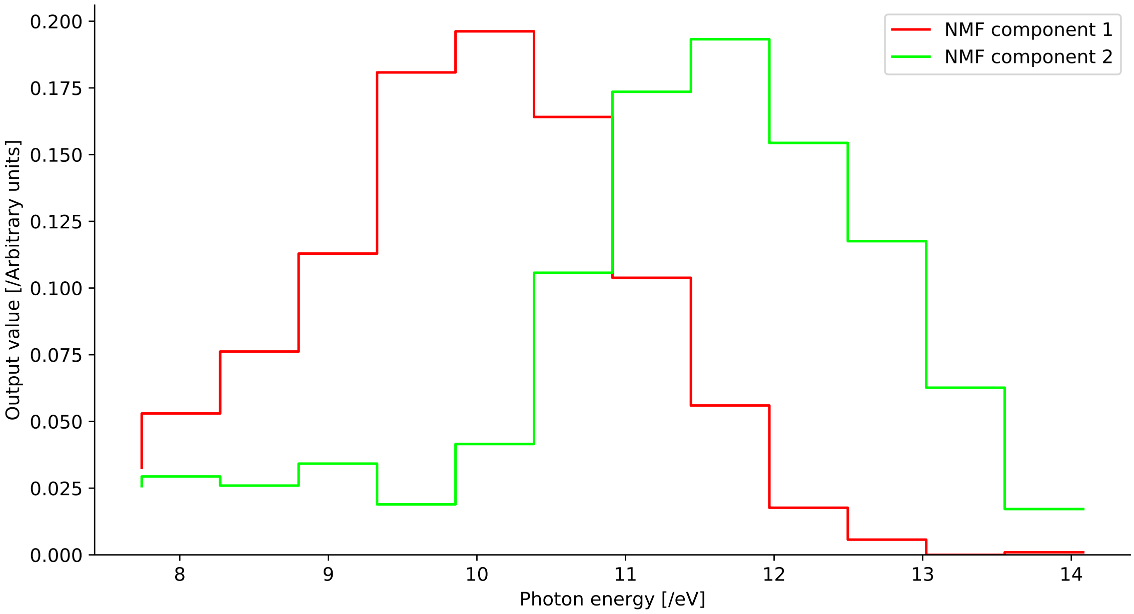

Figure 8.50: Reference spectra obtained by NMF analysis

The α and β values found from each spectrum, are shown in Figures 8.51(a) and 8.51(b) and suggest a very similar distribution to the fluorophores as is indicated by the χ^2 analysis.

((a)) MKID image of red microsphere in green worm, α channel. The high readings of α, indicate a large number of photons coming from a spectrum similar to the red *reference spectrum*, corresponding to the expected location of the red microsphere.

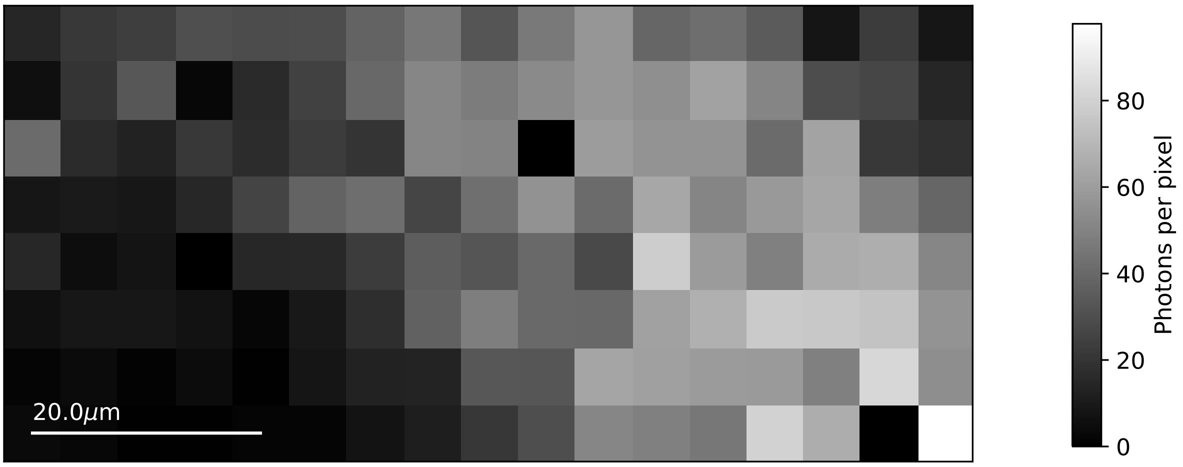

((b)) MKID image of red microsphere in green worm, β channel. The high readings of β, indicate that more photons originate from a source which is spectrally similar to the green *reference spectrum.* Higher β values occur at the locations where the worm is expected to be based on the results from the AiryScan microscope.

Figure 8.51: Results from NMF analysis performed on the worm scanned with the MKID microscope.

8.3.5.1 Comparing NMF Results to Commercial Microscope

The AiryScan microscope images are compared side by side with the NMF results, in the Figures 8.52 (a-d), and show microspheres in the α (red) channel, and worm in the β (green) channel as expected, as well as microsphere in the green channel for reasons already described.

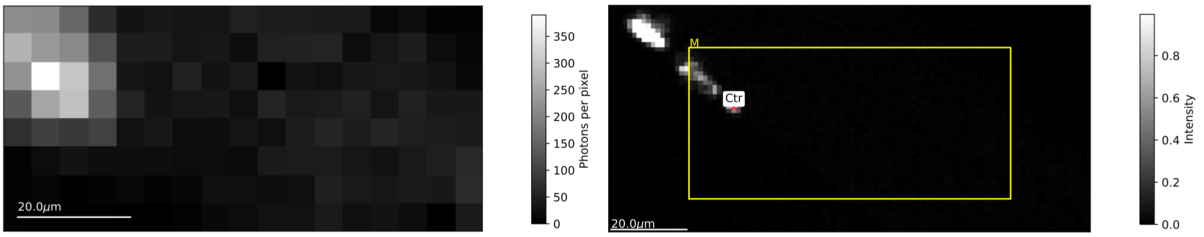

((a)) MKID image, α_{NMF} channel ((b)) AiryScan microscope image, α channel

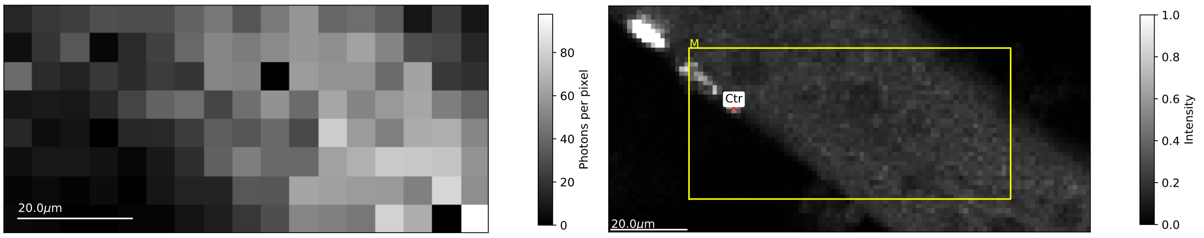

((c)) MKID image, β_{NMF} channel ((d)) AiryScan microscope image, β channel

Figure 8.52: NMF analysis compared to AiryScan microscope

A cross section through each intensity profile at the locations shown in 8.53, to give the intensity profiles, is presented in Figure 8.54. Both the AiryScan microscope and MKID intensity profile cross sections, show a red microsphere, however it is better spatially resolved in the AiryScan microscope with a FWHM=2.29 µm, whereas the MKID scan has a FWHM=14.63 µm.

The larger FWHM is a result of the microsphere not being in focus, due to difficulties aligning the system in the Z axis. Locating the sample in the X,Y dimension was possible using the epi-illuminated viewing scope, however optical distortions caused by the worm meant that it was not possible to use the wide field microscope to achieve Z-focus. With each scan taking multiple hours and causing photo bleaching of the fluorophores within the sample, as well as the system drifting slightly in X,Y and Z over time, it was not possible to achieve optimal focus in Z within the time frame given. Nevertheless there is good similarity between both samples, and agreement between the location and identity of the features.

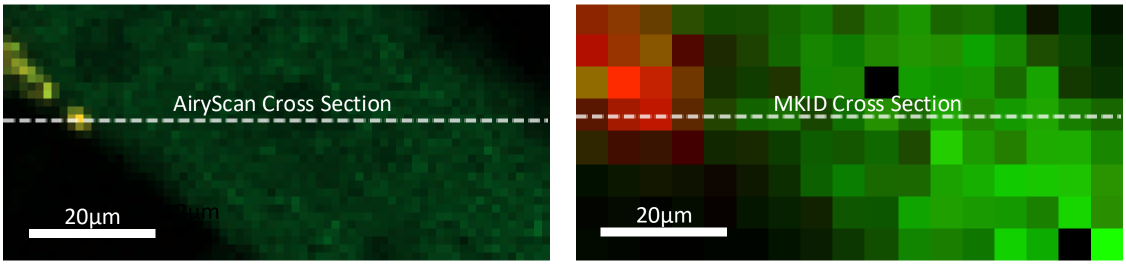

Figure 8.53: Location of the cross section, in each image.

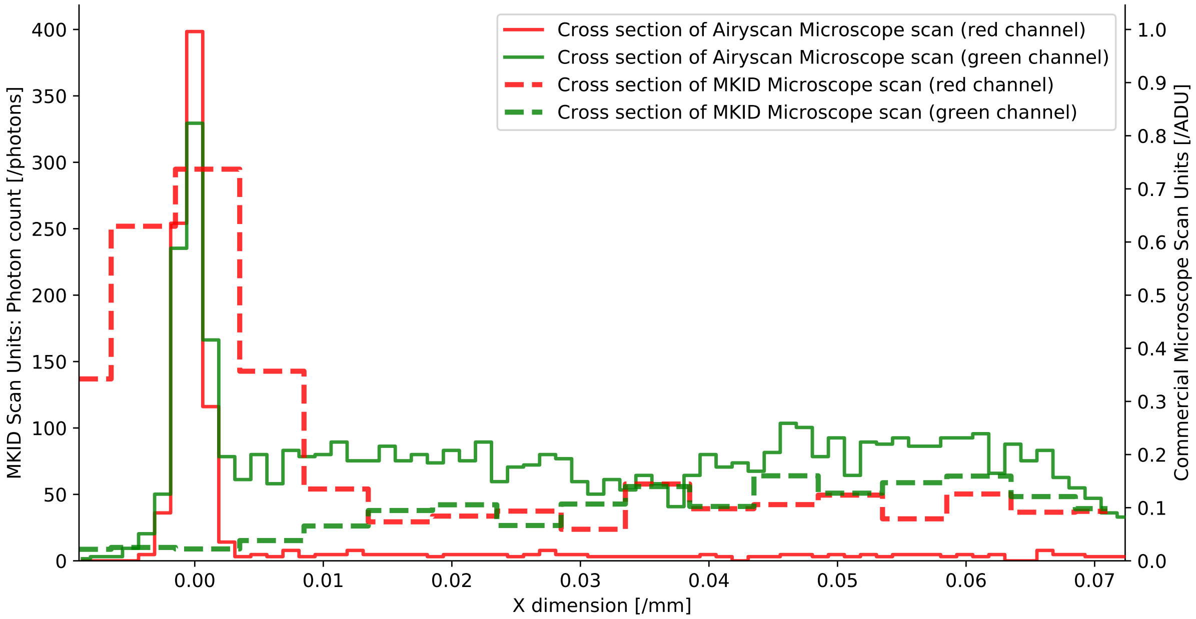

Figure 8.54: Intensity profile of a cross section through the microsphere

The intensity profile through the microsphere of the AiryScan microscope, clearly shows that the red microsphere features in the red channel of each scan. The FOV of the AiryScan microscope extends further than the MKID scan, so also shows the contrast between the worm and background, in the green channel.

8.3.6 Imaging with Fewer Photons

All photons from a given area (shown circled in Figures 8.55 *a* and *b*) were summed to make a single spectrum, which was then analysed to find α and β values, and confidence intervals. Because each photon is time-stamped, the integration time (or duration over which the photons are recorded) could be adjusted, to understand the effect of exposure time vs confidence. The result of this is shown in Figure 8.56 and suggests that it took 0.25s to identify the red fluorophore to 5σ confidence, but as long as 3.16s (corresponding to between 24 and 399 photons) to positively identify the green fluorophores. For reference, photon fluxes were around 95 to 130 photons per second.

In practice, the time taken to identify photons, can be decreased by increasing the illumination level to the point where the detector is receiving its maximum allowable count-rate (in the case of this detector, $\approx$ 500 photons/s. Table 8.7 puts the required exposure time into context of the number of photons required, at a given confidence level.

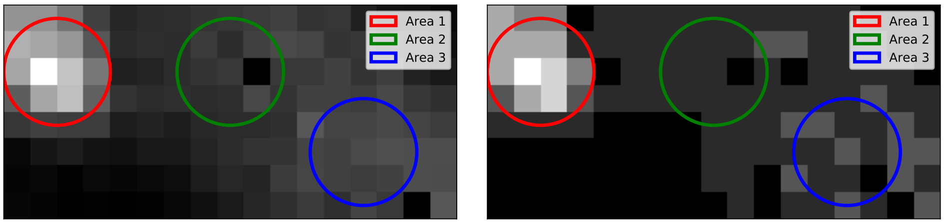

((a)) Full integration time (104s)

((b)) 0.63s integration time

Figure 8.55: Bead locations, overlaid onto an intensity maps showing two different integration times.

σ	**p-value**	**Red (Area 1)**	**Green (Area 2)**	**Green (Area 3)**
5	3e-7	93	399	224
3	0.0027	34	158	62
2.807	**0.005**	33	158	62
2.576	**0.01**	33	116	36
1.96	**0.05**	33	49	29

Table 8.7: Table indicating how many photons are required, in order to identify the fluorophore to a given confidence level. Between 93 and 399 photons were required to determine the fluorophore present to 5σ

The values in this table describe how many photons from a single microsphere, would need to be collected before it could be positively identified. The values were determined by calculating the confidence at many integration times, until the confidence exceeded the specified σ. This was subject to noise, especially at lower exposure times, so these numbers are indicative.

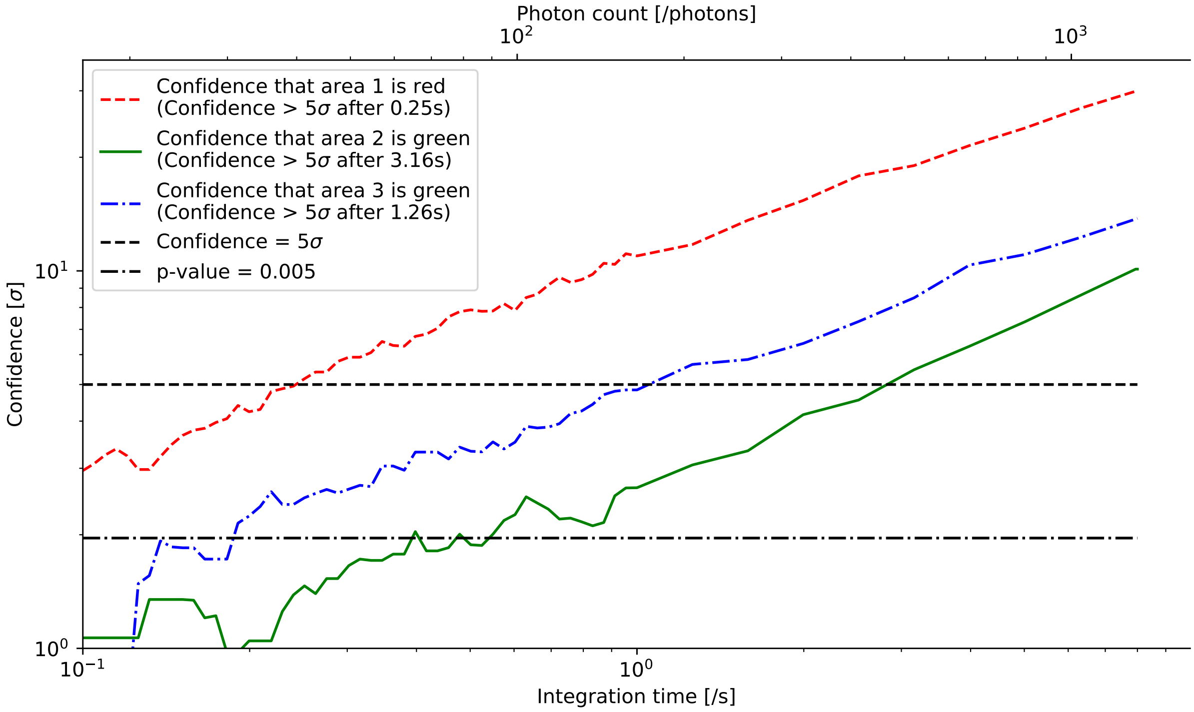

Figure 8.56: Plot of the confidence level that the worm and microsphere has been correctly identified. At the photon fluxes experienced in the experiment, the plot suggests that the microspheres can be correctly identified to a high degree of certainty (5σ) after 3.16s. Confidence levels that the objects are *incorrectly* identified, remains around 0, irrespective of integration time.

8.3.7 Discussion

Using an MKID microscope was able to **detect** and **identify** fluorophores from both the microsphere, and the *ex vivo* biological sample. While the features in the MKID are not in focus, the results largely agree with measurements taken with an AiryScan microscope. A confidence of 5σ, can be achieved using between 93 and than 399 photons depending on the fluorophore.

8.4 Summary

A single MKID as a detector with $R \approx 10$ can be used to sequentially scan a sample, to **detect** and **identify** spectrally separated fluorophores to a high degree of confidence, by using tens to hundreds of photons. Because these detectors can be easily multiplexed into large arrays, spectra can be gathered from many points across a sample simultaneously by re-imaging the sample onto the array using optics. The sample can be epi-illuminated, or more interestingly a thin plane, orthogonal to the direction of imaging can be illuminated using the process of light-sheet microscopy (LSM).

Chapter 9

Summary and Conclusion

The research presented in this thesis demonstrated the potential for **M**icrowave **K**inetic **I**nductance **D**etectors (MKIDs) to be used as a detector in a laser confocal fluorescence microscope. This is believed to be a significant advancement in the field of biomedical photonics, and the first implementation of these devices, there being no similar reports in the published literature. The research focused on exploiting the energy sensitive, noise-free, single photon counting abilities of the MKID to successfully distinguish between fluorescent dyes.

9.1 The Experiment

Samples, each containing one of two fluorescent dyes, were simulated, analysed, then experimentally observed by point-scanning using a purpose-built laser confocal microscope that employed an MKID as a fibre spectrometer (Chapter 4.3). The samples selected were 2 µm diameter microspheres, containing either a Nile Red fluorophore or Yellow-Green fluorophore dye. Excitation of these microspheres within the target sample was performed by a 450 nm laser diode. The emission was filtered using dichroics and long pass filters before they reached an optical fibre. The optical fibre relayed the light into a cryostat and flood-illuminated an MKID device (Chapter 2), enabling a single detector to detect and quantify the energy of each individual photon. The MKID device used in the experiment, and assumed in simulations, had a spectral sensitivity of R=10 at 400nm (Sections 6 and 8.1.4). A USB spectrometer was utilised to provide a reference scan, which served to verify the results.

9.2 Analysis and Results

Six analytical methods were proposed, verified and compared through a sequence of simulations. These looked firstly at analysing a single spectra, then at a simulated 'image' that consisted of many pixels, some of which contained a mixture of the two fluorophores.

The simplest classification, which involved categorising a given spectrum as being from either Nile Red fluorophore (α) or Yellow-Green fluorophore (β), used a Kolmogorov–Smirnov test (KS test) that produces a binomial result (Section 6.5.1). By way of illustration, this method succeeded in correctly identifying 95.85% of 1000 fluorophores when given only 4 photons at each test/setup/experiment. The small number of required photons is likely to be far higher when comparing fluorophores which are less spectrally separated or have a broader emission spectrum. While promising, there may prove to be little practical use for this approach beyond potentially providing a fast analysis in a graphical user interface.

In locations on the sample where the spectrum was a mixture of two known fluorophores (i.e. *reference spectra*), three approaches were considered. Firstly, a KS test against various ratios of the two *reference spectra* was found to provide a very coarse fit and, while it gave an indication of the correct ratio, it scored far lower than alternative methods on the comparison metric (MSE, see Section 7.2). The χ^2 and *scipy.curve_fit* tests both relied on least-mean-squared fitting and so produced similar results. However interestingly the χ^2 test performed marginally better when higher photon counts were present, *scipy.curve_fit* was slightly more effective at lower photon counts. Whether this result was significant, requires further investigation.

It was possible to determine to a high confidence (5σ) which fluorophore a microsphere contained, with as few as 43 to 84 photons, owing in part to the absence of readout noise (no false counts) afforded by this particular quantum detector.

Blind spectral un-mixing methods allowed analysis of samples for which the spectra of the fluorophores present was unknown. Analyses determined that non-negative matrix factorisation (NMF) had a similar effectiveness to analytical methods in which the spectra of the fluorophores present was known in advance. NMF was applied to the *ex vivo* sample of a nematode worm (see Chapter 8.3) to successfully obtain an image that closely resembled a reference image taken by a commercial laser scanning confocal microscope, validating the results produced by the MKID microscope.

This research project has confirmed that MKIDs are a useful and reliable tool for detecting and identifying fluorophores within a biological sample. These findings present a particularly exciting prospect for future biological studies given that they are a broadband detector capable of identifying photons in the near-infrared (NIR), allowing illumination by light sources which cause lower levels of phototoxicity, and can image deeper into biological tissue (see Section 3.1.3.1).

9.3 Instrument Limitations Going Forward

MKID Microscope systems of the future will have improved optical efficiency, imaging speeds and spectral resolution compared to the system used.

The current system, while fit for purpose, only used <1% of the emission photons from the sample, owing to factors such as the choice of Microscope Objective, the presence of a permanent beam splitter to couple the wide-field imaging system, and the crude optical coupling of the fibre to the detector. These aspects can be optimised to specific applications and detectors to greatly improve efficiency. For example, simply using a microscope objective with a higher NA (which would be more expensive than the one used) and focusing the light from the fibre directly onto a detector, would see a large increase in performance.

Improving readout electronics (higher sampling frequency and lower phase noise) combined with advancing detector design (using methods such as phonon trapping) will allow a photon to be determined to a given spectral resolution but with a shorter decay time (tuned at the MKID design stage), allowing each detector to process a higher photon flux.

The main advantage with MKID based system will likely prove to be its highly efficient use of photons, and absence of false photon counts rather than improved imaging speeds. This is set to be achieved at a lower cost-per-pixel than comparable detectors because many MKIDs can be multiplexed and read out by the same readout electronics (Section 2.2.2).

9.4 Next Steps

This study, while successful, did not fully explore all of the attributes and capabilities of the MKID detector, highlighting that there is far more potential for this technology. The next steps would aim to capitalise on the remaining attributes.

Looking to the future, the analytical tools developed during this research project could potentially be used to analyse how effectively three or more fluorophores could be differentiated, especially with respect to the spectral resolution (R) value of the detector used. Better understanding the interdependence between R, and the ability to spectrally unmix subtly different component spectra, would assist in prioritising the attributes of the detector arrays being developed by research groups producing MKIDs, and offer guidance to their further development.

Developmental MKID arrays have recently been produced and received from SRON, allowing spectra to be taken from many positions across a sample simultaneously, and in a fraction of the time required to perform sequential measurements. It is proposed that a logical next step would be to lens-couple this detector to the microscope and perform wide-field measurements (a facility that was planned into the design of the microscope from the outset). In order to achieve a narrow depth-of-field (excluding the out-of-plane contributions), the sample could be optically sectioned using a thin plane of light normal to the direction of imaging selective/single plane illumination microscopy (SPIM) (Bourgenot et al., 2013) by adopting systems such as *Snouty* (Millett-Sikking and York, 2019).

The ideal applications for MKIDs would leverage their high effective frame-rate, at a photon flux which does not cause 'pile-up' (a state where the next photon arrives, before the quasiparticles have recombined, and individual photons become more difficult to resolve). These could include a photon-starved application that benefits from noise-free photon acquisition capability, their ability to observe NIR, and also investigations that could exploit their potential to be multiplexed into large arrays. One such application identified could involve observing neurons labelled with genetically encoded, near-infrared voltage indicators, a technique that Adam et al. (2019) developed at the Cohen Lab, Harvard. Dentrites of neurons, described by Park et al. (2023), took 2.5 ms to propagate an electrical signal 230 mm and were observed at a temporal resolution of 1 ms (compared to 1 µs, effective, with MKID). Observing the low number of photons emitted from the dendrite as the signal propagates rapidly though it, could be done very well with an MKID array.

Quantum dots are a bright, photostable alternative to traditional fluorescent dyes, and have an emission spectra that is tunable in the manufacture process (Pandey and Bodas, 2020; Smith et al., 2008). Given that these quantum dots can be excited by a common wavelength of laser light, they are the perfect candidates for imaging with the microscope herein developed. This is because multiple species can be placed into one sample and functionalised to different features within it (Karakoti et al., 2015), and the spectral information derived/emitted from them can be used to differentiate between regions.

The author holds out great hope for the many applications that will be made possible by this quantum detector. One example in particular is the potential for colour imaging the bioluminesence of human skin to detect subtle changes in luminescence which give insights into the metabolism across a subject (Kobayashi et al., 2009).

9.5 Final Remarks

In conclusion, the research project described in this thesis has provided a robust proof of concept, confirming that MKIDs are a viable detector, full of potential for adoption by microscope application requiring ultra-sensitive hyperspectral imaging. It is confidently asserted that, while there is still work to be done improving and refining the technology, MKIDs have the capacity to play a major role in the future development of next generation confocal and wide field microscopes.

Bibliography

Y. Adam, J. J. Kim, S. Lou, Y. Zhao, M. E. Xie, D. Brinks, H. Wu, M. A. Mostajo-Radji, S. Kheifets, V. Parot, S. Chettih, K. J. Williams, B. Gmeiner, S. L. Farhi, L. Madisen, E. K. Buchanan, I. Kinsella, D. Zhou, L. Paninski, C. D. Harvey, H. Zeng, P. Arlotta, R. E. Campbell, and A. E. Cohen. Voltage imaging and optogenetics reveal behaviour-dependent changes in hippocampal dynamics. *Nature*, 569(7756): 413–417, May 2019. ISSN 1476-4687. doi: 10.1038/s41586-019-1166-7. URL `http://dx.doi.org/10.1038/s41586-019-1166-7`.

H. Aguinis, M. Vassar, and C. Wayant. On reporting and interpreting statistical significance and p values in medical research. *BMJ Evidence-Based Medicine*, 26(2):39–42, 2021. ISSN 2515-446X. doi: 10.1136/bmjebm-2019-111264. URL `https://ebm.bmj.com/content/26/2/39`.

C. Albrecht. Joseph r. lakowicz: Principles of fluorescence spectroscopy, 3rd edition. *Analytical and Bioanalytical Chemistry*, 390(5):1223–1224, Mar 2008. ISSN 1618-2650. doi: 10.1007/s00216-007-1822-x. URL `https://doi.org/10.1007/s00216-007-1822-x`.

E. Baldwin, M. De Lucia, C. Bracken, G. Ulbricht, O. Creaner, J. Piercy, and T. Ray. Frequency Domain Multiplexing for Microwave Kinetic Inductance Detectors: Comparing the Xilinx ZCU111 RFSoC with the New 2x2 RFSoC Board. *Journal of Low Temperature Physics*, 209(3):640–648, 2022. ISSN 15737357. doi: 10.1007/s10909-022-02785-x. URL `https://doi.org/10.1007/s10909-022-02785-x`.

J. Bardeen, L. N. Cooper, and J. R. Schrieffer. Theory of superconductivity. *Physical Review*, 108(5): 1175–1204, Dec. 1957. doi: 10.1103/PhysRev.108.1175. URL `https://link.aps.org/doi/10.1103/PhysRev.108.1175`.

J. Bartlett, G. Hardy, M. Whillock, M. Hailey, P. Coker, C. Theobald, I. Hepburn, and A. Smith. The first millikelvin cryocooler (mkcc): Design and performance. *Cryogenics*, 128:103592, 2022. ISSN 0011-2275. doi: https://doi.org/10.1016/j.cryogenics.2022.103592. URL `https://www.sciencedirect.com/science/article/pii/S0011227522001746`.

C. Bockstiegel. *The MKID Camera for PICTURE-C and Photon Counting Stochastic Speckle Discrimination.* PhD thesis, UCSB, 2019.

C. Bourgenot, J. M. Taylor, C. D. Saunter, J. M. Girkin, and G. D. Love. Ao modal optimization in a live, beating zebrafish heart. In *Imaging and Applied Optics Postdeadline*, AOPT. OSA, 2013. doi: 10.1364/aopt.2013.ow4a.4. URL `http://dx.doi.org/10.1364/aopt.2013.ow4a.4`.

C. Bruschini, H. Homulle, I. M. Antolovic, S. Burri, and E. Charbon. Single-photon avalanche diode imagers in biophotonics: review and outlook. *Light: Science and Applications*, 8, 2019. ISSN 20477538. doi: 10.1038/s41377-019-0191-5. URL `http://dx.doi.org/10.1038/s41377-019-0191-5`.

V. Buschmann, E. Ermilov, F. Koberling, M. Loidolt-Krüger, J. Breitlow, H. Kooiman, J. W. N. Los, J. van Willigen, M. Caldarola, A. Fognini, M. U. Castaneda, J. de Wild, B. Vermang, G. Brammertz, and R. Erdmann. Integration of a superconducting nanowire single-photon detector into a confocal microscope for time-resolved photoluminescence (TRPL)-mapping: Sensitivity and time resolution. *Rev. Sci. Instrum.*, 94(3):033703, Mar. 2023.

F. W. Carter, T. S. Khaire, V. Novosad, and C. L. Chang. scraps: An open-source python-based analysis package for analyzing and plotting superconducting resonator data. *IEEE Transactions on Applied Superconductivity*, 27(4):1–5, June 2017. ISSN 1051-8223. doi: 10.1109/TASC.2016.2625767.

R. Casini and P. G. Nelson. On the intensity distribution function of blazed reflective diffraction gratings. *J. Opt. Soc. Am. A*, 31(10):2179–2184, Oct 2014. doi: 10.1364/JOSAA.31.002179. URL `https://opg.optica.org/josaa/abstract.cfm?URI=josaa-31-10-2179`.

J. Colas, M. Calvo, J. Goupy, A. Monfardini, M. De Jesus, J. Billard, A. Juillard, and L. Vagneron. Improvement of contact-less kid design using multilayered al/ti material for resonator. *Journal of Low Temperature Physics*, 211(5):281–288, Jun 2023. ISSN 1573-7357. doi: 10.1007/s10909-023-02976-0. URL `https://doi.org/10.1007/s10909-023-02976-0`.

P. J. de Visser, S. A. H. de Rooij, V. Murugesan, D. J. Thoen, and J. J. A. Baselmans. Phonon-trapping-enhanced energy resolution in superconducting single-photon detectors. *Phys. Rev. Applied 16, 034051*, 16:034051, 2021. doi: 10.1103/PhysRevApplied.16.034051. URL `https://ui.adsabs.harvard.edu/abs/2021PhRvP..16c4051D`. ADS Bibcode: 2021PhRvP..16c4051D.

R. Dodkins. *Development of MKID Instrumentation for exoplanet direct imaging*. PhD thesis, University of Oxford, 2018.

U. Fano. Ionization yield of radiations. ii. the fluctuations of the number of ions. *Phys. Rev.*, 72:26–29, Jul 1947. doi: 10.1103/PhysRev.72.26. URL `https://link.aps.org/doi/10.1103/PhysRev.72.26`.

R. A. Fisher. *Statistical Methods for Research Workers*, pages 66–70. Springer New York, New York, NY, 1992. ISBN 978-1-4612-4380-9. doi: 10.1007/978-1-4612-4380-9_6. URL `https://doi.org/10.1007/978-1-4612-4380-9_6`.

N. Fruitwala. *Readout and Calibration of Large Format Optical / IR MKID Arrays and Applications to Focal Plane Wavefront Control.* PhD thesis, UCSB,

2021. URL `https://www.proquest.com/dissertations-theses/readout-calibration-large-format-optical-ir-mkid/docview/2597453009/se-2?accountid=14522`.

N. Fruitwala, P. Strader, G. Cancelo, T. Zmuda, K. Treptow, N. Wilcer, C. Stoughton, A. B. Walter, N. Zobrist, G. Collura, I. Lipartito, J. I. Bailey, and B. A. Mazin. Second generation readout for large format photon counting microwave kinetic inductance detectors. *Review of Scientific Instruments*, 91 (12):1–12, 2020. ISSN 10897623. doi: 10.1063/5.0029457.

J. Gao. *The Physics of Superconducting Microwave Resonators*. PhD thesis, UCSB, 2008. URL `https://thesis.library.caltech.edu/2530/`.

J. Gao, J. Zmuidzinas, B. A. Mazin, H. G. LeDuc, and P. K. Day. Noise properties of superconducting coplanar waveguide microwave resonators. *Applied Physics Letters*, 90(10):102507, 03 2007. ISSN 0003-6951. doi: 10.1063/1.2711770. URL `https://doi.org/10.1063/1.2711770`.

J. Gao, M. Daal, J. M. Martinis, A. Vayonakis, J. Zmuidzinas, B. Sadoulet, B. A. Mazin, P. K. Day, and H. G. Leduc. A semiempirical model for two-level system noise in superconducting microresonators. *Applied Physics Letters*, 92(21):212504, 05 2008. ISSN 0003-6951. doi: 10.1063/1.2937855. URL `https://doi.org/10.1063/1.2937855`.

J. Girkin. *A practical guide to optical microscopy*. CRC Press, London, England, June 2019.

E. D. R. R. P. Group. The 2021 ECFA detector research and development roadmap. Technical report, CERN, Geneva, 2020. URL `https://cds.cern.ch/record/2784893`.

G. Hong, S. Diao, J. Chang, A. L. Antaris, C. Chen, B. Zhang, S. Zhao, D. N. Atochin, P. L. Huang, K. I. Andreasson, C. J. Kuo, and H. Dai. Through-skull fluorescence imaging of the brain in a new near-infrared window. *Nature Photonics*, 8(9):723–730, Sep 2014. ISSN 1749-4893. doi: 10.1038/nphoton.2014.166. URL `https://doi.org/10.1038/nphoton.2014.166`.

I. Hughes and T. Hase. *Measurements and Their Uncertainties: A Practical Guide to Modern Error Analysis*. OUP Oxford, 2010. ISBN 9780199566327. URL `https://books.google.co.uk/books?id=AbEVDAAAQBAJ`.

J. P. A. Ioannidis. Why most published research findings are false. *PLOS Medicine*, 2(8):null, 08 2005. doi: 10.1371/journal.pmed.0020124. URL `https://doi.org/10.1371/journal.pmed.0020124`.

C. Jorel, P. Feautrier, and J.-C. Villegier. Tantalum stj for photon counting detectors. *IEEE Transactions on Applied Superconductivity*, 15(2):587–590, 2005. doi: 10.1109/TASC.2005.849949.

A. S. Karakoti, R. Shukla, R. Shanker, and S. Singh. Surface functionalization of quantum dots for biological applications. *Advances in Colloid and Interface Science*, 215:28–45, 2015. ISSN 0001-8686. doi: https://doi.org/10.1016/j.cis.2014.11.004. URL `https://www.sciencedirect.com/science/article/pii/S0001868614002887`.

M. Kobayashi, D. Kikuchi, and H. Okamura. Imaging of ultraweak spontaneous photon emission from human body displaying diurnal rhythm. *PLoS ONE*, 4(7):e6256, July 2009. ISSN 1932-6203. doi: 10.1371/journal.pone.0006256. URL `http://dx.doi.org/10.1371/journal.pone.0006256`.

T. Konno, S. Takasu, K. Hattori, and D. Fukuda. Development of an optical transition-edge sensor array. *Journal of Low Temperature Physics*, 199:27–33, 2020. ISSN 15737357. doi: 10.1007/s10909-020-02367-9. URL `https://doi.org/10.1007/s10909-020-02367-9`.

K. Kouwenhoven, D. Fan, E. Biancalani, S. A. de Rooij, T. Karim, C. S. Smith, V. Murugesan, D. J. Thoen, J. J. Baselmans, and P. J. de Visser. Resolving power of visible-to-near-infrared hybrid $\beta-\mathrm{Ta}/\mathrm{Nb}-\mathrm{Ti}-\mathrm{N}$ kinetic inductance detectors. *Phys. Rev. Appl.*, 19:034007, Mar 2023. doi: 10.1103/PhysRevApplied.19.034007. URL `https://link.aps.org/doi/10.1103/PhysRevApplied.19.034007`.

A. G. Kozorezov, A. F. Volkov, J. K. Wigmore, A. Peacock, A. Poelaert, and R. den Hartog. Quasiparticle-phonon downconversion in nonequilibrium superconductors. *Phys. Rev. B*, 61:11807–11819, May 2000. doi: 10.1103/PhysRevB.61.11807. URL `https://link.aps.org/doi/10.1103/PhysRevB.61.11807`.

M. Kurakado. Possibility of high resolution detectors using superconducting tunnel junctions. *Nuclear Instruments and Methods in Physics Research*, 196(1):275–277, 1982. ISSN 0167-5087. doi: https://doi.org/10.1016/0029-554X(82)90654-1. URL `https://www.sciencedirect.com/science/article/pii/0029554X82906541`.

J. A. Lau, V. B. Verma, D. Schwarzer, and A. M. Wodtke. Superconducting single-photon detectors in the mid-infrared for physical chemistry and spectroscopy. *Chemical Society Reviews*, 52:921–941, 2023. ISSN 14604744. doi: 10.1039/d1cs00434d.

P. Liu, X. Mu, X. D. Zhang, and D. Ming. The Near-Infrared-II Fluorophores and Advanced Microscopy Technologies Development and Application in Bioimaging. *Bioconjugate Chemistry*, 31(2):260–275, 2020. ISSN 15204812. doi: 10.1021/acs.bioconjchem.9b00610.

L. Lyons. Discovering the significance of 5 sigma, 2013.

B. A. Mazin. *Microwave Kinetic Inductance Detectors.* PhD thesis, UCSB, 2005.

B. A. Mazin. Superconducting Materials for Microwave Kinetic Inductance Detectors. *Handbook of Superconductivity*, pages 756–765, 2022. doi: 10.1201/9781003139638-58.

B. A. Mazin, S. R. Meeker, M. J. Strader, P. Szypryt, D. Marsden, J. C. van Eyken, G. E. Duggan, A. B. Walter, G. Ulbricht, M. Johnson, B. Bumble, K. O'Brien, and C. Stoughton. Arcons: A 2024 pixel optical through near-ir cryogenic imaging spectrophotometer. *Publications of the Astronomical Society of the Pacific*, 125(933):1348, nov 2013. doi: 10.1086/674013. URL `https://dx.doi.org/10.1086/674013`.

B. A. Mazin, E. Artigau, V. Bailey, C. Baranec, C. Beichman, B. Benneke, J. Birkby, T. Brandt, J. Chilcote, M. Chun, L. Close, T. Currie, I. Crossfield, R. Dekany, J. R. Delorme, C. Dong, R. Dong, R. Doyon, C. Dressing, M. Fitzgerald, J. Fortney, R. Frazin, E. Gaidos, O. Guyon, J. Hashimoto, L. Hillenbrand, A. Howard, R. Jensen-Clem, N. Jovanovic, T. Kotani, H. Kawahara, Q. Konopacky, H. Knutson, M. Liu, J. Lu, J. Lozi, B. Macintosh, J. Males, M. Marley, C. Marois, D. Mawet, S. Meeker, M. Millar-Blanchaer, S. Mondal, S. N. Bose, N. Murakami, R. Murray-Clay, N. Narita, T. S. Pyo, L. Roberts, G. Ruane, G. Serabyn, A. Shields, A. Skemer, L. Simard, D. Stelter, M. Tamura, M. Troy, G. Vasisht, J. K. Wallace, J. Wang, and S. Wright. Directly Imaging Rocky Planets from the Ground. *Bulletin of the American Astronomical Society*, 2019a. URL `http://arxiv.org/abs/1905.04275`.

B. A. Mazin, J. Bailey, J. Bartlett, C. Bockstiegel, B. Bumble, G. Coiffard, T. Currie, M. Daal, K. Davis, R. Dodkins, N. Fruitwala, N. Jovanovic, I. Lipartito, J. Lozi, J. Males, D. Mawet, S. Meeker, K. O'Brien, M. Rich, J. Smith, S. Steiger, N. Swimmer, A. Walter, N. Zobrist, and J. Zmuidzinas. Optical and near-IR microwave kinetic inductance detectors (MKIDs) in the 2020s. *Astro2020 APC White Pape*, 2019b. URL `http://arxiv.org/abs/1908.02775`.

S. R. Meeker. *DARKNESS: The first microwave kinetic inductance detector integral field spectrograph for exoplanet imaging*. University of California, Santa Barbara, 2017.

A. Millett-Sikking and A. York. AndrewGYork/high_na_single_objective_lightsheet: Work-in-progress, 2019.

M. Nagai, Y. Murayama, T. Nitta, H. Kiuchi, Y. Sekimoto, H. Matsuo, W. Shan, M. Naruse, and T. Noguchi. Resonance Spectra of Coplanar Waveguide MKIDs Obtained Using Frequency Sweeping Scheme. *Journal of Low Temperature Physics*, 199(1-2):250–257, 2020. ISSN 15737357. doi: 10.1007/s10909-019-02262-y. URL `https://doi.org/10.1007/s10909-019-02262-y`.

P. Nicaise, J. Hu, J.-M. Martin, S. Beldi, C. Chaumont, P. Bonifacio, M. Piat, H. Geoffray, and F. Boussaha. Investigation of optical coupling in microwave kinetic inductance detectors using superconducting reflective plates. *Journal of Low Temperature Physics*, 209(5):1242–1248, Dec 2022. ISSN 1573-7357. doi: 10.1007/s10909-022-02789-7. URL `https://doi.org/10.1007/s10909-022-02789-7`.

Nikon MicroscopyU Website. The diffraction barrier in optical microscopy, 2023. URL `https://www.microscopyu.com/techniques/super-resolution/the-diffraction-barrier-in-optical-microscopy`. Accessed: 2021-01-01.

K. Niwa, T. Numata, K. Hattori, and D. Fukuda. Few-photon color imaging using energy-dispersive superconducting transition-edge sensor spectrometry. *Scientific Reports*, 7:1–7, 2017. ISSN 20452322. doi: 10.1038/srep45660.

R. Nuzzo. Scientific method: Statistical errors. *Nature*, 506:150–2, 02 2014. doi: 10.1038/506150a.

K. O'Brien, B. A. Mazin, S. McHugh, S. Meeker, and B. Bumble. ARCONS: A highly multiplexed superconducting UV-to-Near-IR camera. *Proceedings of the International Astronomical Union*, 7(S285): 385–388, 2011. ISSN 17439213. doi: 10.1017/S1743921312001159.

E. O'Connor, A. Shearer, and K. O'Brien. Energy-sensitive detectors for astronomy: Past, present and future. *New Astronomy Reviews*, 87:101526, 2019. ISSN 1387-6473. doi: https://doi.org/10.1016/j.newar.2020.101526. URL `https://www.sciencedirect.com/science/article/pii/S1387647320300038`.

Z. Pan, K. R. Dibert, J. Zhang, P. S. Barry, A. J. Anderson, A. N. Bender, B. A. Benson, T. Cecil, C. L. Chang, R. Gualtieri, J. Li, M. Lisovenko, V. Novosad, M. Rouble, G. Wang, and V. Yefremenko. Noise Optimization for MKIDs with Different Design Geometries and Material Selections. *Instrumentation and Methods for Astrophysics*, 0(0):1–8, 2023.

S. Pandey and D. Bodas. High-quality quantum dots for multiplexed bioimaging: A critical review. *Advances in Colloid and Interface Science*, 278:102137, 2020. ISSN 0001-8686. doi: https://doi.org/10.1016/j.cis.2020.102137. URL `https://www.sciencedirect.com/science/article/pii/S0001868619302969`.

P. Park, D. Wong-Campos, D. G. Itkis, Y. Qi, H. Davis, J. B. Grimm, S. E. Plutkis, L. Lavis, and A. E. Cohen. Dendritic voltage imaging reveals biophysical basis of associative plasticity rules. *bioRxiv*, 2023. doi: 10.1101/2023.06.02.543490. URL `https://www.biorxiv.org/content/early/2023/06/02/2023.06.02.543490`.

J. B. Pawley. *Fundamental Limits in Confocal Microscopy*, pages 20–42. Springer US, Boston, MA, 2006. ISBN 978-0-387-45524-2. doi: 10.1007/978-0-387-45524-2_2. URL `https://doi.org/10.1007/978-0-387-45524-2_2`.

A. V. &. J. Z. Peter K. Day, Henry G. LeDuc, Benjamin A. Mazin. A broadband superconducting detector suitable for use in large arrays. *Nature*, 425(October):12–14, 2003. doi: 10.1038/nature01981.1.

N. Rando, A. Peacock, A. van Dordrecht, C. Foden, R. Engelhardt, B. Taylor, P. Gare, J. Lumley, and C. Pereira. The properties of niobium superconducting tunneling junctions as x-ray detectors. *Nuclear Instruments and Methods in Physics Research Section A: Accelerators, Spectrometers, Detectors and Associated Equipment*, 313(1):173–195, 1992. ISSN 0168-9002. doi: https://doi.org/10.1016/0168-9002(92)90095-L. URL `https://www.sciencedirect.com/science/article/pii/016890029290095L`.

E. Slenders, E. Perego, M. Buttafava, G. Tortarolo, E. Conca, S. Zappone, A. Pierzynska-Mach, F. Villa, E. M. Petrini, A. Barberis, A. Tosi, and G. Vicidomini. Cooled spad array detector for low light-dose fluorescence laser scanning microscopy. *Biophysical Reports*, 1:100025, 2021. ISSN 26670747. doi: 10.1016/j.bpr.2021.100025. URL `https://doi.org/10.1016/j.bpr.2021.100025`.

A. M. Smith, H. Duan, A. M. Mohs, and S. Nie. Bioconjugated quantum dots for in vivo molecular and cellular imaging. *Advanced Drug Delivery Reviews*, 60(11):1226–1240, 2008. ISSN 0169-409X. doi: https://doi.org/10.1016/j.addr.2008.03.015. URL `https://www.sciencedirect.com/science/article/pii/S0169409X08000987`. Inorganic Nanoparticles in Drug Delivery.

J. P. Smith, B. A. Mazin, A. B. Walter, M. Daal, J. Bailey, C. Bockstiegel, N. Zobrist, N. Swimmer, S. Steiger, and N. Fruitwala. Flexible coaxial ribbon cable for high-density superconducting microwave device arrays. *IEEE Transactions on Applied Superconductivity*, 31(1):1–5, 2021. doi: 10.1109/TASC.2020.3008591.

S. Steiger, J. I. Bailey, N. Zobrist, N. Swimmer, R. Dodkins, K. K. Davis, and B. A. Mazin. The mkid pipeline: A data reduction and analysis pipeline for uvoir mkid data. *The Astronomical Journal*, 163 (5):193, apr 2022. doi: 10.3847/1538-3881/ac5833. URL `https://dx.doi.org/10.3847/1538-3881/ac5833`.

F. Stelzle, M. Rohde, M. Riemann, N. Oetter, W. Adler, K. Tangermann-Gerk, M. Schmidt, and C. Knipfer. Autofluorescence spectroscopy for nerve-sparing laser surgery of the head and neck—the influence of laser-tissue interaction. *Lasers in Medical Science*, 32(6):1289–1300, Aug 2017. ISSN 1435-604X. doi: 10.1007/s10103-017-2240-8. URL `https://doi.org/10.1007/s10103-017-2240-8`.

N. Swimmer, W. H. Clay, N. Zobrist, and B. A. Mazin. Characterizing the dark count rate of a large-format mkid array. *Optics Express*, 31(6), 2023. doi: 10.1364/OE.485003. URL `https://par.nsf.gov/biblio/10400973`.

P. Szypryt. *Development of Microwave Kinetic Inductance Detectors for Applications in Optical to Near-IR Astronomy*. PhD thesis, UCSB, 2017. URL `http://web.physics.ucsb.edu/~bmazin/Papers/szypryt_dissertation.pdf`.

M. Tinkham. *Introduction to Superconductivity*. Dover Publications, 2 edition, June 2004. ISBN 0486435032. URL `http://www.worldcat.org/isbn/0486435032`.

A. Walter, B. B. Mazin, C. Bockstiegel, N. Fruitwala, P. Szypryt, I. Lipartito, S. Meeker, N. Zobrist, G. Collura, G. Coiffard, P. Strader, O. Guyon, J. Lozi, and N. Jovanovic. MEC: the MKID exoplanet camera for high contrast astronomy at Subaru (Conference Presentation). In C. J. Evans, L. Simard, and H. Takami, editors, *Ground-based and Airborne Instrumentation for Astronomy VII*, volume 10702, page 107020V. International Society for Optics and Photonics, SPIE, 2018. doi: 10.1117/12.2311586. URL `https://doi.org/10.1117/12.2311586`.

J. Zmuidzinas. Superconducting microresonators: Physics and applications. *Annual Review of Condensed Matter Physics*, 3(1):169–214, 2012. ISSN 19475454. doi: 10.1146/annurev-conmatphys-020911-125022.

N. Zobrist, W. H. Clay, G. Coiffard, M. Daal, N. Swimmer, P. Day, and B. A. Mazin. Membraneless phonon trapping and resolution enhancement in optical microwave kinetic inductance detectors. *Phys. Rev. Lett.*, 129:017701, Jul 2022. doi: 10.1103/PhysRevLett.129.017701. URL `https://link.aps.org/doi/10.1103/PhysRevLett.129.017701`.